Ultraselective Nanocatalysts in Fine Chemical and Pharmaceutical Synthesis

By

Mr. Chun Wong Aaron Chan (MSci)

410166

University College

A dissertation submitted for the degree of Doctor of Philosophy at the Inorganic Chemistry Laboratory, Department of Chemistry, University of Oxford

2012

Ultraselective Nanocatalysts in Fine Chemical and Pharmaceutical Synthesis

By

Mr. Chun Wong Aaron Chan (MSci)

410166

University College

Supervisor

Prof. S. C. Edman Tsang

Industrial Supervisor

Dr. James Cookson

Internal Assessor

Prof. John Foord

A dissertation submitted for the degree of Doctor of Philosophy at the Inorganic Chemistry Laboratory, Department of Chemistry, University of Oxford

2012

TABLE OF CONTENTS

DECLARATION

I confirm that this is my own work and the use of all material from other sources has been properly and fully acknowledged.

C. W. Aaron Chan

DEDICATION

To my wife Weijie and parents.

ACKNOWLEDGEMENTS

First I would like to thank Prof. S.C. Edman Tsang my supervisor for the opportunity to work in his laboratory, for his advice, help and guidance throughout my research project. My industrial sponsor Dr. James Cookson (Johnson Matthey Technology Centre) for his discussions and assistance, especially the catalyst screening that saved me a lot of weeks of testing. I like to thank Dr. Peter Bishop (Johnson Matthey Technology Centre), University of Oxford, Engineering and Physical Science Research Council for the funding, chemicals, precious metals and use of testing equipments during my D.Phil.

My research documented herein would not have been possible without their expert assistance on the experimental techniques which I greatly relied on. I like to thank Mr. Chris Brown (Johnson Matthey Technology Centre) for his help on testing and analysis of new catalysts and reactions. Dr. Kin Yip Tam (AstraZeneca) for his kinetic modelling. Dr. Nick Rees and Miss. Tina Jackson (CRL, University of Oxford) for NMR training and sample acquisition. Dr. Montree Sawangphruk, Dr. Jingping Hu and Prof. John Foord (PTCL, University of Oxford) for their assistance in XPS analysis. Dr. Crina Corbos (Johnson Matthey Technology Centre) for EXAFS analysis. Dr. Richard Smith (Johnson Matthey Technology Centre) for XPS analysis. Dr. Gregory Goodlet and Dr. Jingshan Dong (Johnson Matthey Technology Centre) for TEM characterisations. Dr. Nathan Barrow (Johnson Matthey Technology Centre) for Solid State NMR. Dr. G. Nnorom-Junior (Johnson Matthey Technology Centre) for ICP-ES. Dr. John Hutchinson (Materials, University of Oxford) for training on the TEM. Dr. Phil Wiseman (ICL, University of Oxford) for training on the XRD. Dr.

Robert Jacobs (CRL, University of Oxford) for training on the BET. Mr Nenad Vranješ for electrical and electronics testing and repairs on equipments. Mr. Ashleigh Hewson for lab and equipment service. Mr. Tom Bradshaw and Mr. Keith Waters for IT support. Mrs Terri Adams for glassblower service. Mr Charlie Evans and Mr Les Hill for workshop service. Mr Bill Thompson, Mr Leigh Bennett and Mr Levi Dash for stores assistance. Mrs Pam Cox and Mrs Trish Traynor for administrative assistance. Miss. Yaling Xie (Dalian University of Technology, China) for her collaborations to my catalyst testing. Part II student Mr. Hanif Mahadi for his collaborations to my Pd-B work. Dr. Karaked Tedsree (Burapha University, Thailand) and Mr. Simon Jones for general discussions. Dr. William Oduro for his help and discussions during my start of my D.Phil. Dr. Kai Man Kerry Yu for his great technical expertise on analytical instruments and general advice, who saved me a lot of man hours in the lab. Finally the Tsang group of past and present: Tom Chapman, Terry Wu, Clive Eley, Amy Kolpin, Weiyi Tong, Hongwei Yang, Abdullah Khan, Steven Zhou, Aaron Lau, Max Gordon-Brown, Louis Mather, Chris Newman, Emma Penn, Bow Luksirikui, Vivian Chang, Dr. Zhao Yun, Dr. Gordon Lee, Dr. Chih-Hao Yu, Dr. Ali Al-Saadi, Dr. Nadia Acerbi, Dr. Maria Hurtado, Dr. Teresa Valdes-Solis, Anna Mclaren, Ben Van Zwanenberg.

ABSTRACT

Surface catalysed reactions play an important role in chemical productions. Developments of catalyst requiring high activity whilst improving on product selectivity can potentially have a profound effect in the chemical industry. Traditional catalyst modifications were focused on tuning the size, shape and foreign metal doping to form well defined metal nanoparticles of unique functionalities. Here, we show new approach to engineering of metal nanocatalysts *via* a subsurface approach can modify the chemisorption strength of adsorbates on the surface. Carbon modified nanoparticles were synthesised using glucose to stabilise Pd nanoparticles at a molecular level. Upon heat treatment, the carbonised glucose encapsulated the Pd nanoparticles with carbon atoms take residence in the octahedral holes (15 at.%). These materials were tested in liquid phase stereoselective hydrogenations of 3-hexyn-1-ol and 4-octyne. The former has importance in the fragrance industry towards the production of leaf fragrance alcohol. It was shown for the first time that the geometrically and electronically modified Pd with interstitial carbon atoms reduced the adsorption energy of alkenes, ultimately leading to higher reaction selectivity. Boron modified Pd nanoparticles was synthesised using BH_3.THF in the liquid phase. The material possess high B interstitial saturation (20 at.%), which can be synthesised for the first time below 100°C. These materials were tested in the liquid phase selective hydrogenation of various alkynes and 2-chloronitrobenzene, of which the latter has importance in the pesticides industry. Kinetic modelling on the hydrogenation of 4-octyne suggests these subsurface occupied B does play a pivotal role on increasing the reaction selectivity, as removal of these species lead to decreased selectivity. Au nanoparticles were synthesised and characterised using

$H^{13}COOH$ NMR. The new liquid NMR characterisation method is successfully applied to examine the chemisorption strength of metal nanoparticles. An attempt to synthesise PVP capped B modified Pd nanoparticles with the above NMR characterisation was investigated. It is believed the examples of subsurface atom modifications as shown here may offer future catalyst developments in this area.

Key words: Heterogeneous catalyst, Selective hydrogenation, Liquid phase, Subsurface, Interstitial, Alkynes, Kinetic modelling, 2-chloronitrobenzene, Formic acid, Nuclear magnetic resonance.

LIST OF FIGURES

LIST OF SCHEMES

LIST OF TABLES

normalised parameters, ∑semi/∑iso and ∑semi/∑full, is based on various fittings using different ratios of adsorption constants.

Table 5-11 GC analysis for the hydrogenation of 3-hexyn-1-ol. [a] Sample analysis collected before the change in hydrogen uptake. [b] Sample collected at the end of hydrogen uptake. THEL = *trans*-hexen1-ol. CHEL = *cis*-hexen-1-ol. HAL = 1-hexanol.

Table 5-12 Hydrogenation of *o*-CNB. [a] Sample analysis collected before the change in hydrogen uptake. [b] Sample collected at the end of hydrogen uptake. All samples collected were at 100% conversion of *o*-CNB.

Table 5-13 Hydrogenation of *o*-CNB. Samples collected at the end of hydrogen uptake. All samples collected were after 100% conversion of *o*-CNB.

Table 5-14 Hydrogenations of non B doped catalysts and 25eq. B doped catalysts in: [b] *o*-CNB; [c] *m*-CNB; [d] *p*-CNB. [a] Rates were determined at time between 3 to 18 mins on the hydrogen uptake curve (Fig. XX). All samples were analysed at the end of hydrogen uptake at full conversion of their respective CNB.

Table 6-1 Growth conditions used to prepare larger Au nanoparticles. [a]Au seed solution was basified with K_2CO_3 (0.03 mmol).

Table 6-2 Lattice parameter calculated from PXRD for above samples and the atomic ratio of B for colloidal PVP-Pd-^{int}B.

Table 6-3 ^{13}C NMR values for the formate species observed for the PVP-Pd sample. Ratios of different formate modes were calculated by fitting the total peak area from the raw data.

Table 6-4 ^{13}C NMR values for the formate species observed for the PVP-Pd-^{int}B sample.

Table 6-5 Turnover frequencies for the HCOOH decomposition for 3% Pd/C and 3% Pd-^{int}B/C catalysts assuming total dehydrogenation of HCOOH to H_2 and CO_2 at room temperature. 10.41 mg of Pd metal was used in the reaction. Decomposition rates were based on gas evolved at 30 min of the reaction. The density of the surface Pd atoms was determined from CO chemisorption measurements.

LIST OF SYMBOLS AND ABBREVIATIONS

a_0	Lattice parameter
A	Arrhenius prefactor
C	Concentration
d_{CO}	Particle size measured by CO chemisorption
d_{TEM}	Particle size measured by TEM
D_{CO}	Dispersion measured by CO chemisorption
D_P	Pore size distribution
E_A	Activation Energy
ΔE_0	Inner potential correction in eV
ΔG	Change in Gibbs free energy
ΔH	Change in enthalpy
$\Delta_{ads}H$	Change in enthalpy of adsorption
ΔS	Change in Entropy
N_c	Coordination number
T	Temperature
r	Rate
k	Rate constant
R	Ideal gas constant
R	Interatomic distance in angstroms
S_c	Critical saturation limit
S_{BET}	Surface area of support measured by the Brunauer-Emmett-Teller method
νp	Total pore volume in $cm^3\ g^{-1}$
γ	Surface free energy

σ^2	Debye-Waller factor in angstroms
λ	wavelength
V_{sd}	Coupling matrix element
AN	Aniline
APXPS	Angle resolved x-ray photoelectron spectroscopy
ATR-IR	Attenuated total reflectance infrared spectroscopy
B_3D	2,-Butyne-1,4-diol
B_xO_y	Non-stiochiometric boron oxide
BET	Brunauer−Emmett−Teller
BF	Bright field
BH_3.THF	Borane tetrahydrofuran solution
CAN	Chloroaniline
CCD	Charged couple device
CHEL	*cis*-Hexen-1-ol
CNB	Chloro-nitrobenzene
CTAB	Cetyltrimethylammonium bromide
CN	Coordination number
DCM	Dichloromethane
DFT	Density functional theory
DOS	Density of states
DPA	Diphenylacetylene
DRIFTS	Diffuse reflectance infrared fourier transform spectroscopy
EC-NMR	Electrochemical nuclear magnetic resonance
EDX	Energy dispersive x-ray spectroscopy
EELS	electron energy loss spectroscopy

E_F	Fermi level
EG	Ethylene glycol
EGA	Evolved gas analysis
EtOH	Ethanol
EQ	Environmental quotient
EXAFS	Extended x-ray absorption fine structure
FDA	Food and Drug Administration
FID	Flame ionisation detector
FTIR	Fourier transform infrared spectroscopy
FWHM	Full width half maximum
GC	Gas chromatography
GC/MS	Gas chromatography mass spectrometry
HAADF	High angle annular dark field
HAL	Hexanol
$H^{13}COOH$	Carbon-13 labelled formic acid
ICP-ES	Inductive coupled plasma emission spectroscopy
ISS	Ion scattering spectroscopy
JMTC	Johnson Matthey Technology Centre
L-H	Langmuir-Hinshelwood
LMTO	Linear muffin-tin orbitals
MAS	Magic angle spinning
MBY	2-Methyl-3-butyn-2-ol
MIR	Multiple internal reflection
MeOH	Methanol
MSR	Methane steam reforming

MWCO	Molecular weight cut off
NMR	Nuclear magnetic resonance
ORR	Oxygen reduction reaction
PA	Phenylacetylene
PEMFC	Polymer electrolyte membrane fuel cell
Pd/C	Palladium supported on carbon
Pd-B/C	Palladium modified with boron supported on carbon
Pd-C	Palladium modified with interstitial carbon
Pd_xB_y	Ordered palladium boron alloys
Pd-^{int}B	Palladium modified with interstitial boron
Pd-^{int}B/C	Palladium modified with interstitial boron supported on carbon
PdAu/C	Palladium modified with gold supported on carbon
PdGluC400	Hydrothermally treated Palladium glucose catalyst heat treated at 400°C
PdGluC400[O] catalyst	H_2O_2/NH_4OH Hydrothermally treated Palladium glucose heated at 400°C, followed by mild oxidation using hydrogen peroxide and ammonium hydroxide
$PdPb/CaCO_3$	Lindlar's catalyst
PVP	Polyvinylpyrrolidone
PVP-Ru	Ruthenium capped with polyvinylpyrrolidone
PVP-Au	Gold capped with polyvinylpyrrolidone
PVP-Pd	Palladium capped with polyvinylpyrrolidone
PVP-Pd-^{int}B	Palladium modified with boron capped with polyvinylpyrrolidone
ppm	Parts per million
PTFE	Polytetrafluoroethylene

PXRD	Powder x-ray diffraction
rpm	rotations per minute
RT	Room temperature
SAED	Selected area electron diffraction
SFG-IR	Sum frequency generation infrared spectroscopy
SMSI	Strong metal support interaction
SPR	Surface plasmon resonance
SSNMR	Solid state nuclear magnetic resonance
STEM	Scanning transmission electron microscopy
TCD	Thermo conductivity detector
TDS	Temperature desorption spectroscopy
TEM	Transmission electron microscopy
TGA	Thermogravimetric analysis
THF	Tetrahydrofuran
THEL	*trans*-Hexen-1-ol
TOF	Turnover frequency
TON	Turnover number
TPD/R/O	Temperature programmed desorption/reduction/oxidation
TPR-MS	Temperature programmed reduction mass spectrometry
UHV	Ultra high vaccum
UPS	Ultraviolet photoelectron spectroscopy
UV-Vis	Ultraviolet-Visible spectroscopy
WGS	Water gas shift
XAS	X-ray absorption spectroscopy
XANES	X-ray absorption near edge structure

XPS	X-ray photoelectron spectroscopy
XRD	X-ray diffraction

LIST OF PUBLICATIONS

1. C. W. A. Chan, Y. Xie, N. Cailuo, K. M. K. Yu, J. Cookson, P. Bishop and S. C. Tsang, *Chem. Commun.*, 2011, **47**, 7971-7973.

2. C. W. A. Chan, K. Y. Tam, J. Cookson, P. Bishop and S. C. Tsang, *Catal. Sci. Technol.*, 2011, **1**, 1584-1592. Selected as Hot Article in the themed issue 'Heterogeneous catalysis for Fine Chemicals'. Graphical illustration selected as an Inside Front Cover.

3. K. Tedsree, C. W. A. Chan, S. Jones, Q. Cuan, W.-K. Li, X.-Q. Gong and S. C. E. Tsang, *Science*, 2011, **332**, 224-228.

4. K. Tedsree, T. Li, S. Jones, C. W. A. Chan, K. M. K. Yu, P. A. J. Bagot, E. A. Marquis, G. D. W. Smith and S. C. E. Tsang, *Nat. Nanotechnol*., 2011, **6**, 302-307.

CHAPTER 1 - INTRODUCTION

1.1 CATALYSIS

Catalysis makes a significant contribution to the modern world. It is estimated that 80% of all commercially produced chemical processes will include one catalytic step.[1] The global market for the chemical industry was estimated at around $2.4 trillion in 2010.[2] Therefore, it is evident that the production of many chemicals has been made possible through the application of catalysis. The continuing contribution of catalysis in the scientific community is recognised by its rapid growth in the last 30 years (Fig. 1-1).

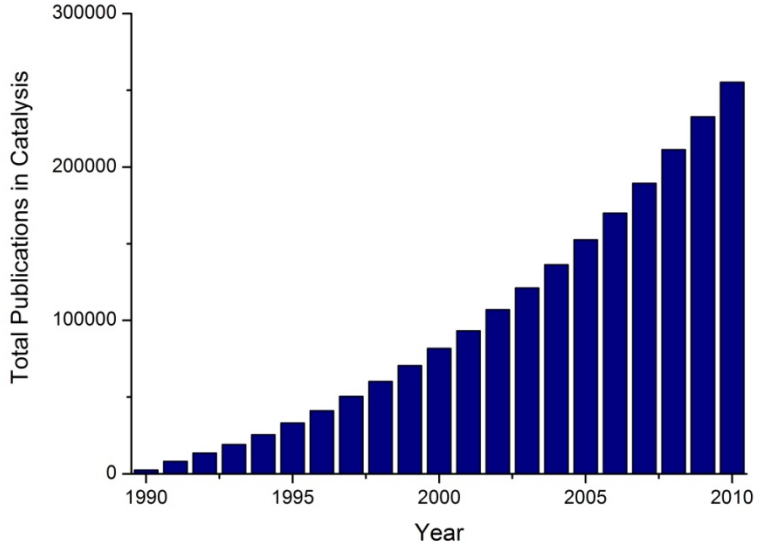

Fig. 1-1 Cumulative total publications in the last 30 years by searching the term ‘catalysis’ on Thomson Reuters Web of Knowledge.

The word ‘catalysis’, first coined by Jöns Jakob Berzelius in 1836, is derived from Greek ‘Katalusis’ meaning ‘wholly loosening’ or ‘dissolution’.[3] This was followed by Armstrong proposing the word ‘catalyst’ in 1885.[4] The scientific definition of a catalyst was defined by Ostwald in 1895 as a substance that accelerates the rate of a reaction, is not consumed itself and does not change the properties of the equilibrated state. It does so by changing height of the activation barrier. The first account of the catalytic phenomenon was observed by Davy and Döbereiner in the

oxidation of hydrogen in the presence of air using platinum, of which Döbereiner built the tinderbox to produce flame in the early 19th century. Since then, a number of developments in catalysis have led to major societal change:

i) The Contact process (1831) for the production of sulphuric acid.

ii) The Haber process (1913) for the synthesis of ammonia from nitrogen using potassium promoted iron catalyst.

iii) Ostwald process (1906) on ammonia oxidation to nitric oxide towards production of nitric acid.

iv) Ethylene hydrogenation over nickel catalyst by Sabatier (1902).

v) The Fisher-Tropsch process (1938) for the synthesis of synthetic fuels.

vi) Naphtha reforming (1940s) for the production of unleaded gasoline to increase the octane number in the fuel stock, omitting the use of lead additive.

1.1.1 TYPES OF CATALYSIS

Catalysis is a broad area and can be divided into three sub-sections:

- Homogeneous catalysis.
- Heterogeneous catalysis.
- Biocatalysis.

In homogeneous catalysis, both the catalyst and the reactants (or substrate molecules) are in the same phase (predominantly liquid). Due to the challenges in process operation and catalyst handling, homogeneous catalysis accounts for less than ten percent of the global catalyst market. The catalyst usually goes *via* several different structures, termed catalytic intermediates, throughout the reaction. Eventually, the catalyst reaches the end of the cycle and is regenerated and ready to catalyse the reaction with new substrate molecules. A classic example is the

formation of carbon-carbon bond forming reactions by palladium complexes.[5] Many homogeneous catalysts involve the use of a ligand stabilised metal atom. By choosing the right metal and ligand, one can tailor the activity and selectivity of the catalyst. In addition, chiral ligands can be utilised to tune the stereospecificity for a given reaction. Another burgeoning field in this area is organocatalysis, where the catalyst consists of non-metal elements.[6] Examples involve the use of secondary amines to perform enamine or iminium catalysis, while chiral organocatalyst opens up avenue for asymmetric catalysis. One classic case is using proline in aldol reactions.[6]

In biocatalysis, enzymes or bioorganisms are used as nature's catalyst. Currently, Biocatalysis contributes to only about two percent of the world catalyst market; but recently this market has been growing rapidly. They are generally large structures, which can result in a stereospecific active centre(s) making highly specific and efficient catalysts. Furthermore, reactions occur under mild conditions, normally at room temperature, atmospheric pressure and in aqueous conditions.

In contrast, in heterogeneous catalysis, the catalyst and reactants are in different phases. Heterogeneous catalysis accounts for about 80 percent of the world catalyst market. Catalysts are usually in solid form with the reactants either in the gas and/or liquid phase. In most cases, solid catalysts are impenetrable so reactions occur on the surface. Typically, catalysts consist of transition or noble metals in their nano-sized regime, in order to maximise its surface area. To maintain even catalyst dispersion, it is commonly supported on porous materials, such as silica or alumina.

Development of heterogeneous catalyst research encompasses three core areas:

i) Development of a suitable catalyst.

ii) Elucidation of reaction mechanism.

iii) Implementation of catalytic process in an industrial scale.

Of the three core areas, the technical implementations of applied catalysts remain at the heart of catalyst research, with a multi-disciplinary approach between chemistry and engineering being required. For these reasons, it is not surprising that the implementation of a new catalyst requires high capital input and takes years from research to production at an industrial scale.

1.2 HETEROGENEOUS CATALYSIS

As discussed in the previous section, catalysis occurs by providing an alternative pathway or mechanism by lowering the overall lower activation energy (E_A) of a reaction. The decrease in activation energy increases the fraction of molecules able to react, in order to overcome the activation barrier that would otherwise be too high for a non-catalysed counterpart and thus, a fast rate of reaction can be achieved (Fig. 1-2). The lowering of activation energy by a catalyst means that reactions can proceed at lower temperatures, hence saving energy costs. Furthermore, lower levels of undesirable products are formed which makes the process more economically attractive. Whilst a catalyst reduces the time needed for the reaction to achieve thermodynamic equilibrium, itself cannot shift the position of that equilibrium. For this reason, a catalyst cannot catalyse a thermodynamically disfavoured reaction.

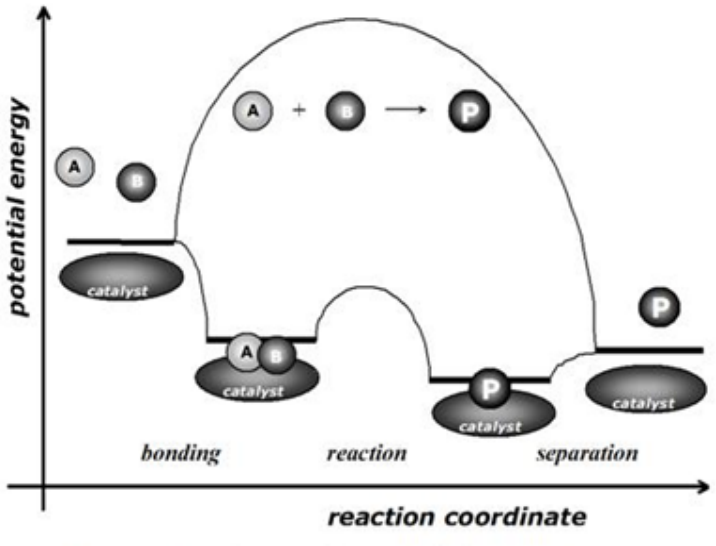

Fig. 1-2 A potential energy diagram for a heterogeneous catalytic reaction, with gaseous reactants and products and solid catalyst.[7]

In surface catalysed processes, the substrates comes in contact or adsorb (or chemisorption) on the catalyst surface. Chemical bonds are broken and the adsorbed substrates rearrange themselves on a specific ensemble of surface sites, otherwise referred to as active sites, forming new bonds. The electronic properties of metal atoms can also influence the adsorption and subsequent activation of substrates. The performance of a catalyst often depends on its structure, such as particle size and ensemble, as well as electronic effects. The newly formed products then desorb and diffuse off the catalyst surface, thus allowing more substrates to diffuse and adsorb onto the catalyst for the next catalytic cycle.

According to thermodynamics, any surface chemical conversions will favour a state with the lowest Gibbs free energy, provided there are no other factors that constrain it from reaching a global equilibrium. The relationship between Gibbs energy, enthalpy and entropy is given by:

$$\Delta G = \Delta H - T\Delta S$$

Therefore for a given process, that allows spontaneous change to occur, the change in Gibbs energy must be negative. Specifically, chemical bonds are broken by many surface processes, for example the dissociation of dihydrogen to atomic hydrogen adsorbed on the metal. Surface adsorption therefore decreases the overall entropy and is energetically disfavoured, unless it is accompanied by a change in enthalpy. Therefore, $\Delta_{ads}H$ must be negative (exothermic) for spontaneous adsorption.[4]

For an efficient catalyst, the substrates are required to adsorb sufficiently strongly on the metals surface, react and the product desorb relatively quickly for a fast catalytic cycle. The balance between the strength of chemisorption and product desorption is referred to as the Sabatier volcano principle (Fig. 1-3).[8] If the substrate adsorbs too strongly then it is unable break the chemisorption bond between the substrate and the metal, hence becoming unreactive. A substrate that forms such strong bonds on metal surfaces can be classified as catalytic poisons, such as CO. On the other hand, if the substrate adsorb too weakly then it only results in a very small surface coverage, resulting in a slow catalytic turnover. Therefore, a catalyst of high activity is a compromise between those two effects.

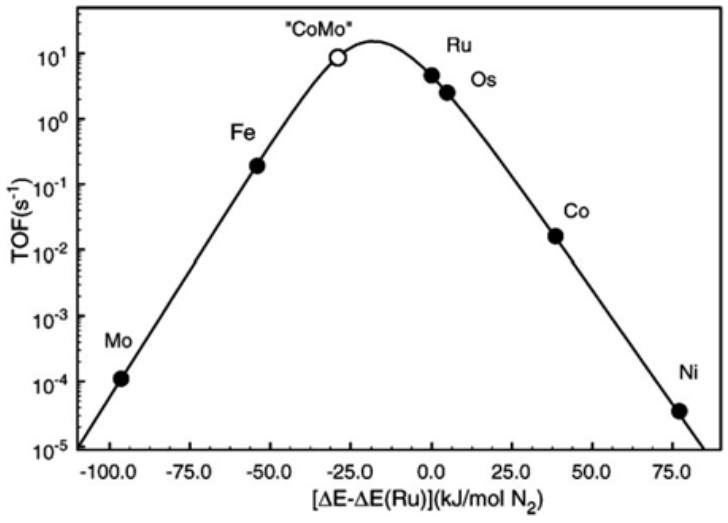

Fig. 1-3 An illustration of a Sabatier volcano curve. Calculated turnover frequencies for ammonia synthesis as a function of the adsorption energy of nitrogen.[8]

1.2.1 KINETICS

Reaction kinetics is the study of rates of chemical processes. This is complex in a surface catalysed reaction, as most surface processes are bimolecular in nature. In the simplest hypothetical chemical conversion:

$$\mathrm{A} + \mathrm{B} \rightarrow \mathrm{C}$$

The overall rate of reaction, *r*, depends on the concentration of reactants, C_A and C_B. The rate expression can be written as:

$$r = kC_A^a C_B^b$$

where *k* is the rate constant and the exponential terms *a* and *b* are the power rate laws for the reaction. The overall rate constant only reflects the rate determining step (RDS), therefore it may precede all other possible elementary steps. Although the rate constant may change upon variations in temperature, pressure, concentrations, catalyst structure and it may also reflect changes in the reaction mechanism.[9] Despite of these effects, the value *k* can be determined using the Arrhenius expression:

$$k = A\, e^{(-\frac{\Delta E}{RT})}$$

where *A* is the pre-exponential prefactor and ΔE is the apparent activation energy. On a solid catalyst surface, the scenario is more complicated as one or more reactants (e.g. A and B above) must adsorb onto the catalyst surface, migrate to each other, react to give product C, and desorb off the surface. This situation, where A and B both adsorb on the surface and react to form C, is known as the Langmuir-Hinshelwood mechanism. This is the most common model used to define surface processes, as many substrates are first activated on the catalyst surface followed by their combination to form the product.

A key parameter for comparing different catalytic materials is the rate (speed) of the reaction and there are a number of ways of representing this. In a surface catalysed reaction:

i) The specific rate is the rate divided by the weight of the catalyst.

ii) The areal rate is the rate divided by the catalyst surface area.

iii) Turnover frequency (TOF), molecules of product per unit time per surface atom or unit surface area of the catalyst.

iv) Turnover number (TON), expressed as molecules of product per surface atom or unit surface area of the catalyst.

TOFs are usually derived from the initial rate of reaction, a high initial rate may result in an overall lower TOF due to factors such as catalyst deactivation, where as a higher TOF can be due to changes in catalyst morphology or conformation during a catalytic reaction.

1.2.2 SELECTIVITIES

The activity of a catalyst is a key parameter; it had been the key driver to catalyst research in the past 50 years. Currently, in the 21st century, more emphasis is dedicated towards the enhancement of the selectivity of a reaction because an unselective catalyst can result in large amounts of side-products, which pushes up separation and hence production costs. Therefore, the design of a catalyst to achieve 100% selectivity to the desired product whilst maintaining high activity can be regarded as the holy grail in heterogeneous catalysis.

In general, there are three types of selectivity:

i) Chemoselectivity.

ii) Regioselectivity.

iii) Stereoselectivity.

Chemoselectivity is driven by selective conversion of one type of functional group over another. Regioselectivity can be classified as the selective positional formation/abstraction of one bond over another on a molecule. Stereoselectivity is classified as the preference to form one type of stereoisomer over another to form a new stereocentre. This category can be further divided into enantioselectivity (one chiral centre is formed) and diastereoselectivity (two chiral centres formed relative to one another).

1.2.3 DEACTIVATION

Catalysts are prone to deactivation over the course of their catalytic life cycles. Catalytic activity and/or selectivity may deteriorate specifically during operation conditions under high temperature and pressure. Catalyst deactivations range from metal evaporation, leaching, reduction, oxidation, corrosion, change in active sites during operation, coking, poisoning or sintering.[10] The poisoning of the metal surface can also be attributed to strong adsorption of impurities such as S derivatives or CO. Sintering (*i.e.* particle growth and subsequent loss of surface area) is the result of the thermodynamic stability of metal nanoparticle, due to their high surface area to volume ratios. They coalescence/agglomerate together to form larger particles, hence losing their catalytic active sites. Some deactivations are reversible; in the case of coking the catalyst can be regenerated. In contrast, others are irreversible and will require a fresh batch of catalyst. As a result, an industrial catalyst has a limited lifetime.

1.3 SYNTHESIS OF NANOPARTICLES

Catalysis is a surface phenomena, for efficient use of the metal surface it must have a high dispersion *i.e.* a high ratio of surface atoms to the total metal atoms. Furthermore, a small size is preferable as this means that the nanoparticles have a

large surface to volume ratios. However, this means that they are physically unstable. This is especially evident under catalytic reaction conditions where particles sinter, resulting in decrease in dispersion and activity. There are many ways in which nanoparticles can be stabilised against sintering and agglomeration. The preparation of nanomaterials can be classified by two approaches. The first is a "top-down" approach, which uses physical means such as metal evaporation, ball milling or sputtering. One advantage of the top down approach is the ability to generate large quantities of materials. However, a major drawback of this method is its poor control of metal size and shape, both of which are important parameters to consider when designing solid catalysts. The second is the "bottom up" approach by using chemical means, for example catalyst supports or capping agents. Nanomaterials with controlled size and shapes can be obtained using this method, however, only a limited amount can be made at one particular time. The chemical approach can be further divided in two categories: i) High surface area supports; ii) Stabilisers such as polymers or surfactants. A general discussion in both advantages and disadvantages on their use is given in the following sections.

1.3.1 CATALYST SUPPORTS

The most common method to protect nanoparticles against sintering is by depositing them onto an inert support material. Commonly used inorganic supports include silica or alumina, with organic supports such as activated carbon or charcoal can also be applied. One property common to all catalyst supports is that they have a high surface area to mass ratio, *i.e.* they have a highly porous structure which helps to disperse the active catalyst particles. A supported metal catalyst allows substrates to migrate to the surface of support then diffuse through the pores to the active metal. Mass transport plays a crucial role in dictating the properties of a surface catalysed

reaction and if not properly controlled it can lead to changes in activity/selectivity. When choosing catalyst supports, one must consider its thermal stability, especially when catalytic reactions are undertaken at elevated temperatures. Catalyst supports may help to dissipate local heat thus reducing sintering. Chemical reactivity to substrates is another factor to consider, where the support may participate in a reaction (termed bifunctional catalysts). Inorganic supports that may have this property include magnesia, titania, zirconia, zinc oxide or zeolites.

1.3.2 DEPOSITION OF METAL ON SUPPORT

When depositing metal nanoparticles on supports, impregnation is one of the most simple and widely used chemical techniques. The method, as the name implies, starts by filling the pores of the support by a solution of metal precursor/salts. The material is then thermally treated to form the desired metallic nanoparticles. In impregnation, the pore size distribution, and surface functional groups plays an important role in the overall size of the particles. An advantage in impregnation is large amounts of material can be prepared, but the method lacks control of the final size and distribution of the nanoparticles, except for cases when the supports have well defined pore structures.

The use of precipitation technology is commonly used in catalyst preparation to deposit active metals on support. Precipitation is where chemical agents such as hydroxides or carbonates are added to a metal/support solution. The addition of base changes the metal species by hydrolysis and in doing so is deposited on support. Lastly, co-precipitation is similar to the above method but the metal and support precursors are precipitated simultaneously, and these are often highly sensitive to the experimental procedure. For example, factors such as molarity of starting metal solution, concentration of precipitant, length of addition, pH, washing and

temperature may affect outcome of the formed nanoparticles and therefore can cause changes in catalytic characteristics.

Another method is deposition of preformed metal nanoparticles onto the support. This method offers good size control compared to the impregnation method, however, only small amount of material can be prepared at once and its preparation is more complex and a time consuming technique.

1.3.3 COLLOIDAL METHOD

Metal nanoparticles can also be synthesised in the absence of a support in liquid phase by using colloidal methods. Polymers and surfactants are most commonly used as stabilisers (Fig. 1-4). They all work under similar principles, that is, they have heteroatoms whose lone pair(s) binds weakly onto the metal surface of the nanoparticle. The rest of the stabiliser prevents agglomeration of the particles by preventing close contact of adjacent particles in solution. In general, there are three types of stabilisation:

i) Electrostatic, where anions and cations remain in solution and coordinate onto the metal surface, forming an electrical double layer.

ii) Steric, where large molecules such as polymers or surfactants prevent aggregation by using their steric bulk, forming a protective shell by van der Waals repulsion.

iii) Electrosteric, where stabilisation is brought about by a combination of electrostatic and steric (Fig. 1-4, right).

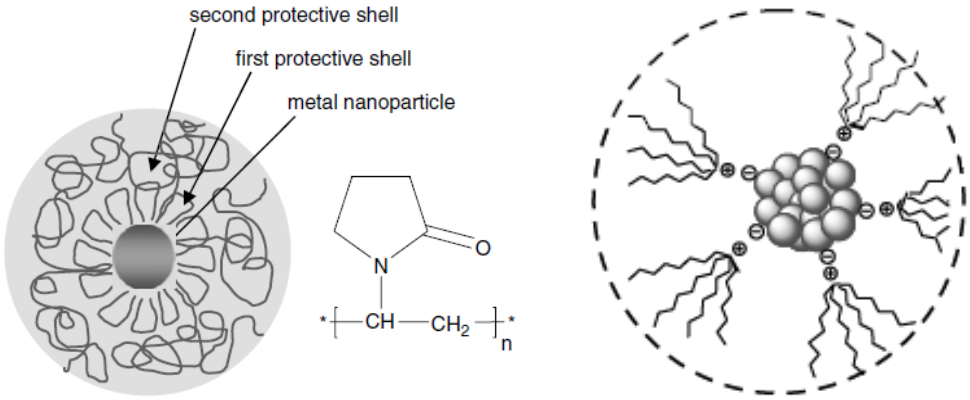

Fig. 1-4 An illustration of: (Left) Polymer stabilised metal nanoparticle. (Right) Surfactant stabilised metal nanoparticle.[11]

Under standard conditions, the stabilisers will not reduce the metal precursors in solution. Therefore, reduction processes must be brought about, predominantly by chemical methods, although alternatives such as photochemical, sonochemical and laser ablations have also been used. The most common reduction techniques are outlined below:

i) Wet chemical reduction – This is one of the most common chemical method and was reported by Faraday in 1853 on colloidal gold sol (nanoparticles) from the reduction of $HAuCl_4$ with phosphorus.[12] The method involves using variety of reductants such as borohydride, hydrogen, hydroxide, hydrazine or alcohols. The schematic approach can be represented as:

$$x\mathrm{M}^{\mathrm{n}+} + nxe^{-} + \text{stabiliser} \rightarrow \mathrm{M}^{0}n\ (\text{cluster})$$

ii) Electrochemical reduction – This method involves dissolution of the metal from the anode of an electrochemical cell, followed by its migration to the cathode, where the metal ions reduces to zero valent metal atoms. The nascent particles are allowed to further undergo nucleation and growth to M^0n of which growth stage can be halted by stabilisation with suitable stabilising agents. An advantage of using this method is that the precipitated metal nanoparticles can be

isolated and is free from contaminates resulted from chemical reducing agents. Furthermore, the particle size can also be controlled by adjusting the distance between electrodes, time, temperature, solvent and current density; with a high current leading to smaller nanoparticles.[11]

iii) Solvothermal – The process involves using a sealed apparatus (bombs or autoclaves) so that solvents (typically water) can reach temperatures above their boiling points. This is achieved by increasing the autogenous pressures that results from heating. This is termed hydrothermal when using aqueous and a solvothermal process when using non-aqueous solvent systems.[13]

iv) Microemulsions – This involves using combinations of water, oil, or surfactants with alcohol or amine based co-surfactants to achieve a homogeneous solution. The oil phase has a long chain hydrocarbon tail with a hydrophilic head, normally a quaternary amine or sulphate. Most common example of this is cetyltrimethylammonium bromide (CTAB) that was discovered by Schulman in the 1940's, and this microemulsion technique is still used frequently today.

iv) Thermal decomposition – This method involves the decomposition of organometallic precursors. Metal-surfactant complexes are subsequently formed by reflux in high boiling organic solvents such as octyl or benzyl ether. Advantages in using organic methods include high crystallinity, narrow size distribution and good dispersibility in organic solvents.[14]

1.3.4 BURST OF NUCLEATION

First proposed by LaMer *et. al.* in the 1940's a technique for the fabrication of uniform colloidal nanoparticles is the concept of burst of nucleation.[15] The process starts with many nuclei being generated at the same time, followed by growth without further nucleation. This is important because all particle growth histories are

approximately similar. On the other hand, if nucleation event continues into the growth process it will result in different growth histories, leading to different sizes and therefore poor size control. It is therefore essential to separate nucleation events to the growth phase in order to prepare highly monodisperse nanoparticles, which is the essence of the burst of nucleation technique. Fig. 1-5 explains how this concept works. In stage I, the concentration of homogeneous metal is increasing, but precipitates have not yet been formed as supersaturation has not reached to levels for spontaneous homogeneous nucleation. Stage II is where rapid self nucleation takes place as the metal concentration reaches the critical saturation limit (S_c). At the later stages of II, supersaturation decreases due to consumption of metal by the nascent particles. Eventually nucleation stops at stage III as it reaches below the S_c and enters the growth stage and eventually further growth will stop when it reaches the minimal critical solubility limit.[16]

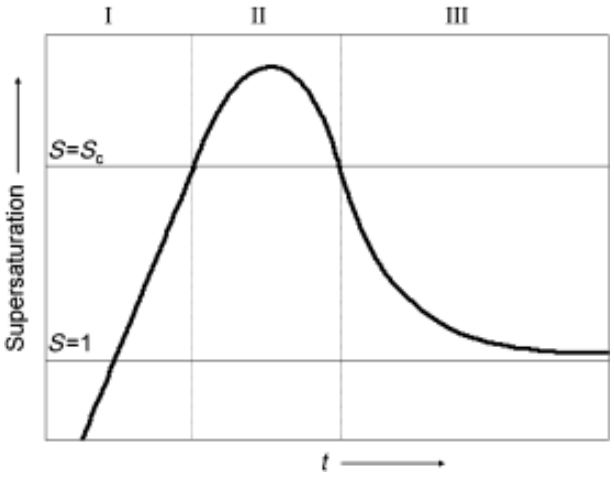

Fig. 1-5 LaMer plot: Change of degree of supersaturation as a function of time.[15]

1.4 NANOPARTICLE ENGINEERING

As detailed in previous Sections, there are many ways to synthesise monodispersed nanoparticles with a high degree of control. Furthermore, studying the underlying properties may gain significance from both a fundamental and

practical point of view, with the goal of understanding reaction mechanisms or maximising reaction activity and/or selectivity in catalytic processes. In this section, we will discuss some of the methods, whereby tuning particle parameters can have dramatic consequences on various molecular scale factors; for example electronic, geometric/surface structure, support interaction, oxidation state of the surface, which in turn affects the fundamental characteristics of surface catalysed chemical reactions.

1.4.1 SIZE CONTROL

The effect of crystallite size variation in optimising reaction activity/selectivity relationships has been one of the most intensely examined research areas over the past decade. The size of a metal nanoparticle determines the nature of the metal surface. Metals in the bulk tend to have the full complement of nearest neighbours. For instance, a metal that has a face centred cubic structure has twelve nearest neighbours (Fig. 1-6a). Metal atoms located on surfaces therefore must possess one or more valencies with reduced coordination number, resulting in a net force acting inwards on surface atoms, hence giving rise to the term surface energy phenomena.[17] The implication of this effect is dependent on the size of the nanoparticle (Fig. 1-6b). Decreases in size result in higher surface energies, leading to a more unstable particle structure and *vice versa*. Furthermore, this lowers the average coordination number, which can drastically change the relative population of surface sites. For example, decreasing the size will increase sites with lower coordination numbers, *i.e.* those located at the corners and edges (CN = 6 and 7, respectively) with respect to those of surfaces such as 111 or 100 (CN = 9 or 8, respectively), while larger nanoparticles will predominantly be dominated by surface sites (Fig. 1-6c). Other high index sites can be found on solid surfaces include kinks, steps or adatoms with varying numbers of nearest neighbours, which the former two are more commonly found on single

crystal surfaces (Fig. 1-6d).[9] This illustrates why the majority of nano research are conducted within 1-10 nm size regime, as a small change in particle size has drastic effects on particle structure. Theoretically, a reduced coordination number results in overall higher lying *d*-orbitals compared to their higher coordination surface counterparts. This may ultimately strengthen the adsorbate-surface interaction, also known as the electronic/ligand effect, thereby may fundamentally alter the activity/selectivity of a given reaction.[18]

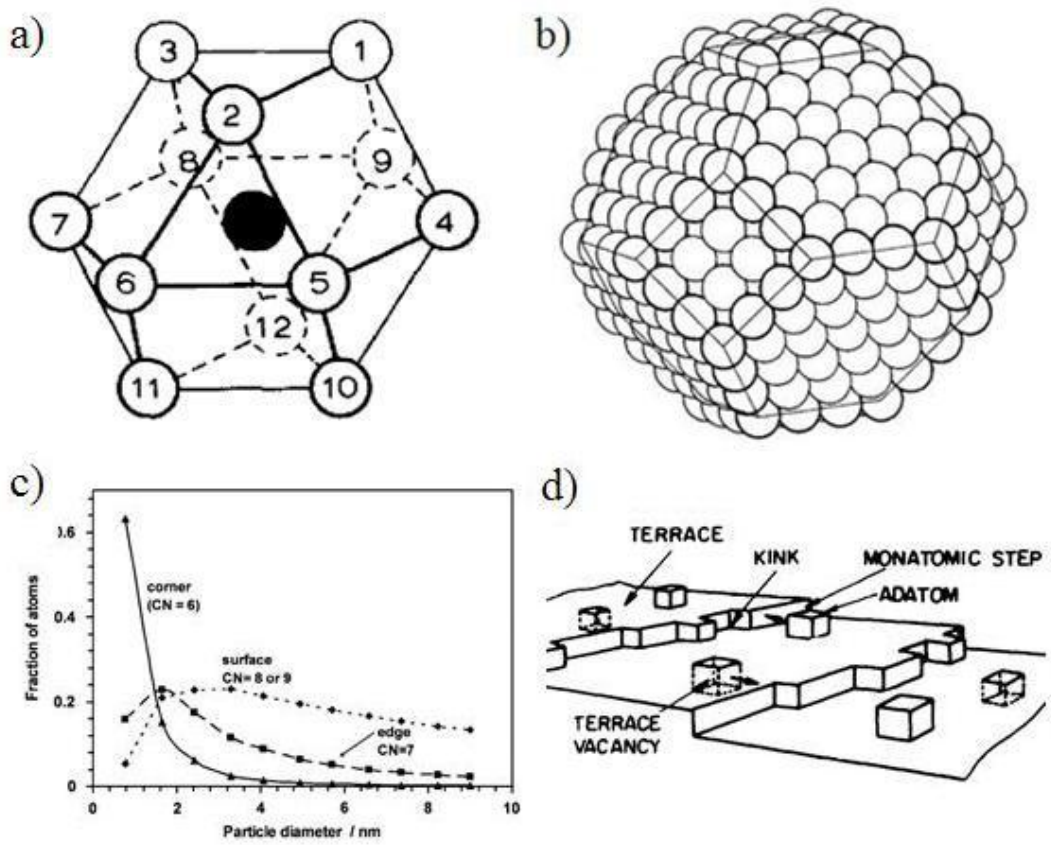

Fig. 1-6 Size effect of nanoparticles showing: (a) Full coordination effect for metals with fcc structure[19]; (b) A cuboctahedron nanoparticle; (c) Change in average coordination number and site distribution with respect to size for a truncated cuboctahedron nanoparticle[20]; (d) Heterogeneous solid surface showing various defective sites.[9]

The quantum size effect is another well known phenomena arising from changes within nanodimensional materials. This peculiar effect is explained by the

nanoparticles inherent structure which is neither bulk nor molecular like. Metal atoms in a bulk structure have overlapping orbitals, thus forming a continuous density of states. Alternatively, metals that are molecular in nature like have few neighbours and therefore have more discrete states, similar to the mono-nuclear species. A nanoparticle sits between these two extremes, where its energy levels are either a continuous band or discrete. A classic example is the case of semiconductor nanoparticles, also known as quantum dots, which exhibit different optical and electrical properties upon changes in its particle diameter.[21-24]

A good example that shows size dependent reactivity is the C-C coupling reaction using Pd nanoparticles.[25] El-Sayed and co-workers synthesised a series of Pd nanoparticles of determined size using a stepwise growth method and tested their activity by a Suzuki reaction between phenylboronic acid and iodobenzene. When results were normalised per Pd surface atoms, they found that there was a general increase in catalytic activity as the Pd size decreases (Fig. 1-7). This was attributed to the increased numbers of low coordinated sites (corners and edges) giving rise to the observed activity, whereas no trends were observed when normalised against surface facets. These reactive sites were able to activate molecular substrates due to stronger adsorption, although much lower activity was observed for the smallest size where the authors attributed to overly strong adsorbed species on the metal surface therefore acts as surface poisons and decreasing the rate of reaction.

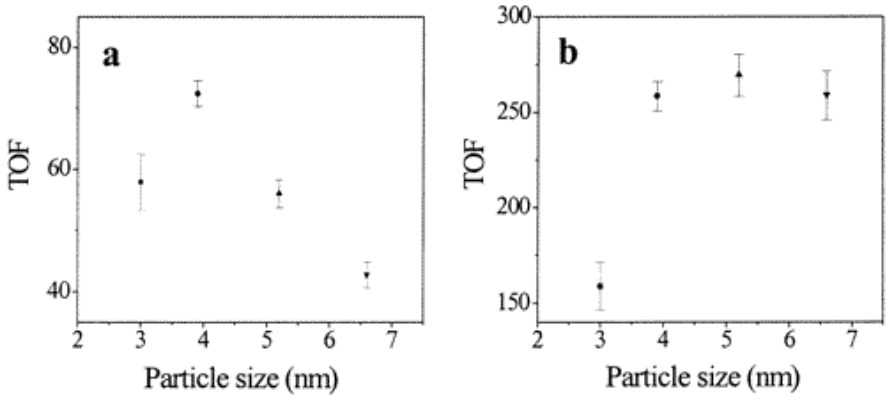

Fig. 1-7 Turnover frequency as a function of particle size for the Pd catalysts in Suzuki coupling reaction. The TOF is calculated on the basis of (a) total number of surface atoms and (b) total number of vertex and edge surface atoms.[25]

Ever since Haruta *et. al.* reported the observation of nanosized Au being active for CO oxidation research in to Au metal catalysis has increased.[26-28] Numerous rationales have been proposed to explain high activities observed in nano Au catalysts and it remains a debatable area. For example, Valden *et. al.* deposited Au clusters in the size range of 1-6 nm on TiO_2 and performed CO oxidations.[29] The authors observed structure sensitivity to the maximum specific activity of their model catalysts. Au clusters one atom thick have large band gaps whereas clusters three atom thick exhibits more metallic behaviour. Whereas two atom thick Au with an intermediate band gap possesses maximum activity, the effect was attributed to the size quantisation phenomena. Boyen *et. al.* observed "magic-number" Au-55 cluster catalysis on CO oxidation being particularly effective due to the closed-shell nature of such clusters rather than size quantisation phenomena.[30] Guzman *et. al.* synthesised Au on MgO with mixed oxidation states surface Au (I or 0).[31] The authors concluded that their relative proportions is more important in CO oxidation activity, with oxidised Au being the active species and metallic Au reduced by CO diminishes activity. Lastly, Janssens *et. al.* performed CO oxidation on supported Au catalysts

and correlated catalytic reactivity to theoretical calculations. They concluded it is the increasing populations of low coordinated corner sites which are the active sites for the reaction due to their higher lying *d*-states, an effect that is much larger than electronic effects arising from small nanoparticles. Furthermore, the authors compiled past literatures and plotted activity to size to fractions of corner sites (Fig. 1-8). They found all the data closely resembles the latter, characterised by a $1 / r^3$ relationship. These reports illustrates that detailed study is needed to elucidate and explain catalytic activity to nanoparticle size, as its variation may encompass changes in the many effects as mentioned above.

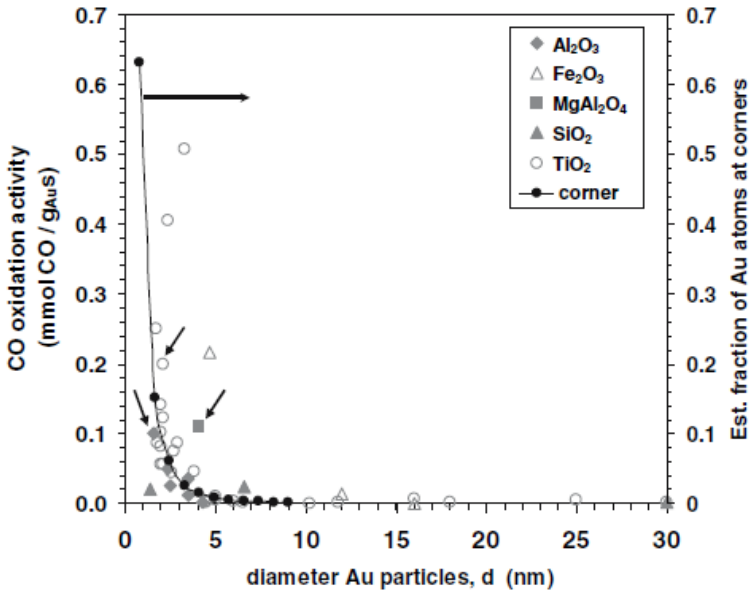

Fig. 1-8 Reported catalytic activities for CO oxidation at 273 K over different Au catalysts as a function of the particle size. Different supports are indicated by the symbol shape, open/close symbols correspond to reducible and irreducible supports, respectively. Solid curve shows the calculated fraction of atoms located at the corners of the nanoparticles as a function of particle diameter.

1.4.2 SHAPE CONTROL

Shape control of nanoparticles is another burgeoning area of nano research. Major efforts have been devoted in understanding anisotropic particle growth in solution media. Shape control involves manipulating surface growth kinetics in order

to preferentially promote the growth of one particular surface plane, for example, the more open (100) in preference to the more tightly packed (111) plane. However, the former is more difficult to form due to higher surface free energies. For example in the case of palladium[32]:

$$\gamma_{111} = 1.920 < \gamma_{110} = 2.225 < \gamma_{100} = 2.326 \ \mathrm{J.m^{-2}}$$

Therefore, it is evident that an additional force is needed in order to promote such preferential growth of a more unstable plane. This stabilising force may be obtained, for example, by adjusting the binding affinity of stabilising agents (such as L-ascorbic acid, citric acid and polyvinylpyrrolidone) to interact with the (111) surface.[33] Addition of silver or bromide ions that selectively bind on (100) facets, subsequently promote its formation.[34] Controlling oxidative etching by oxygen and chloride ions can also be used to form multiply twinned particles and suppress the growth of thermodynamic preferred cuboctahedron.[35] Platinum anisotropic structures that are grown organically have also been reported by using oleylamine under a pressurised atmosphere of hydrogen to form cubes or multipods.[36] In essence, nanoparticle shape can be controlled by choosing a suitable capping agent, addition of ions, and conducting the reaction under a controlled atmosphere in a pressurised vessel. A plethora of shape controlled nanoparticle synthesis has been summarised by Xia *et. al.* (Fig. 1-9).[34]

Structures	Shapes	Schematic drawings	Metals
single-crystal	perfect/truncated cube[a]		Pd, Ag, Au, Pt, Cu, Rh, Bi, Fe
	perfect/truncated octahedron[a]		Pd, Ag, Au, Pt
	perfect/truncated tetrahedron[a]		Ag, Au, Pt, Rh
	rectangular bar		Pd, Ag, Pt
	octagonal rod		Pd, Au, Fe, Co, Ni
	rectangular or octagonal wire	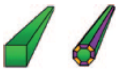	Pb, In, Sn, Sb, Fe, Co

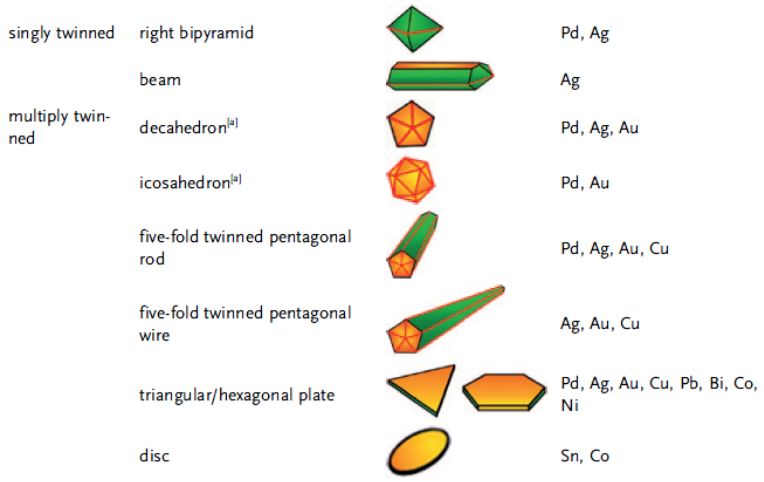

Fig. 1-9 A summary of different shapes that have been achieved for various metal nanocrystals.[34]

In this section a few examples are highlighted where shape controlled synthesis of nanoparticles in solution has been applied and demonstrates to be superior to the thermodynamically controlled cuboctahedron nanoparticle. Shao *et. al.* studied Pd nanoparticles and its structural dependence on the oxygen reduction reaction (ORR).[37] The reaction is of relevance towards the design and implementation of low temperature fuel cells. The authors synthesised classes of Pd octahedra and cubes less than 10 nm, where the former and latter are enclosed by (111) and (100) facets, respectively. They reported an order of magnitude higher ORR activity for the nanocubes compared to the octahedra, indicating structural sensitivity in this kind of reaction. Interestingly, the highest activities are comparable to the more expensive counterpart using Pt catalysts. The same group had expanded their methodology, where concave nanocubes bound by high index (730) facets are synthesised following a seeded method with carefully controlled kinetics for particle growth (Fig. 1-10).[38] Catalytic results were compared to Pd nanocubes synthesised by the same method in Suzuki coupling as well as electro-oxidation of formic acid. They observed 3.5 times increased catalytic activity and 1.9 times increase in the peak current, thus demonstrating the superior nature of these high indexed sites.

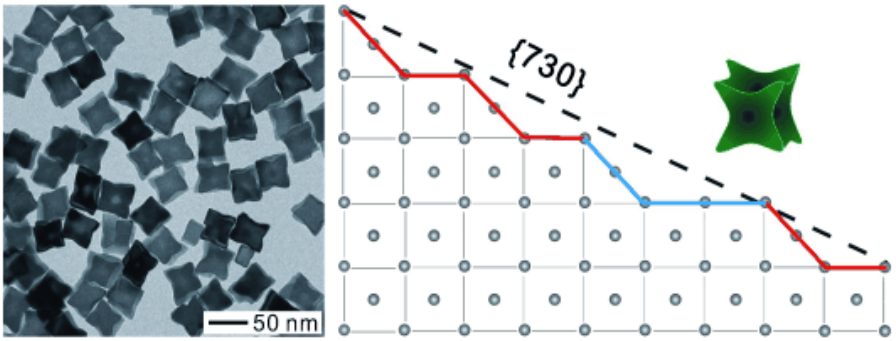

Fig. 1-10 Concave nanocubes showed a much higher catalytic activity than the conventional Pd nanocubes enclosed by (100) facets for both electro-oxidation of formic acid and Suzuki coupling.[38]

Recently, Crespo-Quesada *et. al.* studied the hydrogenation of 2-methyl-3-butyn-1-ol using cubes, octahedra and cuboctahedron Pd nanoparticles (Fig. 1-11).[39] They observed differing activity/selectivity at two types of active sites: those on the surface and those at the edges. Semi-hydrogenation occurred on plane sites with either the (111) or (100) configuration, whereas full-hydrogenation occurred mainly at the edge sites. This work demonstrates that structure sensitive reactions are strongly correlated to their size and shape, and is fully dependent on the adsorption characteristics of the substrate in question.

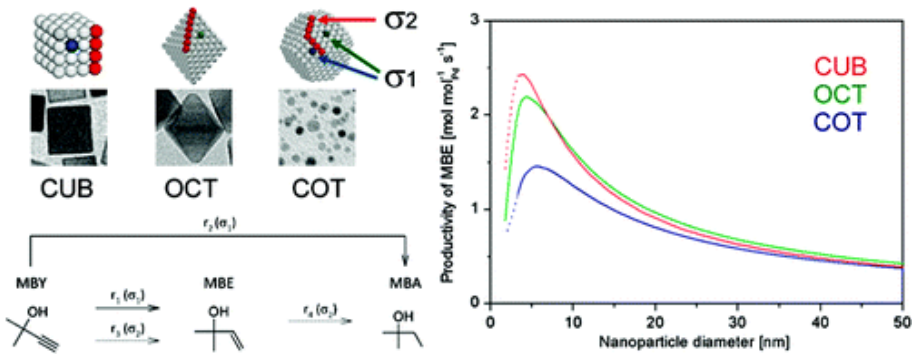

Fig. 1-11 Hydrogenation of 2-methyl-3-butyn-1-ol is shown to be structure sensitive by using cubes, octahedra and cuboctahedron nanoparticles.[39]

It was shown that changes in particle shape with respect to changes in rates of reaction can be linked to the geometric/ensemble effect, with the adsorption of molecular substrates requiring multiple atoms in a specific arrangement. Such

structure sensitivities have been traditionally studied using single crystals, where metal surfaces are cut and polished in the required orientation. Although this technique provides a direct correlation between activity and surface ensembles, it falls short from the ideal working nature of nanocatalysts, meaning that other effects such as the electronic effect may come into play. Therefore, it is more important to study controlled shape synthesis of nanoparticles to reaction sensitivity as compared to single crystal counterparts.

1.4.3 SUPPORT

Interactions between metal and support are the most researched areas in surface catalysed reactions. With the appropriate choice of supports, one can dramatically change the outcome of a given reaction. Whilst numerous examples of metal support interactions exist in literature, here in this section are some examples on how optimising the use of supports can maximise activity/selectivity of catalysed reactions.

The most common case where the support in reactions directly alters the electronic and geometric nature of the active metal catalyst, is called strong metal support interaction (SMSI) and has been widely reported in literature.[40-42] A classic case in the observation of the SMSI is during the 1970s, where Pt particles supported on titania, alumina and ceria and others lose the ability to chemisorb H_2 and CO after a high temperature reduction step.[43] The authors observed that a decreased chemisorption ability was not due to particle sintering, and subsequently attributed to SMSI with charge transferred from the titania to Pt. The effect was later explained in terms of a partial coverage of partially reduced mobile TiO_x species on the metal, thus maximising the metal-metal oxide contact.[44, 45] As seen in Carrettin *et. al.* synthesised Au nanoparticles of 2-3 nm on nanosized CeO_2 of 4 nm, The authors

reported high selectivity towards CO oxidation in H_2 even at high temperatures.[46] Furthermore, catalytic activity was observed to be two orders of magnitude higher in activity than catalysts prepared by coprecipitation or impregnation methods. The study illustrates that support properties can change drastically in the nanosized regime.[46, 47] Recently, Yamada *et. al.* constructed two distinct metal-metal oxide interfaces, CeO_2-Pt and SiO_2-Pt (Fig. 1-12).[48] The material was applied in a bilayer tandem catalysis firstly by converting MeOH to CO and H_2 selectively on the CeO_2-Pt interface. Subsequently, the reaction of the first products reacts with ethylene forming propanal on the SiO_2-Pt interface. The overall reaction is known as the olefin hydroformylation reaction, and is usually carried out using homogeneous catalysts. Interestingly, the reaction was unselective by using conventional mixtures of the mixed oxides prepared by impregnation. This illustrates that the metal-metal interface is crucial in order to promote such tandem reaction.

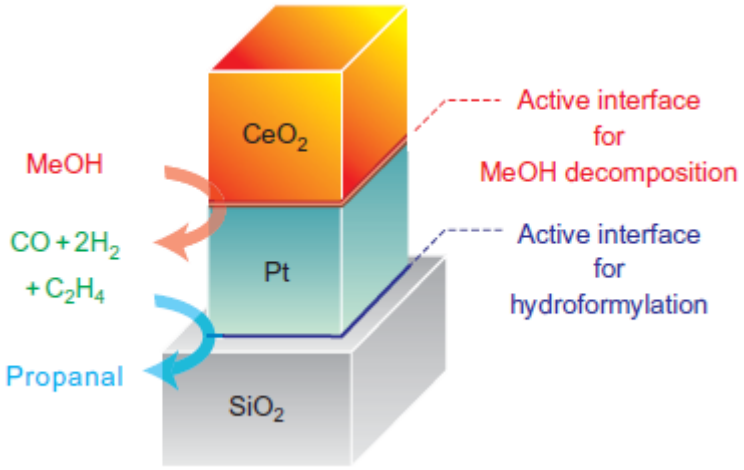

Fig. 1-12 Illustration of the CeO_2–Pt–SiO_2 tandem catalyst.[48]

Apart from contact between the metal and metal oxide interface, changing the shape of the support nanostructure can also affect reaction activity/selectivity. Mclaren *et. al.* reported hexagonal ZnO nanoplatelets exhibit more than 5 times in the decomposition of methylene blue compared to their rod shaped counterparts.[49] This is

because plates have a higher population of polar (001)/(00-1) faces compared to the non-polar (100) face. In an extension to this methodology, Liao *et. al.* deposited Cu nanoparticles on these shaped ZnO nanostructures and found that the hydrogenation of CO_2 and H_2 can be selectively promoted to form MeOH using these nanoplatelets.[50] The enhanced selectivity is related to formation of defects such as oxygen vacancies, changes in surface morphology as well as electronic properties of the more polar surface. This demonstrates that tuning the support plays a key role in the outcome of surface reactions is made only available by careful preparation using nanoscale synthetic techniques.

1.4.4 BIMETALLICS

Bimetallic modification of nanocrystals is another sought after area in nano-research. The addition of a foreign metal can alter catalytic activity/selectivity through changes in the physical and chemical properties of the metals, the result of which changes reaction mechanisms/pathways. The structure of bimetallic nanoparticles is complex, although three main classes are identified in the literature (Fig. 1-13):

i) Core/shell, where the second metal is deposited heteroepitaxially on the first metal acting as a seed. Shell overgrowth is kinetically controlled to avoid self nucleation.

ii) Cluster-cluster, where two metals self nucleate with the sharing of a mixed interface.

iii) Alloyed or intermetallic, where there is a random distribution of both metals in one particle.

The formation of these bimetallic architectures is highly dependent on the compatibility of the two metals, termed “lattice mismatch”, this is the difference of

lattice parameters between two metals. For example, Pd and Pt have a small lattice mismatch (0.77%), which results in conformal growth of Pd on Pt to form core/shell structures. On the other hand, Au and Pt have a big lattice mismatch (4.08%) resulting in non-conformal overgrowth that promotes anisotropic growth forming heterostructures where surface facets are observed from both metals.[51] Below are some rationales to explain bimetallic modification in general and also some examples where bimetallic can dramatically effect surface catalysed reaction.

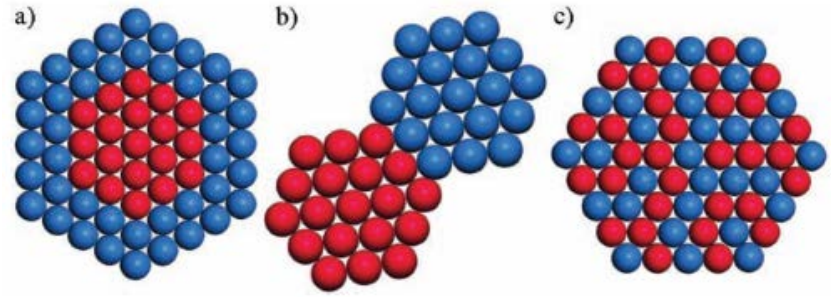

Fig. 1-13 Bimetallic nanoparticles architectures: a) core/shell; b) cluster-cluster; c) alloyed or intermetallic structures.

The physical and chemical changes in bimetallic nanoparticles are often explained in terms of electronic, bifunctional or an ensemble effect. Electronic effects are where the metals have different work functions that influence its electronic character. For example, if a metal is doped with a second metal that has a higher work function, the effect on the first metal is a net decrease in electron density. Band theory can also be used to explain this behaviour. Charges will flow from a metal with high Fermi level to a lower one, which changes its *d*-band centre.[52] Another type of electronic effect is called the strain effect. This results from a subtle change in surface lattice parameter. As mentioned, overgrowth depends on the lattice mismatch of different metals. In terms of core/shell materials, the metal surface has a tendency to adapt to the lattice parameter of the core, especially if the shell is only a few atomic

layers. This may lead to two effects, lattice expansion of the metal lattice leads to upshift in *d*-band center resulting in stronger adsorption of surface adsorbates. Whereas lattice compression leads to downshift results in weaker adsorption. A good example is in the oxygen-reduction reaction for applications in fuel cells and batteries, where compressive strain was found to cause weaker chemisorption of oxygenated species and a decrease in electrocatalytic activity.[53]

A further example of the bimetallic effect is where a foreign metal decorates onto the low coordinated sites of the first metal. Our group has demonstrated a bimetallic CoPt system where Co is preferentially decorated on the corner sites of the Pt.[54, 55] Co blocks the unselective sites helps to promote the selective hydrogenation of cinnamaldehyde to the unsaturated alcohol in near quantitative yields (99%).

Finally, another interesting observation in the literature is where bimetallic particles can change physical states under operation conditions. Somorjai *et. al.* demonstrated experimentally the surface restructuring phenomena *in situ* in bimetallic systems.[56] Surface segregation effect is driven by a change in the oxidising and reducing atmospheres, with metals of differing chemical potentials to the reactive gas feed. Accordingly, Rh was found to migrate to the surface under an oxidising atmosphere of NO, whereas Pd or Pt migrates to the surface under a reducing atmosphere of CO. This highlights that the designed bimetallic architectures can change in real conditions where the working phase of the catalyst may not be of the same initial states and that *in situ* characterisation techniques are needed to rationalise catalytic results.

1.4.5 INTERSTITIAL MODIFICATION

Modification of nanoparticles using interstitial elements has been far less investigated when compared to the above modification methods. Interstitial

modification involves the insertion of non-metal light atoms (such as C or H) into the subsurface sites of metals, for example Pd. Two principal effects arise from such modification: An electronic effect caused by the direct overlap of non metal orbitals with that of metal orbitals. This degree of overlap depends on the non metal compared to the metal forming a tightly bound *d-s* and strongly mixed *d-p* bonding states.[57] For example, such strong degree of mixing can be found in the case of Pd-B, where there is sufficient mixing due to metal *d*- and non metal *s-p* states being degenerate. Other than an electronic effect there is also the geometric effect caused by expansion of the metal in order to accommodate the light atom occupying its subsurface sites (Fig. 1-14). As the metal is forced apart, the degree of overlap decreases which ultimately destabilises metal-metal interactions. In terms of band theory, *d*-band width decreases to push up the centre of *d*-band relative to the Fermi level in order to conserve both *d*-band filling and the total number of *d*-states.[58] This results in overall stronger adsorbate interaction that may have profound effects in surface catalysed reactions.

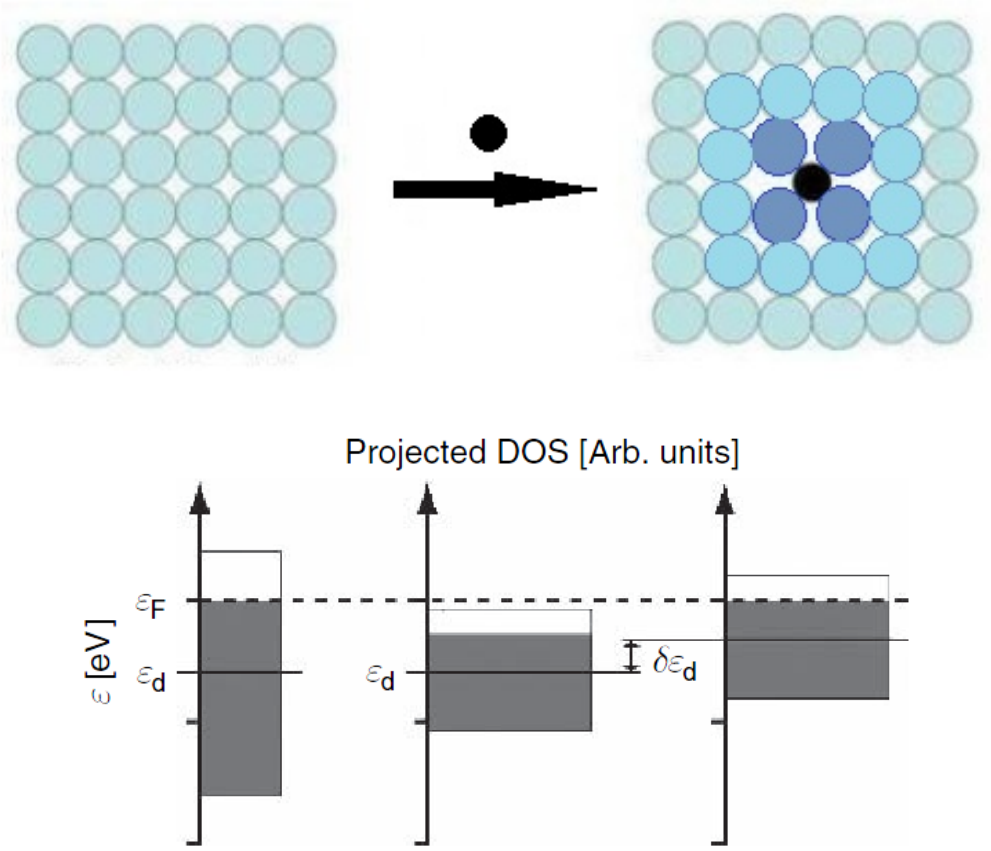

Fig. 1-14 Addition of a light atom to metal may exert an electronic effect from orbitals overlap and a geometric effect caused by the expansion of metal-metal distance (top); Illustration of the coupling between bandwidth and *d*-band centre for a band with a fixed number of *d* electrons. When the bandwidth is decreasing the only way of maintaining the number of *d* electrons is to shift up the centre of the band (bottom). DOS is the density of state of a metal.

Although traditional surface science techniques are able to characterise these components, experimental evidence of their catalytic properties are scarce, arguably due to instrumental limitations. Recently, however, Teschner *et. al.* reported by changing the ratio of H_2 gas and hydrocarbon source, either subsurface H or C in Pd can be formed (Fig. 1-15).[59] The latter is able to selectively catalyse alkynes to alkenes by blocking the unselective β-Pd-H phase and the electronic effect of subsurface C; whereas the former is unselective and goes straight to the alkane. Selective hydrogenation of alkynes to alkenes is fundamentally important in polymer manufacture, where the alkyne component interferes with the polymerisation process.

This observation is only made possible due to the development of *in situ* high pressure XPS experimental technique, where subsurface C alters the electronic structure of Pd. This work illustrates that subsurface chemical events can dictate the outcome of surface chemical events. However, one major drawback in the development of these class of catalysts is that they can only be formed under a saturation of reactive gas, for example acetylene, ethylene, methane or CO, which severely limits catalyst development in this area.[60-64] The subject of this thesis will be formation of such phase *via* alternative methods and one that is stable in the absence of reactive gases, this will be most profound in catalyst development of this area.

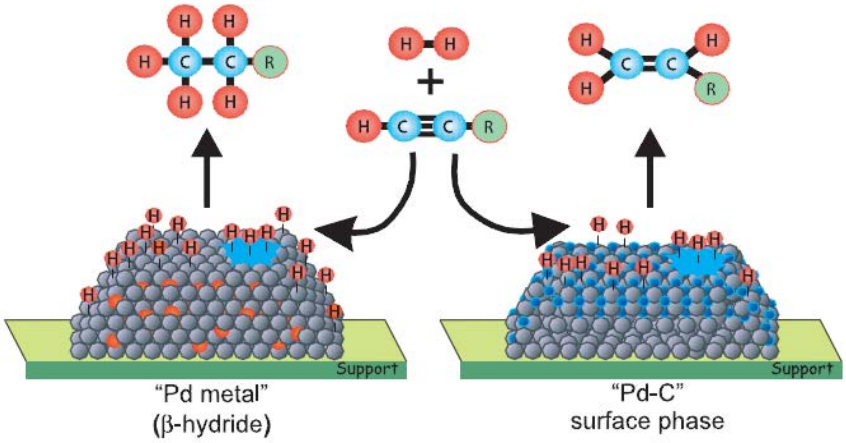

Fig. 1-15 Illustration of Pd catalysts operating in the selective and unselective alkyne hydrogenation regimes.[59] Blue and orange balls indicate C in Pd-C and β-hydride in Pd, respectively. Green balls indicate an alkyl group or H. Blue patches symbolize carbonaceous deposits.

1.5 FINE CHEMICAL AND PHARMACEUTICAL CHEMICAL APPLICATIONS

Fine chemicals manufacture is an area of major importance within the chemical industry with an estimated market value of $75 billion in 2007,[65] representing approximately 4-5% of the $1800 billion of the chemicals industry. The fine chemicals sector can be divided into three sectors: commodities, fine chemicals and specialty chemicals. The commodities market is a large volume and low cost with

chemicals produced at dedicated plants. Petrochemicals, basic chemicals, organic and inorganic monomers, as well as fibres and plastics belong to this category. Fine chemicals are pure and have more complex structures. Its manufacturing generally requires multiple batch steps, using a variety of production equipment, as compared to bulk chemicals that generally relies on a continuous process. Due of the production time and added value, they are produced in limited quantities (< 10000 tons/year) and sold at a high price (>10 USD/kg). This category can be further sub-divided based on their added value, whether they are applied as building blocks, as advanced intermediates or active ingredients. Such compounds belonging to this category are β-lactames and *N*-heterocyclic compounds such as imidazoles or pyrimidines. Specialty chemicals are defined as chemicals that contain one or more fine chemical active ingredients. They are classified according to their functions as a product. Industries belonging to this category are agrochemicals, catalysts, dyes, flavours and fragrances, food and pharmaceutical products. The target compounds are often highly substituted, with high levels of complexity and therefore have limited stability and/or volatility, hence reactions are typically carried out in the liquid phase. Although fine and specialty chemicals seemingly belongs to the same category, however, they are fundamentally different in that fine chemicals are sold as it is, whereas specialty chemicals are sold according to their functions. For example, active ingredients can be classified as fine chemicals, whereas the final drug formulations as specialty chemicals in the pharmaceutical industry.

1.5.1 ENVIRONMENTAL FACTORS

Recently, increasing attention has been paid to monitor the quantity of waste produced in this field. The E-factor is typically used to quantify the levels of waste generated, with each type of reagent being assigned an environmental quotient

(EQ).[66] As seen in Table 1-1, the E-factor increases from bulk to fine chemical synthesis. This is predominantly due to the use of classic organic synthesis, for example stoichiometric reducing and oxidising agents such as $NaBH_4$ and $KMnO_4$, which also have the disadvantage of being toxic. This poses limitations from both economical and environmental viewpoints regarding product purification and waste management. Therefore, applications that use green chemistry are favoured, benefiting from more efficient protocols by employing non-toxic and non-waste producing reagents. For example, the use of molecular hydrogen for chemical reductions and hydrogen peroxide for oxidations are typically preferred. The ease of use of solid catalytic systems to facilitate separation of product solutions must also be considered in the development of novel environmentally aware protocols.

Industry	Annual production (tonne)	E (kg of waste / kg of product)
Bulk chemicals	Less than $10^4 – 10^6$	Less than 1 to 5
Fine chemicals	$10^2 – 10^4$	5 to more than 50
Pharmaceuticals	$10 - 10^3$	25 to more than 100

Table 1-1 *E* factors in various chemical industries.[66]

1.5.2 SELECTIVE HYDROGENATION TECHNOLOGIES

The utilisation of molecular hydrogen in hydrogenation technologies is one of most important catalytic methods in a range of chemical industry processes. The scope of this is very board with many functional groups that can be hydrogenated with high conversion and selectivity. The classic hydrogenation catalysts are transition metals, for example Cu, Ni, Pt, Pd, Rh, Ru supported catalysts. Commercial type catalysts supplied are often highly dispersed with high specific surface area. There are several factors to consider on the catalysts used. First, obviously, is choice of type of metal as mentioned above and each metal varies greatly in terms of their

activity/selectivity. The type of catalyst is important, as one metal can be supplied in many form factors, such as Pt black, oxidised PtO_2 or reduced Pt. Metal loading can differ from 0.5 to 50%, with 5% being the most preferred loading for noble metals. The type of support can affect the reaction, with active carbon most commonly used. The catalyst is often supplied with 50% water content for safety reasons. The knowledge of availability of different types of catalyst can greatly reduce the time needed for a reaction, which is why hydrogenation technologies are most used in the production of fine and specialty chemical industries. Table 1-2 illustrates the most important functional groups to be hydrogenated coupled with the preferred metal and solvents.[67]

Substrate	Reaction	Metal	Solvent
Azides	$RN_3 \rightarrow RNH_2$	Pd, Pt, Ni	Polar
Aromatic NO_2	$ArNO_2 \rightarrow ArNH_2$	Ni, Pd, Pt	Various
Benzyl derivatives	$ArCH_2X \rightarrow ArCH_3 + HX$ (X=OR, NR_2)	Pd	Protic, acidic, basic
Alkenes	$R_2C=CR_2 \rightarrow R_2HC\text{-}CHR_2$	Pd, Pt, Rh, Ni	Various
Alkynes	$R_2C\equiv CR_2 \rightarrow R_2HC=CHR_2$	Pd/Pb	Low polarity
Aliphatic C=O	$R_2CO \rightarrow R_2CHOH$	Ni, Ru, Pt, Rh	Polar
Aromatic C=O	$ArCOR \rightarrow ArCH(OH)R$	Pd, Pt, Cu	Polar
Aryl halides	$ArX \rightarrow ArH$ (X=Cl, Br, I)	Pd	Basic
Nitriles	$RCN \rightarrow RCH_2NH_2$	Ni, Ph/Pd, Pt	Basic/acidic
Imines	$R_2C=NR \rightarrow R_2CHNHR$	Pd, Pt	Various
Oximes	$R_2C=NOR \rightarrow R2CHNH_2$	Ni/Pt, Pd	Basic/acidic
(Hetero)aromatic rings		Rh, Ru, Pt	Various

Table 1-2 Important catalytic hydrogenation reactions with preferred types of metal and solvents.[67]

Chemoselectivity is a common problem when molecules have multiple types of reducible functional groups. This is often the case in the production of higher value

products in fine chemical and pharmaceutical applications. Fig. 1-16 shows some general rules for chemical selective hydrogenations for combinations of different substrates.[68]

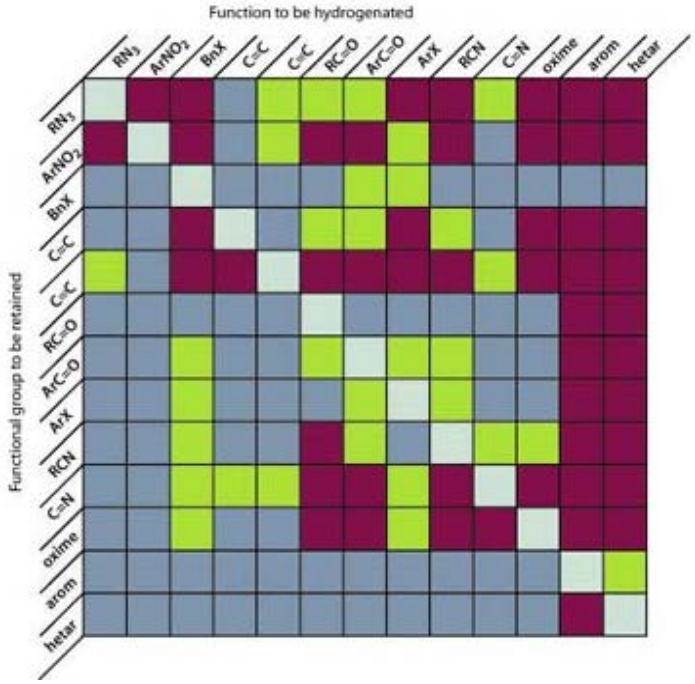

Fig. 1-16 Rules for chemoselective hydrogenation of various combination of reducible functional groups: Good selectivity (>90%) using standard catalysts (blue); Moderate selectivity (<90%) using modified catalysts (green); Poor selectivity (<50%) using special catalysts (purple).[68]

1.5.3 STEREOSELECTIVE HYDROGENATION OF ALKYNES

The selective hydrogenation of alkynes is an important class of reaction in fine chemicals manufacture. It has been extensively studied for the last 50 years. However, significant interest remains in understanding the factors that govern reaction selectivities, as evidenced by many books and reviews covering this area of chemistry.[69-73] Its lasting interests can be linked to its versatility, as many chemical transformations can be carried out using the acetylenic moiety as the starting material. For example, it can participate in substitution reactions to form new C-C bonds or hydrogenated to form alkene or alkane species. Notably, selective hydrogenation of alkynes to alkenes are used in gas phase industrial polymerisations for of bulk

chemicals production by removing residual alkynes from an excess of alkene streams to avoid poisoning of the subsequent polymerisation catalyst. On the other hand, liquid phase hydrogenations has been exploited in the synthesis of pesticides, as well as vitamins.[66]

The nature of the electronic configuration of the acetylenic moiety dictates much of its catalytic activity and selectivity. This is attributed to the electronic and geometric nature of the triple bond, with the *sp*-hybridised C atomic orbitals forming a distributed symmetrical electron density along its molecular axis. This results in its distinctively cylindrical shape and linear geometry, together with high electron density and restricted rotation of the C≡C bond makes the function group strongly adsorbed on metal surfaces. Therefore, upon hydrogenation predominant *cis*-selectivity is observed occurring *via* the *syn* addition of atomic hydrogen, characteristic of alkynes adsorbing on a flat metal surface. The situation is different once the alkyne is hydrogenated to the alkene, where the adsorption strength of the latter is much weaker. In the case between different alkynes and alkenes, their adsorption strength can be ranked as:

$$Terminal\ Alkynes > Internal\ Alkynes \gg Terminal\ Alkenes > Internal\ Alkenes$$

Therefore, hydrogenation of alkynes to alkanes often exhibit two apparent rates of hydrogenations, occurring *via* consecutive reaction steps (Scheme 1-1). That is, the hydrogenation of alkyne to alkene, followed by the latter being hydrogenated to the alkane. In this reaction, zero valent Pd is the preferred choice of metal as it exhibits the best overall activity/selectivity for semi-hydrogenation. This is because chemisorption requires vacancies in the *d*-band that can accept electrons from the electron rich alkyne/alkene. Pd has a nearly filled *d*-band and can therefore bind these

substrates relatively strongly but not so much that is difficult to desorb (the case of left hand group metals). Similarly if electron rich metals are used (the case of Group IB metals) they have a filled *d*-band that is inefficient at accepting electrons, which makes the substrates weakly chemisorb and reduces the activity. Specifically, the stability of the surface chemisorption bond requires synergistic charge transfer of d_π-d_π or d_π-π^* between the metal and alkyne/alkene.[66]

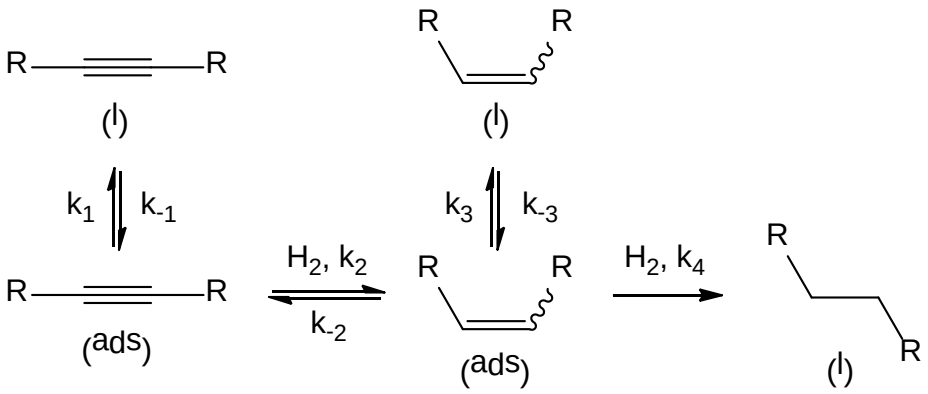

Scheme 1-1 Generalised liquid phase hydrogenation of hydrocarbons with multiple unsaturation.

In the context of selective formation of alkene, one may expect the term k_2 being much larger than k_4, resulting in mechanistic selectivity.[70] The other scenario is where the equilibrium k_1/k_{-1} is much greater than the equilibrium k_3/k_{-3}. This is where the strong adsorption of alkyne replaces alkene adsorption on the surface, a thermodynamically driven selectivity. The final case is where all the alkynes are hydrogenated to the alkene, leaving the latter to excessively readsorb and further hydrogenate to the alkane. Semi-hydrogenation selectivity may arise if k_3/k_{-3} is larger than k_4, another mechanistic driven selectivity.

Despite big differences between their adsorption on the metal surface, the hydrogenations of alkynes and alkenes usually have rates of similar magnitude and therefore, selectivity difference is predominantly thermodynamic. As such, one may device an experiment using only one equivalent of hydrogen to afford the alkene.

However, this frequently results in an incomplete reaction, leaving residual concentrations of the undesirable alkyne. Moreover, at complete conversion of alkyne, the subsequent further hydrogenation can still be relatively facile as well as rapid isomerisations arising from substrate re-adsorption. For example internal alkynes hydrogenate selectively to *cis*-alkene may undergo rapid isomerisation to the *trans*- or double shifted isomerisation by-products makes control desired alkene selectivity difficult. Therefore, on this basis, the selective formation of alkene cannot be interpreted without detailed knowledge of reaction kinetics, the Pd catalyst with factors such as size, shape, modifiers as well as promoters. Minimising isomerisation rates (kinetically driven selectivity) is desired when designing more selective hydrogenation catalysts.

There are numerous reports that exist in the literature on promoting the selective hydrogenation to alkene. Out of all the metal modified catalysts, Ag is the most commonly used and it is still applied as a commercial catalyst for hydrogenation of acetylene.[74] It generally uses alumina as the support and Ag to Pd ratio can be as much as 80%.[75] Another well known example is the classical Lindlar's catalyst, a Pb promoted Pd catalyst supported on calcium carbonate.[76] Quinoline is often added to promote selectivity. For example the catalyst is used in the production of a *cis*-vitamin D precursor (Scheme 1-2).[77]

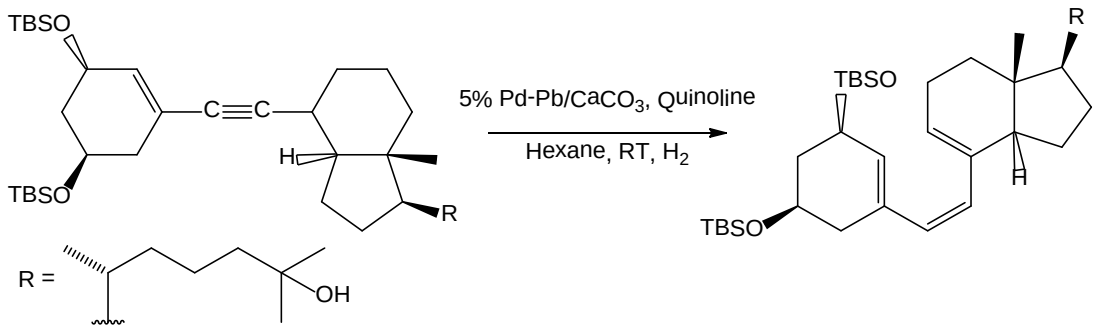

Scheme 1-2 Lindlar catalyst in the application towards the synthesis of vitamin D.[77]

1.5.4 CHEMOSELECTIVE HYDROGENATION OF NITROBENZENE

Hydrogenation of nitroaromatics to the corresponding anilines is an important class of reaction that is relevant to the agrochemical, pharmaceutical, dye and pigment industries.[78] Heterogeneous catalysis with hydrogen as the reductant are often applied to these reactions because only water is formed as a by-product. This is in contrast to non-catalytic processes using the Béchamp process (stoichiometric amounts of Fe powder and HCl) or reduction by sulphides (H_2S or NaSH), where large amounts of iron oxide sludges (up to 500 $g.mol^{-1}$ of nitro) or highly toxic and smell (by-products) are formed.[66] The use of these processes still exists today but only in few cases where selectivity poses problems when using a heterogeneous technology.

The reduction of nitroaromatics was discovered over 100 years ago when Haber proposed a reaction network for their electrochemical reduction (Scheme 1-3).[79] The mechanism remains generally accepted to date and all of the proposed experimental intermediates have been verified. The mechanism starts with the reduction of the nitro group to the nitroso intermediate. Experiments have shown that this intermediate, if present, only exists at very low concentrations due to its strong adsorption on metal surfaces and is quickly reduced further to the hydroxylamine. This is then further reduced to aniline in the rate limiting step involving the hydrogenolysis of the N-O bond. Some studies suggest this limiting step instead of hydrogenolysis is a disproportionation reaction to the nitroso and aniline species, although detailed mechanistic study is lacking.[80] Other reaction intermediates may include condensation products formed between nitroso and hydroxylamine to the azo and azoxy by-products. Like many surface catalysed reactions, hydrogenation of

nitroaromatics can be modelled by a Langmuir-Hinshelwood mechanism with good agreement by assuming an equilibrium adsorption of substrates.[81-83]

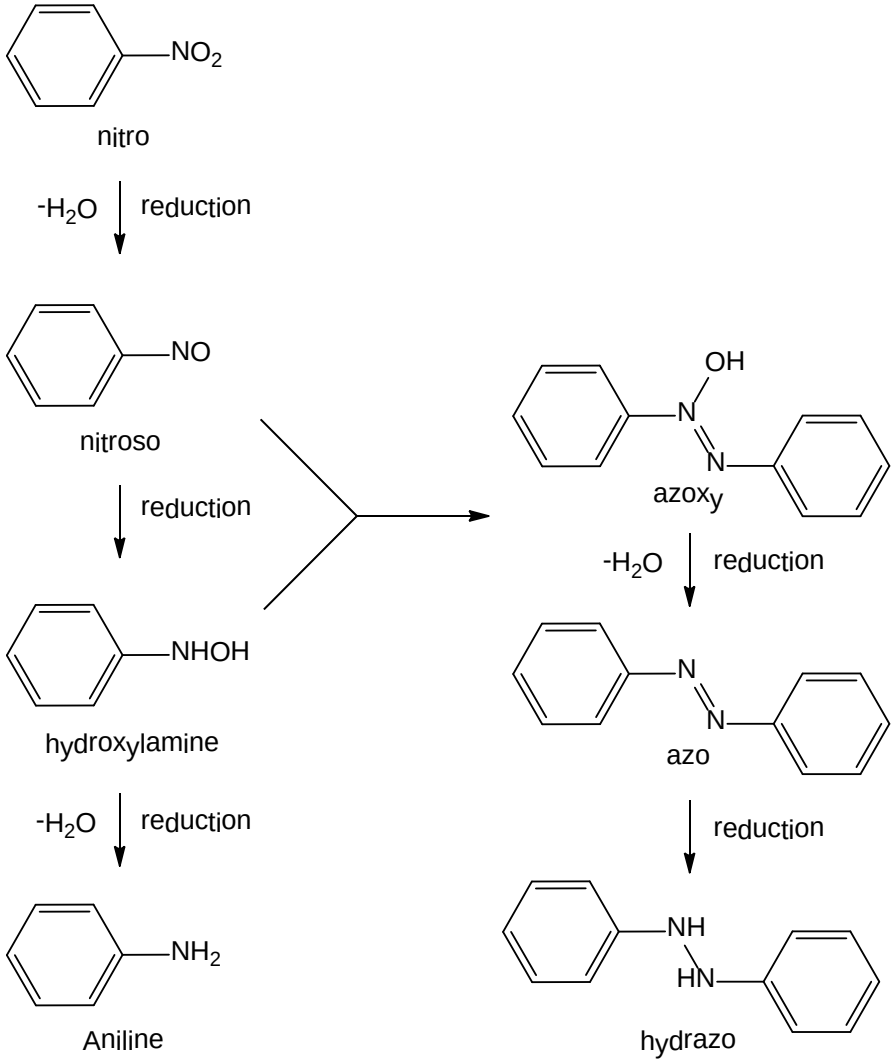

Scheme 1-3 Reaction network for the reduction of nitroaromatics proposed by Haber.[79]

The selectivity of nitroaromatics over heterogeneous catalysts normally has few problems because hydrogenation of the aromatic ring is much slower than the nitro group. One problem is the accumulation of hydroxylamine intermediates as they are highly carcinogenic and together with their high exothermic decomposition potential (approx. 2000 $kJ.mol^{-1}$), if uncontrolled, may pose serious risk of explosion.[66] Furthermore, their build up increases the chance of condensation to the azo and azoxy by-products, leading to poor selectivity. Therefore, suppression of hydroxylamines is

of paramount industrial importance. The condensation of azo and azoxy products are favoured when the reaction is slow or in strong basic conditions. Furthermore, the removal of hydrazo is difficult because it involves hydrogenolysis of N-N bond. On the other hand, formation of hydroxylamine varies greatly according to the applied reaction conditions, for example the nature and concentration of starting material, catalyst/substrate ratio, pH, hydrogen pressure, temperature, solvent and stirring. Generally speaking, their evolution is particularly evident when the reaction is conducted at low temperature and in high hydrogen pressure.

1.5.5 MULTIFUNCATIONAL NITROAROMATICS

Perhaps the main challenge in maintaining high selectivity in nitro group hydrogenation is when they are functionalised with other reducible functional groups, for example, C=O, C=C, C≡C, C-X, C=N and C≡N. This is because the reduction of the second functional group is at times more facile. Problems can be overcome by tailoring the size and shape of metal nanoparticles, modifiers as well as additives. Many examples in the literature, metallic Pt nanoparticles are shown to be the most selective. For example, using the Lindlar approach in the case of Pd catalysts, Pb can be added to Pt, offering additional selectivity.[84] Additives may include H_3PO_2, $FeCl_2$ or V, Ce, Ni and Zn complexes.[85-88] Light modifiers can also be applied such as S-, P-, N-, X-containing compounds. Strong metal support interaction using partially reduced TiO_x deposited on Pt. Metallic Pd based catalysts have been investigated due its lower costs, despite the metal is often less selective compared to Pt. For example, modifying the catalyst with modifiers/additives such as ethylene diamine[89], diphenyl sulphide[90], Lindlar catalyst[91] and reduced iron oxide.[92] Recently, noble metals Au and Ag have also been demonstrated to be active and selective in their nanosized regime, at times affording total selectivity at full conversion.[93-95]

1.6 COMPUTER APPLICATIONS IN HETEROGENEOUS CATALYSIS

A huge breakthrough in heterogeneous catalysis would be *in silico* catalyst optimisation, where reaction data is entered into a program and the output is an optimised structure of the best catalyst in a reaction. Although such a program does not exist to date, significant advances have been made in the development of computer modelling for heterogeneous catalysis, thanks to the increase in computing power in the last 20 years. It is difficult to develop catalyst/experimental descriptors for heterogeneous catalysis, mainly because solid catalysts are not uniform. For example a catalyst has different types of active sites, solid catalyst surfaces/phases can change drastically under real reaction conditions so real active sites may not be observed in *ex situ* characterisation studies. Nevertheless, some breakthroughs have been made in formulating descriptors for heterogeneous catalysis and will be outlined below.

1.6.1 DENSITY FUNCTIONAL THEORY OF METAL SURFACES

The application of density functional theory (DFT) calculations to provide experimental guidance and validation of modelling concepts has had a tremendous impact in the heterogeneous catalysis community. The *d*-band model is fundamental in understanding trends in reactivity across the groups of transition metal. It is of great interest to an experimental chemist in understanding surface chemical reactivity and bond formation between a surface and a substrate. The *d*-band model is an approximate description of bond formation on a metal surface (Fig. 1-17).[96] It forms a description of chemical bonding between metal *s* and *d* states, and the adsorbate states. The model works to a first approximation by projecting the adsorbate valence

states onto the metal *s* states, giving rise to its downshift and broadening because all transition metal *s* states are diffuse and board. The second projection is the metal *d* states, where significant differences arise from the position of the metal. This leads to the formation of their bonding and antibonding states. The difference in chemical bonding is explained by the degree of filling of the adsorbate antibonding states relative to the Fermi level, as antibonding states are always above the metal *d* states. The centre of *d* states relative to the Fermi level is the first indicator to the strength of the surface chemical bond. Other factors contributing to the surface bonding include:

i) Filling of *d* bands, which increases towards the right of the periodic table.

ii) Metal cohesive energy, increases down the periodic table.

iii) Coupling matrix element, V_{sd}, estimated by linear muffin-tin orbitals (LMTO) theory, the value of which increases down the group and left of the periodic table as the *d* states are more tightly bound.

Applying the *d* band model explains why Au is the noblest of all metals due to its large cohesive energy, V_{ad} and fully filled *d* band, leading to a completely filled adsorbate antibonding states resulting in net Pauli repulsions in the dissociation of molecular hydrogen.[97]

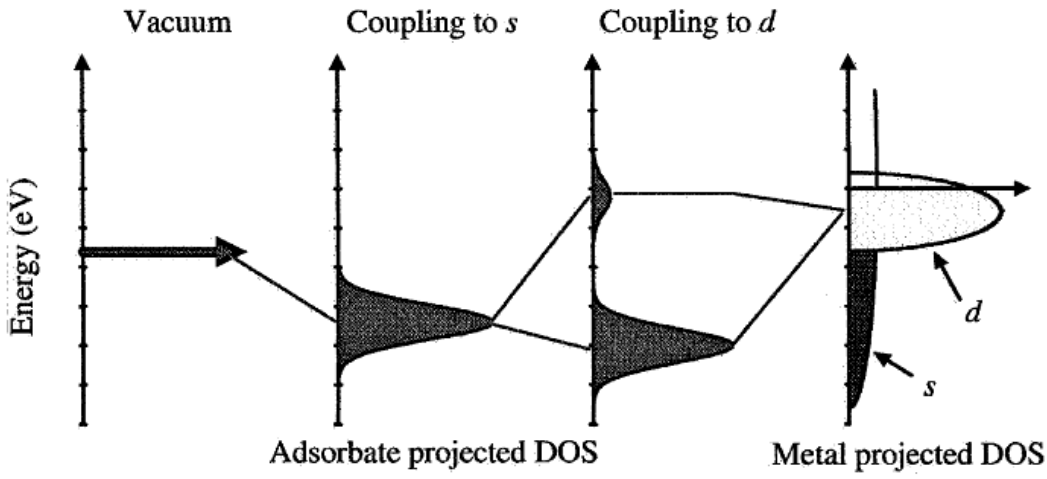

Fig. 1-17 Illustration of bond formation between an adsorbate and the *s* and *d* states on a metal surface.

The generality of the *d* band model can be extended to changes in size, shape and alloying with another metal. As the size decreases, there is a net increase in the number of lower coordinated atoms. For example, edges and corners have coordination numbers of 6 and 5, respectively, as compared to a (111) surface with 9 nearest neighbours. The variation in coordination numbers changes the band width, which leads to considerable variations in *d* band centres. This is because the *d* filling is constant for a metal and therefore changes in its band width shift the *d* states up or down, with lower coordinated metal atoms higher in *d* band centres compared to flat surfaces. This explains the variations in CO adsorption on different Pt surfaces, where strong structure sensitivity was observed by as much as 1 eV.[98] Strain effects on the metal lattice can also be explained by the *d* band model. As the lattice expands, the overlaps between d electrons on the neighbouring metal atoms are weakened. This decreases the bandwidth in order to keep the *d* occupancy fixed, as detailed above. The *d* states move closer to the Fermi level, leading to a stronger adsorbate interaction.[99] The effect of alloying or ligand effect can also be understood by changes in the *d* band. In general, electronic charge is transferred from the metal with higher Fermi level to ones with a lower Fermi level, which results in the *d* band centre shift. This is termed charge redistribution, where it has been applied to investigate the oxygen reduction reaction (ORR).[100, 101] It is difficult to separate the strain and ligand effect in core shell nanoparticles, as the metal overlayers will adopt the lattice parameter of the core especially if the shell is thin.[52]

1.6.2 DESCRIPTORS IN HETEROGENEOUS CATALYSIS

It is well known that the macroscopic kinetics of a catalysed reaction can be modelled based on theoretical calculations.[102, 103] Kinetics can be obtained when all energy steps and activation barriers are calculated as a function of adsorbate coverage

and catalyst structure. However, calculating all these parameters in one reaction is highly demanding, even with today's computational power. Therefore, trends can be used as an alternative to model surface reactivity. The trends in reactivity can be described by variations in the kinetics of the catalyst. An understanding of these trends may lead to designing low cost, more effective catalysts. Theoretical descriptors can be derived to model the most important microscopic properties of the catalyst that determines its macroscopic performance, where they can be scanned much more quickly in the search to designing new catalyst materials.

A recent example can be found in the literature where theoretical descriptors have been derived and reactivity trends rationalised in the selective hydrogenation of acetylene in excess ethylene.[104] A selective catalyst should desorb any adsorbed ethylene much faster than before it is further hydrogenated to ethane. In this case, the adsorption energies of acetylene and ethylene are used as theoretical descriptors that determine activity and selectivity (Fig. 1-18). Accordingly, scaling relations were shown to be well correlated by using a methyl adsorption energy (acetylene is 4 and ethylene is 2). The study found the best catalyst is a compromise between activity and selectivity. Once these theoretical descriptors are developed, one can rapidly screen potential new catalysts. Thus, a much lower cost NiZn and NiGa type catalysts were identified and subsequently verified experimentally, where the catalysts were demonstrated to have comparable selectivity to that of commercial PdAg catalyst.[105]

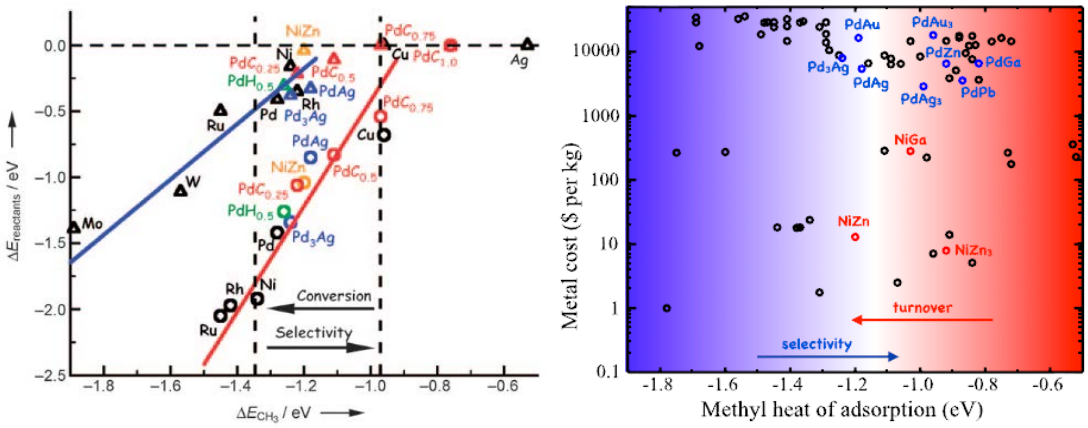

Fig. 1-18 (left) A plot of adsorption energy of acetylene (blue) and ethylene (red) against a methyl group. Solid lines represent predicted adsorption energies from scaling.[104] (right) Screening of bimetallic catalysts based on the calculated methyl adsorption energies plotted against metal price.[105]

Although applications of DFT and theoretical descriptors have demonstrated to be powerful tools to guide experimental chemists in designing more efficient catalysts, the goal in designing a similar basis sets to rationalise metal oxide assisted/catalysed reactions is far less developed.

1.7 OBJECTIVES

The objective of this research is concerned with development of a novel class of metal/alloy ultraselective nanocatalysts that could make a profound impact to the fine chemical and pharmaceutical industries.

The aim is to undertake a feasibility study of developing a new class of metal catalysts for fine chemical conversions of pharmaceutical interest where the benefits of improving reaction selectivity and insensitivity towards catalytic poisons would be most profound. We sought to develop a new class of metal catalysts, where the metal is modified with interstitial atoms at the atomic level through nano-engineering of catalyst particles. The modifier may offer geometric, electronic or synergetic effects to the metal by creating a catalyst of well defined size and composition. It is anticipated that this generic approach could offer a totally new generation of catalysts

for chemical synthesis, thus may replace traditional supported metal catalysts. In the course of the project, we aim to achieve the following:

- Develop totally new chemical based methods for synthesising well-defined preformed metal/non-metal catalysts in solution.
- Modify metal sites with required 'local' metal-metal, metal/non-metal or metal-support interactions, with a particular focus to replace expensive PGM metals to cheaper alternatives without compromising activity and selectivity.
- Control the surface structure, composition and morphology of the nanocatalysts using nano synthetic approach in solution.
- Investigate these new classes of nanocatalysts for hydrogenation reactions in the liquid phase including hydrogenation of targeted functional group(s) with ultrahigh specificity: α,β-unsaturated aldehyde to alcohols; alkynes to alkenes; nitros/nitriles to amines, etc.
- Optimise the size, composition, structure and interface of the composites of the new class of catalysts.

1.8 THESIS OVERVIEW

This thesis is divided into seven chapters with three chapters outlining the research that I had done over the three and a half years of my D.Phil study.

CHAPTER ONE – Introduces the basics of heterogeneous catalysis, design, synthesis and control of catalyst surface structure, selective hydrogenation technologies in the liquid phase and computer aided design of solid catalysts.

CHAPTER TWO – Introduces the most commonly applied analytical tools to characterise solid catalysts.

CHAPTER THREE – Experimental description in the synthesis and testing of solid catalyst materials.

CHAPTER FOUR – Describes the synthesis and characterisation of palladium modified with interstitial carbon using a hydrothermal method with glucose. Materials were tested in stereoselective hydrogenation of alkynes in the liquid phase.

CHAPTER FIVE – Describes the synthesis and characterisation high quality palladium modified with interstitial boron using a liquid fabrication process at mild temperatures. Materials were tested in a variety of liquid phase hydrogenations.

CHAPTER SIX – Describes the synthesis of colloidal gold and palladium-boron nanoparticles. The materials were characterised using spectroscopic techniques using FTIR and ^{13}C formic acid NMR.

CHAPTER SEVEN – Conclusions and perspectives of the research.

1.9 REFERENCES

1. G. Ertl, H. Knoezinger, F. Schueth, J. Weitkamp and Editors, *Handbook of Heterogeneous Catalysis; Volume 8*, Wiley-VCH Verlag GmbH & Co. KGaA, 2008.
2. J. A. Kent and Editor, *Kent and Riegel's Handbook of Industrial Chemistry and Biotechnology, 11th Edition*, Springer Science, 2007.
3. J. J. Berzelius, *Jahresbericht*, 1836, **15**, 237 and 243.
4. K. W. Kolasinksi and Editor, *Surface Science: Foundations of Catalysis and Nanoscience, Second Edition*, John Wiley & Sons, Ltd., 2008.
5. J.-P. Corbet and G. Mignani, *Chem. Rev.*, 2006, **106**, 2651-2710.
6. A. Dondoni and A. Massi, *Angew. Chem. Int. Ed.*, 2008, **47**, 4638-4660.
7. I. Chorkendorff and J. W. Niemantsverdriet, *Concepts of Modern Catalysis and Kinetics*, John Wiley & Sons, 2003.
8. C. J. H. Jacobsen, S. Dahl, B. S. Clausen, S. Bahn, A. Logadottir and J. K. Norskov, *J. Am. Chem. Soc.*, 2001, **123**, 8404-8405.
9. G. A. Somorjai, *Introduction to Surface Chemistry and Catalysis*, Wiley, 1994.
10. R. B. King and Editor, *Encyclopedia of Inorganic Chemistry*, Wiley, 2005.
11. L. D. Pachón and G. Rothenberg, *Appl. Organomet. Chem.*, 2008, **22**, 288-299.
12. M. Faraday, *Philos. Trans. R. Soc. London*, 1857, **147**, 145-181.
13. B. L. Cushing, V. L. Kolesnichenko and C. J. O'Connor, *Chem. Rev.*, 2004, **104**, 3893-3946.
14. J. Park, J. Joo, S. G. Kwon, Y. Jang and T. Hyeon, *Angew. Chem. Int. Ed.*, 2007, **46**, 4630-4660.
15. V. K. La Mer and R. H. Dinegar, *J. Am. Chem. Soc.*, 1950, **72**, 4847-4854.
16. S. Tadao, *Adv. Colloid. Interface Sci.*, 1987, **28**, 65-108.

17. G. C. Bond, *Heterogeneous catalysis : principles and applications*, Clarendon Press, Oxford, 1987.
18. T. Janssens, B. Clausen, B. Hvolbæk, H. Falsig, C. Christensen, T. Bligaard and J. Nørskov, *Top. Catal.*, 2007, **44**, 15-26.
19. R. Van Hardeveld and F. Hartog, *Surf. Sci.*, 1969, **15**, 189-230.
20. B. Hvolbæk, T. V. W. Janssens, B. S. Clausen, H. Falsig, C. H. Christensen and J. K. Nørskov, *Nano Today*, 2007, **2**, 14-18.
21. H. Weller, *Angew. Chem. Int. Ed. Engl.*, 1993, **32**, 41-53.
22. W. A. de Heer, *Reviews of Modern Physics*, 1993, **65**, 611-676.
23. A. Henglein, *Chem. Rev.*, 1989, **89**, 1861-1873.
24. C. B. Murray, C. R. Kagan and M. G. Bawendi, *Annu. Rev. Mater. Sci.*, 2000, **30**, 545-610.
25. Y. Li, E. Boone and M. A. El-Sayed, *Langmuir*, 2002, **18**, 4921-4925.
26. M. Haruta, *Catal. Today*, 1997, **36**, 153-166.
27. M. Haruta, T. Kobayashi, H. Sano and N. Yamada, *Chem. Lett.*, 1987, 405-408.
28. M. Haruta, N. Yamada, T. Kobayashi and S. Iijima, *J. Catal.*, 1989, **115**, 301-309.
29. M. Valden, X. Lai and D. W. Goodman, *Science*, 1998, **281**, 1647-1650.
30. H.-G. Boyen, G. Kastle, F. Weigl, B. Koslowski, C. Dietrich, P. Ziemann, J. P. Spatz, S. Riethmuller, C. Hartmann, M. Moller, G. Schmid, M. G. Garnier and P. Oelhafen, *Science*, 2002, **297**, 1533-1536.
31. J. Guzman and B. C. Gates, *J. Am. Chem. Soc.*, 2004, **126**, 2672-2673.
32. L. Vitos, A. V. Ruban, H. L. Skriver and J. Kollar, *Surf. Sci.*, 1998, **411**, 186-202.

33. B. Lim, M. Jiang, J. Tao, P. H. C. Camargo, Y. Zhu and Y. Xia, *Adv. Funct. Mater.*, 2009, **19**, 189-200.

34. Y. X. B. L. Sara E. S. Younan Xia, *Angew. Chem. Int. Ed.*, 2009, **48**, 60-103.

35. Y. Xiong and Y. Xia, *Adv. Mater.*, 2007, **19**, 3385-3391.

36. J. Ren and Richard D. Tilley, *Small*, 2007, **3**, 1508-1512.

37. M. Shao, T. Yu, J. H. Odell, M. Jin and Y. Xia, *Chem. Commun.*, 2011, **47**, 6566-6568.

38. M. Jin, H. Zhang, Z. Xie and Y. Xia, *Angew. Chem. Int. Ed.*, 2011, **50**, 7850-7854.

39. M. Crespo-Quesada, A. Yarulin, M. Jin, Y. Xia and L. Kiwi-Minsker, *J. Am. Chem. Soc.*, 2011, **133**, 12787-12794.

40. F. C. Meunier, *ACS Nano*, 2008, **2**, 2441-2444.

41. P. Reyes, H. Rojas and J. L. G. Fierro, *Appl. Catal., A*, 2003, **248**, 59-65.

42. B. Coq, A. Tijani, R. Dutartre and F. Figuéras, *J. Mol. Catal.*, 1993, **79**, 253-264.

43. S. J. Tauster, S. C. Fung and R. L. Garten, *J. Am. Chem. Soc.*, 1978, **100**, 170-175.

44. P. L. J. Gunter, J. W. Niemantsverdriet, F. H. Ribeiro and G. A. Somorjai, *Catal. Rev.-Sci. Eng.*, 1997, **39**, 77 - 168.

45. B. Coq and F. Figueras, *Coord. Chem. Rev.*, 1998, **178-180**, 1753-1783.

46. S. Carrettin, P. Concepción, A. Corma, J. M. López Nieto and V. F. Puntes, *Angew. Chem. Int. Ed.*, 2004, **43**, 2538-2540.

47. J. Xu, J. Harmer, G. Li, T. Chapman, P. Collier, S. Longworth and S. C. Tsang, *Chem. Commun.*, 2011, **46**, 1887-1889.

48. Y. Yamada, C.-K. Tsung, W. Huang, Z. Huo, S. E. Habas, T. Soejima, C. E. Aliaga, G. A. Somorjai and P. Yang, *Nat Chem*, 2011, **3**, 372-376.

49. A. McLaren, T. Valdes-Solis, G. Li and S. C. Tsang, *J. Am. Chem. Soc.*, 2009, **131**, 12540-12541.

50. F. Liao, Y. Huang, J. Ge, W. Zheng, K. Tedsree, P. Collier, X. Hong and S. C. Tsang, *Angew. Chem. Int. Ed.*, 2011, **50**, 2162-2165.

51. S. E. Habas, H. Lee, V. Radmilovic, G. A. Somorjai and P. Yang, *Nat Mater*, 2007, **6**, 692-697.

52. W. Tang and G. Henkelman, *J. Chem. Phys.*, 2009, **130**, 194504-194506.

53. P. Strasser, S. Koh, T. Anniyev, J. Greeley, K. More, C. Yu, Z. Liu, S. Kaya, D. Nordlund, H. Ogasawara, M. F. Toney and A. Nilsson, *Nat Chem*, 2010, **2**, 454-460.

54. S. C. Tsang, N. Cailuo, W. Oduro, A. T. S. Kong, L. Clifton, K. M. K. Yu, B. Thiebaut, J. Cookson and P. Bishop, *ACS Nano*, 2008, **2**, 2547-2553.

55. W. O. Oduro, N. Cailuo, K. M. K. Yu, H. Yang and S. C. Tsang, *Phys. Chem. Chem. Phys.*, 2011, **13**, 2590-2602.

56. F. Tao, M. E. Grass, Y. Zhang, D. R. Butcher, J. R. Renzas, Z. Liu, J. Y. Chung, B. S. Mun, M. Salmeron and G. A. Somorjai, *Science*, 2008, **322**, 932-934.

57. C. D. Gelatt, A. R. Williams and V. L. Moruzzi, *Phys. Rev. B*, 1983, **27**, 2005.

58. J. R. Kitchin, J. K. Nørskov, M. A. Barteau and J. G. Chen, *Phys. Rev. Lett.*, 2004, **93**, 156801.

59. D. Teschner, J. Borsodi, A. Wootsch, Z. Revay, M. Havecker, A. Knop-Gericke, S. D. Jackson and R. Schlogl, *Science*, 2008, **320**, 86-89.

60. S. B. Ziemecki, G. A. Jones and D. G. Swartzfager, *J. Less-Common Met.*, 1987, **131**, 157-162.

61. S. B. Ziemecki, G. A. Jones, D. G. Swartzfager, R. L. Harlow and J. Faber, *J. Am. Chem. Soc.*, 1985, **107**, 4547-4548.

62. S. B. Zlemecki and G. A. Jones, *J. Catal.*, 1985, **95**, 621-622.

63. J. Stachurski and A. Frackiewicz, *J. Less-Common Met.*, 1985, **108**, 249-256.

64. M. Maciejewski and A. Baiker, *J. Phys. Chem. A*, 1994, **98**, 285-290.

65. P. Pollak, *Fine Chemicals: The Industry and the Business*, John Wiley & Sons, Inc., 2007.

66. R. A. Sheldon, B. H. Van and Editors, *Fine Chemicals through Heterogeneous Catalysis*, Wiley-VCH Verlag GmbH, 2001.

67. M. Beller, C. Bolm and Editors, *Transition Metals for Organic Synthesis: Building Blocks and Fine Chemicals Second Revised and Enlarged Edition, Volume 2*, Wiley-VCH Verlag GmbH & Co. KGaA, 2004.

68. F. Cavani, G. Centi, S. Perathoner, F. Trifiro and Editors, *Sustainable Industrial Processes*, Wiley-VCH Verlag GmbH & Co. KGaA, 2009.

69. L. Cerveny and V. Ruzicka, *Catal. Rev.-Sci. Eng.*, 1982, **24**, 503 - 566.

70. Á. Molnár, A. Sárkány and M. Varga, *J. Mol. Catal. A: Chem.*, 2001, **173**, 185-221.

71. R. L. Burwell, *Chem. Rev.*, 1957, **57**, 895-934.

72. P. N. Rylander, *Best Synthetic Methods: Hydrogenation Methods*, Academic Press, 1985.

73. S. Nishimura, *Handbook of Heterogeneous Catalytic Hydrogenation for Organic Synthesis*, Wiley, 2001.

74. M. M. Johnson, D. W. Walker and G. P. Nowack, Phillips Petroleum Company, US Patent, 4,404,124, 1983.

75. C. N. Thanh, B. Didillon, P. Sarrazin and C. Cameron, Institut Francais du Petrole, US Patent, 6,054,409, 2000.

76. H. Lindlar, *Helvetica Chimica Acta*, 1952, **35**, 446-450.

77. L. A. Sarandeses, J. Mascarenas, L. Castedo and A. Mourino, *Tetrahedron Lett.*, 1992, **33**, 5445-5448.

78. H.-U. Blaser, H. Steiner and M. Studer, *ChemCatChem*, 2009, **1**, 210-221.

79. F. Haber, *Z. Elektrochem. Angew. Phys. Chem.*, 1898, **4**, 506.

80. J. A. Makaryan, V. I. Savchenko, F. S. L. Guczi and T. T. N. P, in *Studies in Surface Science and Catalysis*, Elsevier, 1993, pp. 2439-2442.

81. V. R. Choudhary and M. G. Sane, *Ind. Eng. Chem. Res.*, 1999, **38**, 4594-4599.

82. V. R. Choudhary, M. G. Sane and S. S. Tambe, *Ind. Eng. Chem. Res.*, 1998, **37**, 3879-3887.

83. G. Neri, M. G. Musolino, L. Bonaccorsi, A. Donato, L. Mercadante and S. Galvagno, *Ind. Eng. Chem. Res.*, 1997, **36**, 3619-3624.

84. P. Baumeister, H. U. Blaser, U. Siegrist and M. Studer, *Catal. Org. React.*, 1998.

85. X. Han, R. Zhou, X. Zheng and H. Jiang, *J. Mol. Catal. A: Chem.*, 2003, **193**, 103-108.

86. P. Baumeister, H. U. Blaser and M. Studer, *Catal. Lett.*, 1997, **49**, 219-222.

87. G. Wu, M. Huang, M. Richards, M. Poirier, X. Wen and R. W. Draper, *Synthesis*, 2003, 1657-1660.

88. W. Tu, H. Liu and Y. Tang, *J. Mol. Catal. A: Chem.*, 2000, **159**, 115-120.

89. H. Sajiki, K. Hattori and K. Hirota, *J. Org. Chem.*, 1998, **63**, 7990-7992.

90. A. Mori, T. Mizusaki, M. Kawase, T. Maegawa, Y. Monguchi, S. Takao, Y. Takagi and H. Sajiki, *Adv. Synth. Catal.*, 2008, **350**, 406-410.

91. J. M. Hawkins and T. W. Makowski, *Org. Process Res. Dev.*, 2001, **5**, 328-330.

92. H. Liu, M. Liang, C. Xiao, N. Zheng, X. Feng, Y. Liu, J. Xie and Y. Wang, *J. Mol. Catal. A: Chem.*, 2009, **308**, 79-86.

93. Y. Chen, C. Wang, H. Liu, J. Qiu and X. Bao, *Chem. Commun.*, 2005, 5298-5300.

94. A. Corma and P. Serna, *Science*, 2006, **313**, 332-334.

95. A. Corma, C. González-Arellano, M. Iglesias and F. Sánchez, *Appl. Catal., A*, 2009, **356**, 99-102.

96. A. Nilsson, L. G. M. Pettersson, B. Hammer, T. Bligaard, C. H. Christensen and J. K. Nørskov, *Catal. Lett.*, 2005, **100**, 111-114.

97. B. Hammer and J. K. Norskov, *Nature*, 1995, **376**, 238-240.

98. B. Hammer, O. H. Nielsen and J. K. Nrskov, *Catal. Lett.*, 1997, **46**, 31-35.

99. M. Mavrikakis, B. Hammer and J. K. Norskov, *Phys. Rev. Lett.*, 1998, **81**, 2819.

100. J. Zhang, M. B. Vukmirovic, K. Sasaki, A. U. Nilekar, M. Mavrikakis and R. R. Adzic, *J. Am. Chem. Soc.*, 2005, **127**, 12480-12481.

101. T. Toda, H. Igarashi, H. Uchida and M. Watanabe, *J. Electrochem. Soc.*, 1999, **146**, 3750-3756.

102. E. W. Hansen and M. Neurock, *J. Catal.*, 2000, **196**, 241-252.

103. K. Reuter, D. Frenkel and M. Scheffler, *Phys. Rev. Lett.*, 2004, **93**, 116105.

104. F. Studt, F. Abild-Pedersen, T. Bligaard, R. Z. Sørensen, C. H. Christensen and J. K. Nørskov, *Angew. Chem. Int. Ed.*, 2008, **47**, 9299-9302.

105. F. Studt, F. Abild-Pedersen, T. Bligaard, R. Z. Sorensen, C. H. Christensen and J. K. Norskov, *Science*, 2008, **320**, 1320-1322.

CHAPTER 2 - ANALYTICAL TECHNIQUES

2.1 INTRODUCTION

The characterisation and understanding a working catalyst is of paramount importance in surface catalysis. A wide variety of techniques based on spectroscopy, microscopy, diffraction, adsorption, desorption and surface reactions can all provide information on the nature of a working catalyst. The knowledge thus gained in understanding how a catalyst works can hopefully lead to improvements of existing catalyst as well as designing new catalysts.

The ultimate goal in catalyst characterisation is to evaluate its composition, structure/surface feature at the atomic scale. In other words, the examination of a working catalyst on an atom by atom basis under real operational conditions. However, catalysts often come as small metal particles deposited on a support material. Furthermore, promoters are often added to enhance its performance, on top of elevated temperature and/or pressure as well as changes in surface characteristics of the catalyst often applied under real conditions can make such characterisations a difficult task.

Nevertheless, several spectroscopic, microscopic and diffraction techniques can be used to investigate metal catalysts (Fig. 2-1). These techniques are based on how the catalyst responds to matter, whether its subjected to irradiation, electrons, probe molecules or heat, then after their interaction its outgoing source is analysed. For example, in electron microscopy, a catalyst is radiated with high energy electrons which generate electrons with different outward energies, as well as photons and X-rays. These can therefore be analysed to extract information on the catalyst.

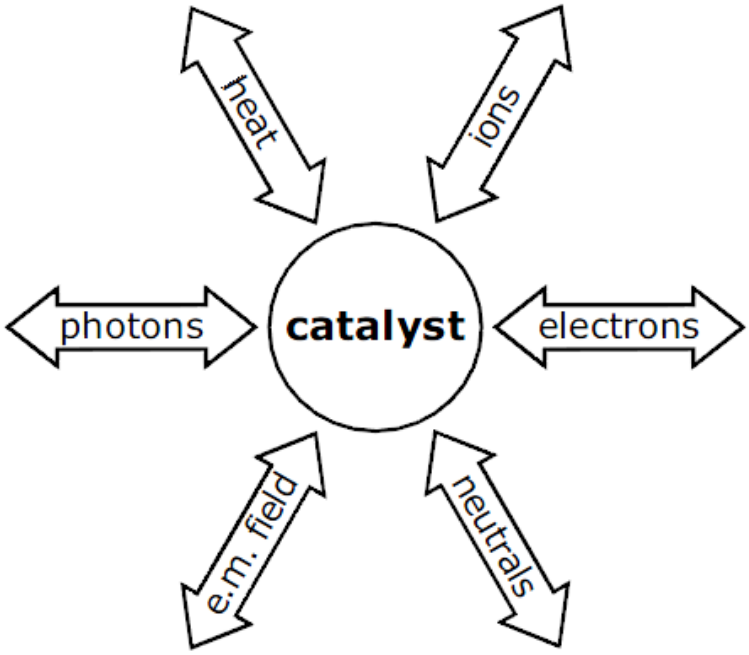

Fig. 2-1 Catalyst characterization techniques: The circle represents the sample under study, the inward arrows denote excitation processes, and the outward arrows indicate that the information is extracted.[1]

2.2 X-RAY DIFFRACTION

X-Ray diffraction (XRD) is one of the most applied techniques in catalyst characterisation (Fig. 2-2). The technique is mainly used to identify crystalline phases in a catalyst by obtaining a pattern of its structural lattice parameters. Furthermore, an estimation of catalyst particle size can be calculated in a timely manner when compared to electron microscopy techniques. XRD works because the X-rays have wavelengths in the Ångström range that can penetrate solids and probe their internal structure. The X-rays are generated by electrons from a tungsten filament bombarding a copper anode at high voltage. This produces an X-ray spectrum to those arising from the electrons being slowed down by the anode, forming a continuous background spectrum as well as discrete lines that is characteristic of the anode. This is called the Cu Kα line which possesses an energy and wavelength of 8.04 keV and 0.154 nm, respectively. The line arises because a core hole is created in the K-shell and then filled by an electron from the L-shell which subsequently emits an X-ray in

the process. Accompanying this is the less intense Kβ line which is emitted when the K-hole filled from the M-shell.

Fig. 2-2 A PANalytical X'Pert Pro X-ray diffractometer.

XRD is measured with a static X-ray arm coupled with a movable detector. The incident X-rays is illuminated onto a specimen that causes elastic scattering of X-ray photons by the sample atoms. The scattered photons that are in phase produces a constructive interference in relation given by the Bragg equation:

$$n\lambda = 2d \sin\theta \; ; n = 1, 2 \ldots$$

where λ is the wavelength of the X-rays; *d* is the distance between two lattice planes; θ is the angle if the incident X-rays and normal to the reflecting lattice plane; *n* is the integer correspond to the order of reflection. Therefore, XRD is measured with respect to angles 2θ, under which constructive interference gives rise to the sample lattice spacings that is characteristic of the compound.

A good limitation of XRD is that if the sample does not possess long range order particle size of a specimen can be calculated. In this case line broadening occurs due to incomplete destructive interference where the scattered X-rays are out of phase. Therefore particle size can be calculated based on the width of diffraction peaks by using the Scherrer equation:

$$L = \frac{K\lambda}{\beta \cos\theta}$$

where L is the volume weight average crystallite size of the particles; λ is the incident X-ray wavelength; β is the peak width; θ is the angle between the beam and normal to the reflecting plane; K is a constant (normally 1).

2.3 TRANSMISSION ELECTRON MICROSCOPY

Transmission electron microscopy (TEM) can reveal information on the internal structure, composition as well as size and shape of particles. The technique uses a high energy electron beam that is eradiated onto a very thin specimen. The electron beam interacts and passes the material where the beam is refocused through sets of lenses then projected onto a phosphor screen. Lenses in a TEM instrument uses electromagnetic lenses instead of optical lenses. Images can be captured either by using a charge coupled device (CCD) camera or by film.

According to the Rayleigh criterion, diffraction limit to resolution is:

$$\delta_d = \frac{0.61\ \lambda_0}{n\ \sin\alpha}$$

where α is the semi-angle subtended at the object by the lens; λ_0/n is the wavelength of radiation in the object space; n is the refractive index. Thus, the minimum resolvable distance in microscopes is the order of the wavelength. For example,

visible light has λ typically 500 nm and hence cannot be used to resolve atomic structures. To do that, a wavelength of $\lambda_0 < 0.1$ nm is needed to look at crystal lattices on an atomic scale. Therefore, electrons are the ideal choice because they are much smaller than atomic scales (electrons accelerated at 200 keV has $\lambda_0 = 2.5$ pm). Mode of operation of a typical TEM has electrons accelerated around 30 – 400 kV. In practice, however, resolutions are much poorer than the theoretical limit because of the non-spherical nature of the lens, called lens aberrations. For example, the typical resolution of a 200 kV TEM microscope is 0.24 nm, about 2 orders of magnitude lower than the wavelength of electrons. As mentioned, resolution can be improved by shortening the wavelength by increasing the accelerating voltage, or one can reduce the aberration coefficients for the magnetic lenses. By using aberration corrected microscopes for the condenser and objective lenses, one can increase resolution to sub-Ångström levels on a 200 kV microscope.

For electrons to travel through the specimen, powdered samples must be 100 nm or less. Powdered samples are dusted onto a holey carbon grid of a few millimetres thickness, alternatively it can be dispersed in a solvent and a drop of suspension added onto the grid and dried. Liquid samples are diluted and several drops added on the grid. Fig. 2-3 shows a typical cross section of a TEM microscope. Electrons can be generated from a tungsten filament, LaB_6 crystal or by a field emission tip. The beam of electrons is focused into a coherent beam by the double condenser lenses (lens 1 for spot size control and lens 2 for brightness control) and passes through the condenser aperture to filter out higher angle electrons. The beam strikes the sample and the transmitted beam is refocused by the objective lens. The objective aperture restricts high angle electrons while selected area diffraction aperture enables the user to interrogate diffraction patterns of electrons by the

arrangements of atoms in the specimen. Intermediate and projector lenses enlarge the image to high magnification. For example electrons accelerated between 100 – 200 keV have a point resolution of 0.5 nm with magnification typically in range of 3×10^5 to 10^6. Finally the image is projected onto a phosphor screen for user investigation. In bright field mode, dark areas of the image represent areas with fewer electrons being transmitted either due to thinner regions of the sample or heavier atoms and vice versa. In contrast, dark field images can be obtained when the electron beam is slightly off angle from the bright beam.

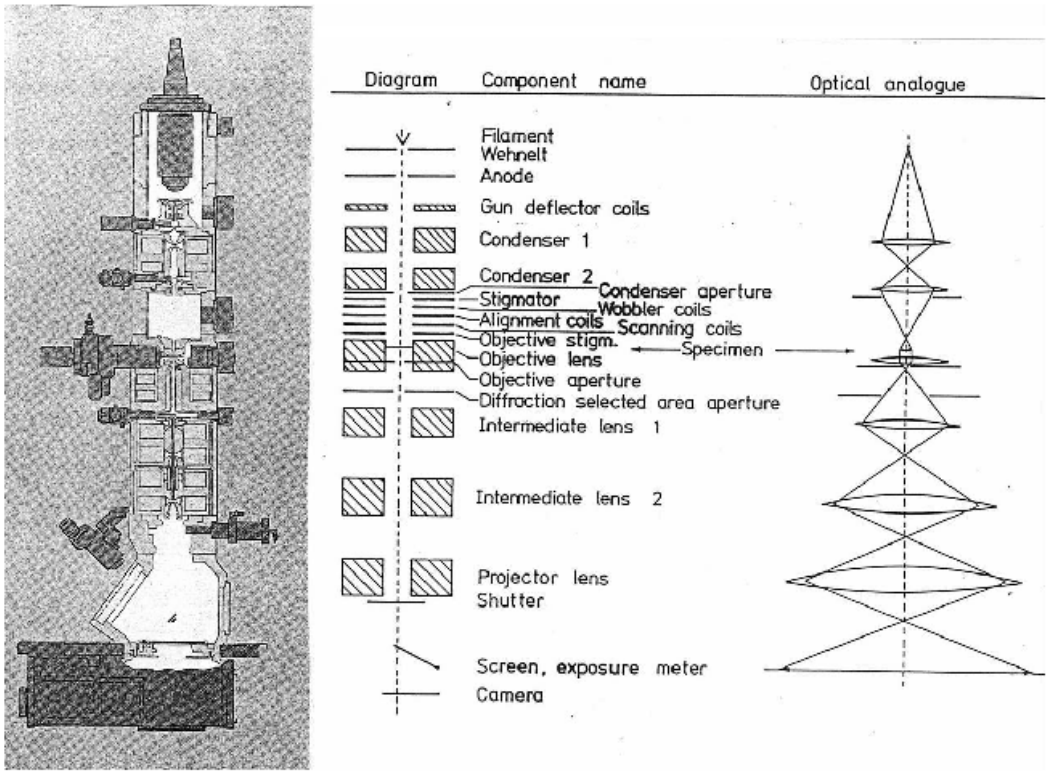

Fig. 2-3 Cross section of a TEM microscope.

Similar to XRD, selected area electron diffraction (SAED) mode can be used to reveal the structure of surfaces and any ordered adsorbate layers. Diffraction is possible by inserting a selected area aperture into the plane of an intermediate image with lenses below the objective lens that is focused on the back focal plane of the

objective lens. Long range order of the sample is needed for good diffraction patterns to achieve regular array of spots, whereas concentric ring patterns are formed where many particles are present due to their superimposed crystallographic orientations. The lattice phase can be determined by measuring the spacing ratios as well as the lattice parameter, although one must measure a standard sample of known spacing under the same operating conditions for calibration.

2.4 ENERGY DISPERSIVE X-RAY SPECTROSCOPY

This technique uses the phenomena that X-rays are generated as a secondary product in electron microscopy (Fig. 2-4). Energy dispersive X-ray spectroscopy (EDX) is operated normally in conjunction with TEM. The interaction of electron with atoms generates X-rays when the firing electron ejects an electron from an atomic orbital. The unstable ionised core then undergoes decay *via* two competing pathways. The first is X-ray fluorescence, where initial core hole is filled from a higher shell, for example L to K shell. The process gains energy and emits a Kα X-ray photon that is characteristic of the emitting atom. The second is Auger decay, where energy gained in the previous process is transferred to another electron in the L or higher shell. The atom then leaves with kinetic energy, hence called KLL Auger electron. The latter is more probable for lighter elements, whereas the former process is more pronounced for heavier elements ($Z > 12$) and hence it is frequently utilised to study the composition of bimetallic catalysts.

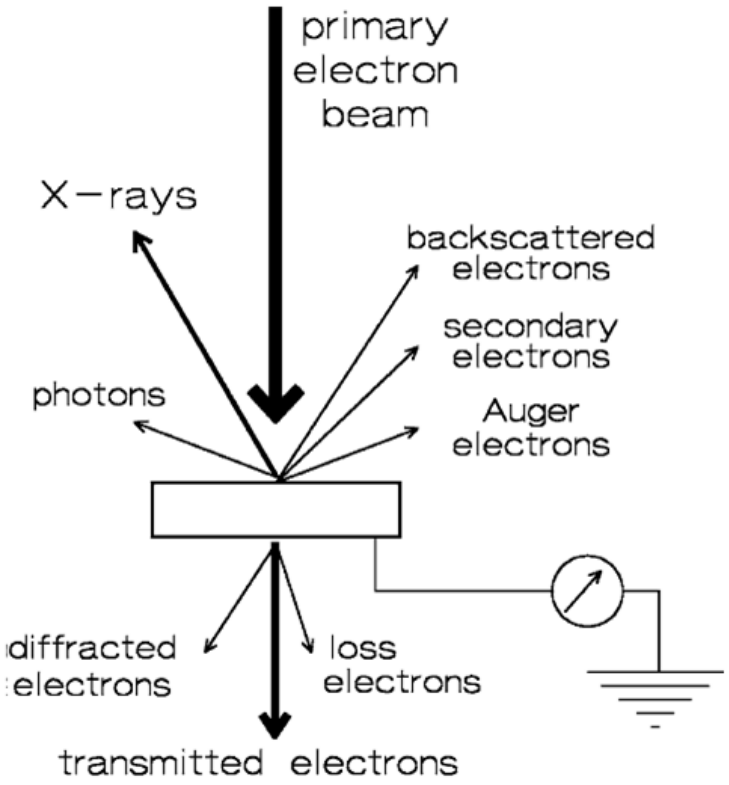

Fig. 2-4 Possible signals detected when the primary electron beam strikes the sample in an electron microscope.[2]

2.5 X-RAY PHOTOELECTRON SPECTROSCOPY

X-ray photoelectron spectroscopy (XPS) is one of the most applied characterisation techniques in surface science. The technique provides valuable information on the sample element composition near the surface region, their oxidation states as well as details of surface composition in a quantitative manner.[3]

Measurements of XPS are carried out in a UHV chamber where a controlled monochromatic X-ray source, typically in the form of Mg Kα with energy hν of 1253.6 eV and an Al source with Kα with hν of 1486.3 eV, is radiated at the sample. The sample atom then absorbs the photon energy and a photoelectron is emitted. Photoelectrons are collected using an electron energy analyser. Typical spatial sensitivity for XPS can vary from 100 μm to 1 mm but in some cases can be down to

10 μm. Surface sensitivity is about 5-10 nm but it can be increased by a using more grazing angle between the detector and sample stage (termed angle resolved XPS or APXPS). Thus, quantitative depth profile distribution of the elements can be readily obtained with depth resolution as high as 0.2 nm. On the other hand, higher energy X-rays, for example Ti Kα with hν of 2040 eV or synchrotron, can be used to increase analysis depth. The energy resolution of the technique can be within 0.2 eV, which is sensitive enough to detect an element in different chemical environments/states arising from their minor shifts in the kinetic energy of photoelectrons, therefore revealing vital information about the nature of chemical bonding environment for each element. As a general rule, binding energy increases with increasing oxidation states for each element. Peak shape can be analysed to reveal relative proportions of different chemical states of an element as well as atomic bonding from references.

The kinetic energy gained by the photoelectron is related to the energy of the incoming photon based on the photoelectric effect[2] (Fig. 2-5):

$$E_k = h\nu - E_b - \varphi$$

where E_k is the kinetic energy gained by the photoelectron; h is Planck's constant; ν is the frequency of the incoming photon; E_b is the binding energy of the photoelectron with respect of the Fermi level of the sample; φ is the work function of the spectrometer. XPS spectrums are usually plotted using the number of photoelectrons (N(*E*)) against their binding energy (E_b). Anger electrons can also be detected when ionised core relax to lower energy. Characteristics of Auger electrons can be distinguished by recording the spectrum at two different incident X-ray energies as they have fixed kinetic energies that is independent of the incident X-ray energy. Whilst Auger electrons may appear to offer similar information as XPS, an advantage of using Auger electrons is that as they may offer higher surface sensitivity

in terms of chemical bonding compared to XPS as the mean free path of electrons is at their minimum, thus reveals the fine structure/finger-print of the element in question.

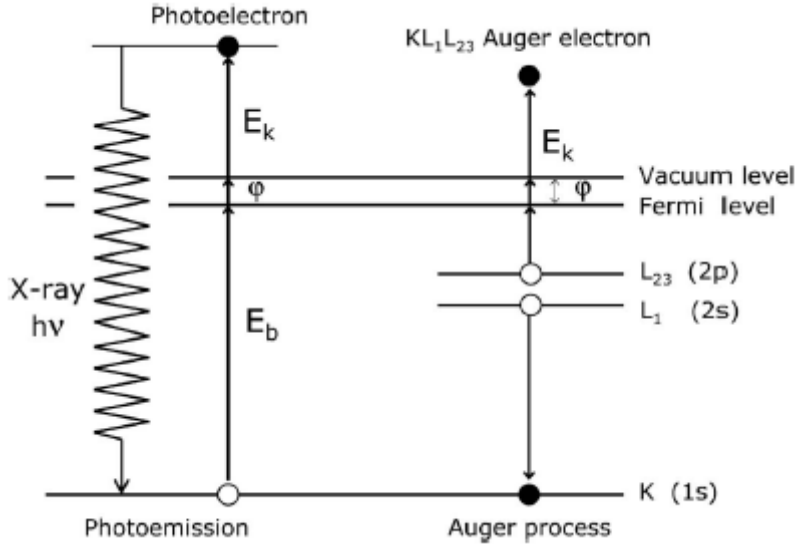

Fig. 2-5 Photoemission and the Auger process.[2]

Photoelectron peaks from XPS are labelled using the quantum numbers where the electron is ejected. Spin orbit coupling arise from the fact that spins can either be up or down ($s = \pm 1/2$) when the orbital momentum is $l \geq 1$ with the total momentum $j = l + s$. Therefore Pd 3d level gives rise to two peaks, the $3d_{5/2}$ ($l = 2$ and $j = 2 + 1/2$) and $3d_{3/2}$ ($l = 2$ and $j = 2 - 1/2$). Their intensity ratio is determined by the multiplicity according to $2j + 1$, therefore ratio for Pd $3d_{5/2}$ and $3d_{3/2}$ is 3:2.

The binding energy of a photoelectron represents the state of the atom before an electron is ejected (initial state) as well as the ionised core after ejection (final state). The presentation of XPS data are frequently interpreted by using only initial state effects and it is often correct to do so. The physics behind any binding energy shifts can be explained base in the charge potential model[1]:

$$E_b^i = kq_i + \sum_j \frac{q_j}{r_{ij}} + E_b^{ref}$$

where E_b^i is the binding energy of an electron from atom I; q_i is the charge on the atom; k is a constant; q_j is charge on a neighbouring atom j; r_{ij} is the distance between atom i and j; E_b^{ref} is an energy reference. The first term explains why binding energy increases with increasing positive charge. Second term counteracts the first term, where charge is balanced in ionic solids.

For supported catalysts, XPS can be used to access the dispersion of catalyst. For small particles, majority of atoms are located on the surface, which is reflected by the high intensity of particles detected when compared to support peaks, resulting in high I_p/I_s ratio, whereas poorly dispersed particles have the majority of atoms in the bulk, resulting in low I_p/I_s ratio. Therefore this implement any dispersion data collect using traditional surface techniques such as TEM and H_2/CO chemisorptions. In addition, valence band spectras can be obtained using XPS. The technique generates plots corresponding to density of states of the valence band with respect to the element Fermi level ($E_b = 0$). However, valence band spectras acquired in this way are far less sensitive and more difficult to interpret. Rather, ultraviolet photoelectron spectroscopy (UPS) is used instead with higher surface sensitivity and energy resolution.

One experimental problem with the technique is that non conducting samples may charge up during measurement. The build up of positive charge on the sample means all XPS peaks shift to higher binding energies by the same amount to each other. Luckily this can easily be corrected by using an element with which a binding energy that can be referenced, normally C 1s from the conducting tape is used with a

binding energy of 284.6 eV. Alternatively, an electron gun low energy electrons can be radiated on the sample that removes any inhomogeneous charging of the sample.

2.6 FOURIER TRANSFORM INFRARED SPECTROSCOPY

Fourier transform infrared spectroscopy (FTIR) is one of the most popular spectroscopic technique used in surface science.[2] Two common applications of this technique is the identification of surface adsorbed species, either *ex situ* or *in situ*, as well as investigating the nature of chemisorbed species on the catalyst. For example, spectra of pre-adsorbed surface probe molecule such as CO or NO can reveal dispersion and adsorption sites on a catalyst.

The application of infrared spectroscopy forms a part of the larger field called vibrational spectroscopy. Molecules possesses levels of rotational and vibrational energy and transitions can occur by the absorption of photons with the wave field applied and in doing so causes a vibration by mutual interaction. Specifically, only the mid IR region that is of interest (200 – 4000 cm^{-1}). According to the simple harmonic oscillator model, vibrational frequencies increase with increasing bond strength and as the mass of the vibrating atom decreases. A general selection rule for the absorption of photon is a change in dipole moment in the molecule during the vibration process. Furthermore, different vibrations can be observed (stretch, bend in/out of plane, torsion, symmetric and asymmetric), where increasing number of vibrations occur with increasing degrees of freedom.

To date, several forms of infrared spectroscopy exists: i) transmission; ii) diffuse reflection (DRIFTS); iii) emission; iv) attenuated total reflection (ATR-IR); v) reflection absorption; vi) raman scattering; vii) sum frequency generation (SFG-IR); electron energy loss spectroscopy (EELS). The most common form is transmission, where the sample is pelletised into a self-supporting disk less than 1 mm and about 1

cm^2. The technique can be applied to materials that absorbs weakly, for example inorganic oxides. Another prerequisite is support particles have to be smaller than the radiation. In DRIFTS, samples are measured as powders, therefore avoiding the need to prepare pellets and any diffusion issue which may arise from tightly packed samples. DRIFTS is ideal for specimens that are strongly absorbing or is a strong scatterer themselves. ATR-IR, or otherwise known as internal reflection or multiple internal reflection (MIR), is another popular technique. IR measurements reported in this thesis were recorded based on this technique. ATR criteria is satisfied when an optical beam transverse through an optically dense substrate undergoes total reflection at the interface to an optically rare medium at an angle greater than the critical angle.[3] Fig. 2-6 illustrates this phenomena as the beam propagates through the optical interface which generates evanescent fields. Optically rare mediums used in this technique are made of either diamond, Si, Ge or ZnSe. Each evanescent wave generated on the surface can be used to examine surface absorption. Major advantage of this technique is that examination of various interfaces are possible, e.g. solid/solid, solid/liquid, solid/gas. This opens up opportunities to study semi conductor solutions, electrochemical solutions, planar model catalysts supported on flat substrates, aqueous as well as turbid solutions. Sensitivity is also greatly increased because multiple evanescent waves are generated before the beam exit the optical rare medium. Such high sensitivity is particularly important when studying model catalysts as the metal surface area is low compared to those of the support. Reaction cell coupled with gas in/outlet can be placed on top of the crystal to enable *in situ* studies, a technique especially useful to study coverage dependent adsorption of gaseous molecules on metal surfaces.

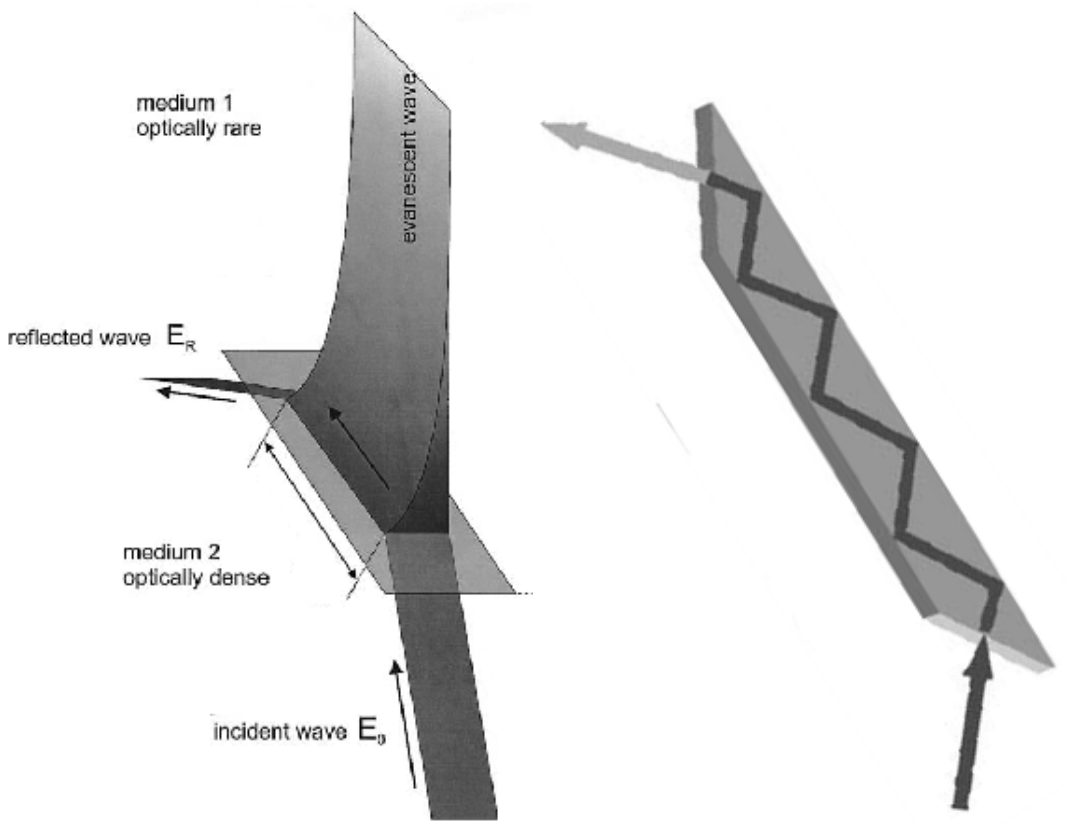

Fig. 2-6 An illustration of an ATR process to generate evanescent waves.[3, 4]

2.7 THERMOGRAVIOMETRIC ANALYSIS

Thermogravimetric Analysis (TGA) measures the amount and rate of change in the weight of a material as a function of temperature or time in a controlled atmosphere (Fig. 2-7, top). Measurements are used primarily to quantitatively determine the composition of materials and to predict their thermal stability at temperatures up to 1000°C. The technique can characterise materials that exhibit weight loss or gain due to decomposition, oxidation, or dehydration. A thin layer of sample is loaded onto either a platinum, ceramic (alumina) or aluminium pan. Gas flow rates are controlled using two mass flow controllers (balance purge and purge gas inlet). Temperature is monitored by an onboard computer with a ramp up capability as well as ramp down *via* a water circulation unit. Weight change is measured against a reference tare pan (Fig. 2-7, bottom). One drawback of TGA is

that it only measures weight changes in the sample but does not separate and identify the individual degraded products. However, this problem can be reduced by coupling the purge gas outlet to an FTIR or mass spec unit for evolved gas analysis (EGA).

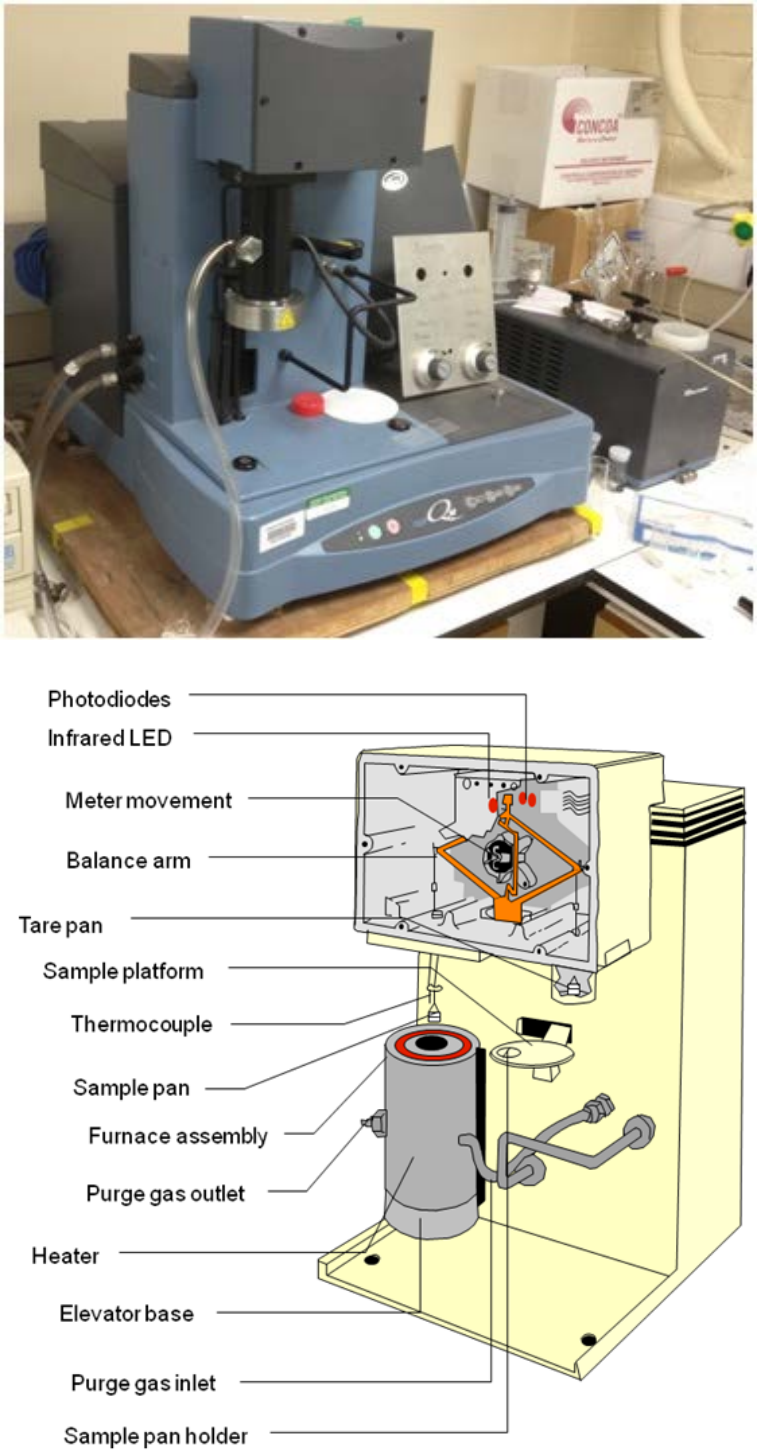

Fig. 2-7 A TA instrument Q50 (top); Schematic for the TGA Q50 (bottom).

2.8 TEMPERATURE PROGRAMMED DESORPTION REDUCTION AND OXIDATION

Temperature programmed desorption/reduction/oxidation (TPD/R/O) consists of passing a continuous gas stream (e.g. H_2, O_2, CO, etc) to the quartz reactor under a user pre-defined temperature ramp (Fig. 2-8, top). Three types of temperature programmed experiments can be performed: i) reduction (TPR); ii) oxidation (TPO); iii) desorption (TPD). These methods are particularly useful to determine the type and number of active sites, determine thermodynamic or kinetic parameters as well as quantitative measurements of acid/base properties of the catalyst. Catalysts are loaded between a bed of quartz wool and in turn is packed between the internal quartz tube and internal quartz reactor (Fig. 2-8, bottom). The internal tubes are placed inside the external quartz tube where it is merged with the stainless steel holder and sealed by a rubber o-ring. Twisting the metal head allows reactive gas to either flow into or by-pass the reactor.

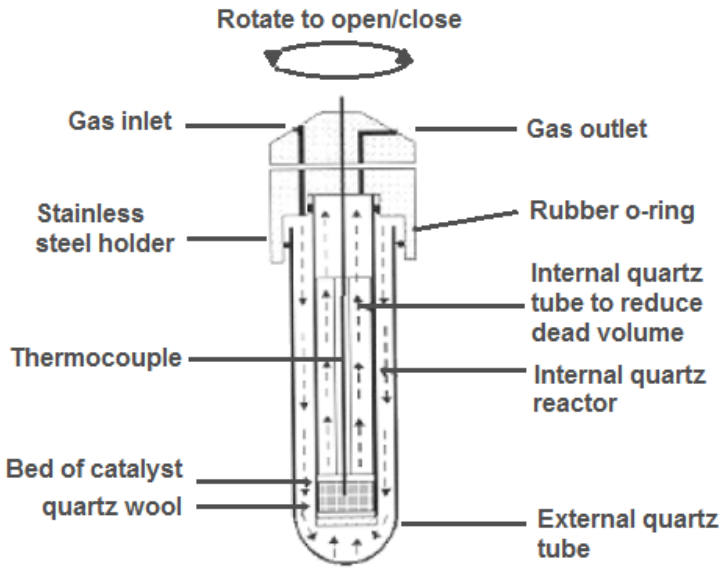

Fig. 2-8 A CE instrument TPD/R/O 1100 (top); Diagram for the reactor assembly (bottom).

TPR analysis determines the number and quantity of reducible species present in the sample and at what temperature its reduction occurs. The analysis is dependent on the flow conditions used, the percentage of reactive gas, the amount of sample and how fast the temperature increases. A constant flow 5% H_2 mixed with an inert gas like Ar is normally used in this analysis. Generally, the sample is pre-oxidised in a pretreatment run to ensure complete oxidation of metal as well as removing any contaminants that may persist in the sample. As the sample starts to reduce at a certain temperature the consumed H_2 is monitored through a thermo conductivity detector (TCD). Signals are detected according to change in polarity compared to a reference gas (Table. 2-1). High sensitivity of the TCD allows for the analysis of samples with very low metal content and linear response factors allowing for very accurate calibrations. The latter is needed in order to calculate the uptake of H_2 by integration of peak area to calculate the number of reacting sites using the correct reaction stiochiometry. This technique is particularly useful when looking at different oxidation states in the sample. Similarly in TPO, the sample is pre-reduced in the

pretreatment and a constant gas mixture of 5% O_2/He is passed through the sample at increasing temperatures. Total oxygen consumption can be calculated by integrating the overall area from the TCD signal and thus calculates the number of reactive sites oxidised. TPD analysis evaluates the binding strength, the number and types of reactive site on a catalyst measuring the amount of gas desorbed at increasing temperatures. Pretreatment and degassing the sample is required to remove adsorbed water and any contaminants. A reactive gas is passed onto the sample to allow surface adsorption/chemisorption to take place. Gases other than H_2 or O_2 can be used to calculate acid and basic sites in a sample. Desorption is performed by gently increasing the temperature with a constant flow of inert gas such as N_2, He or Ar acting as a carrier gas for the desorbed reactive gas. Again the desorbed gas is detected using a TCD detector. These techniques can be coupled to a mass spectrometer where the exact chemical nature of effluent gas can be traced.

Analysis	Carrier	Detected gas	Polarity
TPD	Nitrogen	Hydrogen	-
	Argon		
	Helium	Oxygen	++
		Water vapor	
		Ammonia	
		Carbon monoxide	
TPR	Nitrogen + X% Hydrogen	Hydrogen	+
	Argon + X% Hydrogen		
TPO	Helium + X% Oxygen	Oxygen	-

Table 2-1 Polarities for different types of experiments.

2.9 PULSE CHEMISORPTION

Pulse chemisorption injects a pulse of known volume of probe gas into the quartz reactor under isothermic conditions until there is no change in the response/constant. The reactive gas comes into contact on the available metal surface sites where chemisorption occurs until enough pulses are feed through to saturation. Several pulses after saturation are necessary for the self-calibration. Total number of

pulses depends on the loop volume and sample uptake. The total amount of gas chemisorbed can be calculated by the difference between total peak area during sample analysis and compared to a blank run with no sample capable for chemisorption to take place. The technique is extremely quick (subject to proper pretreatments as above) and provides complimentary information when measuring the dispersion of a metal catalyst. Gases such as H_2, O_2 and CO are the preferred choices because they chemisorb strongly on metals but less on support materials such as active carbon or metal oxides.

As mentioned, calibration must be undertaken if quantitative measurements are to be accurate. Determination of calibration factor takes into account the peak integration value with the total amount of gas chemisorbed onto the metal. Calibration runs must be performed under the exact same conditions where the sample is to be measured (reactive gas flow/concentration, temperature, number of injections, frequency of injections, carrier gas). The calibration factor can be obtained using the formula[5]:

$$C_F = \frac{N_d \, V_{loop} \, X_{gas} \, P_{inj} \, 10^{-3}}{R \, T_{inj} \, \int_{sum}}$$

where C_F is the calibration factor (mmol/mV s); N_d is the total detected peaks; V_{loop} is the total loop volume (mL); X_{gas} is the reactive gas percentage (%); P_{inj} is the injection pressure (hPa); G is the gas constant (J/mol K); T_{inj} is the injection temperature (K); $\int_{sum}$ is the total sum of peak areas (mV s). In the case where manual injection is needed, the V_{loop} term is replaced by the term V_{syr}, the syringe injection volume (mL). The amount of gas chemisorbed, n_{ads} (mmol/g), is now possible if the calibration factor is properly determined:

$$n_{ads} = \frac{\left\{\sum N_d(\int_{av\ pulse} - \int_{pulse} N_d) + N_h \int_{av\ pulse} \right\} C_F}{S_m}$$

where N_d is the total number of detected peaks; $\int_{av\ pulse}$ is the average peak area in the pulse injections (mV s); $\int_{pulse}$ is the peak area in pulse injections (mV s); N_h is the number of hidden peaks in the pulse chemisorption; S_m is mass of sample (g). We are now in a position to determine the metal surface area of the sample, A_{sam} (m^2/g of sample):

$$A_{sam} = L\, n_{ads}\, F_s\, a_{met}\, 10^{-23}$$

where L is the Avogadro's number (molecules/mol); F_s is the stoichiometric factor (metal mol/gas mol); a_{met} is the square section of a metal atom (Å^2/metal atom). This can also be conveniently expressed in terms of metal surface are to metal, A_{met} (m^2/g of metal) and to the support mass unit, A_{sup}, (m^2/g of support), respectively:

$$A_{met} = \frac{A_{sam}\ 100}{X_{met}}$$

$$A_{sup} = \frac{A_{sam}\ 100}{100 - X_{met}}$$

where X_{met} is percentage of metal in the sample. The metal dispersion, D_{met}, is defined as amount of adsorbed metal atoms to the total amount of metal contained in the catalyst:

$$D_{met} = \frac{n_{ads}\ F_s\ 10\ M_{met}}{X_{met}}$$

where M_{met} is the metal atomic weight (g/mol). Complimentary information on the average metal aggregate diameter, d_{met} (nm), can be obtained assuming they adopt a spherical shape on the support surface:

$$d_{met} = \frac{S_f \, 10^3}{A_{met} \, \rho_{met}}$$

where S_f is the shape factor (assumes metal takes on a spherical shape); ρ_{met} is the metal density (g/cc).

2.10 GAS CHROMATOGRAPHY

Chromatography remains the most powerful separation technique available (Fig. 2-9). It is easy to apply this technique to the separation of multi-component samples on a small analytical scale.[6] Chromatography is primarily based on the rate at which different components of a mixture travel through a stationery phase under the influence of a mobile phase. Gas chromatography (GC) is the interaction between the gaseous mobile phase and the stationery solid phase. Analytes must be volatile and thermally stable below 350 to 400°C. Analyte solubility depends only on its vapour pressure with the role of the mobile phase being purely mechanical. Retention of analytes is achieved mainly by changing the temperature apart from when polar gases are used where its solubility becomes an important factor. Nanogram to microgram quantities are normally used for qualitative and quantitative analysis. Much of the separated components are discarded due to its minute scale. Operating pressures are kept at a minimum where possible. The carrier gas flows continuously through the injection port, column and detector (Fig. 2-10). Flow rates are typically 2 to 50 $mL.min^{-1}$ with high flow rates applied for packed columns and low flow rates for capillary columns. Capillary columns are more widely used because of their higher

separating power compared to packed columns. Constant flow rates are maintained by a needle value. Carrier gases such as N_2, He or H_2 are frequently used. Liquid samples are injected in the GC via a self sealing rubber septum using a 1 to 10 μL syringe (gas compositions can be analysed using head space analysis). Liquids must be diluted to low concentrations for capillary columns, although a split injector can be used in cases where the sample is concentrated. Optimal chromatographic efficiency is achieved by injecting the sample in as narrow band as possible. The column is housed in a thermostatically controlled oven where temperatures can be finely controlled during analysis. Separated components are detected using a more widely used flame ionisation detector (FID), where the effluent gas is mixed with H_2 and air and then pyrolysed. Organic compounds are burned in the flame which creates ions to form a current between the electrolytic cell. Alternatively, a mass spectrometer (GC/MS) is coupled to further enhance identification of sample mixtures.

Fig. 2-9 A Perkin Elmer AutoSystem XL gas chromatograph.

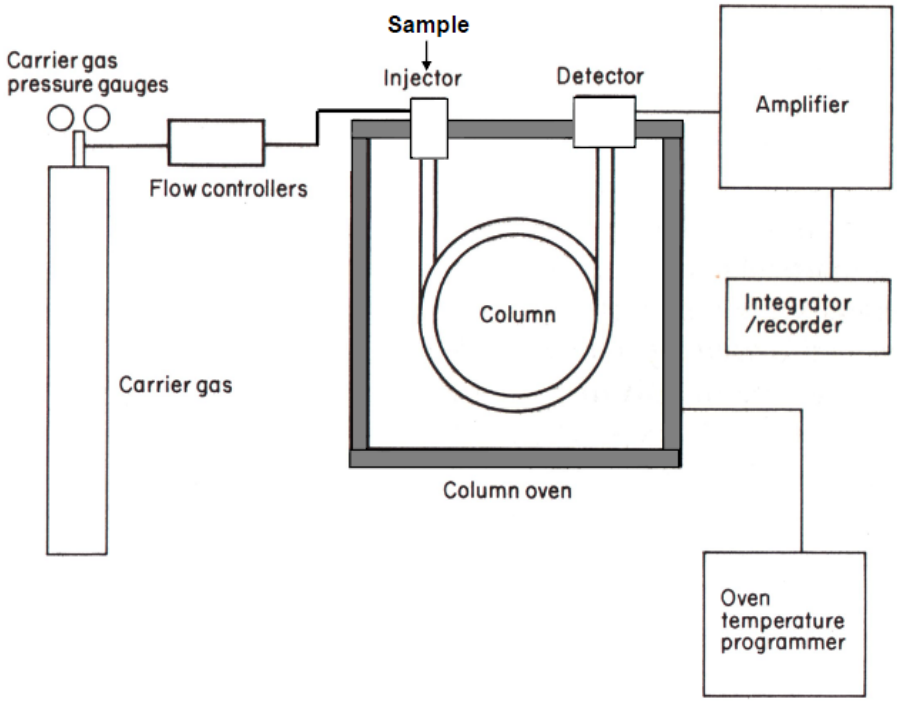

Fig. 2-10 Working illustration of a GC.

The performance of a chromatographic separation is characterised using theoretical plates, where it assumes that a column can be divided into a finite number of identical plates. The width of an analyte peak can be used to measure the efficiency of the column:

$$N = 16\left[\frac{t_R}{W}\right]^2$$

where N is the number of theoretical plates; t_R is the retention time of the analyte; W is the base width of the eluted analyte. Obviously, a higher value of N is more efficient and is more likely to achieve separation. The plate height, H = L/N, takes into account the length of the column, hence a smaller H results in more efficiency of the column. An alternative expression of H is the van Deemter equation:

$$HETP = \frac{B}{u} + C_S u + C_M u$$

where HETP is the height equivalent to a theoretical plate; u is the mobile phase velocity; B/u term it takes into account the diffusion of analyte molecules in the mobile phase caused by concentration gradients (Longitudinal diffusion); $C_S u$ term takes into account the rate of mass transfer to/from the stationery phase (eddy diffusion); $C_M u$ term takes into account resistance of mass transfer in the mobile phase. Again minimisation of the HETP term results in best separation conditions.

On selecting a capillary column for the most efficient compound separation, four parameters must be considered:

i) Stationery phase. The general rule of thumb is to select the least polar phase required for separation. Non-polar stationery phases (methyl or phenyl) separate components predominantly by order of boiling point. Increasing amounts of phenyl or cyanopropyl groups causes separation to be more dependent on the differences between dipole moments or charge distributions. Polyethylene glycol phases can be used for even more polar components (alcohols or aldehydes) where separation depends on hydrogen bonding interactions.

ii) Column internal diameter. The smaller the diameter the greater the efficiency.

iii) Film thickness. Thicker film column is needed when there is a large variation in sample concentration. This will reduce any broad overloaded peaks hence reducing compounds co-eluting. Thinner columns can be used if there is large variation in sample concentration but less likely for them co-eluting. As a rule, increasing the film thickness increases the retention of analytes, therefore requires a higher temperature for elution. In general, doubling the film thickness results in an increase in elution temperature of approximately 15-20° under isothermal conditions.

On the other hand, the increase in elution temperature is slightly less if a temperature program is used.

iv) Column length. Generally select the shortest column that provides good acceptable separation. If the maximum column length available is used but is still unable for separation then change either the stationary phase or internal diameter is needed. As separation resolution is proportional to the square root of the column efficiency, and then doubling the column length will only increase the column separation by about 40%.

If in doubt, the phase ratio, β, can be used to evaluate a suitable column for separation (Fig. 2-11):

$$\beta = \frac{id}{4d_f}$$

where id is the column internal diameter (μm); d_f is the film thickness (μm). The smaller the β, greater the ratio of phase to column internal diameter making it more ideal for volatile compounds. The larger β, the thinner the film thickness making it better suited for higher molecular weight compounds.

Film thickness (μm)	Column ID (mm)					
	0.1	0.15	0.22	0.25	0.32	0.53
0.10	250	-	550	625	800	1325
0.15	-	250	-	-	-	883
0.25	-	150	220	250	320	530
0.50	-	75	110	125	160	265
1.00	-	-	55	63	80	132
3.00	-	-	-	-	27	44
5.00	-	-	-	-	16	26

Fig. 2-11 Phase ratio according to the film thickness and column internal diameter from SGE.

For GC where MS is deployed as the detector, the effect of on-column bleeding from analysis and dirty samples can contaminate the MS source. Cleaning the MS source can take up to a few days leading to unnecessary instrument downtime. Column bleeding is characterised by the normal background signal generated by the stationery phase. A small amount of column bleed is still possible even when using high temperature stable polymers. Therefore, in order to minimise this effect it is important that MS grade columns (the stationery phase is anchored to surface of fused silica) are selected for these applications.

2.11 REFERENCES

1. I. Chorkendorff and J. W. Niemantsverdriet, *Concepts of Modern Catalysis and Kinetics*, John Wiley & Sons, 2003.
2. J. W. Niemantsverdriet and Editor, *Spectroscopy in Catalysis: An Introduction; Third, Completely Revised and Enlarged Edition*, Wiley-VCH Verlag GmbH & Co. KGaA, 2007.
3. G. Gauglitz and T. Vo-Dinh, *Handbook of Spectroscopy, Volume 1*, Wiley-VCH Verlag GmbH & Co. KGaA, 2003.
4. K. W. Kolasinksi and Editor, *Surface Science: Foundations of Catalysis and Nanoscience, Second Edition*, John Wiley & Sons, Ltd., 2008.
5. *Suite software for TPD/R/O 1110 Instruction manual*, ThermoQuest CE instruments, TMA-Milan, 1999.
6. H. Gunzler, A. Williams and Editors, *Handbook of Analytical Techniques, Volume 1*, Wiley-VCH, 2001.

CHAPTER 3 - EXPERIMENTAL AND CHARACTERISATION

3.1 GLUCOSE ENCAPSULATED PALLADIUM NANOCATALYST

3.1.1 SYNTHESIS

The preparation of glucose encapsulated palladium was performed using a 300 mL Parr autoclave high pressure compact reactor serie 5500 equipped with overhead mechanical stirring, gas inlet and outlet values, liquid sampling valve, pressure gauge, safety rupture disc, internal cooling loop and an internal thermal couple connected to a 4836 serie temperature controller. Typically, a solution of Palladium (II) nitrate solution (0.7084 g, 1.006 mmol, 15.11% Pd assay, Johnson Matthey) was added to a 90 mL deionised water solution of D-(+)-Glucose (9.0161 g, 50.0 mmol, ≥99.5%, Aldrich) in a PTFE coated beaker. The pH was adjusted to the desired value by dropwise addition of 1M NaOH solution (pellets 'AnalaR', BDH) to allow particle size control during the hydrothermal treatment. After assembling the reactor it was placed in the heating jacket and heated to 180°C for 4 hours at 800 rpm. The pressure reading from the autoclave at 180°C was approximately 12 bar. The reactor was allowed to naturally cool down to room temperature in which a black solid was obtained, confirming the conformal growth of carbon materials during the hydrothermal treatment. This was filtered using whatman grade 1 filter paper washed with copious amount of water followed by ethanol until the filtrate is colourless. The material was then dried with a steady stream of nitrogen overnight.

3.1.2 CALCINATION

Calcination of the dried catalyst was conducted in a nitrogen saturated atmosphere at a flow rate of 60 $mL.min^{-1}$. The furnace was programmed using a ramp rate of 10°C per min up to the desired final temperature (400 - 1000°C) and held for 1 h. The furnace was air cooled back to room temperature. This yields the respective palladium catalysts.

3.1.3 OXIDATION

An oxidation step of the calcined glucose encapsulated palladium catalyst is needed in order to increase the rate of reaction by etching some of the external carbon. Typically, the catalyst (approx. 1 g) was added to a 1:1 v/v 120 mL of hydrogen peroxide solution (30 wt.% in H_2O, Aldrich) and 120 mL of ammonium hydroxide solution (28 - 30%, NH_3 basis, Aldrich). This mild oxidation step was employed because it introduces minimal amount of surface functional groups (may have undesirable effects on reaction selectivity) compared to a much harsher condition for example using conc. nitric acid or piranha solution.[1] The suspension stirred at 40°C for 4 hours after which the black material was filtered and washed with water followed by ethanol until the filtrate solution is colourless then dried in nitrogen overnight at room temperature.

3.2 β-CYCLODEXTRIN PALLADIUM NANOCATALYST

The preparation of β-cyclodextrin encapsulated palladium nanocatalyst was carried out similarly compared to the glucose counterpart as described above.

3.3 PALLADIUM SUPPORTED ON ACTIVATED CARBON

3.3.1 IMPREGNATION

A known amount of palladium (II) nitrate solution (15.11% Pd assay, Johnson Matthey) was dissolved in *n*-butanol and impregnated dropwise into a butanoic solution of Norit GSX activated carbon (Johnson Matthey) to achieve the desired theoretical metal loading. *n*-Butanol was used as solvent because the hydrophobic properties of water may have a detrimental effect to the final metal particle size.[2] This was stirred overnight after which the suspension was filtered and washed with copious amount of water followed by ethanol. A non orange coloured filtrate

indicates the successful anchoring of palladium onto the activated carbon support. The retentate catalyst was dried at 80°C in the oven overnight.

3.3.2 REDUCTION

Reduction of the dried catalyst was conducted in a 50:50 hydrogen to nitrogen atmosphere at a flow rate of 60 $mL.min^{-1}$. The furnace was programmed using a ramp rate of 5°C per min up to the 500°C and held for 1 h. The furnace was then air cooled back to room temperature.

3.4 BORON MODIFIED PALLADIUM SUPPORTED NANOCATALYST

Preparation of boron modified palladium nanocatalysts were performed in a 3-neck round bottom flask equipped with hydrogen and nitrogen switch, rubber bung and an oil bubbler. Typically, 3% Pd/C[R]500C (250 mg, 0.07 mmol) was added and purged with hydrogen. Catalyst was pretreated *in situ* at 100°C for 1 h then cooled down to room temperature in nitrogen. 2 mL of THF was added to pre-wet the catalyst followed by a dose of borane THF solution (1.8 mL, 1.76 mmol, Aldrich). The mole ratio of Pd to BH_3.THF was 1:25. Other ratios were also performed such as 1:5, 1:10 and 1:50. The flask was warmed to 40°C to aid solvent evaporation and heated to 200°C for 1 hour and cooled back to room temperature. All processing of these Pd-^{int}B/C materials were carried out under inert conditions.

3.5 POLYVINYLPYRROLIDONE STABILISED COLLOIDAL GOLD NANOPARTICLES

3.5.1 SYNTHESIS

Au nanoparticles were synthesised using a modified seed mediated growth method.[3] Briefly, stock solutions of $HAuCl_4$ (0.05 mmol, 5 mL, 49% min, Alfa Aesar) and PVP 40T (3 mmol, Aldrich) were dissolved in milliQ water (45 mL) and

cooled to 0°C for 30 min. An aliquot of $NaBH_4$ (0.5 mmol, 5 mL, 99%, Aldrich) cooled to 0°C was rapidly injected into the Au solution. The colour changed from yellow to brown indicating formation of small Au clusters. The seed Au hydrosols was rapidly stirred for 15 min before purification by ultra centrifugal dialysis (MWCO = 10 kDa). The PVP stabilised Au nanoparticles were freeze dried overnight to yield a powder.

3.5.2 SEED MEDIATED GROWTH

Larger sizes of Au were grown by a modified slow reduction of degassed $AuCl_4^-$ and PVP solution in the presence of the seed Au cluster by a dose of Na_2SO_3 (BioUltra, anhydrous, ≥98.0%, Aldrich).[3] For the seed mediated growth of larger nanoparticles, both the Na_2SO_3 and the Seed Au cluster solutions were degassed by repeated freeze-pump-thaw cycles until no bubbles were observed during the thaw cycle. Experimental details are summarized in table 3-1. After the addition of all the ingredients the solution was further degassed by a nitrogen purge for 30 mins at 4°C. The growth mixtures were stirred for 3 h before purified by ultra centrifugal dialysis. All growth sample colour changed from brown to red (except G1 which retain a tint of brown and red), indicating growth of Au nanoparticles. Total volume of the growth solutions was kept at 50 mL. Au atom and PVP concentrations for all samples were kept at ~1 and 60 mM, respectively. PVP stabilised Au nanoparticles were freeze dried overnight to yield a powder.

Growth Samples	Vol Au Seed (mL)	30 mM $HAuCl_4$ (mL)	90 mM Na_2SO_3 (mL)	PVP (mmol)	Water (mL)	Ratio of $HAuCl_4$ to Seed
G1[a]	40	0.332	0.334	0.600	9.4	0.25
G2	25	0.830	0.834	1.500	23.4	1.0
G3	12	1.245	1.251	2.250	35	3.0
G4	7	1.423	1.429	2.571	40	6.0

Table 3-1 The growth conditions used for larger Au clusters. [a] Au seed solution was basified with K_2CO_3 (0.03 mmol, ≥99.0%, Aldrich).

3.6 POLYVINYLPYRROLIDONE STABILISED COLLOIDAL PALLADIUM NANOPARTICLES

In a 50 mL three necked round bottom flask, PVP 40T (0.022 g, 0.200 mmol, Aldrich) was added followed by Palladium (II) nitrate solution (2 mL, 0.200 mmol, 15.11% assay, Johnson Matthey). H_2O (8 mL) was then added and stirred (700 - 800 rpm) to dissolve all the PVP to which ethylene glycol (30 mL, anhydrous, 99.8%, Aldrich) was added. Solution darkened to black, indicating Pd is slowly reduced by ethylene glycol. The metal concentration was approximately 0.005 M. The flask was fitted with a condenser (centre), a bubbler bung and a stopper and the mixture was heated up to the boiling point of the EG/H_2O mixture. The solution was allowed to reflux for 1 hour under a nitrogen atmosphere and cooled down to 40 - 50°C, where additional PVP 40T (0.422 g, 3.80 mmol) was added and stirred for 15 - 30 min to dissolve the excess polymer, followed by reflux for a further 1 hour and cooled down to RT. Acetone was added to precipitate the black product and separated by centrifugation. The PVP-Pd was redispersed in water where it was redissolved into a vial and dried in nitrogen at 50°C overnight. Sample was split into two portions for the borylation step.

3.7 BORYLATION OF POLYVINYLPYRROLIDONE STABILISED COLLOIDAL PALLADIUM NANOPARTICLES

In a 50 mL 3 neck flask equipped with nitrogen line, rubber bung and outlet bubbler, dried PVP-Pd (10.64 mg, 0.1 mmol) was added in DCM (8 mL). The solution was then degass with nitrogen for 30 min. Borane THF solution (2.62 mL, 2.500 mmol, Aldrich) was then added with nitrogen taken out of the solution. Solution was stirred at RT until fully evaporated where it was heated at 95°C for 1 hour and naturally cooled down to RT. The PVP-Pd-^{int}B was redissolved with 5 mL H_2O and purified with 5 part acetone to remove excess B_2O_3. The catalyst was redispersed in H_2O, dried in vial with N_2 blow with overnight (no heating).

3.8 HYDROGENATION

3.8.1 4-OCTYNE

Hydrogenations of 4-octyne were performed in a standard 100 mL 3-neck round bottom flask. Typically, 50 mL of toluene was added followed by the catalyst (4.70 μmol) whilst maintaining a constant nitrogen purge. Agitation (800 rpm) was induced using a glass coated stirrer bar. Hydrogenation rate was found not influenced by the agitation speed at the set stirrer speed, therefore a gas-liquid mass transfer can be excluded and the intrinsic reaction kinetics can be studied. The suspension was sonicated to disperse the particles. Hydrogen connected with a needle valve was fitted to one side neck on the flask and bubbled through the suspension at a flow rate of ~30 mL.min^{-1} at 50°C. Hydrogen purge was maintained for a further 30 mins before 4-Octyne (1.390 mL, 9.38 mmol, 99%, Aldrich) and internal standard *p*-Xylene (310 μL, 2.51 mmol, anhydrous, ≥99%, Aldrich) were added to initiate the reaction. The concentration of 4-octyne was 0.188M. Molar ratio of catalyst to substrate was 1:2000. Samples were taken out at specific time intervals to probe the reaction

kinetics. About 0.5 mL of sample was withdrawn and filtered through a cotton wool plug to separate the catalyst and made up using 0.5 mL toluene to clean the filter. Samples collected were taken immediately for GC/MS analysis.

3.8.2 3-HEXYN-1-OL

Hydrogenations of 3-hexyn-1-ol were performed in a 100 mL Parr autoclave. To a PTFE lined beaker, the catalyst (0.028 mmol) was added followed by a made up mixture of 1,4-dioxane (60 ml, 30.0 mmol, ≥99.0%, Aldrich) and 3-hexyn-1-ol (60 mL, 30.0 mmol, 98%, Aldrich). The autoclave was flushed 5 times with hydrogen and charged up to 3 bar at 30°C with stirring speed of approx. 400 rpm. Reaction progress was monitored using an hydrogen uptake apparatus. Sample was taken using a sampling port at the theoretical half hydrogenation point as well as at the end of the reaction for GC analysis.

3.8.3 OTHER ALKYNES

Hydrogenations of other alkynes (phenylacetylene, diphenylacetylene, 2-butyne-1,4-diol and 2-methyl-3-butyn-2-ol) were performed using the HEL high pressure ChemSCAN parallel reaction system at Johnson Matthey Technology Centre (Fig. 3-1). The apparatus is equipped with 8 reactor system, each with hydrogen uptake, pressure, temperature and magnetic stirring independently controlled and monitored. To a 5 mL glass vial, the catalyst (2.50 μmol) was added followed by a standard solution containing the alkyne (2.50 mmol) in 5 mL EtOH. The concentration of alkynes was 0.5 M and catalyst to substrates ratio were kept at 1:1000. The reactor was pre-programmed to flush a few times with nitrogen gas followed by hydrogen. Vessels were heated up to 30°C then reactor charged with 3 bar hydrogen followed by magnetic stirring at 1200 rpm to allow reaction to commence. Hydrogen uptake monitored by the custom software.

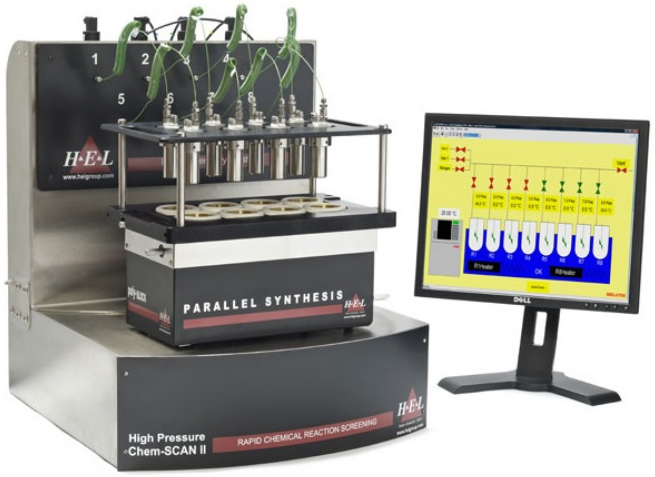

Fig. 3-1 HEL high pressure ChemSCAN apparatus used at Johnson Matthey Technology Centre.

3.8.4 ORTHO-CHLORONITROBENZENE

Hydrogenations of *o*-chloronitrobenzene were performed using the HEL high pressure ChemSCAN, as described above. To a 5 mL glass vial, catalyst (3.80 μmol) was added then a standard solution containing 1-chloro-2-nitrobenzene (394 mg, 2.476 mmol, 99%, Aldrich) and octane (0.400 mL, 2.451 mmol, anhydrous, ≥99%, Aldrich) as internal standard in 5 mL EtOH. The concentration of 1-chloro-2-nitrobenzene was 0.5 M and catalyst to substrates ratio were kept at 1:670. The reactor was pre-programmed to flush a few times with nitrogen gas followed by hydrogen. Vessels were heated up to 50°C to pressure of 3 bar and stirring at 1200 rpm was turned on to initiate the reaction. Hydrogen uptake monitored by on-board software.

3.8.5 OTHER SUBSTRATES

Hydrogenation of other substrates, benzonitrile (anhydrous, ≥99%, Aldrich), 2-chlorobenzonitrile (98%, Aldrich), acetophenone (puriss. p.a., ≥99.0%, Aldrich), benzaldoxime (predominantly (E)-isomer, 98%, Alfa Aesar), were performed using the HEL high pressure ChemSCAN, as described above. To a 5 mL glass vial, the catalyst (7 μmol) was added then a standard solution containing the respective

substrate (2.5 mmol) in 5 mL EtOH. Concentration of the substrates were 0.5 M and catalyst to substrates ratio were kept at about 1:350. The reactor was pre-programmed to flush a few times with nitrogen gas followed by hydrogen. Vessels were heated up to 50°C to pressure of 3 bar and stirring at 1200 rpm was turned on to initiate the reaction. Hydrogen uptake monitored by on-board software.

3.9 DECOMPOSITION OF FORMIC ACID BY EVOLVED GAS

The catalytic activity of nanoparticles was tested on the decomposition of HCOOH at 25°C. Pd catalysts (10.41 mg of Pd metal) was dispersed in 10 mL H_2O. The suspension was vacuumed and purged with N_2. HCOOH (575 μL, 15 mmol) was then added via a sealed rubber septum to initiate the reaction. The evolved gases were corrected by an inverted burette filled with water. The suspension was stirred at 1250 rpm and the volume of evolved gas was recorded at designated time intervals.

3.10 DECOMPOSITION OF FORMIC ACID BY LIQUID ^{13}C NMR

The chemical shift was measured as soon as the colloid was mixed with the given concentration of formic acid. It was found that the chemical shift value is very sensitive with many experimental parameters such particle size, size distribution, shape, surface feature and local factors such as type of adsorbate, surface coverage, dipole interaction and solvent effects, etc. Thus, chemical shift values reflect these effects leading to differentiation and optimization for each respective parameter. However, a meaningful comparison can only be made for one respective parameter by keeping all the other parameters constant. For example, it is crucially important to keep the synthesis procedure (drying, heating, heating rates and storage with controlled moisture) identical and check TEM and XRD results to make sure the particles are kept at designated particle size with a narrow particle distribution (within 15%) before chemical shift evaluation. The rate of formic acid decomposition and

CO_2 production was calculated from the integration of ^{13}C NMR signal intensity compared with 1,4 dioxane (7.0×10^{-11} mol, ≥99.0%, Aldrich) signal as internal standard.

3.11 CHARACTERISATIONS

3.11.1 ATR-IR

FTIR spectra were acquired using a Nicolet 6700 ATR-IR spectrometer with a liquid-nitrogen-cooled MCT detector. The solid samples were pressed onto the smart golden gate-ZeSe/diamond crystal. Alternatively, a drop of sample was casted on the crystal and evaporated under a N_2 atmosphere before measurment. The spectra were obtained by averaging 128 scans with a resolution of 2 cm^{-1} over the wavenumbers ranging from 650 to 4000 cm^{-1}.

3.11.2 BET

Nitrogen adsorption experiments were acquired using a CE instrument Sorptomatic 1990 system. The samples were degassed under vacuum at 100°C overnight prior to analysis. Textual properties (porosity, surface area, pore distribution) of the samples were acquired using the standard N_2 Brunauer−Emmett−Teller (BET) method at a range of partial pressures at 77 K. Specific surface area S_{BET} (m^2 g^{-1}) was deduced by the BET method in a relative pressure range of p/p_0 = 0.03 - 0.3, assuming a surface area of 0.162 nm^2 per N_2 molecule at 77 K. Total pore volume was measured at p/p_0 = 0.99. Pore size distributions were obtained by applying the Barrett-Joyner-Halenda (BJH) method.

3.11.3 ICP-ES

Inductive coupled plasma emission spectroscopy (ICP-ES) was conducted using a Perkin Elmer Optima 3300RL instrument. Samples were prepared by Na_2O_2

infusion in a zirconium crucible and compared against standard gravimetrically determined solutions.

3.11.4 NMR

Nuclear Magnetic Resonance (NMR) was used to probe the formation of formate species from aqueous formic acid during the adsorption and its decomposition by colloidal PVP-Au nanoparticles. The ^{13}C NMR spectra were recorded by 500 MHz (^{1}H resonance) Bruker AVII, 300 MHz (^{1}H resonance) and Varian Mercury 300 NMR spectrometers. Colloidal samples were prepared by dispersing the PVP-Au nanoparticles in 0.50 mL of deuterium oxide followed by the addition of 0.20 mL of 1 M $H^{13}COOH$ (^{13}C 99%, Cambridge Isotope Laboratories) in deuterium oxide. All of the spectra were recorded using 3075 scans taken with a 2 s recycle delay.

3.11.5 SSNMR

SSNMR spectras were recorded at JMTC and the University of Warwick with assistance from Dr. Nathan Barrow of JMTC. The oxygen-sensitive samples were packed in an argon glovebox and transferred under argon to the spectrometers. SSNMR spectra were acquired at a static magnetic field strengths of 9.4 T ($\nu_0(^{1}H)$ = 400.16 MHz) or 14.1 T (ν_0 (^{1}H) = 600 MHz) on a Bruker Avance III console. Widebore Bruker 4mm WVT (JMTC) or DVT (Warwick) MAS probes tuned to ^{11}B were used. Spectra were referenced to $NaBH_4$ at -42.06 ppm. Powdered samples were packed into zirconia MAS rotors with Kel-F caps, with before and after weighings providing the sample mass. The rotors were spun using room-temperature compressed nitrogen. A special nitrogen line was made for this experiment at Warwick.

3.11.6 TEM

TEM for the palladium samples were undertaken on a Tecnai F20 microscope using a voltage of 200 kV, and C_2 aperture of 30 & 50 m, in bright field (BF) STEM (HAADF) mode with *in situ* EDX analysis. Specimens were crushed and dusted onto a holey carbon coated Cu grid. TEM for the gold samples were examined on a JEOL 2000FX microscope using an accelerating voltage of 200 kV. Specimens were diluted to a low concentration in H_2O, drop casted onto a holey carbon coated Cu grid then dried. The average diameter of over 300 nanoparticles were measured with a calculated standard deviation.

3.11.7 TGA

TGA was performed using a TA instruments Q50 thermogravimetric analyser. Specimens were loaded onto a platinum or ceramic sample pan and heated from RT to 1000°C under nitrogen at a ramp rate of 10°C.min^{-1} and holding at the final temperature for 1 h.

3.11.8 TPD/R/O

TPR was performed using a CE instrument TPD/R/O 1100. Samples were pretreated in H_2 at 100°C for 1 h then cooled down to RT. Analyses were taken in a flow of 5% hydrogen in argon at a flow rate of 20 mL.min^{-1} with a linear ramp rate at 2 °C.min^{-1} from room temperature to 1000°C. TPO was performed using the same instrument. Samples were pretreated in H_2 at 100°C for 1 h then cooled down to RT. Analyses were taken in a flow of 5% oxygen in helium at a flow rate of 20 mL.min^{-1} with a linear ramp rate at 2 °C.min^{-1} from room temperature to 1000°C.

3.11.9 PULSE CHEMISORPTION

Pulse Chemisorptions were performed using a CE instrument TPD/R/O 1100. Samples were pretreated in H_2 at 100°C for 1 h then cooled down to RT. Analyses

were taken by pulsing research grade CO on the pretreated sample. Ten pulses were recorded per analyse and referenced to a blank run without adding any solid catalyst. Helium was used as the carrier gas at a flow rate of 20 $mL.min^{-1}$. Loop volume used was 0.456 ccm with pulse decay set to 15 min. A 1:1 CO to metal stiochiometric factor for dispersion calculations.

3.11.10 XPS

XPS for the glucose encapsulated palladium samples were performed using a Thermo V. G. Scientific ESCALAB 250. Powders of the supported nanoparticles were dusted onto carbon tape and thereby mounted on a sample stub. The exciting radiation used in the studies was monochromatised aluminium Kα radiation in a 650 nm spot at 200 W power. Charge compensation was activated, provided by the in-lens flood gun at a 2 eV setting and the 401 argon ion flood source at a "zero energy" setting.

XPS of the 3% Pd/C and 3% Pd-^{int}B/C were conducted in collaboration with Dr Jingping Hu and Prof. John Foord group at the University of Oxford. The XPS facility was in-house self built. XPS spectra were measured using an Al Kα (1486.6eV) X-ray source and a hemispherical electron energy analyser. The acceleration voltage is 10 kV and the emission current is 12 mA for the X-ray source. The spectra was measured at around 90 degree emission angle. The electron energy analyser operates in FAT mode (Fixed Analyzer Transmission), with constant pass energy of 50 eV for survey (wide) scans and high resolution scans. The peak fitting was conducted using CasaXPS, with a Shirley background subtraction, lineshape is a mixed Lorentzian (30%) and Gaussian (70%).

3.11.11 XRD

Powder X-ray diffraction (PXRD) patterns were obtained on a PANalytical X'Pert Pro diffractometer operating at 40 kV and 30 mA (step size at 0.004°, time per step at 15 s, scan rate 0.000267°/s, total number of steps at 15000). Samples were dusted and pressed onto either a glass or an aluminium preparative slide. Angles 30 to 90° and 20 to 80° 2θ were used for palladium and gold/silver samples, respectively. Calculation of the lattice parameter on the palladium samples are calibrated against the aluminum background peaks.

3.11.12 UV-VIS

UV-Vis spectras for the Au samples were recorded on Cintra 10 UV-Vis spectrometer at room temperature using a quartz cuvette with an optical path length of 1 cm. Au concentrations were kept at absorbance of ~1 at 300 nm.

3.12 REFERENCES

1. V. Datsyuk, M. Kalyva, K. Papagelis, J. Parthenios, D. Tasis, A. Siokou, I. Kallitsis and C. Galiotis, *Carbon*, 2008, **46**, 833-840.
2. C. Park and M. A. Keane, *J. Colloid Interface Sci.*, 2003, **266**, 183-194.
3. H. Tsunoyama, H. Sakurai and T. Tsukuda, *Chem. Phys. Lett.*, 2006, **429**, 528-532.

CHAPTER 4 - SUBSURFACE CARBON MODIFIED PALLADIUM NANOCATALYST

4.1 INTRODUCTION

Heterogeneous catalytic hydrogenation of alkynes to alkenes represents one of the most important steps in fine chemicals manufacture.[1] It has been widely-established that heterogeneous palladium-based catalysts are highly effective for this hydrogenation reaction, affording high alkene selectivities. Furthermore, the catalytic activity and selectivity can be enhanced by using amines/polymers[2,3], shape control[4], support effects[5] and bimetallic[6] systems. Recent work by Teschner *et. al.* demonstrated that the formation of subsurface C in Pd during catalysis greatly promotes the selectivity towards alkenes, in the gas phase.[7] However, it has not been possible to isolate this active species, with interstitial subsurface carbon atoms only being formed in transient conditions at temperatures under an atmosphere of reactive gas. Therefore, it is highly desirable to develop a Pd analogue modified with subsurface carbon atoms that is stable under atmospheric conditions. It is anticipated that such a material would prove highly beneficial for liquid phase hydrogenations of alkyne to alkene, one of the key steps in the pharmaceuticals, fragrance and fine chemicals catalysis.

Some previous work within our group identified saccharide derived materials such as glucose, offer a potentially green route to stabilise nano-sized catalysts. The sugar acts as a reducing agent as well as a capping agent, thus mitigating the use of potentially toxic reducing agents such as borohydride or Superhydride®. Furthermore, modification to the electronic structure of Pd to the "Pd-C" catalyst may be possible by utilising the glucose derived carbon.

Here in this chapter, we report using glucose, which acts as a reducing and capping agent as well as a supporting matrix for the Pd nanoparticles that are formed. After heat treatment, the glucose derived carbon atoms reside in the octahedral

interstitial sites of the metal, hence blocking the formation of β-hydride under reducing conditions. The Pd particles are geometrically and electronically modified by the interstitial carbon atoms and subsequently demonstrate the ability to substantially reduce undesirable processes such as alkene over-hydrogenation and isomerisations in the liquid phase. The alkyne reductions are stereoselective, occurring via *syn* addition affording mainly *cis*-alkenes with this new class of stable 'Pd-C' catalyst.

4.2 SYNTHESIS OF ENCAPSULATED PALLADIUM

4.2.1 HYDROTHERMAL SYNTHESIS USING GLUCOSE

Pd encapsulated in the carbon spheres with tunable diameters were synthesised from aqueous glucose solutions at temperatures of 160-180°C (Fig. 4-1).[8] Typically, an aqueous solution of $Pd(NO_3)_2$ was added to a solution of glucose at a metal to sugar ratio of 1:50. The mixture was placed in a Teflon lined beaker in an autoclave, flushed with N_2 and heated to the set temperatures for 4 h. Under these conditions, glucose readily undergoes glycosidation and carbonisation, with the growth of the carbon spheres conforming to the LaMer model.[9] The samples were analysed by a range of techniques including PXRD, where a characteristic shift in the lattice parameter was observed. A comprehensive examination of these materials is outlined in Section 4.3.

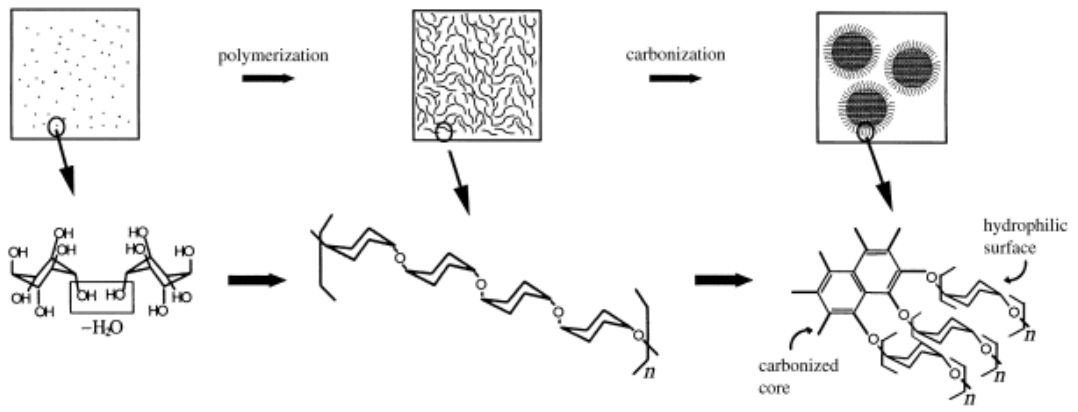

Fig. 4-1 The growth of carbon spheres under typical hydrothermal condition.[8]

4.2.2 EFFECT OF TEMPERATURE

Following this methodology, it is envisaged that the percentage of final carbon content and carbon encapsulation of palladium can be tailored by tuning the temperature of the hydrothermal conditions. Initially, the temperature was investigated with a temperature of 140°C and 180°C, while keeping all other parameters constant. At 180°C, carbon spheres were clearly observed after extraction by centrifugation. However, at 140°C, no carbon spheres were isolated. This highlights the importance that the glycosidation temperature was not achieved and only oligomerised product was observed as characterised by only a dark brown solution. The average metal crystallite size was found to be 25 nm under these conditions, as estimated using PXRD by applying the Scherrer equation.

4.2.3 EFFECT OF REACTION TIME

The reaction time was varied from 4 to 8 h to determine its effect on the final Pd crystallite size as well as the degree of carbon content. It was found no significant change was observed to the particle size of Pd, which remained approximately 25 nm. No significant mass change was observed for both samples. Therefore, subsequent hydrothermal treatments were performed at 4 h thereafter.

4.2.4 EFFECT OF PH

It was envisaged that varying the pH may alter the binding strength of glucose to Pd and therefore one can optimise the particle size after hydrothermal treatment. Ikushima *et. al.* reported on the formation of Au and Pt nanocrystals using $NaBH_4$ reduction which stabilised β-D-glucose into nanowire like structures. They found nanoparticle dispersions can be stabilised for prolonged periods by varying the pH.[10, 11] The underlying mechanism was attributed to the pH-dependent equilibrium between surface -OH and $-O^-$ on the metal surface. At higher pH, relative to the p*K*

value of the hydroxyl groups, the deprotonated form $-O^-$ predominates and *vice versa*. This enhances the effective binding of the metal. Therefore, the effect of pH in the hydrothermal treatment was investigated (Table 4-2). It was found that highest pH lead to dramatic decrease in Pd particle size from 25 to 5 nm, in agreement with the literature.

pH	Particle Size (nm)
1.8	25.2
4.3	18.8
6.9	5.9
10.0	5.0

Table 4-2 The effect of pH to the Pd particle size analysed by PXRD after hydrothermal conditions.

4.2.5 HYDROTHERMAL SYNTHESIS USING β-CYCLODEXTRIN

β-cyclodextrin, a cyclic oligosaccharide material that consists of seven fused sugar ring molecule (Fig. 4-2), can be used to act as 'bumpers' thus avoiding contact between the metal nanoparticles to prevent their aggregation[12]. It has also been reported that increasing the pH can also reduce the size of metal nanoparticles.

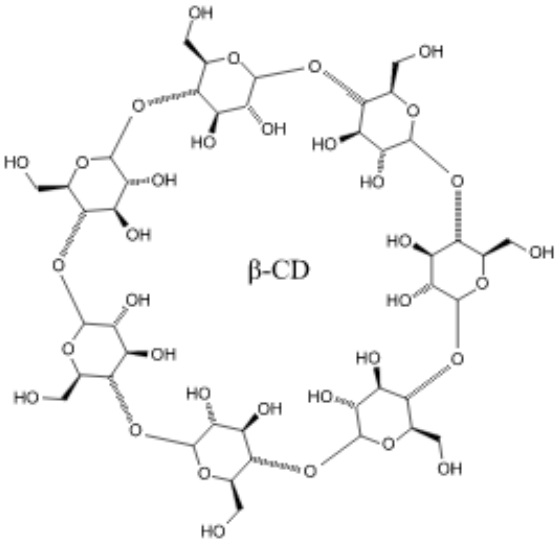

Fig. 4-2 Chemical structure of β-cyclodextrin.

The same reaction conditions were applied for synthesis of β-cyclodextrin encapsulated Pd nanoparticles, where the ligand may act as a capping agent and a reducing agent. It was found the size of Pd for the β-cyclodextrin derived sample is approximately 4 times larger than the glucose counterpart, as determined by PXRD. Therefore glucose encapsulated Pd was chosen and the use of β-cyclodextrin was not pursued further.

4.3 CHARACTERISATIONS OF ENCAPSULATED PD

4.3.1 FTIR

Fig. 4-3 shows FTIR spectra used to identify the functional groups present before and after hydrothermal treatment. The bands centred around 3000-3500 cm^{-1} are assigned to the O-H stretching, with glucose exhibiting greater intensity compared to the Pd encapsulated in the carbonised glucose. The bands at 1000-1300 cm^{-1} are attributed to the C-O and O-H bending vibrations, implying the large number of hydroxyl groups for glucose. The peaks at 2950 cm^{-1} for glucose are the C-H stretches and the bands at 1690 and 1600 cm^{-1} are assigned to >C=O and >C=C<,

respectively. The evolution of these peaks verified the aromatisation of glucose after the hydrothermal treatment.

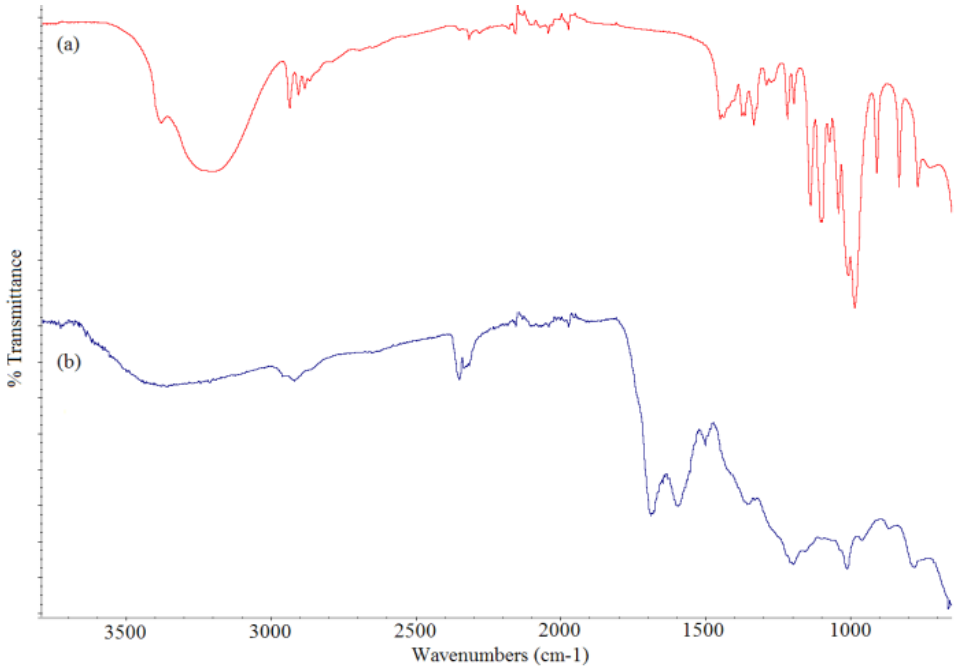

Fig. 4-3 FTIR spectra in transmission mode of: (a) glucose (b) Pd encapsulated in carbonised glucose.

4.3.2 PXRD AND TGA

Fig. 4-4 and Table 4-3 shows the heat treatment of the Pd glucose nanocatalysts and subsequent weight loss observed using TGA. Heat treatments at various temperatures were used to investigate the stability of the synthesised nanocatalysts and the binding ability of the carbonised glucose to Pd. Analysis showed the carbonised Pd catalyst has increased stability as compared to glucose is characterised by the weight loss at higher temperatures.

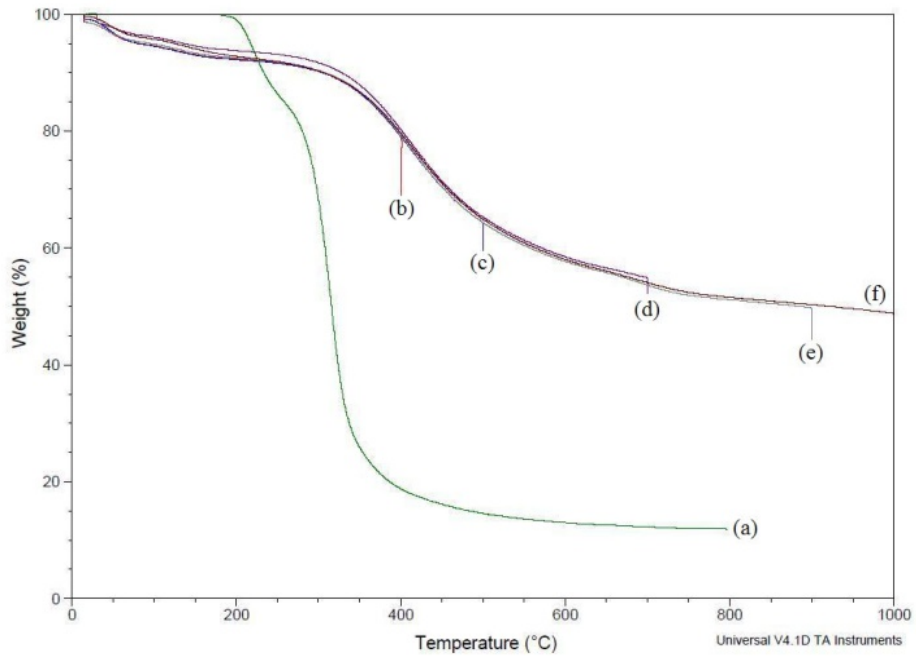

Fig. 4-4 TGA spectras showing percentage mass remaining versus temperature: (a) glucose (b) 400°C (c) 500°C (d) 700°C (e) 900°C (f) 1000°C. Specimens were heated from RT to 1000°C under N_2 at a ramp rate of 10°C/min and holding at the final temperature for 1 h.

Final temperature (°C)	Mass remaining (%)
400	70.3
500	60.4
700	53.8
900	46.0
1000	42.7

Table 4-3 Mass remaining of the Pd-Glucose nanocatalyst at various final temperatures as determined by TGA.

PXRD was used to investigate the Pd crystallite size of the heat treated samples and any evidence of carbon atom diffusion into the bulk of Pd (Fig. 4-5). A mild growth in the Pd crystallite was observed from 5 to 7 nm for the sample heated to 400°C but this was accompanied by a peak shift to lower 2θ, which became

increasingly evident at higher angles. This is consistent with previous reports by Zlemecki and Jones that the lattice parameter, a_0, of the bulk Pd with carbon occupying interstitial octahedral holes has increased from 0.3890 to 0.3995 nm (Table 4-4).[13] The amount of interstitial carbon occupation in Pd can be calculated using the equation below:

$$a = a_0 + 6.9 \text{ x } 10^{-2} \text{ x } x$$

where a_0 is the lattice parameter of pure Pd.[14, 15] This represents carbon modified palladium with the formula $Pd_{1-x}C_x$ (independent of size) where carbon saturation is reached at 15%. The occupation of C atoms in the tetrahedral sites may be ruled out as this was calculated to be too unstable and confirmed by Zlemecki *et. al.* using neutron diffraction studies of differing amounts of doped carbon atoms.[16] The occupation of the bulky O atoms can also be ruled out, as the ionic radii of O atoms is too large to occupy these interstitial octahedral or tetrahedral sites, which can cause destabilisation to the Pd lattice.[17] Moreover, based on quantitative size calculations, only the octahedral sites in Pd possess a reasonable size to occupy interstitial carbon atoms.[18]

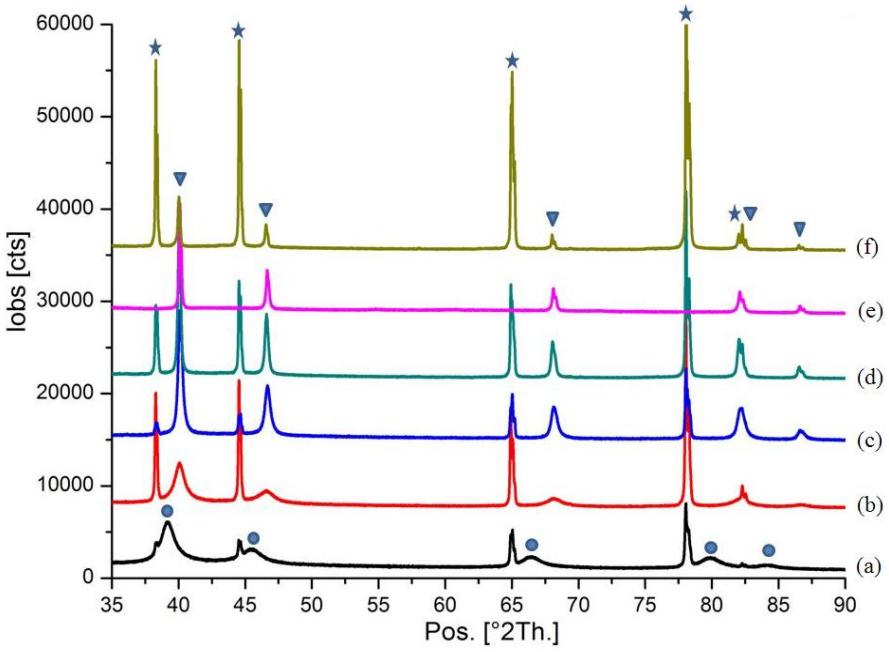

Fig. 4-5 PXRD patterns illustrating the effect of thermal treatments to the phase and Pd particle size for samples heated to: (a) 400°C (b) 500°C (c) 600°C (d) 700°C (e) 900°C (f) 1000°C. (Star): Aluminium preparative slide. (Triangle): Pure Pd peaks corresponding to the *fcc* structure. (Circle): Pd-C peaks. Pd phases from left to right correspond with phases <111>, <200>, <220>, <311> and <222>, respectively. Plots are offset by 7000 units along the y-axis.

Calcination of Pd Glucose Catalyst (^{o}C) in N_2	**Lattice Parameter a_0**	**Approx. C at.%**
As-Synthesised	0.3923(4)	4.7
400	0.3977(4)	12.6
400 in H_2	0.3892(3)	0.3
500	0.3887(2)	0
600	0.3887(0)	0
700	0.3892(1)	0.3
900	0.3889(1)	0
1000	0.3894(2)	0.6

Table 4-4 Calcination temperatures with respect to the variation on the average lattice parameter of Pd nanoparticles. The values in brackets represent the standard deviation of all measured Pd phases.

$Pd_{1-x}C_x$ is a metastable phase and it is evident that interstitial carbon can be expelled when heating in N_2 at 500°C or higher but also by reducing the sample at 400°C (Fig. 4-6). Under these conditions, the interstitial carbon atoms are unstable, hence are expelled from the metal lattice to form the most thermodynamically stable pure Pd phase. PXRD also suggests that the carbonised glucose is amorphous in nature as no graphitic peaks were observed. Based on this observation, the sample calcined to 400°C was studied further due to the maximum subsurface carbon being achieved at this temperature. Furthermore, severe metal sintering effect was encountered at more elevated temperatures undermining the usefulness of such catalysts.

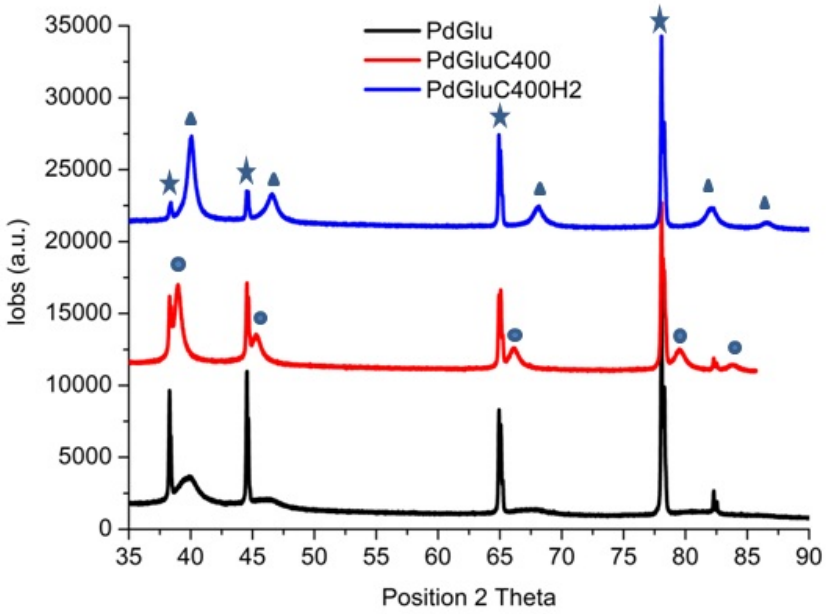

Fig. 4-6 PXRD spectra of Pd and Pd-C phases. (Star): Signal from aluminium preparative slide. (Triangle): Metallic Pd peaks corresponding to fcc structure. (Circle): Pd-C peaks. Pd phases from left to right corresponds to (111), (200), (220), (311) and (222) reflections, respectively. Plots are offset by 10000 units along the y-axis.

4.3.3 TPR

Fig. 4-7 shows the TPR profile of the Pd glucose nanocatalyst calcined at 400°C in H_2 and N_2. It was evident that the sample pretreated in N_2 inhibits the formation of subsurface hydride. This is in contrast with sample pretreated in H_2, where a strong negative peak characteristic of the decomposition of Pd-H is observed. It is well documented that the presence of subsurface carbon blocks the formation of β-hydride species by competing for the same octahedral interstices.[13, 19] This is consistent with the evidence that carbon is situated in the interstitial sites of Pd.

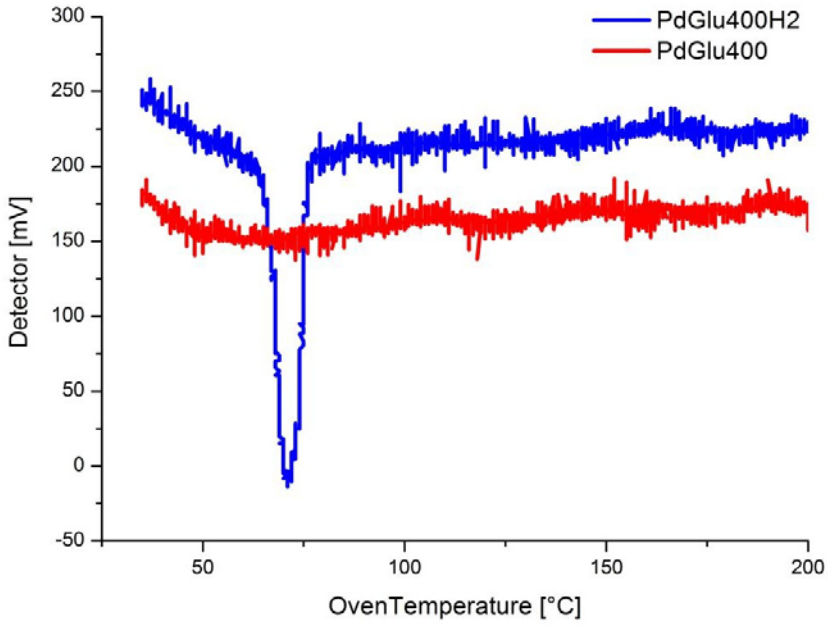

Fig. 4-7 TPR highlighting the decomposition of β-Pd-H phase on the catalyst with: (Blue) Pd glucose sample pretreated in H_2 atmosphere to selectively remove subsurface carbon. (Red) Pd glucose sample pretreated in N_2 atmosphere.

4.3.4 TEM

TEM was used to probe the morphology and size of the glucose carbonised Pd catalyst after calcination (Fig. 4-8). Pd particles are clearly seen inside the amorphous carbon derived from carbonised glucose. Furthermore, the metal appears to be clustered together rather than being spherical. The mean particle size was calculated

at 7.0 nm with the mode at 6 nm, after calcination at 400°C, which complements the calculation using the Scherrer equation by PXRD. HAADF and EDX confirmed the presence of Pd in the specimen (Fig. 4-9). The *d* spacing calculation of the lattice fringes along the <111> direction was calculated at 2.35 Å, also in agreement with the PXRD data and the literature value.

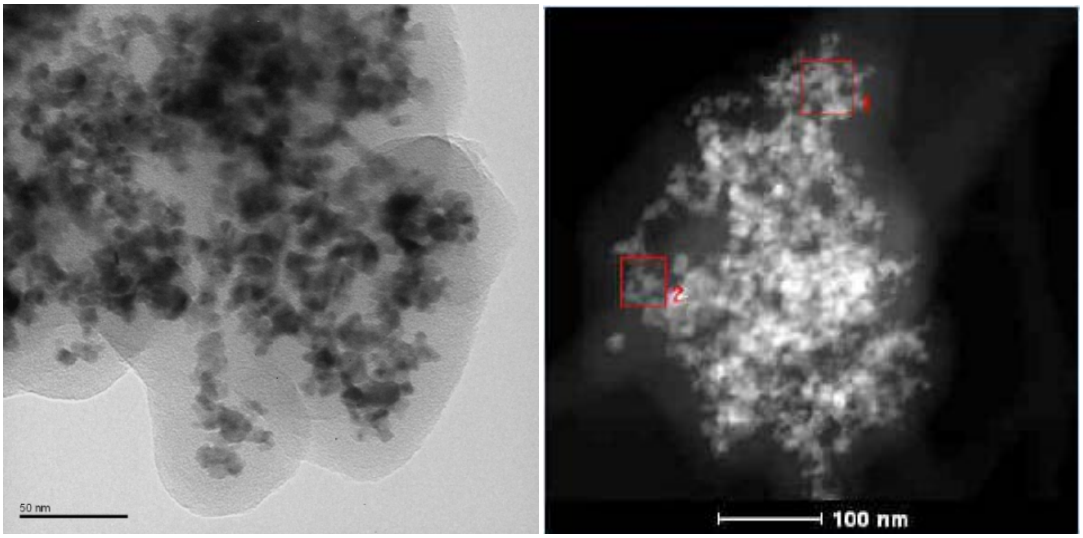

Fig. 4-8 (left) TEM micrograph of glucose carbonised Pd nanocatalyst. Scale bar 20 nm; (right) HADDF image of the glucose carbonised Pd nanocatalyst.

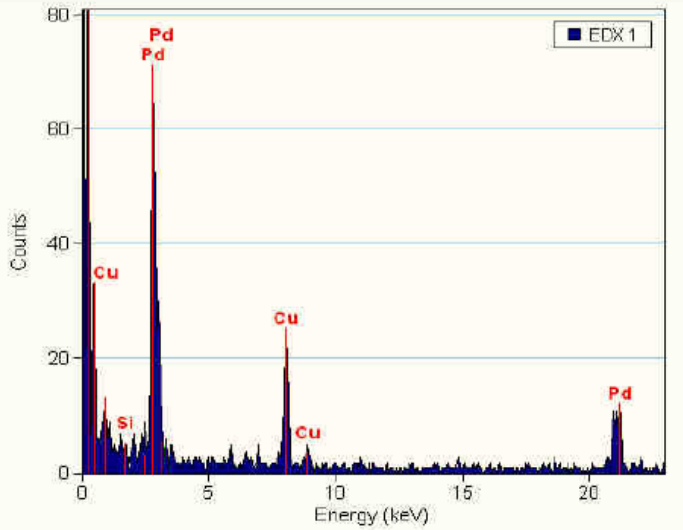

Fig. 4-9 EDX analysis of the glucose carbonised Pd nanocatalyst confirming the presence of Pd in the specimen.

It is evident that the Pd is covered by the carbonised glucose, therefore, it was hypothesised that the carbon coating will need to be partially removed in order to expose more metal in order to increase the catalytic activity. This was later confirmed by catalytic testing. Thus, the catalyst was treated in a mixture of 1:1 hydrogen peroxide and ammonium hydroxide at 40°C for 4 h. This mixture is known to oxidatively remove amorphous carbon.[20, 21] More importantly, no Pd leaching was observed under the applied mild oxidising conditions. This is in contrast with using harsher treatments such as nitric acid or piranha solution, both of which are susceptible to Pd leaching. Another advantage is the mixture is known to reduce surface functionalisation such as carboxylic groups created under typical oxidative conditions. TEM analysis of the partially oxidised sample (Fig. 4-10) demonstrated that there was no increase in the Pd particle size as a result of the oxidative treatment.

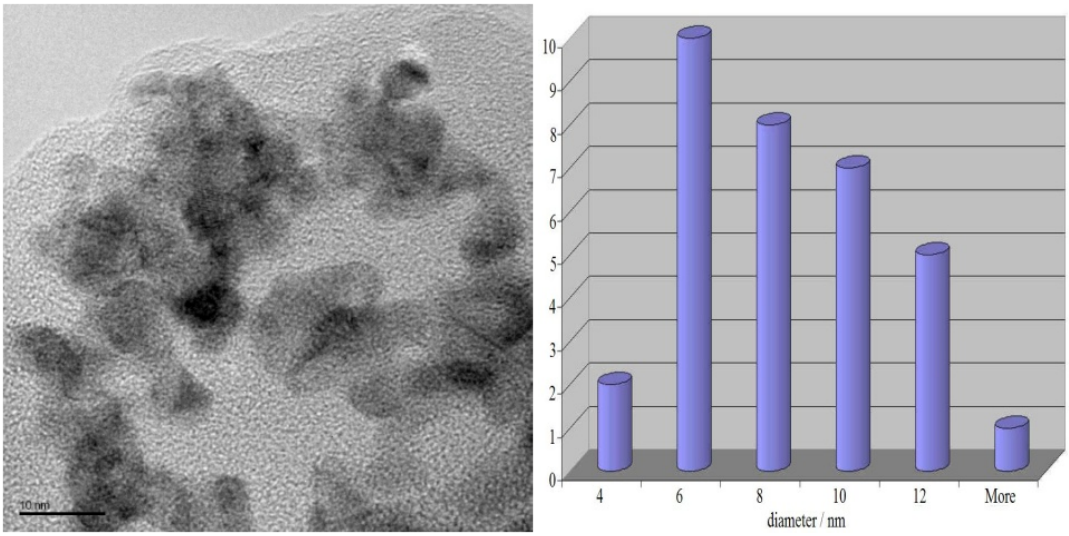

Fig. 4-10 (left) TEM micrograph of glucose carbonised Pd nanocatalyst after peroxide treatment. Scale bar 10 nm; (right) Particle size distribution after peroxide treatment.

4.3.5 XPS

XPS was utilised to study the electronic structure of the calcined Pd nanocatalyst and a sample partially oxidised with peroxide solution (Table 4-5). The

carbon 1s signals are typical of elemental carbon with some carbon-oxygen functions present. More carbon-oxygen functions are present on the sample surfaces, which includes alcohols/ethers at ~286.5 eV and carboxyl groups at ~288.5 eV (FTIR for sample after oxidation displayed an increased C=O stretch intensity). Oxygen 1s signals were present mainly from carbon-oxygen functions such as alcohol (~533.5 eV) and carboxyl groups (~532 eV). An increase in surface oxygen concentration confirmed the oxidative treatment. The Pd 3d signals indicated the presence of metallic Pd phase for both samples, illustrating that the relatively mild oxidative nature of the said peroxide treatment does not detrimentally affect the palladium. The information here, however, is limited on determining any peak shift in the Pd 3d binding energies that arise from the carbon in the interstitials, due to the weakness of the Pd signals. XPS is a surface-sensitive technique, probing the outermost atomic layers of the material. This contrasts to the metal loading at 9% determined from ICP. The comparatively low Pd at.% observed here suggests the Pd was saturated with the external modifications, agrees with TEM analysis.

Catalyst	Peak BE			At.%			
	C 1s	O 1s	Pd 3d	C	O	Pd	Others
PdGluC400	284.61	533.24	335.58	84.2	11.7	0.05	4.05
PdGluC400[O]H_2O_2/NH_4OH	284.63	532.42	335.61	76.8	19.4	0.03	3.8

Table 4-5 Results from the XPS analysis.

4.4 HYDROGENATION TESTING

4.4.1 3-HEXYN-1-OL

The ability of the carbonised Pd nanocatalyst following oxidative treatment was probed in the stereoselective hydrogenation of 3-hexyn-1-ol to corresponding alkenol (Scheme 4-1). This is a highly valuable reaction widely used in the fragrance industry

for the production of leaf fragrance alcohol.[22] The new catalyst also showed high stability with no apparent deactivation or loss in selectivity upon repeated testing. Results were compared to the classical Lindlar catalyst and a commercial Pd/C in order to assess their activity and selectivity in low temperature, liquid phase conditions.

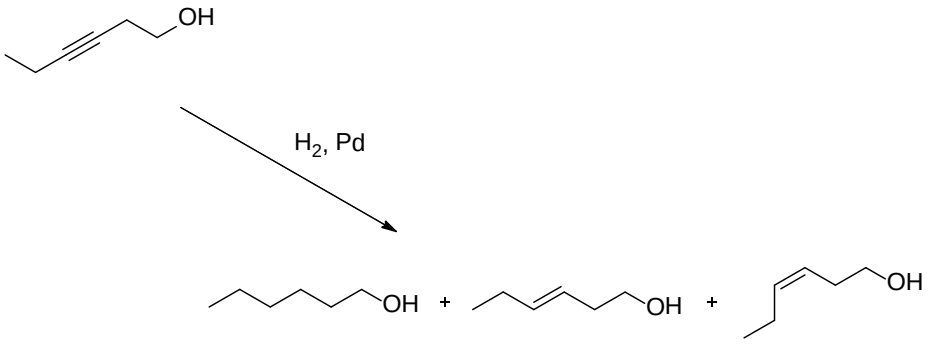

Scheme 4-1 Stereoselective hydrogenation of 3-hexyn-1-ol.

Fig. 4-11 displays typical H_2 gas uptakes for the catalysts in the hydrogenation. The compositions of the final solutions were determined by GC analysis (Fig. 4-12). Strikingly, the glucose derived catalyst was significantly different from Pd/C, and maintained an impressive selectivity to alkene. Only one equivalent of H_2 was taken up even after prolonged exposure to excess H_2 after complete alkyne conversion, while two equivalents of H_2 were consumed over Pd/C, which led to total alkane formation. While the more active Lindlar catalyst (Pd/$CaCO_3$ modified with Pb) also resulted in the uptake of one mole of H_2, however, it suffers rapid isomerisation processes leading to reduced alkene yields compared to the glucose derived catalyst. This therefore demonstrates the superior performance of this new class of Pd-C catalyst in minimising the undesirable alkene isomerisations and over-hydrogenation, despite prolonged exposure to a H_2 atmosphere. Thus, the carbonised glucose catalyst demonstrated here thus offers a green Pb free alternative, with a superior selectivity towards the semi-hydrogenated product, *cis*-hexen-1-ol. Such alkyne reductions are

stereoselective, occurring *via* syn addition of the alkyne, which affords mainly *cis*-alkenes is consistent according to a heterogeneous process on a metal surface.[1]

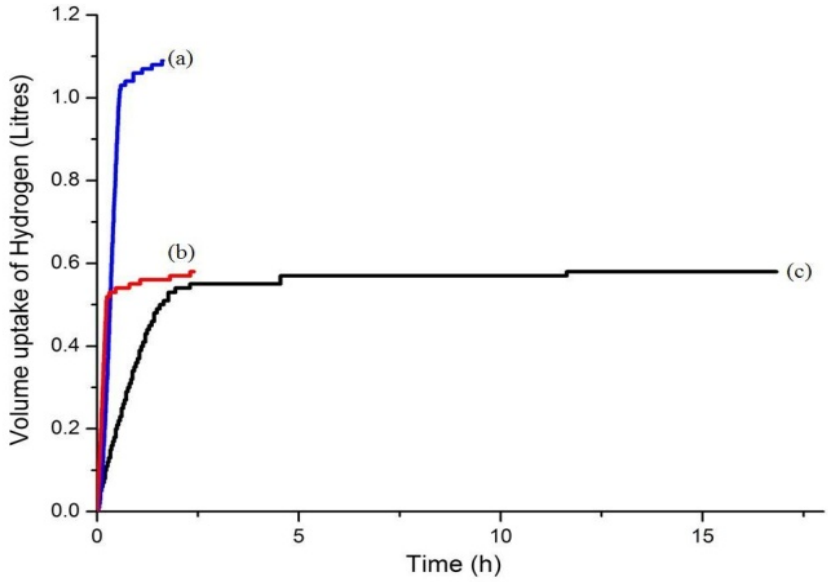

Fig. 4-11 H_2 uptake curves in the stereoselective hydrogenation of 3-hexyn-1-ol using: (a) 5% Pd/C (b) 5% PdPb/$CaCO_3$ (c) PdGluC400[O]H_2O_2/NH_4OH. Conditions: Catalyst to substrate ratio 1:1000, 3 bar H_2, 30°C, 400 rpm.

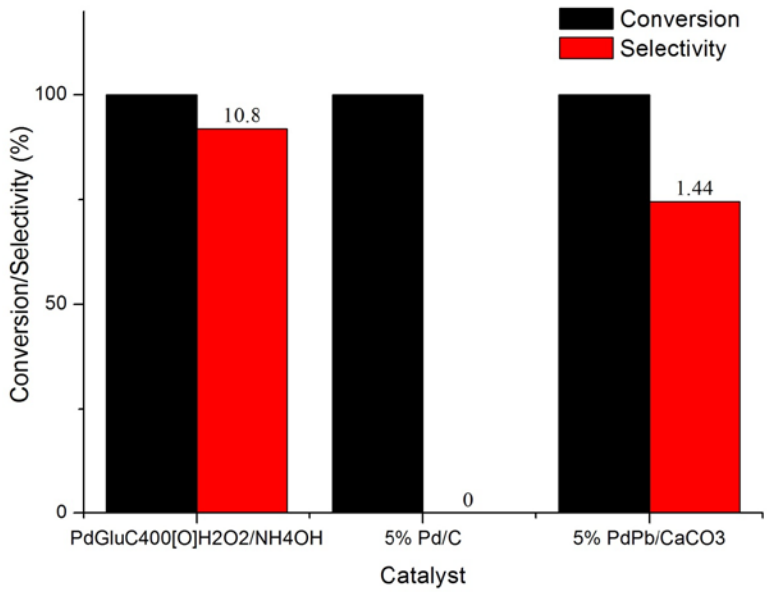

Fig. 4-12 GC analysis of 3-hexyn-1-ol hydrogenation at the end of the H_2 uptake (above). Conversion based on alkyne consumed and selectivity sum of *cis* and *trans*-hexan-1-ol. The numbers on the graph represent the *cis/trans*-alkene ratio.

4.4.2 4-OCTYNE

Stereoselective hydrogenation of the non-polar substrate 4-octyne was also studied in order to investigate the scope and the general utility of this new class of subsurface modified Pd nanocatalyst and to observe any underlying effects due to subsurface C in Pd (Scheme 4-2).

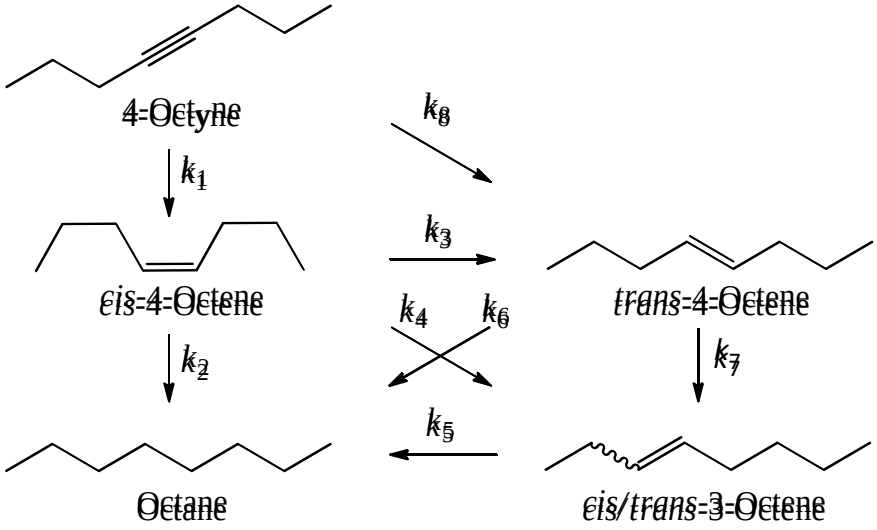

Scheme 4-2 Proposed reaction pathways for the stereoselective hydrogenation of 4-octyne.

The hydrogenation of 4-octyne was examined using two catalysts:

i) Catalyst A - Pd glucose nanocatalyst heat treated at 400°C in N_2 followed by oxidation using peroxide solution, contains subsurface C.

ii) Catalyst B - Pd glucose nanocatalyst heat treated at 400°C in H_2 followed by oxidation using peroxide solution, subsurface C removed.

These catalysts were also compared with a commercial 5% Pd/C, Lindlar 5% PdPb/$CaCO_3$ and BASF LF100 0.6% Pd/C. Thus, these catalysts were investigated and any attenuation on alkene adsorption was monitored. The hydrogenation was performed in a three neck flask with constant bubbling of H_2. The liquid composition was followed by GC by withdrawing aliquots at specific time intervals. Furthermore, the hydrogenation kinetic reaction profiles were fitted based on the Langmuir-

Hinshelwood (L-H) kinetic model. This model assumes equilibrium establishment of hydrocarbons observed in the reaction and a weak H_2 adsorption, based on previous experiments.[23] The rates equations were written according to the Scheme 4-2 with the assignment of an absorption equilibrium constant for each observed product:

$$\frac{dA}{dt} = -k_1\theta_A + \ -k_8\theta_A$$

$$\frac{dB}{dt} = k_1\theta_A - (k_2 + k_3 + k_4)\theta_B$$

$$\frac{dC}{dt} = k_3\theta_B + k_8\theta_A - (k_6 + k_7)\theta_C$$

$$\frac{dD}{dt} = k_4\theta_B + k_7\theta_C - k_5\theta_D$$

$$\frac{dE}{dt} = k_2\theta_B + k_6\theta_C + k_5\theta_D$$

$$\theta_i = \frac{K_i P_{(i)}}{1 + \sum_E^A K_i P_{(i)}}$$

where the species were defined as follows: A = 4-octyne; B = *cis*-4-octene; C = *trans*-4-octene; D = 3-octene; E = *n*-octane, respectively. K_i was defined as the adsorption constant of specie *i*, $P_{(i)}$ was the equilibrium concentration of specie *i* and θ_i was the probability of a surface site occupied by specie *i*.

The defined equations used for the model fittings to the experimental data were excellent with good reproducibility, reinforcing the validity of our model (Fig. 4-13).

Table 4-6 shows the result of the optimised kinetic model fittings. The initial unit from the optimised calculations was defined as per minute and this was re-normalised against the initial amount of substrate used per mol of catalyst per hour.

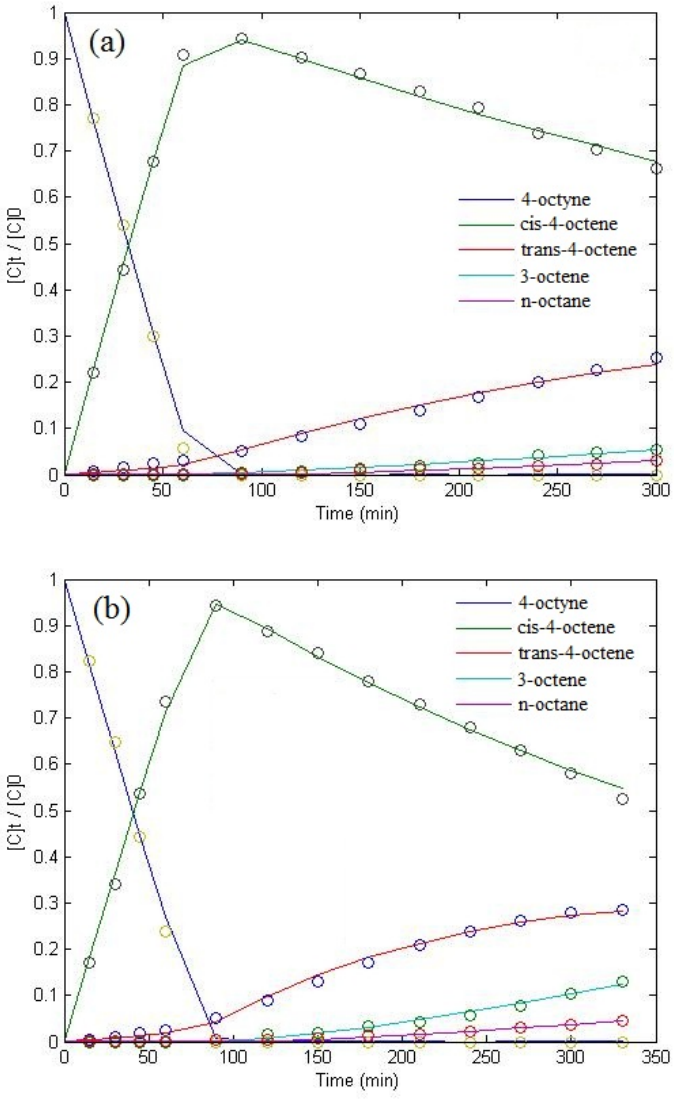

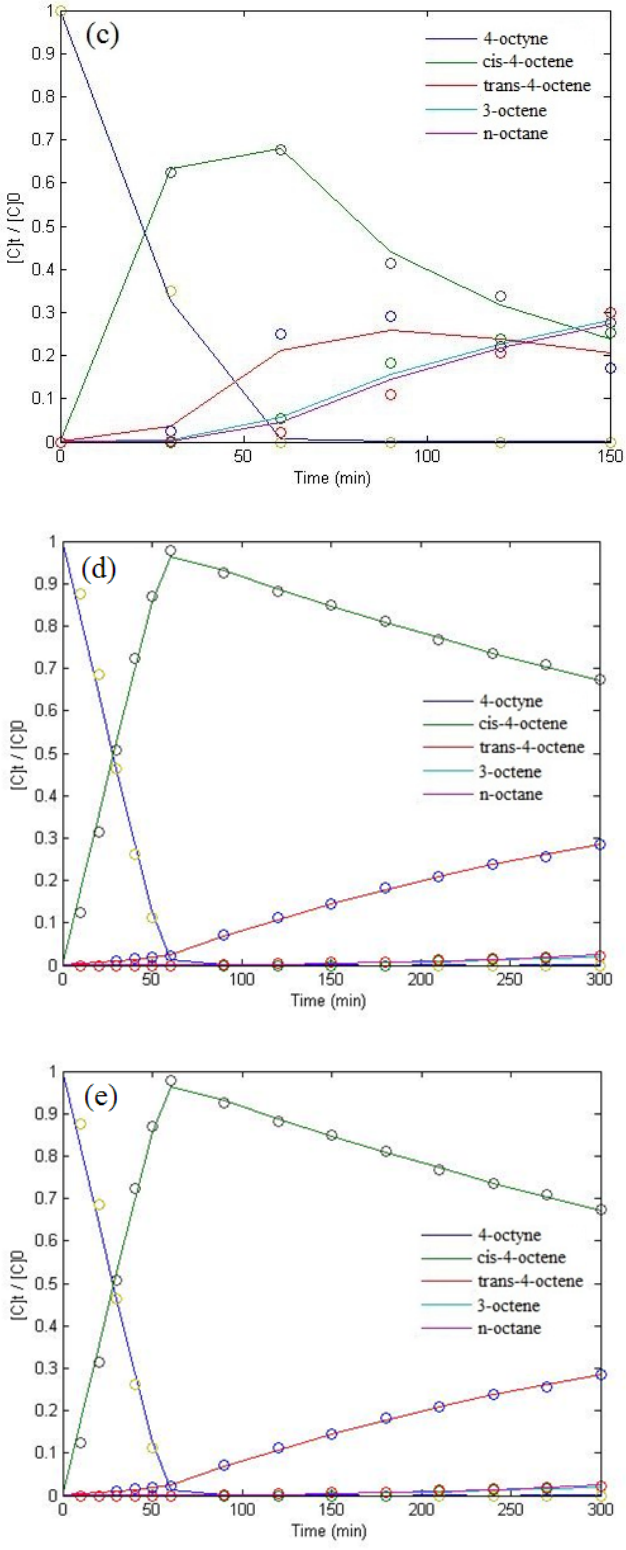

Fig. 4-13 Kinetic model fittings based on the L-H model of : (a) Catalyst A (b) Catalyst B (c) 5% Pd/C (d) Lindlar's catalyst (e) BASF LF100 0.6% Pd/C. Condition: 2000:1 ratio of 4-octyne:catalyst (Lindlar and 5% Pd/C) and 500:1 ratio of 4-octyne:PdGlu catalysts. 50 mL toluene, 50°C, 30 mL.min^{-1} H_2 bubbling with stirring at 650 rpm. Points and lines are experimental and fitted data, respectively.

Dataset ($mol_{sub}.mol^{-1}_{cat}.h^{-1}$)	Catalyst A	Catalyst B	5% Pd/C	Lindlar	BASF LF100
k_1	494	397	3005	2177	1584
k_2	0	0	0	0	0
k_3	111	248	9406	558	341
k_4	10	9	3228	0	24
k_5	0	0	0	0	0
k_6	67	106	7311	207	378
k_7	69	254	0	167	138
k_8	10	9	158	40	73

Table 4-6 Rates fitted using the L-H model of each hypothetical step of the catalysts tested in the stereoselective hydrogenation of 4-octyne.

It is evident, from Fig. 4-13 and table 4-6, that the reaction is characterised by the strong adsorption of 4-octyne in all cases, with the adsorption constant approximately two orders of magnitude higher than all alkene species, in agreement with previous calculations.[24] The consequence of this effect was almost exclusive production of *cis*-4-octene (although a small amount of direct semi-hydrogenation to trans-4-octene was also observed), until 4-octyne was nearly consumed both catalyst A and B. This is due to the lower adsorption energy of the weaker adsorbate, in this case alkene over alkyne. The consequence of this is that the catalyst surface will favour re-adsorption of 4-octene after near complete alkyne consumption, only then will undergo isomerisation and over-hydrogenation reactions.

The kinetic plots and adsorption constant calculations clearly demonstrate that alkyne adsorption is much stronger than other surface species and therefore effects between surface modification and subsurface contributions cannot be separated. Thus, an attempt to differentiate these two effects was made using the subsequent isomerisations and over-hydrogenations processes. These two pathways were believed to be sensitive to the adsorption strength on the catalyst surface and

therefore may be able to differentiate the said contributions from $C_{subsurface}$ to those on the surface.

Fig. 4-14 shows a plot of rate ratios normalised using the semi-hydrogenation pathway ($\sum k_{semi}$ or $\sum k_{1,8}$), against two parameters: 1) The sum of isomerisations ($\sum k_{iso}$ or $\sum k_{3,4,7}$); and 2) the sum of over-hydrogenations ($\sum k_{full}$ or $\sum k_{2,5,6}$). The rate ratios give an indication on how the catalyst minimises undesirable processes such as isomerisations and over-hydrogenations. On comparing the catalyst A (contains subsurface C) against B (subsurface C removed), the influence of subsurface carbon atoms were clearly evident on reducing these processes, despite the fact that they have no contact with substrate molecules. This was characterised by the high semi-hydrogenation rates against the suppression of isomerisations and over-hydrogenations, leading to the high rate ratios. The conventional 5% Pd/C, despite having high activity, suffers from excessive isomerisations and over-hydrogenation, leading to the lowest rate ratios. Overall, it was found to be that an apparent 17.5 and 10.6 times less in full hydrogenations and isomerisations for catalyst A when compared with the conventional 5% Pd/C, respectively. Selective removal of subsurface carbon by H_2 yielding catalyst B only gave an apparent 8.9 and 3.2 times in reduction. This provided clear evidence that subsurface C does indeed affect catalytic events in the surface for the first time in liquid phase reactions. Interestingly, the catalyst with subsurface C modification has comparable normalised rates when compared with the classical Lindlar type and BASF 0.6% Pd/C catalysts. Therefore, it is envisaged that Pd modification by subsurface C may offer a good alternative to achieve a selective catalyst for liquid phase reactions.

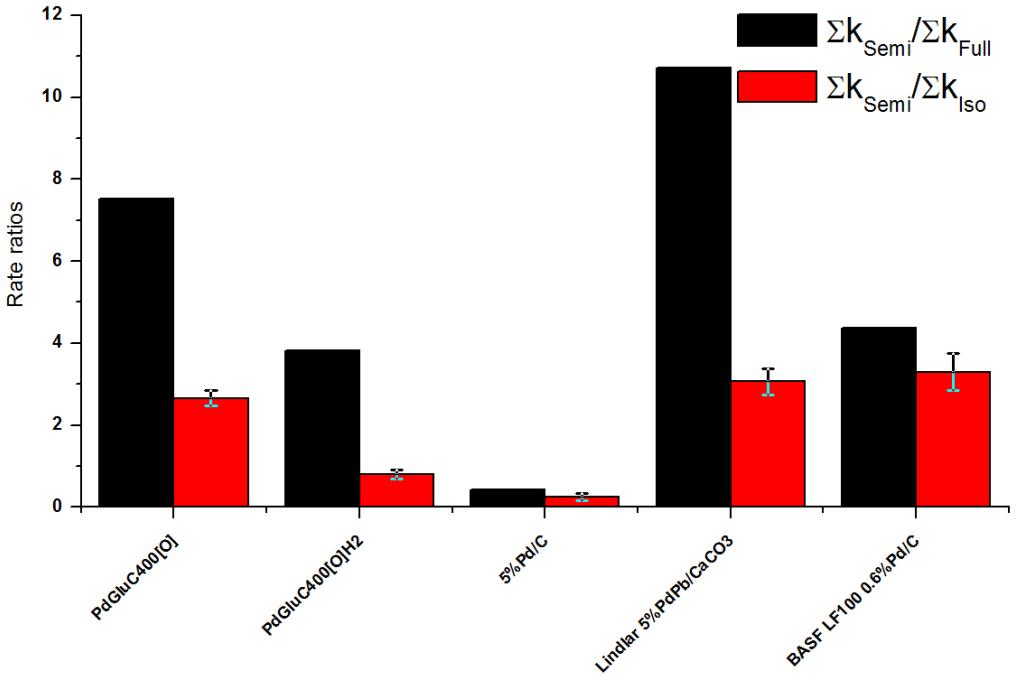

Fig. 4-14 A plot of rate ratios to compare the catalysts tested in the hydrogenation of 4-octyne.

4.5 DISCUSSION

Thus, apart from surface carbon effects, this study had shown that the presence of interstitial carbon atoms in the subsurface of Pd play a significant role in reducing the rates of alkene intermediates from over-hydrogenation and isomerisation reactions. This could be related to the inhibition of the β-Pd-H phase, which is known to alter the hydrogen atom equilibrium as shown here by TPR. In addition, the palladium could also be electronically modified. For example, using density functional theory (DFT) calculations, Yudanov *et. al.* noted that subsurface C weakens the binding energy of CO[17] and this was later reinforced by Lim *et. al*, by DFT calculations.[25] The effect is believed to be due to an increase in the Fermi level of the Pd through the hybridisation of Pd *d*-band with C *s-p* bands, thus favouring desorption and overall reduction of alkene adsorption energy.[26, 27] Electronic effects due to the influence of interstitial C on Pd was not detected by XPS in this study,

however, Teschner *et. al.* enforced our theory as the authors observed changes in electronic character of Pd caused by interstitial C probed using a high energy XPS technique.[7] On the basis of these accounts, we believe an electronic effect must play a more significant role on the dramatic change in catalytic surface events observed in our study. This was achieved by the lowering in adsorption energy of alkenes, leading to increase in desorption rates and therefore reducing undesirable processes, such as isomerisation and over-hydrogenation. On the other hand, the combination of kinetically stable interstitial carbons atoms from our preparation and additional effects in the liquid phase such the solvent cage effect, stronger molecular adsorption, and molecule re-adsorption could render the 'carbon effects' more significant than other gas phase reactions. Nevertheless, we demonstrate that trapped interstitial carbon atoms in Pd subsurface, created by our green methodology using glucose, were indeed effective to catalyse the hydrogenation of alkynes to *cis* alkenes in the liquid phase. This new class of catalysts could open up rational ways to tune substrate adsorption with other subsurface interstitials for ultraselective catalysis.

4.6 CONCLUSION

In conclusion, we report by using glucose, as a reducing and capping agent as well as the supporting matrix, in order to stabilise Pd at a molecular level. The size of Pd nanoparticles can be optimised at higher pH values by enhanced stabilisation with glucose. The catalysts was extensively characterised by PXRD, FTIR, TGA, TEM, ICP, TPR and XPS. Upon heat treatment, the carbonised glucose encapsulated the Pd nanoparticles with carbon atoms also taking residence in the octahedral holes, blocking the formation of β-Pd-H. Stereoselective hydrogenations of 3-hexyn-1-ol and 4-octyne in the liquid phase were compared with Lindlar's catalyst, conventional and BASF Pd/C. Effects by the surface and subsurface were separated using a simple

H_2 pretreatment to remove subsurface C. Kinetic model was fitted according to the Langmuir-Hinshelwood mechanism. It was shown for the first time that the geometrically and electronically modified Pd by interstitial carbon atoms reduced the adsorption energy of alkenes. This substantially reduced undesirable processes such as isomerisations and over-hydrogenation of alkenes, leading to higher overall cis-alkene selectivity. This effect was found likely to be the hybridisation of Pd *d*-states and C *p*-states, which results in an increased Fermi level of Pd, thus facilitates desorption and increase in overall selectivity.

4.7 REFERENCES

1. Á. Molnár, A. Sárkány and M. Varga, *J. Mol. Catal. A: Chem.*, 2001, **173**, 185-221.
2. S. Mori, T. Ohkubo, T. Ikawa, A. Kume, T. Maegawa, Y. Monguchi and H. Sajiki, *J. Mol. Catal. A: Chem.*, 2009, **307**, 77-87.
3. A. Drelinkiewicz, W. Stanuch, A. Knapik, A. Ghanem, R. Kosydar, A. Bukowska and W. Bukowski, *J. Mol. Catal. A: Chem.*, 2009, **300**, 8-18.
4. N. Semagina and L. Kiwi-Minsker, *Catal. Lett.*, 2009, **127**, 334-338.
5. P. Weerachawanasak, O. Mekasuwandumrong, M. Arai, S.-I. Fujita, P. Praserthdam and J. Panpranot, *J. Catal.*, 2009, **262**, 199-205.
6. J. A. Anderson, J. Mellor and R. P. K. Wells, *J. Catal.*, 2009, **261**, 208-216.
7. D. Teschner, J. Borsodi, A. Wootsch, Z. Revay, M. Havecker, A. Knop-Gericke, S. D. Jackson and R. Schlogl, *Science*, 2008, **320**, 86-89.
8. X. Sun and Y. Li, *Angew. Chem. Int. Ed.*, 2004, **43**, 597-601.
9. V. K. L. Mer, *Ind. Eng. Chem.*, 1952, **44**, 1270-1277.
10. Y. Ikushima, J. Liu, G. Qin and P. Raveendran, *Chem. Eur. J.*, 2006, **12**, 2131-2138.
11. J. Liu, P. Raveendran, G. Qin and Y. Ikushima, *Chem. Commun.*, 2005, 2972-2974.
12. J. P. Sylvestre, A. V. Kabashin, E. Sacher, M. Meunier and J. H. T. Luong, *J. Am. Chem. Soc.*, 2004, **126**, 7176-7177.
13. S. B. Zlemecki and G. A. Jones, *J. Catal.*, 1985, **95**, 621-622.
14. P. Canton, C. Meneghini, P. Riello, A. Balerna and A. Benedetti, *J. Phys. Chem. B*, 2001, **105**, 8088-8091.

15. S. B. Ziemecki, G. A. Jones, D. G. Swartzfager, R. L. Harlow and J. Faber, *J. Am. Chem. Soc.*, 1985, **107**, 4547-4548.

16. S. B. Ziemecki, G. A. Jones and D. G. Swartzfager, *J. Less-Common Met.*, 1987, **131**, 157-162.

17. I. V. Yudanov, K. M. Neyman and N. Rosch, *Phys. Chem. Chem. Phys.*, 2004, **6**, 116-123.

18. H. W. King, *J. Mater. Sci.*, 1971, **6**, 1157-1167.

19. N. Krishnankutty and M. A. Vannice, *J. Catal.*, 1995, **155**, 312-326.

20. V. Datsyuk, M. Kalyva, K. Papagelis, J. Parthenios, D. Tasis, A. Siokou, I. Kallitsis and C. Galiotis, *Carbon*, 2008, **46**, 833-840.

21. Y. J. Kim, T. S. Shin, H. D. Choi, J. H. Kwon, Y.-C. Chung and H. G. Yoon, *Carbon*, 2005, **43**, 23-30.

22. J. C. A. A. Roelofs and P. H. Berben, *Chem. Commun.*, 2004, 970-971.

23. N. Semagina, E. Joannet, S. Parra, E. Sulman, A. Renken and L. Kiwi-Minsker, *Appl. Catal., A*, 2005, **280**, 141-147.

24. E. Joannet, C. Horny, L. Kiwi-Minsker and A. Renken, *Chem. Eng. Sci.*, 2002, **57**, 3453-3460.

25. K. H. Lim, K. M. Neyman and N. Rösch, *Chem. Phys. Lett.*, 2006, **432**, 184-189.

26. J. Haglund, A. F. Guillermet, G. Grimvall and M. Korling, *Phys. Rev. B*, 1993, **48**, 11685.

27. C. D. Gelatt, A. R. Williams and V. L. Moruzzi, *Phys. Rev. B*, 1983, **27**, 2005.

CHAPTER 5 - SUBSURFACE BORON MODIFIED PALLADIUM NANOCATALYST

5.1 INTRODUCTION

As demonstrated in Chapter 4, an emerging alternative to the modification of the electronic and geometric structure of metallic nanoparticles is by the insertion of light element atoms into the metal lattices. For example, Pd is well known to absorb large amounts of hydrogen into the bulk by facile dissociation of the dihydrogen bond at ambient temperature and pressure.[1, 2] Recent work by Teschner *et. al.* has shown that the unselective gas phase hydrogenation of various alkenes to alkanes arises from *in situ* formation of unselective Pd-β-hydride phase, of which its stability is highly dependent on the reaction pressure.[3] Furthermore, the authors demonstrated the diffusion of carbon atoms into the sublattices of Pd has dramatic effects on increasing the desired selectivity of the desired semi-hydrogenation from alkynes to alkenes. Subsurface oxygen in Pd at high temperatures has also been documented in the literature, with the active subsurface species found to influence the kinetics of CO oxidation at the high temperature regime.[4, 5] However, it is intriguing that very few literatures that study the effects of subsurface boron. While the majority of the literature has focused on studying ordered Pd_xB_y alloys[6-11], there are several methods to access interstitial subsurface B modified Pd (Pd-^{int}B) materials:

i) A solid state method involving combining boron pieces and Pd foils followed by arc melting under an argon atmosphere. It was shown that the Pd-B phase is only stable at high temperature but it can be rapidly quenched to room temperature in order to trap the ordered alloyed phase (Pd-B_y).[12-14] Although the same method can also be used to generate a partial interstitial B doped phase.[15] It is evident that this method is not suitable for application in catalysis due to the severe sintering effect that would occur in these conditions.

ii) Decomposition of diborane (B_2H_6) gas at room temperature followed by heat treatment. At room temperature, Krawczyk reported the formation of a B-rich overlayer on Pd by decomposition of B_2H_6 and subsequent evolution of H_2 gas.[16] Upon heat treatment, the B overlayer gradually migrates into the bulk of the Pd, as observed by using Auger electron spectroscopy. While this method maybe promising to access Pd-^{int}B materials, the high cost of B_2H_6, high toxicity and difficult to control the concentration of B doping renders this method not viable.

iii) Recently Wang *et. al.* used a liquid phase route using dimethylamine borane ($Me_2NH{\bullet}BH_3$) as the B source.[17] A series of chemical reactions with hydroxide ions generated atomic B, which then doped the Pd forming Pd-^{int}B. However, due to the reactivity of atomic B with hydroxide ions, there was very low amount of doping and side product was significant in the process.

Therefore it is evident that a new method is required to access highly doped Pd-^{int}B nanocatalysts. Ideally these should be rapidly synthesised, coupled with the ease of tuning B concentration whilst maintaining low toxicity precursors.

5.2 OBJECTIVES

The aim of this Chapter is to synthesise, characterise and catalytically evaluate Pd-^{int}B nanomaterials with B occupying the interstitial subsurface. Modification of the Pd nanocatalyst was carried out in the liquid phase by using borane tetrahydrofuran solution (BH_3.THF) as the B source. Its liquid phase fabrication should allow controlled B doping on the catalyst and offer much lower toxicity when compared to diborane gas. The use of BH_3.THF has been applied in the study of the dehydrocoupling of dimethylamine borane.[18] The authors noted a spontaneous

formation of H_2 gas when borane is in contact with transition metals, with ^{11}B NMR and XPS indicating the formation of a passivated B layer that poisons the metal surface for the dehydrocoupling reaction. The mechanism of deposition may be similar to that of B_2H_6 gas at room temperature, as this also forms H_2 gas upon deposition onto a metal surface. However, liquid phase doping should allow better handling and control during the B doping process as mentioned previously.

5.3 SYNTHESIS OF CATALYSTS

5.3.1 SYNTHESIS OF Pd/C

Initially a standard Pd on activated carbon catalyst was prepared in order to subsequently modified with B. The synthesis of Pd/C was carried out using an impregnation technique of $Pd(NO_3)_2$ onto high surface area carbon (Norit GSX) in *n*-butanol. *n*-Butanol was used as the solvent instead of water because the hydrophobic properties of active carbon may have a detrimental effect to the final metal particle size.[19] The 3 wt.% loaded Pd/C was reduced under a stream of H_2 at 500°C. Fig. 5-1 shows the TEM image of Pd/C after reduction. The average metal crystallite size was found to be 13±5 nm. HAADF-STEM and EDX studies confirmed the sample only consists of Pd. The use of a high temperature reduction had generated relatively large Pd nanoparticles, owing to the low lattice energy of Pd. This can be advantageous for several reasons:

i) Migration from surface to interstitial sites is known to be more facile for larger nanoparticles as in the case of H absorption in Pd due to its lower chemical potential or kinetics (Pd contracts at small size for increased stabilisation and hence higher chemical potential for interstitial occupation[20].

ii) The number of interstitial sites is maximised.

iii) Metallic properties can vary in the 1-5 nm size range, where there is a quantum size effect and therefore variance in electronic as well as geometric properties that may obscure any underlying promotion arising from subsurface B.

Thus, an atom statistical model of metal crystals was used to estimate the percentage surface plane sites against defective sites.[21, 22] The use of atom statistics has been successfully employed in the literature, such as Pd C-C coupling and hydrogenation of allylic alcohol.[23, 24] The modelled particle shape used in this case was assumed to be the most thermodynamically stable Pd particle by adopting the cuboctahedron configuration. The parameters used for the calculation are shown below in Fig. 5-2:

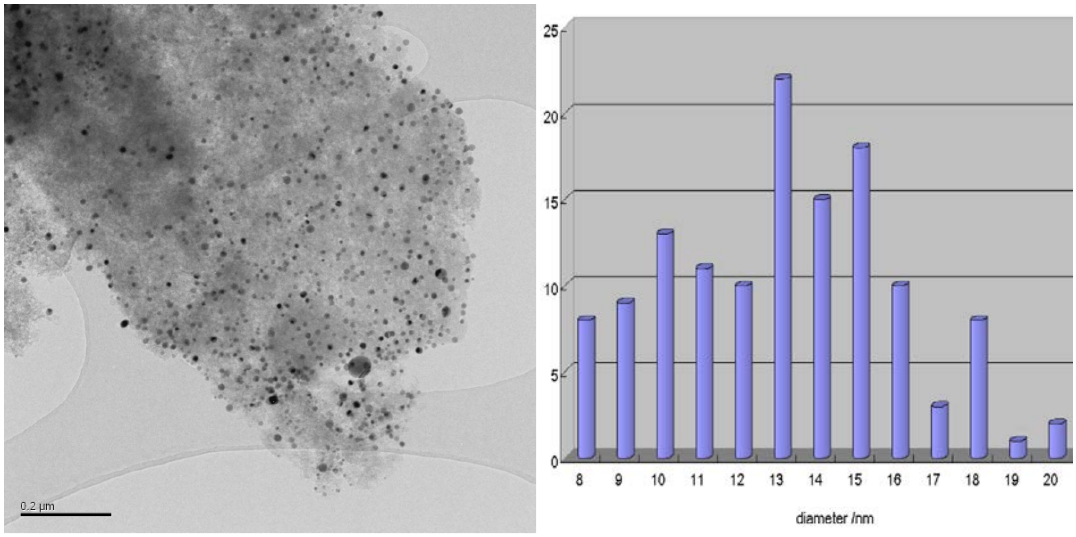

Fig. 5-1 TEM micrograph and size distribution profile of 3% Pd/C after reduction at 500°C.

Cuboctahedron	
Total number of atoms	$\frac{1}{3}(2m-1)(5m^2-5m+3)$
Number of surface atoms	$10m^2-20m+12$
Interstitial (12-coordinate)	$\frac{1}{3}(2m-3)(5m^2-15m+13)$
Vertex (5-coordinate)	12
edge (7-coordinate)	$24(m-2)$
square face (8-coordinate)	$6(m-2)^2$
triangular face (9-coordinate)	$4(m-3)(m-2)$

Fig. 5-2 Formulas used to calculate the population of different surface sites in a cuboctahedron particle as a function of edge length *m*.[22]

Vertex and edge sites are defined as low coordinated sites while square face and triangular face sites are defined as surface face sites. Table 5-1 shows the parameters calculated for a typical nanoparticle at 13 nm. It was found the nanoparticle is mostly dominated by surface sites (~91%) such as <111> and <100> planes, with the rest being defective sites (9%) such as lower coordinate edge and corner sites. Therefore, geometrically, the sample with 13 nm Pd nanoparticle can be used to study effects of subsurface B. Moreover, electronic contribution arising from the quantum size effect can also be neglected as the smallest size observed for our Pd nanoparticle was 8 nm, a size at which Pd is likely to be fully metallic. Therefore this sample was used to study the effect of B doping.

Particle Size (nm)	**Total Number of Atoms (N_T)**	**Surface Atoms (N_S)**	**Low Coordinated Sites**	**Surface Face Sites**	**Theoretical Dispersion (%)**
13	76690	7215	633	6582	9.4

Table 5-1 Atom statistics for a 13 nm Pd nanoparticle adopting the cuboctahedron geometry.

5.3.2 SYNTHESIS OF Pd-^{INT}B/C

The prepared Pd/C catalyst was subsequently treated with BH_3.THF to form the desired B-doped phase. The catalyst was first loaded into a round flask and evacuated for 20 h in vacuum at 80°C to ensure any residual oxygen or moisture do not prematurely oxidise BH_3.THF. The catalyst was subsequently reduced under a H_2 atmosphere at 100°C before the addition of BH_3.THF at room temperature under N_2. A high concentration of BH_3.THF (25 eq. of moles of B to moles of Pd) was used to ensure maximum B incorporation.[18] Fig. 5-3 shows the two PXRD patterns for Pd doped with BH_3.THF measured in N_2 and one exposed to air. It is evident that both the B doped sample are markedly different compared to the non-doped sample. This was characterised by a slight shift to lower 2θ, an effect indicative of B interstitial occupation and thus expanded the Pd metal lattice at room temperature. This contrasts to the high temperature activation needed when arc melting B pieces with Pd foils.[15] This is the first example of synthesising high concentration of subsurface B in Pd in liquid phase. Note that the formal Pd *fcc* phase was retained and that no ordered alloys were observed at room temperature. Interestingly, the PXRD pattern for the sample exposed to air after synthesis is identical to the sample kept in an inert XRD sample cell saturated with N_2. This indicated that interstitial B in Pd appears to be stable in air at room temperature and may be used to study hydrogenation reactions under mild conditions. The ability to form interstitial B solid solution at room temperature could be due to an entropic effect, where B overlayers are formed initially on the Pd surface with the subsequent evolution of H_2 gas.[18] However, on comparison of the atomic radii between the light elements (H, C, B and N), boron is the largest and yet B atomic fraction of up to 0.186 formation of interstitial Pd-B was observed. Theoretically, no solid solutions should ever be formed between Pd and B,

according to the Hagg's criterion, the critical atomic radius ratio between the light element (r_i) and the metal (r_m), is satisfied only if the atomic radius ratio (r_i/r_m) is less than 0.59 (r_B/r_{Pd} = 0.67).[15] Furthermore, it is energetically disfavoured to expand the metal lattice and thus extra stabilisation is needed for the migration of light elements from the metal surface to interstitial sites. Therefore, this extra stabilisation must come from the hybridisation between B *s*-*p* orbitals and Pd *d*-orbitals *i.e.* an electronic effect, on increasing the overall stability of B interstitial in Pd[25, 26]. Although some near surface oxidation of subsurface B cannot be neglected. Surface sensitive techniques such as XPS are needed to observe any surface oxidation of B or Pd.

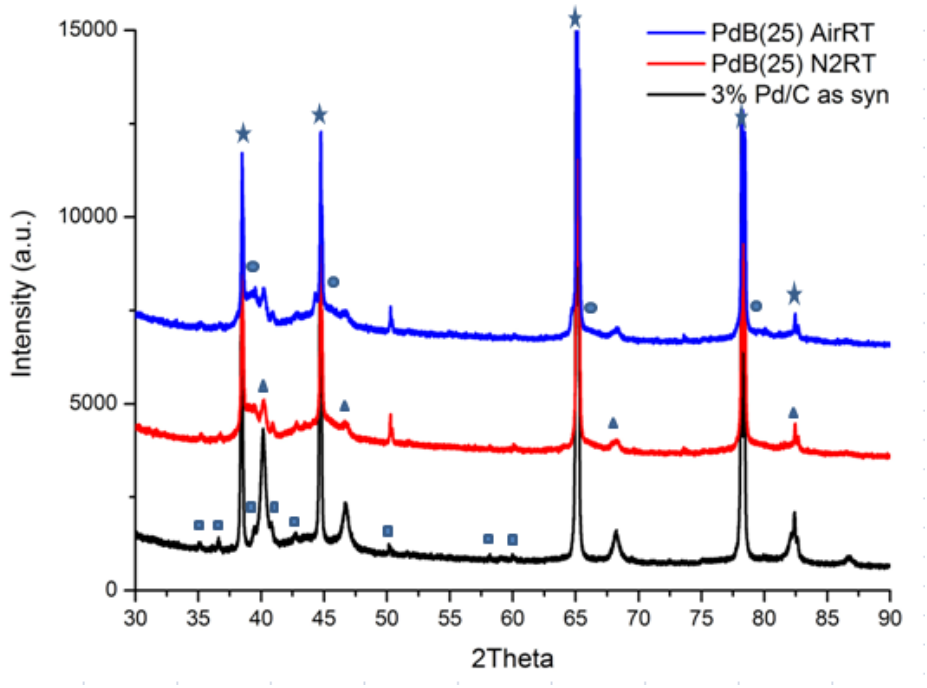

Fig. 5-3 PXRD profiles showing the *fcc* Pd <111>, <200>, <220> and <311> peaks for: i) the as-synthesised Pd/C (black); ii) Doped with 25 eq. of BH_3.THF saturated in N_2 (red); iii) Doped with 25eq. of BH_3.THF and exposed to air. Stars: Background peaks from the aluminium sample stage. Squares: Peaks from the carbon support. Triangles: metallic Pd peaks. Circles: Boron doped Pd peak.

5.3.3 HEAT TREATMENT OF Pd-^{INT}B/C IN NITROGEN

Since metallic Pd peaks are still present for the samples doped with B at room temperature, it was anticipated that a heat treatment was needed to drive surface B to deeper subsurface sites of Pd. Fig. 5-4 shows the PXRD pattern of these samples heated to various final temperatures for 1 h. Some satellite peaks were observed (at angles 31.0°, 33.6°, 35.9°, 40.5°, 43.3°, 47.8°, 50.3° and 51.2°) could be due to oxidised B species (also referred in Section 6.4.2). The amount of boron in the sample can be calculated using the linear relation[15]:

$$\mathrm{Pd(B)}: a(x_B^r) = 0.38920 + 0.06882(44)x_B^r(\mathrm{nm})$$

where a is the unit cell parameter, x^r_B is the atomic ratio (B at.%) and metallic Pd unit cell parameter is 0.3892 nm. Table 5-2 shows the estimated lattice parameters and boron atomic ratios. It can be seen that metallic Pd peaks when heated to 200°C is no longer present in the sample and maximum B incorporation was achieved, thus verified the hypothesis that a heat treatment was indeed needed to drive the B overlayers migration process.[27] The observed lattice parameter corresponds to a 3.5% lattice expansion. At 300°C atomic ratio of B dropped slightly with a weak metallic Pd signal, which is more evident when the sample was heated to 400°C. The evolution of metallic Pd peaks could be due to particle sintering, so creating empty Pd interstitial sites and the Pd signal observed or B re-migrating back to the surface under these conditions, as metallic Pd is thermodynamically favoured at higher temperatures.

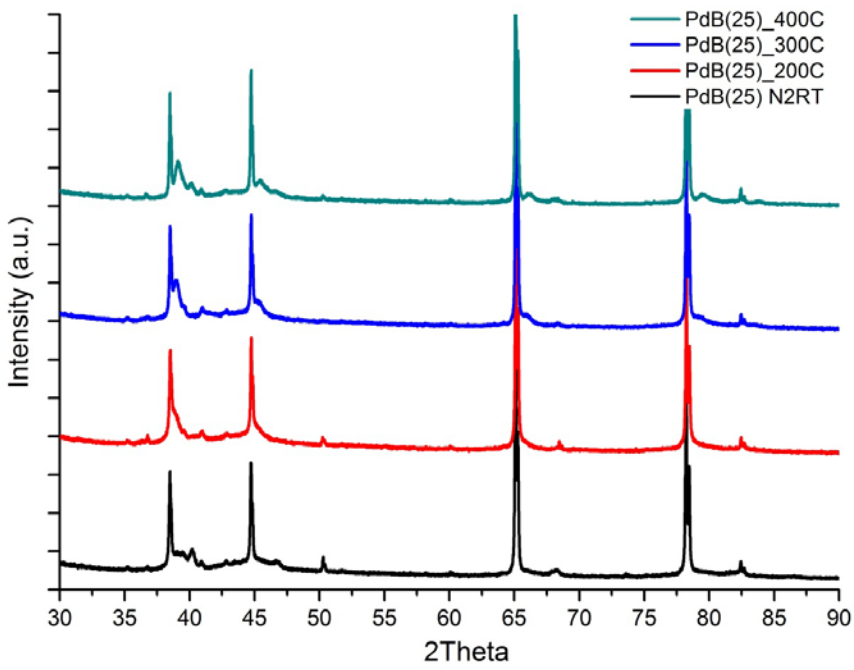

Fig. 5-4 PXRD patterns of Pd-^{int}B/C heat treated in N_2 at: B doped sample at room temperature; 200°C (red); 300°C (blue); 400°C (cyan).

Heat Treatment (°C)	Lattice Parameter a_0	B at.%
RT	0.3891(2)	0
200	0.4026(7)	19.4
300	0.4018(3)	18.6
400	0.3998(3)	15.7(70%)

Table 5-2 Lattice parameter and atomic ratio of B with respect to the heat treatment.

Fig. 5-5 shows a TEM micrograph and particle size distribution profile for a sample doped with 25 eq. mole ratio of BH_3.THF with Pd and heat treated to 200°C for 1 h under N_2. The average metal crystallite size was found to be 18±10 nm. The *d* spacing of the lattice fringes along the <111> direction was calculated to be 2.31 Å compared to the non-doped sample measured at 2.26 Å, in agreement with measurements taken from PXRD. This provided further evidence that B has indeed migrated fully to the subsurface of Pd through the applied heat treatment. However, it

is evident that the size distribution has increased when compared with the non-doped sample. The increase in particle size may be ascribed to several factors:

i) Leaching of Pd by BH_3.THF.

ii) Reaction of BH_3.THF with the carbon support, hence destabilising the interaction between the metal and carbon support.

iii) Apparent enlarged size due to B incorporation in the subsurface of Pd.

Nevertheless, a large particle size may be beneficial in observing any B promotion in catalytic testing as previously mentioned.

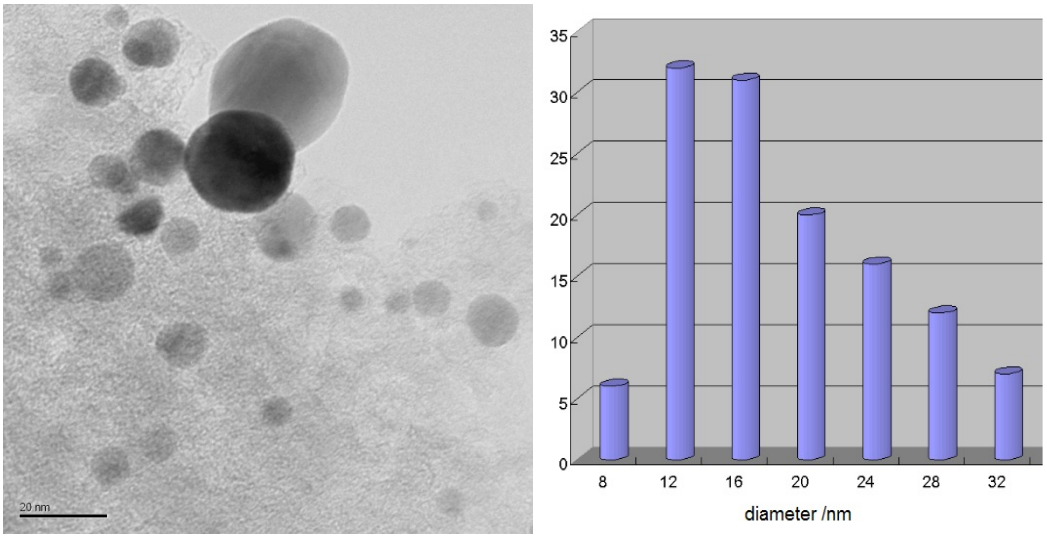

Fig. 5-5 TEM micrograph and size distribution profile of 25eq. Pd-^{int}B/C.

5.3.4 EFFECT OF B:Pd RATIO

The mole ratio of B to Pd was varied between 5 to 50. Fig. 5-6 shows the PXRD pattern of these samples. It was found saturated B interstitials was achieved at B atomic ratio 20% at 10:1 mole ratio of B:Pd (Table 5-3). Similar maximum B concentration was reported in the literature by using the arc melting method.[15] Any further increase in the dosage of BH_3.THF did not increase the concentration of B occupation, within experimental errors. It is surprising to see that a molar ratio of 5eq. of BH_3.THF did not saturate all the Pd interstitial sites, as only 20% of moles of Pd is

theoretically needed to achieve full saturation. Thus, excess boron may be deposited onto the carbon support or given off as a gas either on its own or formed higher B_xH_y clusters.

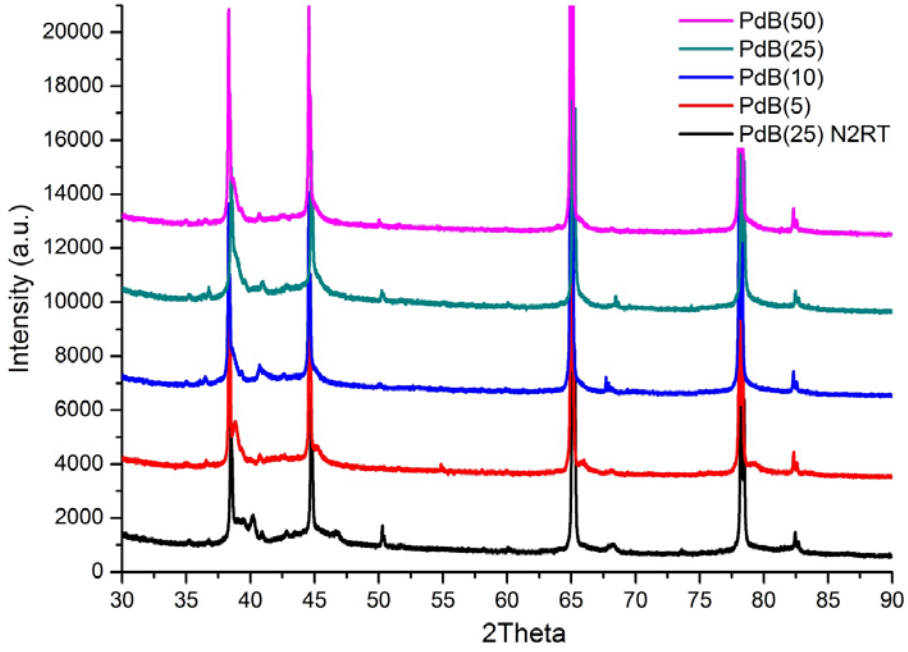

Fig. 5-6 PXRD patterns of Pd-^{int}B/C showing different B:Pd ratios.

Mole ratio of B/Pd	Lattice Parameter a_0	B at.%
5	0.4009(4)	17.1
10	0.4030(6)	20.1
25	0.4026(7)	19.4
50	0.4028(5)	19.8

Table 5-3 Lattice parameter and atomic ratio of B with respect to the B/Pd ratio heat treated at 200°C for 1 h.

5.3.5 HEAT TREATMENT OF Pd-^{INT}B/C IN HYDROGEN

Heat treatment of the 25 eq. B doped samples at 200°C (herein named Pd-^{int}B/C) was used to study the interaction of interstitial B with H_2 for 1 h. Fig. 5-7 shows the PXRD pattern of these samples. No apparent segregation effect was observed when the sample was reduced at 100°C. However, the atomic ratio of B

decreases at increasing temperatures (Table 5-4). The sample treated in 200°C can be compared to the sample treated previously in 200°C in N_2, which resulted in an apparent 3.4% loss in concentration of ^{int}B in the sample. Similarly, this effect is increasingly evident for the same heat treatment at 300°C (loss of 4.4%) and at 400°C (loss of 6.5%) compared with N_2 treatment. Pd-^{int}B phase segregation under reducing conditions may be ascribed to the bonding affinity of boron to hydrogen, in which boron may reside on the metal surface or be given off as a gas in higher B_xH_y clusters. Nevertheless, no change was observed in atomic B concentration when treated at 100°C, therefore the stability of Pd-^{int}B catalyst for hydrogenation reactions can still be applied under these conditions. On comparing these values to the class of Pd-^{int}C catalysts studied in chapter 4, it was apparent that the Pd-^{int}B nanocatalysts exhibited higher thermal stability than the Pd-^{int}C catalyst, as all the interstitial C are converted to CH_4 at 150°C under reducing atmosphere. Therefore, the higher apparent thermal stability of Pd-^{int}B could be ascribed to higher degree of hybridisation, leading to its increased stability compared to Pd-^{int}C.

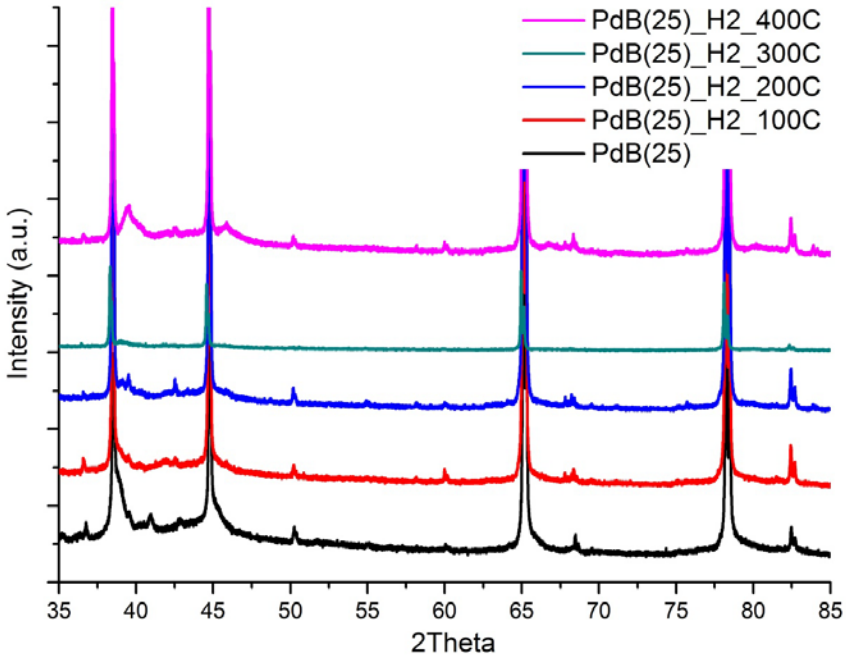

Fig. 5-7 PXRD patterns of Pd-^{int}B/C heat treated in H_2 at: heated in N_2 at 200°C (black); 100°C (red); 200°C (blue); 300°C (cyan); 400°C (purple).

Heat Treatment (°C)	Lattice Parameter a_0	B at.%
200 in N_2	0.4026(7)	19.4
100	0.4032(5)	20.3
200	0.4002(3)	16.0
300	0.3990(6)	14.2
400	0.3955(10)	9.2

Table 5-4 Lattice parameter and atomic ratio of B at various heat treatment in H_2 for 1 h for a 25 eq. Pd-^{int}B/C sample pretreated at 200°C for 1 h in N_2.

5.3.6 HEAT TREATMENT OF Pd-^{INT}B/C IN AIR

A similar heat treatment in air was applied to the Pd-^{int}B/C sample. Fig. 5-8 shows the PXRD pattern of these samples. It was found oxygen treatment had a more severe effect on the Pd-^{int}B phase segregation (Table 5-5). Treatment at 100°C already resulted in a 1.9% loss in the concentration of B, with approximately 70% Pd-^{int}B and 30% metallic Pd phase. Heat treatment at 200 or 300°C resulted in complete

ejection of B with metallic Pd being formed. Boron is likely to have been oxidised and remain on the surface of Pd. It is not surprising to observe oxygen has the propensity to induce chemisorption phase segregation, as there is a strong driving force between the different binding energies of O with B and O with Pd. It is interesting to note that segregation is already occurring here at 100°C compared to 327°C reported in the study of model Pd(111) surface with boron.[27] Due to low temperature oxygen induced segregation, it may deemed not possible to study oxidation reactions with the boron-modified systems.

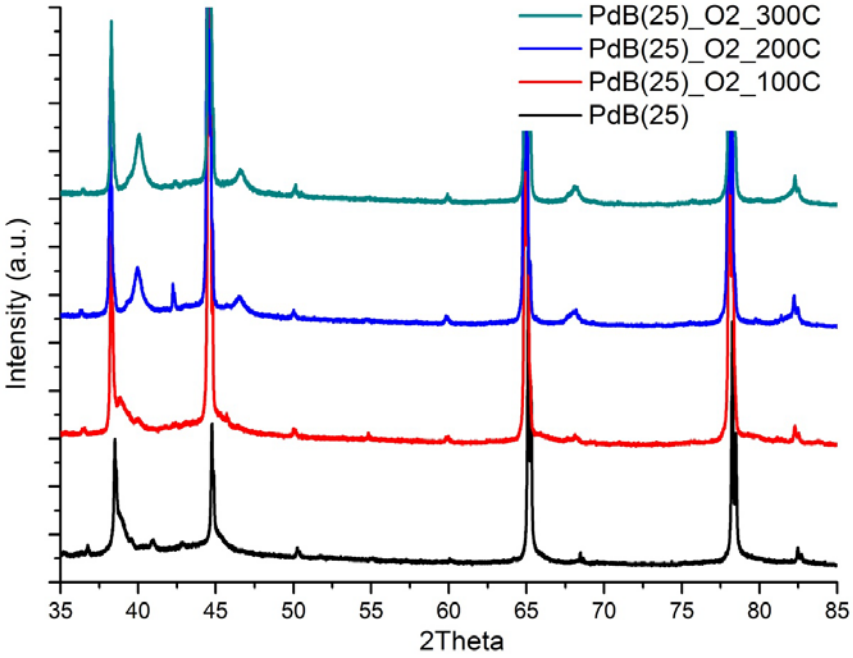

Fig. 5-8 PXRD patterns of Pd-^{int}B/C heat treated in air at: heated in N_2 at 200°C (black); 100°C (red); 200°C (blue); 300°C (cyan).

Heat Treatment (°C)	Lattice Parameter a_0	B at.%
200 in N_2	0.4026(7)	19.4
100	0.4012(4)	17.5(77%)
200	0.3890(2)	0
300	0.3890(4)	0

Table 5-5 Lattice parameter and atomic ratio of B at various heat treatment in air for 1 h for a 25 eq. Pd-^{int}B/C sample pretreated at 200°C for 1 h in N_2.

5.4 OTHER CHARACTERISATIONS OF Pd-^{INT}B/C

5.4.1 TPO-MS

The stability of the Pd-^{int}B phase at lower temperatures was also studied by TPO coupled with MS. It is expected that the MS could detect any volatile boron fragments that might have been given off during the synthesis process that otherwise would have not been detected by PXRD. Fig. 5-9 shows TPO spectra of Pd/C reduced at 500°C and Pd-^{int}B/C. It was found that no appreciative amounts of oxygen consumption signals were observed in the low temperature range and up to 250°C for the Pd-^{int}B/C sample. This result contradicts the fact that B atomic ratio had been reduced by 1.9% when treated with oxygen at 100°C (Table 5-5). The lack of signal could be due to consumption of oxygen that are chemisorbed on the catalyst surface is beyond the detection limit for this technique. No high temperature B_xO_y phase was observed indicated that B_xO_y exists as overlayers and remains on the Pd surface. However, a positive peak (evolution of oxygen) was observed starting from around 270°C up to 400°C. Further analysis using mass spectrometry indicated evolution of C_2 species corresponding to ethene and ethane (Fig. 5-10). On the other hand, no signals were observed between this temperature range for the non-doped sample reduced at 500°C. This indicated that upon deposition of BH_3.THF and subsequent heat treatment at 200°C may be detrimental to the active carbon support. This

conclusion is also supported by the increased particle size and size distribution after B doping (Fig. 5-5).

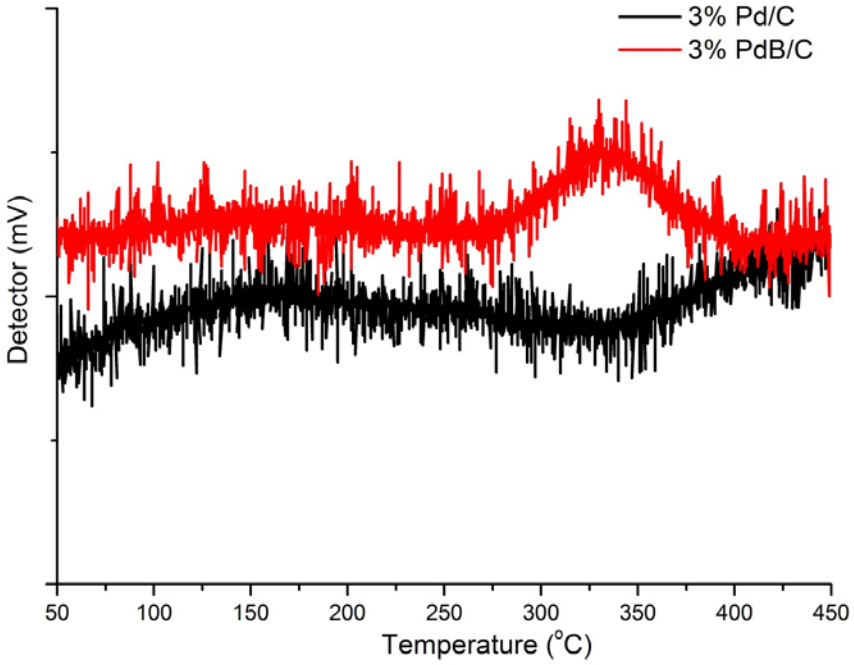

Fig. 5-9 TPO spectra of: i) Pd/C reduced at 500°C (black); ii) Pd-^{int}B/C (red).

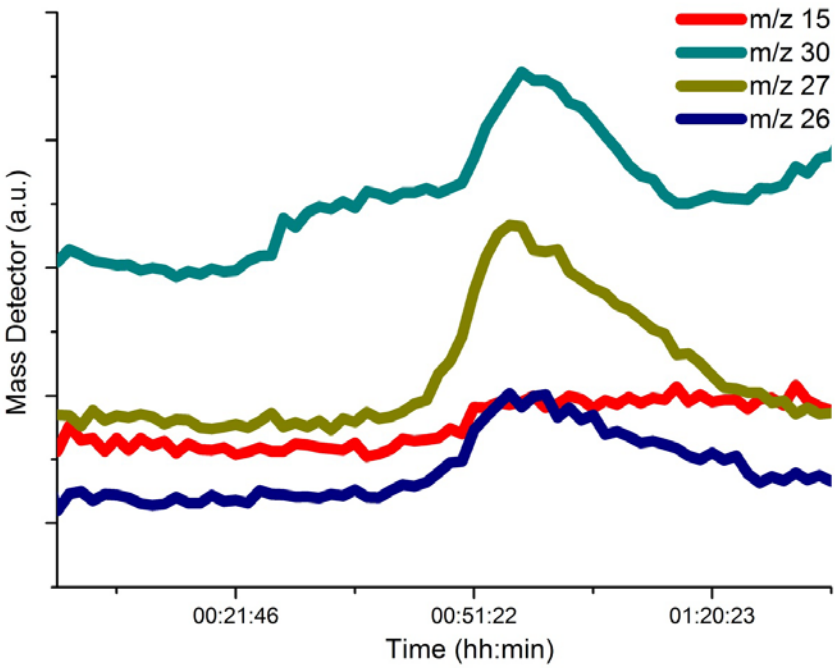

Fig. 5-10 MS spectra for the Pd-^{int}B/C sample.

5.4.2 TPR-MS

TPR-MS was also used in order to probe the interaction between subsurface boron and hydrogen and to detect any volatile B_xH_y species, as above. Fig. 5-11a shows the TPR spectra for a sample of Pd-^{int}B/C and the same sample but pretreated with oxygen at 250°C to ensure there was no decomposition of hydrocarbons from the carbon support. The sample pretreated with oxygen showed a negative peak at 80°C whereas this is not present for the Pd-^{int}B/C sample. The peak is due to decomposition of β-hydride phase in Pd. This confirms that oxygen has induced B segregation leading to formation of B_xO_y overlayers[27] and furthermore gave additional evidence that boron interstitial in Pd has been formed and that boron had fully occupied in all the available subsurface sites. Fig. 5-11b shows the corresponding MS spectra for the Pd-^{int}B/C sample. Peaks consisting of C_2 and C_1 fragments were again detected between 300-700°C. Note that m/z = 26 and 27 may also correspond to B_2H_6 fragments. However at m/z = 24 (a unique identifier for B_2H_6) no signal arising from any boron species was observed (relative percentage mass intensities for B_2H_6 with m/z 24, 26 and 27 are 89.6, 100, 91.4). On the other hand, a small amount of BH_3 was detected in the high temperature range (>800°C) indicates the stability of B in hydrogen and B species are likely to remain on the catalyst surface.

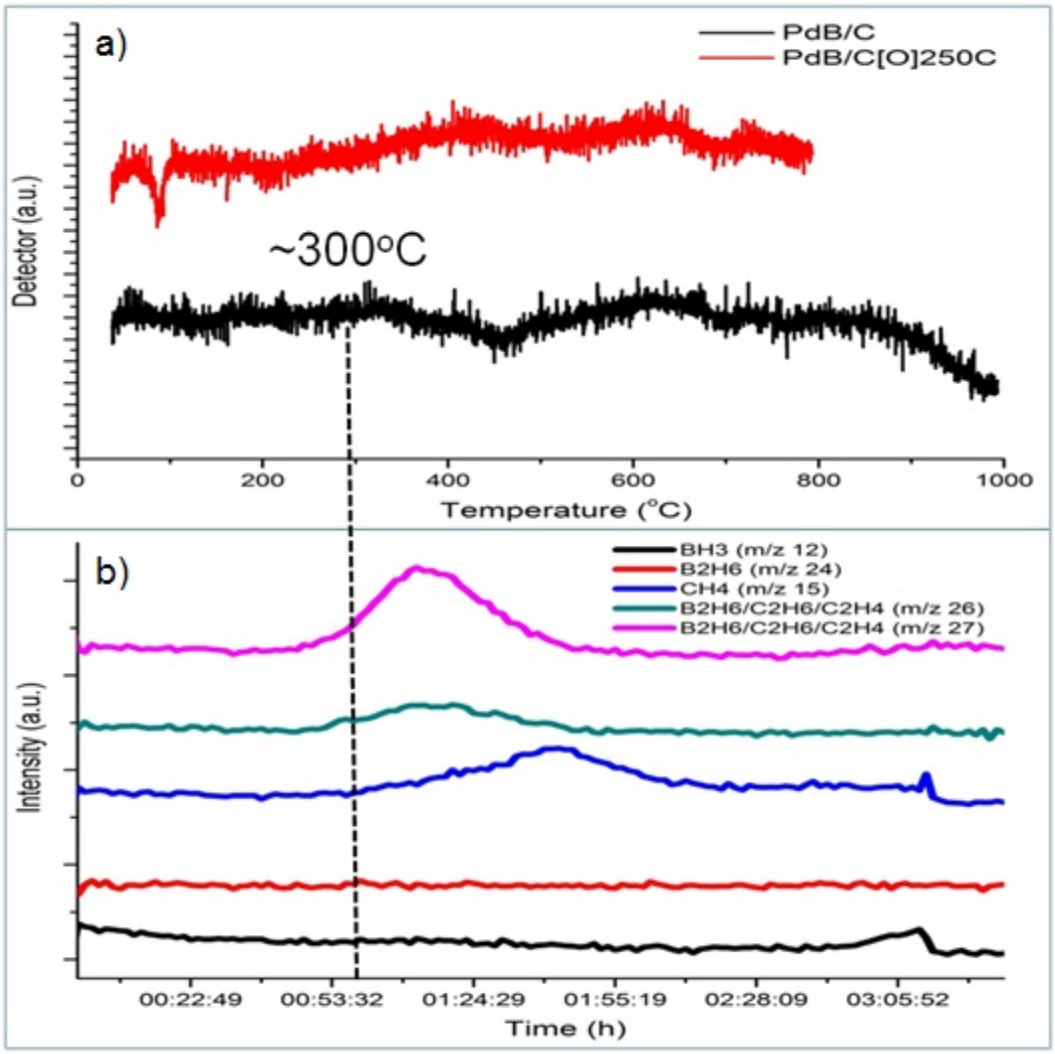

Fig. 5-11 a) TPR spectra of: i) 25eq. B doped Pd/C heated to 200°C in N_2 for 1 h (Pd-^{int}B/C); ii) Pd-^{int}B/C oxidised in air at 250°C.

5.4.3 XPS

As observed from PXRD and TPO studies that oxygen has the propensity to phase segregate Pd-^{int}B/C and that the effect is more severe than under reducing conditions. This prompted us to study the catalyst state near the surface by XPS to observe whether the boron near the catalyst surface is in the oxidised state and any evidence of electronic effect arising from B on Pd. Fig. 5-12 and 5-13 shows the spectra from the Pd/C and Pd-^{int}B/C, respectively.

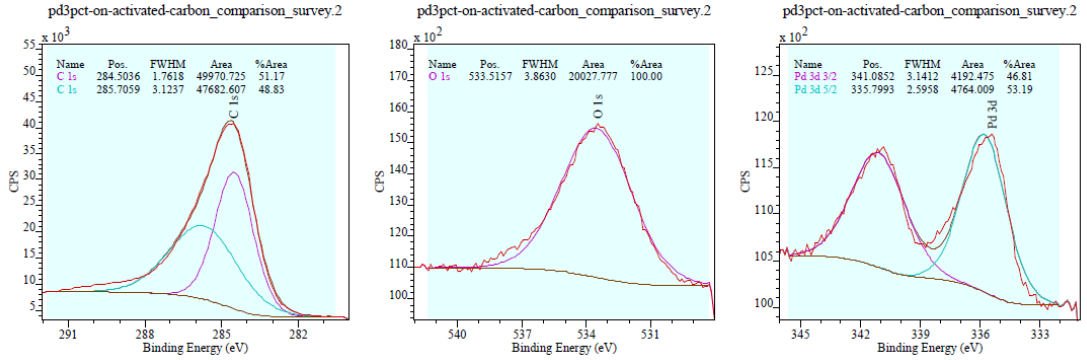

Fig. 5-12 XPS spectra for a Pd/C sample reduced at 500°C.

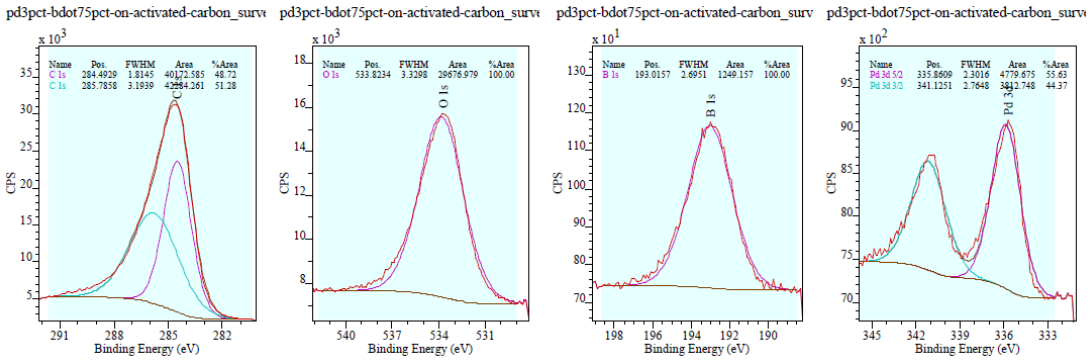

Fig. 5-13 XPS spectra for a 25eq. B Pd-^{int}B/C sample loaded at RT *via* an inert glove bag technique.

It was found the B 1s peak on the B containing sample is in the oxidised state (193.0 eV) and a B signal arising from B alloying with Pd at 188.8 eV was not detected.[28] However, based on the electro-negativity differences between Pd (2.20) and B (2.04), it was anticipated that the ^{int}B may be close to that of the oxidised B peak, since ^{int}B will be delta positive, thus shifting the binding energy towards B_2O_3. Note that repeated study had shown that this B signal remained in the oxidised region even when the sample was kept under reducing conditions during the sample preparation, before mounting the sample stage using an inert glove bag technique that was continuously flushed with N_2. This suggested that near surface ^{int}B could be highly sensitive towards oxygen in the surface, although ^{int}B in the Pd subsurface still remained stable in air at room temperature, as evidenced by PXRD. The fact that no B alloyed Pd peak was observed indicated that ^{int}B has a higher chemical potential

than those directly interacting with Pd.[28] There was more oxygen on the sample with B, which may indicate B is in its oxidised form (B_2O_3). A B/Pd ratio of 5.2 was observed is at variance from the theoretical maximum ratio at $Pd_{0.8}B_{0.2}$. This pointed out that XPS is very surface sensitive (to a few atoms on surface), as there may be more aggregated B on the surface and/or that more oxidised B could have been deposited on the active carbon. On the Pd $3d_{5/2}$ peaks, it was found both of the samples were slightly oxidised with the FWHM being smaller on the sample containing B, indicating Pd is less oxidised compared to B free sample. The sample remained slightly oxidised even when pre-reduced in H_2 followed by mounting under inert conditions. The binding energies of Pd $3d_{5/2}$ peaks on the two samples were similar, indicating no significant chemical shift can be discerned from XPS. Presumably, these inner core electrons might be less sensitive to any change in the nearby chemical environment. This assumption is quite reasonable based on the electro-negativity differences between Pd and B.[29] It is pointed out similar conclusion was observed in a study on Pd-B films.[28] Furthermore, the authors observed a slight change in line shape in the valence band spectra but position of the main peak remained unaltered. The authors concluded a weak interaction of B with Pd. However, electronic effect in the underlying ^{int}B under reducing catalytic conditions cannot be ruled out, as the same study reported a drastic change in selectivity to the *cis/trans* ratios on the gas phase hydrogenation of 1,3-butadiene.

5.4.4 ^{11}B SSNMR

^{11}B MAS SSNMR was studied in collaboration with JMTC on four Pd-^{int}B/C samples synthesised in order to observe any subsurface B species and as well as other states of B species that may arise under various conditions (Fig. 5-14). Unfortunately, the rather severe peak broadening had rendered it not possible to discern any various

states of B from different chemical environments. Peak broadening might arise from a distribution of chemical shifts and quadrupolar parameters. Nevertheless, the sample kept in an inert environment without heat treatment (RT inert) indicated at least two B species, those at 1.8 - 5.9 ppm and those at 16.2 ppm. It was thought that the heat treatment at 200°C may form B_2O_3 either in the presence or absence of air since oxygen was likely derived from the support. In contrast, for the RT inert sample, the extent of oxidation was mild which may have retained some B of lower oxidation state or interstitial B. The co-existence of various states of B on the samples may not be surprising as there could be B species on the active carbon, ^{int}B and B_xO_y that have been oxidised and deposited on the metal surface. Nevertheless, a T_1 relaxation experiment was studied on the Pd-^{int}B/C sample heated at 200°C in air (red). Heating in air will fully oxidise all the available subsurface B, as evidenced by PXRD studies. Remarkably, it was found that the τ_1 of B was at least 2 orders of magnitude faster than one measure on bulk B_2O_3 (3.962 ms and 500 ms for our sample and bulk B_2O_3[30], respectively). The much enhanced T_1 relaxation might be the higher magnetic field employed in our study or suggested a direct metal contribution from the Pd that provided the major relaxation tunnelling through the Knight Shift effect, a hyperfine coupling between the conduction electrons in the metal coupling with the B *sp*-states, causing the drastic reduction in spin-lattice relaxation observed. This therefore may indicate some electronic interaction of B and Pd.

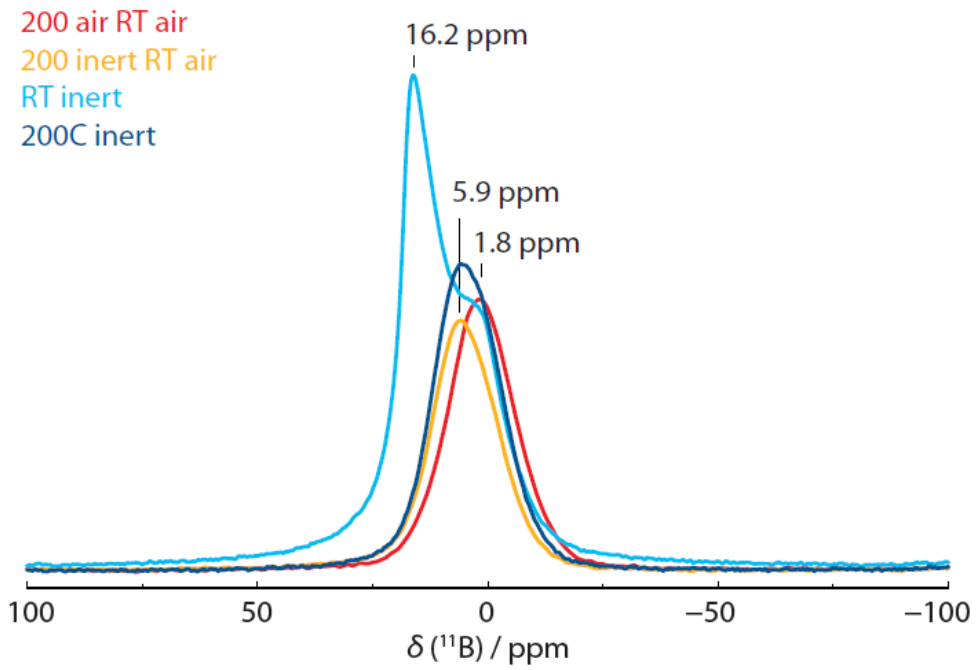

Fig. 5-14 Normalised ^{11}B solid-state MAS NMR spectra on a 25eq. BH_3.THF Pd-^{int}B/C followed by: i) heated to 200°C in air (red); ii) heated to 200°C in N_2 then exposed to air at room temperature (orange); iii) kept in inert conditions at room temperature (cyan); iv) heated to 200°C in N_2 then kept in inert conditions (blue).

5.4.5 BET

The textual parameters of Pd/C and Pd-^{int}B/C were examined by BET (Table 5-6). All samples exhibited a Type II adsorption isotherm with narrow hysteresis, a characteristic for all high surface area carbons that contains predominately micropores.[31] For Pd/C, much lower structural parameters was observed compared to that of the parental active carbon. Such decreases in apparent support area and pore volume were due to addition of metal deposited on the support surface and reduction step at 500°C was not beneficial to the support. On comparing Pd/C to that of Pd-^{int}B/C, further decrease in structural parameters was observed. This was likely due to occupation of partially oxidised B_xO_y species in the surface and blocking pore canals of the support. Furthermore, addition of BH_3.THF was previously shown to exfoliate the active carbon itself, as light hydrocarbon peaks was observed in TPR-MS.

Sample	S_{BET} (m^2 g^{-1})	Total pore volume, v_p (cm^3 g^{-1})
Active carbon	1270	1.189
3% Pd/C	611	0.688
3% Pd-^{int}B/C	222	0.400

Table 5-6 Textual properties of 3% Pd/C after reduction at 500°C and 3% Pd-^{int}B/C after addition of 25 eq. BH_3.THF.

5.4.6 CO CHEMISORPTION

The active metal surface area was evaluated using pulse CO chemisorption (Table 5-7). Irreversible CO chemisorption over the blank support did not occur, hence the measured CO chemisorption can be assigned to exposed areas of Pd catalysts. Differences can be seen between the two catalysts, in that the estimated Pd particle size increased after addition of BH_3.THF. This was assigned to the growth of Pd particles upon addition of the B source and a decrease in support surface area. Furthermore, it was observed that dissimilar particle size measurements were obtained from TEM and CO adsorption. This difference can be attributed to some active metal surface not accessible to molecular CO. For Pd/C, blocked surface sites may be ascribed to the relatively high temperature reduction process leading to some carbon support covering the Pd surface, as evidenced from a decrease in support surface area. In the case of Pd-^{int}B/C, additional size increase can be assigned to surface blockage of B_xO_y species that was otherwise not observed in TEM.

Catalyst	Dispersion, D_{CO} (%)	Metal surface area		Particle size		$Pd_{(s)}$ (Pd atoms $g^{-1}_{(cat)}$)
		(m^2 g^{-1}_{cat})	(m^2 g^{-1}_{Pd})	d_{CO} (nm)	d_{TEM} (nm)	
3% Pd/C	3.59	0.48	16.00	31	13(±5)	6.10×10^{18}
3% Pd-^{int}B/C	2.30	0.31	10.27	48	18(±10)	3.91×10^{18}

Table 5-7 Comparison of CO chemisorption and TEM characterisation of the prepared catalysts. Particle size measurement taken from CO chemisorption was estimated by applying the formula d = (1.12/D) nm and assuming a stoichiometric CO/Pd ratio.[32]

5.4.7 EXAFS

The nature of lattice distortion on the Pd caused by B was examined by EXAFS. The EXAFS data was collected at the Pd K edge, carried out by Dr. Crina Corbos of JMTC, is acknowledged. The data were fitted in k^3-space (Fig. 5-15), in the $2.5 < k < 16.0$ Å$^-$ k-space and the fit corresponded to the first coordination shell of an *fcc* lattice. The R-factor gives an indication of the quality of the fit in k-space, is defined as:

$$R = \sum_{i}^{N} \left(\frac{1}{\sigma_i}\right) \left(\left|\chi^{\text{exptl}}(k_i) - \chi^{\text{th}}(k_i)\right|\right) \text{x } 100\%$$

where N is the number of data points; $\chi^{exptl}(k)$ and $\chi^{th}(k)$ are the experimental and theoretical EXAFS; σ is defined as:

$$\frac{1}{\sigma_i} = \frac{k_i^n}{\sum_j^N k_j^n \left|\chi_j^{\text{exptl}}(k_j)\right|}$$

where n is a number chosen so the denominator term has an approximately constant amplitude over the data range. A good fit can be defined as having an R-factor of around 20%, while an R-factor of higher than 40% is also acceptable depending on

the level of noise.[33] The fit parameters are shown in Table 5-8. It can be seen that acceptable fits were obtained for both catalysts examined. According to the fitted data, B expands the lattice, as evidenced by the reduced amplitudes from the EXAFS oscillations (Fig. 5-15c). The degree of lattice expansion suggested B is occupied in the octahedral holes of Pd.[34] The structure of Pd remained as *fcc* structure and no formal Pd-B bond was observed, in agreement with other characterisation techniques such as PXRD and XPS. The interatomic distance increased upon addition of B in Pd. This result is in agreement with a previous study where Pd foil was homogenised with atomic B followed by rapid quenching to form Pd-B.[34] The coordination number apparently decreased on addition of B, albeit the lower value for Pd/C falls within the upper value for Pd-^{int}B/C. The amount of B in the sample determined from the lattice parameter was estimated at 11.3 at.%. This was less than the degree of B estimated by PXRD (20 at.%). The deviation could be due to the much higher sensitivities achieved from EXAFS compared to PXRD. Accordingly, the deviation as seen from EXAFS indicated B may not be fully incorporated into Pd to a maximum interstitial content of 20 at.%.

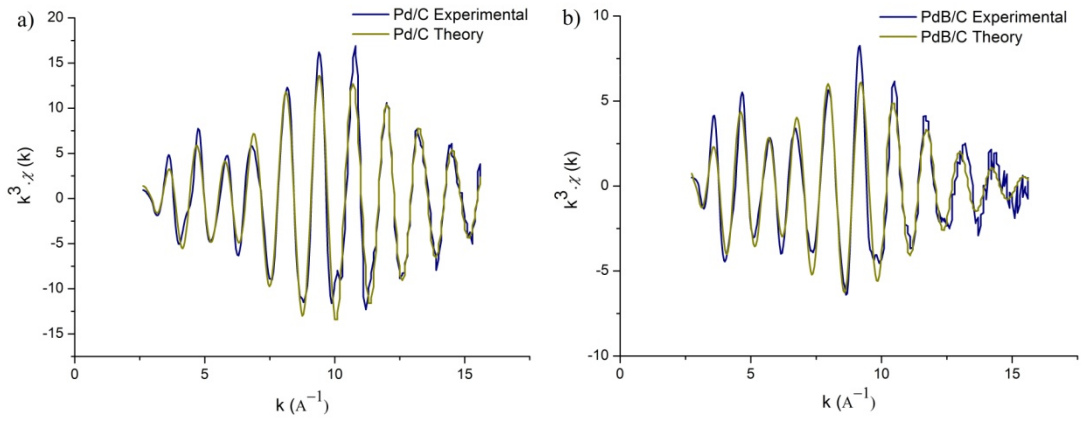

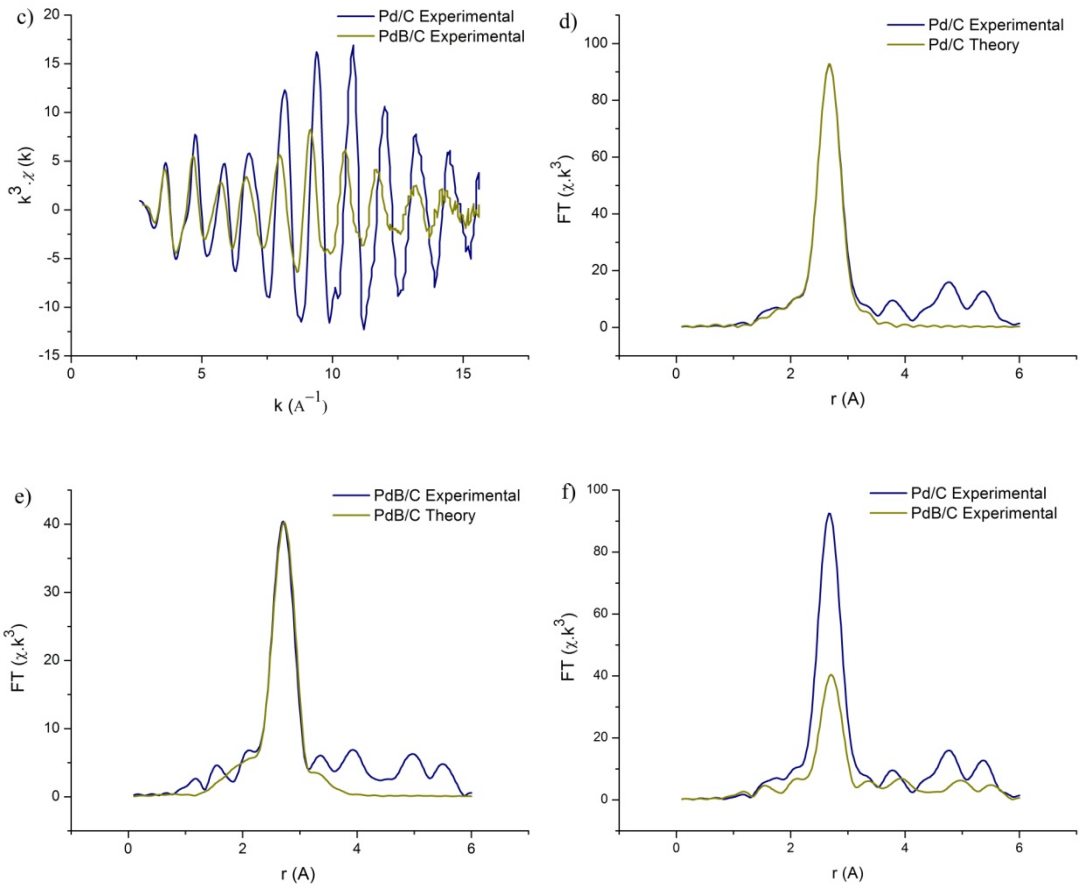

Fig. 5-15 EXAFS plots of: a) $k^3.\chi$ experimental and fitted data for 3% Pd/C; b) $k^3.\chi$ experimental and fitted data for 3% Pd-^{int}B/C; c) $k^3.\chi$ intensity comparison between experimental data for 3% Pd/C and 3% Pd-^{int}B/C; d) $k^3.\chi$ phase corrected Fourier transform of experimental and fitted data for 3% Pd/C; e) $k^3.\chi$ phase corrected Fourier transform of experimental and fitted data for 3% Pd-^{int}B/C; f) $k^3.\chi$ phase corrected Fourier transform intensity comparison between 3% Pd/C and 3% Pd-^{int}B/C. The heights of the first shell contributions have been equalised.

Catalyst	***CN*[a]**	***R* (Å)[b]**	**σ^2 (Å)[c]**	**ΔE_0 (eV)[d]**	**R-factor (%)**	**a_0 (Å)[e]**
3% Pd/C	10.4	2.732±0.002	0.012	0.9	24	3.864
3% Pd-^{int}B/C	9.3	2.789±0.004	0.020	2.2	33	3.944

Table 5-8 Comparison of derived EXAFS parameters with the prepared catalysts. [a] Coordination numbers (±10%). [b] Bond distance. [c] Debye-Waller factor (±0.001). [d] Inner potential correction (±0.6). [e] Lattice parameter, calculated using the formula 4*r/√2 where r is the Pd radius. The reference for coordination number and interatomic distance was set at 12 and 2.734±0.003 Å, respectively.

5.5 CATALYTIC TESTING

5.5.1 HYDROGENATION OF 4-OCTYNE

The catalysts in the presence and absence of B were examined in a range of alkyne hydrogenations reactions. Initially, the hydrogenation of 4-octyne was studied and comparisons were made with the classical Lindlar 5% $PdPb/CaCO_3$, BASF LF100 0.6% Pd/C and a JM 5% Pd/C catalyst (Scheme 5-1). The testings were performed in a three-neck round bottom flask with constant H_2 bubbling (30 $mL.min^{-1}$ in toluene at 50°C, 2000:1 ratio of substrate to metal, 800 rpm, *p*-xylene as internal standard). Fig. 5-16 showed plots of reactant/ products concentration as a function of time. It was observed that 4-octyne concentration decreases linearly with unit time thus confirming the zero order kinetics with respect to 4-octyne. In all cases, the initial selectivity towards *cis*-4-octene was near quantitative maintaining at a level between 94-96% after the full conversion of 4-octyne with the exception of conventional 5% Pd/C at 85%, thus demonstrates the selective nature of the prepared catalysts.

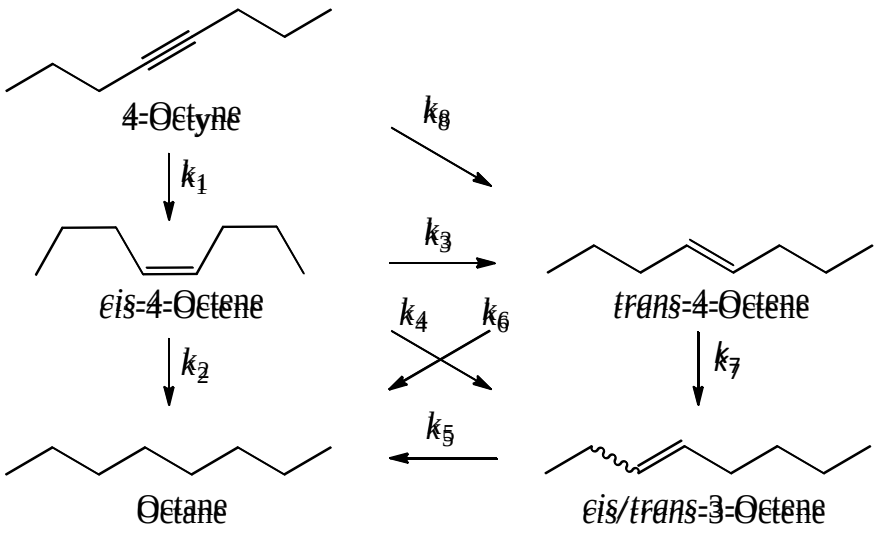

Scheme 5-1 Reaction pathways in the stereoselective hydrogenation of 4-octyne.

Pd-B (0)

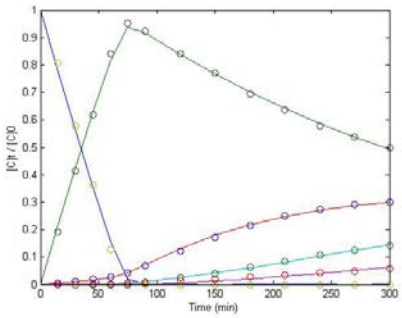

Pd-B (5)

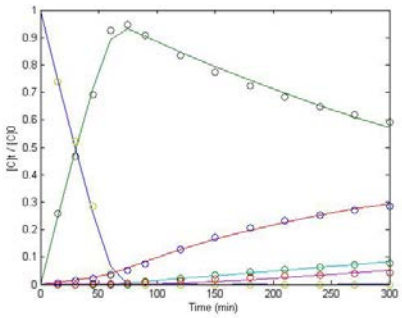

Pd-B (10)

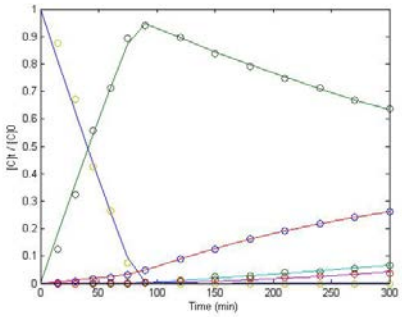

Pd-B (25)

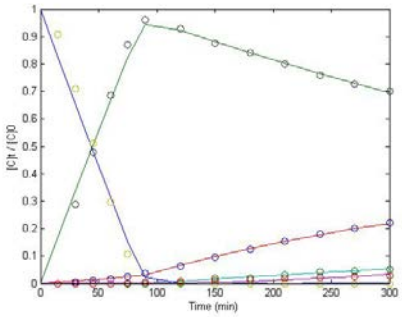

Pd-B (50)

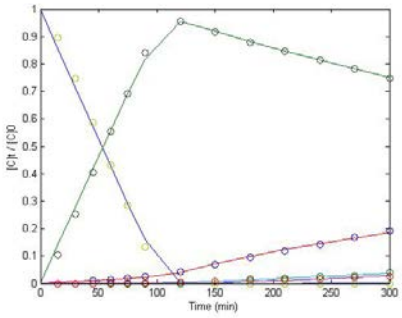

Pd-B(25)[O]200/C

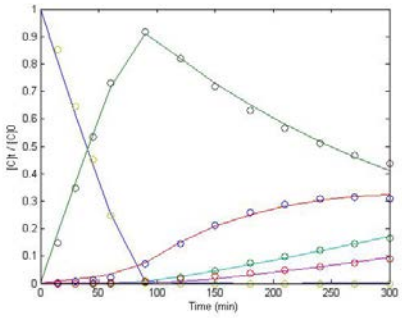

5% Pd/C

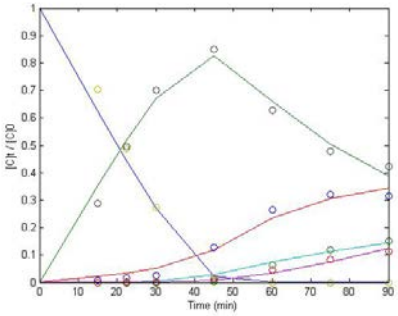

Lindlar's catalyst **LF100**

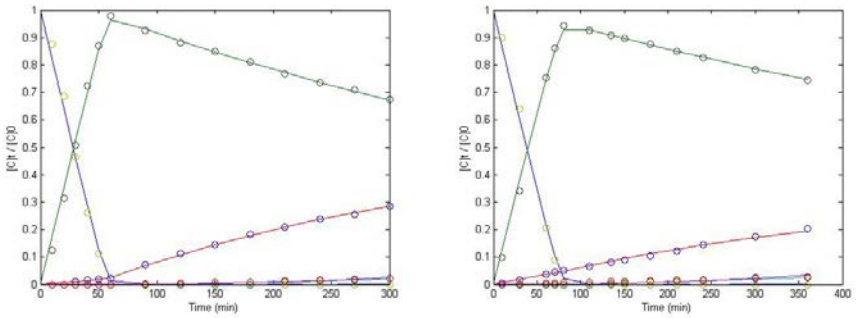

Fig. 5-16 Kinetic curves for hydrogenation of 4-octyne on various catalysts. The data points correspond to real data and the solid lines represent the fitted data by using the L-H relation.

The rates of hydrogenations and isomerisations were modelled according to Scheme 5-1 by using a Langmuir-Hinshelwood (L-H) model, as detailed in Chapter 4. The species were defined as follows: A = 4-octyne; B = *cis*-4-octene; C = *trans*-4-octene; D = 3-octene; E = Octane. K_i was defined as the adsorption constant of specie *i*, $P_{(i)}$ was the equilibrium concentration of specie *i* and θ_i was the probably of a surface site occupied by specie *i*. The defined equations used previously for the model fittings to the experimental data were excellent with good reproducibility, reinforcing the validity of our model (Fig. 5-16). Table 5-9 and 5-10 shows the result of the optimised kinetic model fittings. The initial unit from the optimised calculations was defined as per minute and this was then normalised against initial amount of substrate used per mol of catalyst per hour.

Dataset ($mol_{sub}.mol^{-1}_{cat}.h^{-1}$)	**Pd-B (0)**	**Pd-B (5)**	**Pd-B (10)**	**Pd-B (25)**	**Pd-B (50)**
k_1	1791	2100	1496	1374	1139
k_2	0	0	0	0	0
k_3	1350	1330	604	386	337
k_4	190	238	92	72	52

k_5	0	0	0	0	0
k_6	702	828	426	334	370
k_7	949	355	206	93	80
k_8	39	65	47	36	27
∑semi/∑iso	0.74(±0.18)	1.13(±0.36)	1.71(±0.18)	2.56(±0.18)	2.49(±0.17)
∑semi/∑full	2.61(±0.62)	2.62(±0.80)	3.63(±0.38)	4.22(±0.28)	3.15(±0.21)

Table. 5-9 Kinetic model derived TOFs for all the possible rate processes in the hydrogenation of 4-octyne using Pd-^{int}B/C. Number in the bracket corresponds to the number of moles of BH_3.THF solution used in the preparation. The error calculated on the two normalised parameters, ∑semi/∑iso and ∑semi/∑full, is based on various fittings using different ratios of adsorption constants.

Dataset ($mol_{sub}.mol^{-1}_{cat}.h^{-1}$)	**5% Pd/C**	**Pd-B(25) [O]200/C**	**Lindlar 5% PdPb/$CaCO_3$**	**BASF LF100 0.6% Pd/C**
k_1	3005	1525	2177	1584
k_2	0	0	0	0
k_3	9406	1444	558	341
k_4	3228	168	0	24
k_5	0	0	0	0
k_6	7311	766	207	378
k_7	0	923	167	138
k_8	158	60	40	73
∑semi/∑iso	0.25(±0.08)	0.62(±0.10)	3.06(±0.32)	3.30(±0.46)
∑semi/∑full	0.43(±0.14)	2.07(±0.33)	10.73(±1.13)	4.38(±0.59)

Table. 5-10 Kinetic model derived TOFs for all the possible rate processes in the hydrogenation of 4-octyne using standard 5% Pd/C, Lindlar's 5% PdPb/$CaCO_3$ and LF100 0.6% Pd/C. The error calculated on the two normalised parameters, ∑semi/∑iso and ∑semi/∑full, is based on various fittings using different ratios of adsorption constants.

The adsorption constant of alkyne was found to be at least one or two magnitudes higher than the corresponding alkenes followed by the alkane.[35] This observation is consistent the fact that the alkyne has a much higher adsorption

strength than alkenes which the incoming alkyne displaces until nearly all alkyne species are depleted; only then can the alkene isomerisation or hydrogenation processes takes place. According to Table 5-9 and 5-10 the main undesirable pathway in obtaining high *cis*-selectivity was its isomerisation to *trans*-4-octene, followed by the double bond (db) shifted isomerisation of 4-octene to 3-octene. It can be seen the standard 5% Pd/C had the highest activity but the lowest selectivity. This could be due to the catalyst having very small particle sizes and thus increases the overall adsorption strength of all unsaturated species, leading to excessive isomerisations and over-hydrogenations. Two parameters were defined by using the semi-hydrogenation pathway ($\sum k_{semi}$ or $\sum k_{1,8}$) normalised against: i) sum of isomerisations ($\sum k_{iso}$ or $\sum k_{3,4,7}$); 2) the sum of over-hydrogenations ($\sum k_{full}$ or $\sum k_{2,5,6}$). The rate ratios may give an indication on how the catalyst minimises these undesirable processes such as isomerisations and over-hydrogenations and therefore can be used as an indicator for a more selective catalyst. It was found that the Pd-B(25) increases these two parameters towards the very selective Lindlar's catalyst, as did BASF's selective hydrogenation catalyst LF100, a 0.6% Pd/C (Table 5-10). The higher errors in $\sum_{semi}/\sum_{full}$ ratio for the Lindlar catalyst was due to measuring very low concentrations of octane. On comparing these parameters, it is remarkable to observe at least one order of magnitude reduction on the undesirable isomerisations and over-hydrogenations were observed for Pd-B(25) compared with 5% Pd/C, while only 3 and 6 times reduction on these two processes were observed when comparing unmodified Pd-B(0) with 5% Pd/C. The slight enhanced selectivity is probably due to the bigger particle size leading to overall reduction in adsorption strength on all unsaturated compounds.

5.5.2 HYDROGENATION OF 3-HEXYN-1-OL

Stereoselective hydrogenation of the polar alkyne 3-hexyn-1-ol was investigated on three different catalysts: i) non-doped 3% Pd/C i) B doped 3% Pd-^{int}B/C; iii) Lindlar 5% PdPb/$CaCO_3$ catalyst (Scheme 5-2). This reaction was performed in a 100 mL Parr autoclave (conditions: 0.5 M 3-hexyn-1-ol, 3 bar H_2, 30°C, 400 rpm, 1,4-dioxane as internal standard)

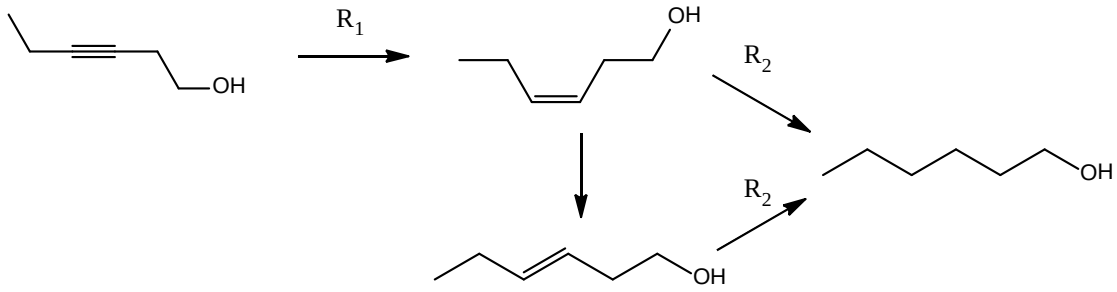

Scheme 5-2 Hydrogenation reaction of 3-hexyn-1-ol.

Selective hydrogenation to *cis*-hexen-1-ol (CHEL) has importance in the fragrance industry towards the manufacturing of leaf fragrance alcohols.[36] The reaction progress was monitored by measuring the H_2 uptake against time (Fig. 5-17). An aliquot was isolated at the theoretical maximum point when the reaction reached the semi-hydrogenation uptake point (1 mole of H_2 uptake with respect to the substrate) as well as at the end of the reaction. It was found all catalysts had good activity, reaching the semi-hydrogenation point between 20-30 mins. Initial hydrogenation activities for the first 5 mins for 3% Pd/C, 3% Pd-^{int}B/C and Lindlar's catalyst were determined at 16.5, 14.0 and 10.6 $mL_{H2}.mol_{cat}.s^{-1}$, respectively. An induction period was observed at the initial stages of H_2 uptake for the Lindlar catalyst, as characterised by the curve having a slight parabolic shape, suggesting the catalyst was in the oxidised state.[37]

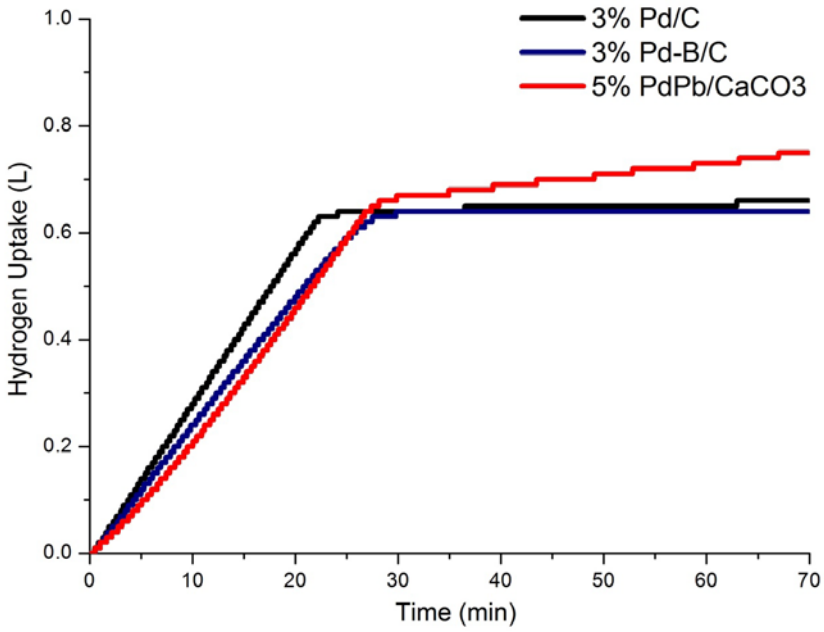

Fig. 5-17 Hydrogen uptake curves in the hydrogenation of 3-hexyn-1-ol for: i) non B doped 3% Pd/C (black); ii) 25eq. BH_3.THF doped Pd-^{int}B/C (blue); iii) Lindlar's catalyst (red). Conditions: 30 mmol 1,4-dioxane and 3-hexyn-1-ol, 0.028 mmol catalyst, EtOH, 3 bar H_2, 30°C, 400 rpm.

The rate ratio R_1 over R_2 (of which rate values correspond to before and after 1 mole of H_2 uptake) were measured and this gave an indication of the reaction selectivity (Table 5-11).[37] The final part of R_1 for the Lindlar's catalyst was measured because of the initial state of the catalyst was oxidised, which gave an initial parabolic rate. It was not possible to measure the rate ratio for 3% Pd-^{int}B/C, as no H_2 uptake was observed in the R_2 region, indicating the very selective nature of the catalyst.

Catalyst	Conv (%)	R_1 / R_2	Selectivity (%)				*cis* / *trans*	*ene* / *ane*
			THEL	CHEL	HAL	Unk		
3% Pd-^{int}B/C[a]	97	-	1.8	98.0	0.0	0.2	53.5	-
3% Pd-^{int}B/C[b]	100		3.8	95.6	0.0	0.7	25.4	-
3% Pd/C[a]	96	38.4	2.2	92.2	0.0	5.6	42.2	-
3% Pd/C[b]	100		8.1	74.3	7.4	10.2	9.1	11.2
Lindlar 5% PdPb/$CaCO_3$[a]	98	9.0	3.1	92.1	0.0	4.8	29.9	-
Lindlar 5% PdPb/$CaCO_3$[b]	100		30.6	43.9	19.0	6.5	1.4	3.9

Table 5-11 GC analysis for the hydrogenation of 3-hexyn-1-ol. [a] Sample analysis collected before the change in hydrogen uptake. [b] Sample collected at the end of hydrogen uptake. THEL = *trans*-hexen1-ol. CHEL = *cis*-hexen-1-ol. HAL = 1-hexanol.

According to the GC analysis, it was found all catalysts were highly selective towards CHEL (>92%) at the end of R_1, with 3% Pd-^{int}B/C being the most selective (98%). This can also be characterised by the very high *cis*/*trans* ratio observed for these catalysts. The ene/ane was not measured due to no alkane being observed at this point. At the end of the reaction, both the 3% Pd/C and Lindlar's catalyst suffered from rapid isomerisation to *trans*-hexen-1-ol (THEL) and over-hydrogenation to hexanol (HAL). However the 3% Pd-^{int}B/C, maintained impressive selectivity of CHEL at over 95% with a high *cis*/*trans* ratio. More importantly, no over-hydrogenation was observed. A longer residence time in the reactor after R_1 allowed for further isomerisation to take place, as in previous experiment with 4-octyne. Therefore, the data suggests the Pd-^{int}B catalyst gave much reduced isomerisation rate than 3% Pd/C, with the Lindlar catalyst the highest isomerisation rates. This result is in steep contrast to the rate ratios in the 4-octyne hydrogenation above. An increase in isomerisation rates could be attributed to the hydrophilic nature of the $CaCO_3$ support in combination with the hydrophilic substrate, giving a longer residence time for

CHEL to undergo isomerisation to THEL. The non-modified Pd/C, on the other hand, possesses intermediate degree of adsorption, whereas the Pd-^{int}B/C (non-hydrophilic) greatly reduced the residence time for substrate adsorption (weaker adsorption) and hence lower isomerisation rates. This demonstrates the B-modified catalyst indeed had a dramatically beneficial effect of ultraselectivity in the stereoselective hydrogenation towards of 3-hexyn-1-ol.

B-modification was also investigated using a JM 5% Pd/C and doped with 25 eq. of BH_3.THF (Fig. 5-18, blue). It was of interest to observe the effect of B modification on smaller particle sized catalyst (The average Pd crystallite size was estimated at ~5 nm as characterised by PXRD). Although the B doped catalyst did indeed modify the catalyst, it suffered rapid hydrogen uptake beyond the maximum theoretical half uptake, indicating its consecutive hydrogenation of alkene to alkane. This was evidenced as only 59% selective to CHEL at 20 min for catalyst 5% Pd-^{int}B/C and only 1% of CHEL remained at 70 min. This illustrates the importance of the aforementioned particle size effect outweighing the modification by B. Note that the smaller the particle size, the fewer the subsurface sites are available as well as overall higher activation energy needed for its occupation.

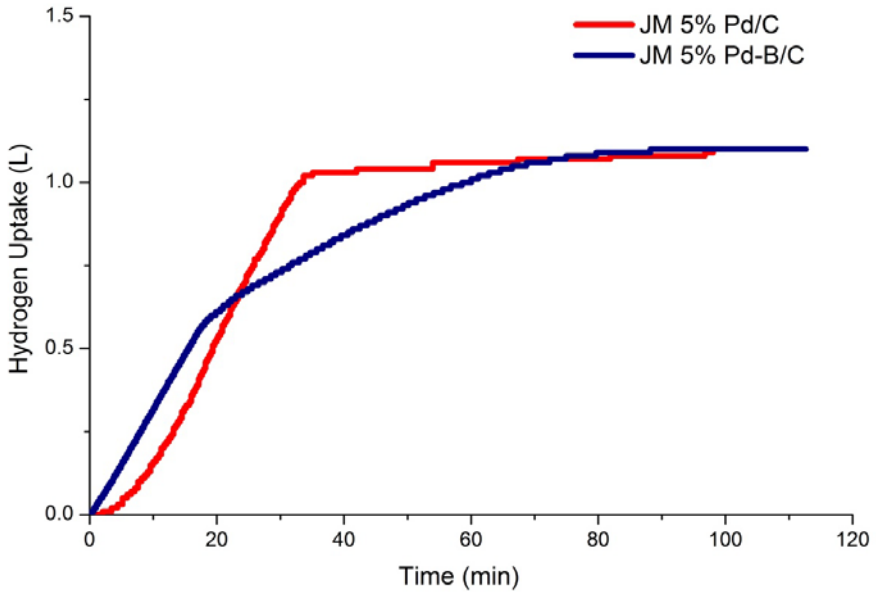

Fig. 5-18 Hydrogen uptake curves in the hydrogenation of 3-hexyn-1-ol for: i) JM 5% Pd/C (red); ii) JM 5% Pd/C modified with 25 eq. BH_3.THF (blue). Conditions: 30 mmol 1,4-dioxane and 3-hexyn-1-ol, 0.028 mmol catalyst, EtOH, 3 bar H_2, 30°C, 400 rpm.

5.5.3 HYDROGENATION OF OTHER ALKYNES

Hydrogenation of internal alkynes diphenylacetylene (DPA) and 2,-butyne-1,4-diol (B_3D) were also examined using 3% Pd-^{int}B/C and Lindlar's catalyst to explore the general utility of the B modified catalyst (Fig. 5-19). The reaction progress was again followed by monitoring the H_2 uptake (Fig. 5-20, conditions: HEL ChemSCAN, 3 bar H_2, 30°C, 2.50 μmol catalyst, 0.5 M alkyne in 5 mL EtOH, 1200 rpm, 1000:1 substrate to metal ratio). The rate difference between H_2 uptakes before/after 1 mole of H_2 consumption (~65 mL of H_2 in this case) gave an indication of semi-hydrogenation selectivity to the alkene, as aforementioned. Lindlar catalyst exhibited higher initial activities for both alkyne hydrogenations compared to 3%Pd-^{int}B/C. However, no selectivity of towards 2-butene-1,4-diol (B_2D) was observed, as indicated by its hydrogenation straight to the alkane (R_1/R_2 near unity). Although some degree of selectivity was observed towards stilbene (R_1/R_2 not determined due

to the parabolic nature of R_2). For 3% Pd-^{int}B/C catalyst, there was little selectivity towards B_3D hydrogenation. The selectivity difference between B_3D and 3-hexyn-1-ol may indicate stronger adsorption of the diol. Interestingly, relatively high selectivity was observed in its hydrogenation of DPA to stilbene. Selectivity difference arising from two different substrates may originate from a steric effect evidenced for DPA hydrogenation. The 3% Pd-^{int}B/C may have islands of adsorbed B_xO_y, which may break up the ensemble size of Pd active sites[38], thus the adsorption of bulky substrate is more hindered.

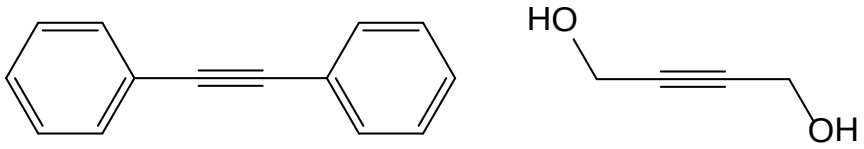

Diphenylacetylene 2-butyne-1, 4-diol

Fig. 5-19 Chemical structures of diphenylacetylene (DPA) and 2-butyne-1,4-diol (B_3D).

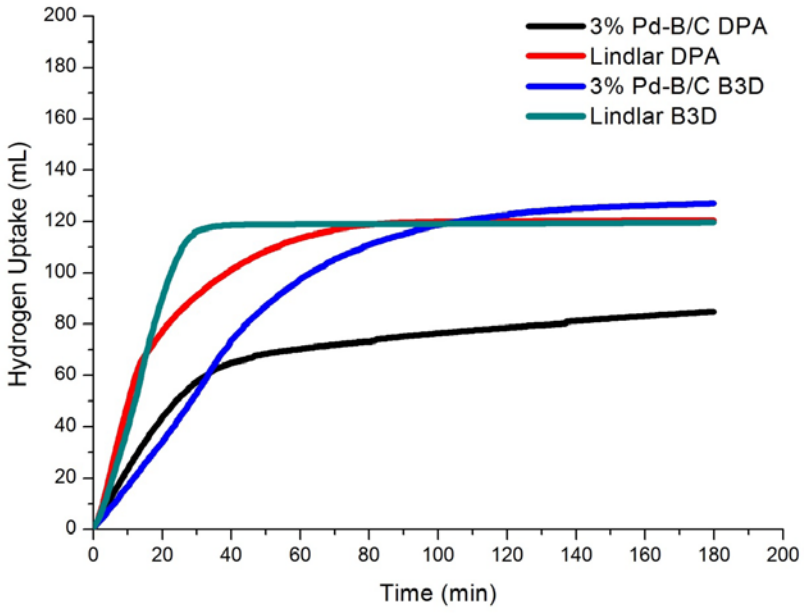

Fig. 5-20 Hydrogen uptake curves for: i) DPA hydrogenation using Pd-^{int}B/C catalyst (black); ii) DPA hydrogenation using Lindlar's catalyst (red); iii) B_3D hydrogenation using Pd-^{int}B/C catalyst (blue); iv) B_3D hydrogenation using Lindlar's catalyst (cyan). Conditions: 2.50 mmol alkyne, 2.50 μmol catalyst, EtOH, 3 bar H_2, 30°C, 1200 rpm.

Hydrogenation using the same catalysts was also examined on terminal alkynes phenylacetylene (PA) and 2-methyl-3-butyn-2-ol (MBY) (Fig. 5-21). For MBY hydrogenation, no selectivity difference was observed between the catalysts (Fig. 5-22). Higher selectivity in PA hydrogenation was observed for 3% Pd-^{int}B/C compared to Lindlar catalyst but less than DPA hydrogenation. This is not surprising as terminal alkynes are in general more difficult to hydrogenate to its unsaturated counterparts due to their stronger adsorption on the metal surface.[39] The higher selectivity of 3% Pd-^{int}B/C may also be due to the aforementioned ensemble effect.

Phen$_y$lacet$_y$lene 2-meth$_y$l-3-but$_y$n-2-ol

Fig. 5-21 Chemical structures of phenylacetylene (PA) and 2-methyl-3-butyn-2-ol (MBY).

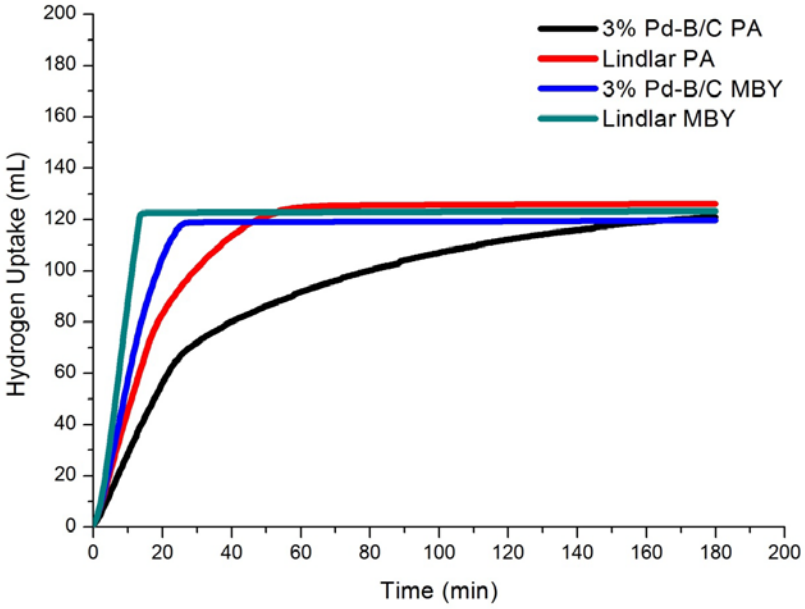

Fig. 5-22 Hydrogen uptake curves for: i) PA hydrogenation using Pd-^{int}B/C catalyst (black); ii) PA hydrogenation using Lindlar's catalyst (red); iii) MBY hydrogenation using Pd-^{int}B/C catalyst (blue); iv) MBY hydrogenation using Lindlar's catalyst (cyan). Conditions: 2.50 mmol alkyne, 2.50 μmol catalyst, EtOH, 3 bar H_2, 30°C, 1200 rpm.

5.5.4 HYDROGENATION OF ORTHO-CHLORONITROBENZENE

The selective hydrogenation of chloro-nitrobenzene (CNB) to the corresponding chloroaniline (CAN) without hydrodechlorination is important in the application of dyes, drugs, herbicides and pesticides.[40] Extensive studies in the literature have focused on using Pt based catalysts to achieve high CNB hydrogenation whilst maintaining low rates of hydrodechlorination.[41-43] Meanwhile, studies using Pd based catalyst generally offered rather low selectivity due to aryl chloride bond cleavage.[44-46] It is therefore advantageous to use Pd instead of Pt mainly due to the lower costs of the former. Recently, studies have been devoted on maximising CAN selectivity either by alloying[47], additives[48], metal support[40], to name but a few. Based on the success of 3% Pd-^{int}B/C catalyst in the alkyne hydrogenations, the versatility of this new class of catalyst was investigated in the hydrogenation of *o*-CNB (Scheme 5-3). Thus, selective hydrogenation of ortho-chloronitrobenzene (*o*-CNB) was examined on JM 5% Pd/C, unmodified B 3% Pd/C and 3% Pd-^{int}B/C catalysts (condition: HEL ChemSCAN, 3 bar H_2, 50°C, 0.5 M *o*-CNB, 3.80 μmol catalyst, 1200 rpm, 670:1 of substrate to metal ratio, octane as internal standard).

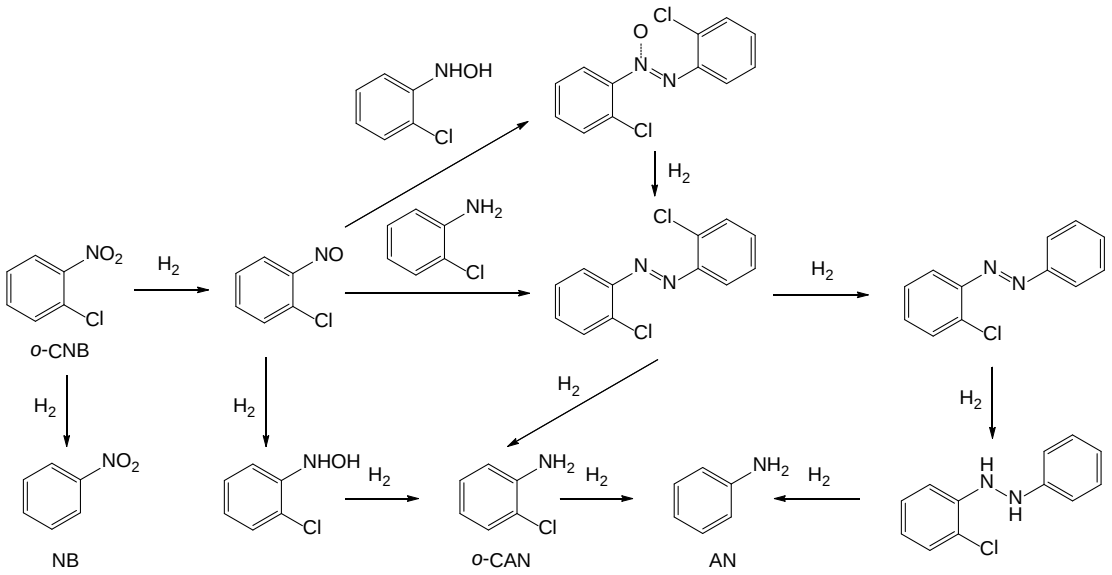

Scheme 5-3 Accepted reaction pathways for the hydrogenation of *o*-CNB.

Fig. 5-23 shows the H_2 uptake curves for those catalysts tested. Initial activities for the first 5 min of uptake for catalysts JM 5% Pd/C, 3% Pd/C and 3% Pd-^{int}B/C catalysts were 37.9, 32.5, and 15.3 $mL_{H2}.mmol_{cat}.s^{-1}$, respectively. The fact that the highest activity was observed for JM 5% Pd/C is not surprising probably due to the smaller particle sizes compared to the 3% Pd/C catalysts. The initial activity for 3% Pd-^{int}B/C was approximately two times lower than that of the unmodified catalyst.

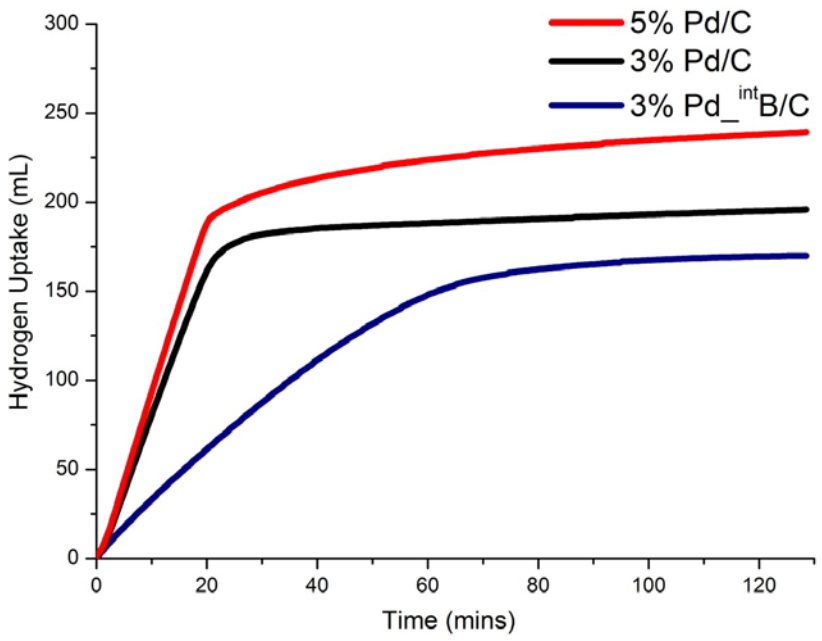

Fig. 5-23 Hydrogen uptake curves for hydrogenation of *o*-CNB on: i) JM 5% Pd/C (red); ii) non B doped 3% Pd/C (black); iii) 3% Pd-^{int}B/C (blue). Conditions: HEL ChemSCAN, 2.46 mmol octane and o-CNB, 3.80 μmol catalysts, EtOH, 3 bar H_2, 50°C, 1200 rpm.

Table 5-12 shows the GC analysis of hydrogenation of *o*-CNB at the end of the reaction and at the rate change in H_2 uptake (Approx. 190, 170 and 155 mL H_2 uptake for JM 5% Pd/C, unmodified B 3% Pd/C and 3% Pd-^{int}B/C, respectively). On comparing the unmodified 3% Pd/C and 3% Pd-^{int}B/C, it was clear that the B modified sample outperforms the latter in terms of selectivity to *o*-CAN with a selectivity enhancement of 14% at the uptake plateau. This increased to 27% difference in selectivity at the end of reaction. The conventional JM 5% Pd/C, however, suffered from excessive hydrodechlorination as evidenced by aniline (AN) being isolated as the main by-product. Further analysis at the end of the reaction led to almost no selectivity to *o*-CAN, also accompanied by formation of higher boiling peaks could be related to the formation of diazo products. On the other hand, no formation of such higher boiling by-products was observed for the B modified sample. This clearly demonstrates the B modified catalyst has the ability to suppress

the hydrodechlorination pathway. This remarkable result suggests Pd-^{int}B/C catalyst can be an alternative for Pt based catalysts in the chemoselective hydrogenation of *o*-CNB to *o*-CAN.

Catalyst	Selectivity (%)			
	Aniline	**Nitrobenzene**	**2-Cl-An**	**Unk**
3% Pd-^{int}B/C[a]	2.4	0.9	95.4	1.3
3% Pd-^{int}B/C[b]	6.9	0.2	92.5	0.3
3% Pd/C[a]	18.1	0.2	81.3	0.3
3% Pd/C[b]	31.7	0.3	66.3	1.8
JM 5% Pd/C[a]	53.3	0.2	42.8	3.8
JM 5% Pd/C[b]	80.8	0.1	1.8	17.3

Table 5-12 Hydrogenation of *o*-CNB. [a] Sample analysis collected before the change in hydrogen uptake. [b] Sample collected at the end of hydrogen uptake. All samples collected were at 100% conversion of *o*-CNB.

The effect of subsurface B modification was also examined on a standard JM 5% Pd/C and compared to one modified with 25 eq. of BH_3.THF (Fig. 5-24). This is similar to the case in the hydrogenation of 3-hexyn-1-ol to compare particle size effect and B. Again, modification by B was observed in this case, as evidenced by a lower overall hydrogen uptake compared to the non-modified catalyst. Although differences can be seen in their selectivities at the end of the reaction (Table 5-13), however, aniline was observed as the major product. This suggests more facile dechlorination pathway as compared to the hydrogenation of the nitro group. Severe dechlorination observed for both catalysts suggest the importance of the particle size effect. The smaller the particle size, the higher ratios of lower coordinated sites such as corners and edges compared to surface plane sites. These low coordinated sites could be accountable for the rapid dechlorination. The change in particle size effecting product selectivity is classified as a 'structure-sensitive' reaction, as

observed here. It is well known that corner/edge sites catalyse Suzuki-Miyaura coupling, which involves the activation of a C-X bond (X = Cl, Br, I).[24, 49, 50] The ease of breaking the C-Cl bond in this reaction could be related to these unselective sites.

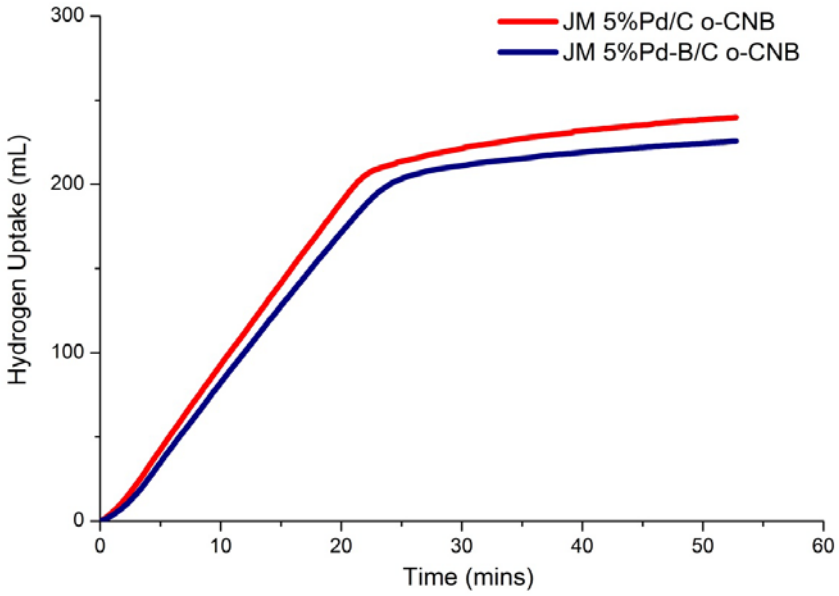

Fig. 5-24 Hydrogen uptake curves for hydrogenation of *o*-CNB on: i) JM 5% Pd/C (red); ii) 25 eq. B doped 5% Pd-^{int}B/C (blue). Conditions: HEL ChemSCAN, 2.46 mmol octane and *o*-CNB, 3.80 μmol catalysts, EtOH, 3 bar H_2, 50°C, 1200 rpm.

Catalyst	Selectivity (%)			
	Aniline	Nitrobenzene	2-Cl-An	Unk
JM 5% Pd/C	82.7	0	8.5	8.7
JM 5% Pd-^{int}B/C	67.3	0	29.2	3.5

Table 5-13 Hydrogenation of *o*-CNB. Samples collected at the end of hydrogen uptake. All samples collected were after 100% conversion of *o*-CNB.

5.5.5 HYDROGENATION OF OTHER ISOMERS OF CHLORONITROBENZENE

Hydrogenation on the isomers of CNB (*o*-, *m*-, *p*-) were also evaluated for non-doped 3% Pd/C and one doped with 25 eq. of BH_3.THF (Fig. 5-25). GC

selectivity results were measured at the end of the reaction (Table 5-14). As expected, rates of all B modified catalysts were lower compared to their non modified counterparts (with 19%, 14% and 27% difference in rates for *o*-, *m*-, *p*-CNB, respectively). Difference in rates was attributed to the reduced metal area after B modification and electronic effects of subsurface B on weakening overall substrate adsorption. Similar to the results as described earlier, all modified catalysts exhibited higher selectivities, also characterised by their reduced total hydrogen uptake. On comparison to the desired chloro-anilines (Cl-An), similar selectivities were observed for the *o*- and *p*-Cl-An. However, on the other hand, decreased in selectivity towards *m*-Cl-An was observed. Similar reduced selectivity for the *meta* system had been documented in the literature.[51] The decrease is related to the activated C-Cl bond in conjugation with the more electron withdrawing nitro group. Decrease in electron density around the C-Cl bond will favour its dissociation, hence decrease in the selectivity to *m*-Cl-An.

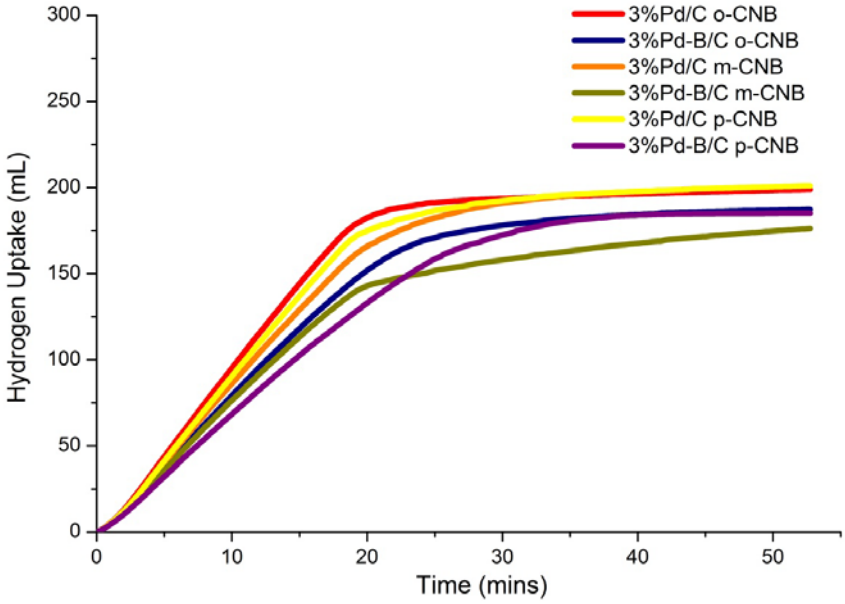

Fig. 5-25 Comparative hydrogen uptake curves for hydrogenation of *o*-, *m*- and *p*- CNB on: i) 3% Pd/C (red, orange and yellow, respectively); ii) 25 eq. B doped 3% Pd-^{int}B/C (blue, gold and purple, respectively). Conditions: HEL ChemSCAN, 2.46 mmol octane and CNB, 3.80 μmol catalysts, EtOH, 3 bar H_2, 50°C, 1200 rpm.

Catalyst	Rate[a] (mL/min)	Selectivity (%)				
		Aniline	2-Cl-An	3-Cl-An	4-Cl-An	Unk
3% Pd/C[b]	9.9	22.1	55.9	-	-	22
3% Pd-^{int}B/C[b]	8.0	6.9	92.5	-	-	0.3
3% Pd/C[c]	8.9	30.2	-	66.6	-	3.2
3% Pd-^{int}B/C[c]	7.6	15	-	81.7	-	3.3
3% Pd/C[d]	9.5	29.2	-	-	69.5	1.3
3% Pd-^{int}B/C[d]	7.0	7.9	-	-	90.6	1.5

Table 5-14 Hydrogenations of non B doped catalysts and 25eq. B doped catalysts in: [b] *o*-CNB; [c] *m*-CNB; [d] *p*-CNB. [a] Rates were determined at time between 3 to 18 mins on the hydrogen uptake curve (Fig. 5-25). All samples were analysed at the end of hydrogen uptake at full conversion of their respective CNB.

5.6 DISCUSSION

5.6.1 HYDROGENATION REACTIONS

It is apparent from the catalytic testing that the subsurface modification with B has a dramatic enhancement in a number of chemoselective transformations. On comparison with the B doped samples in the hydrogenation of 4-octyne (Fig. 5-16), it was observed that increasing addition of equimolar amounts of B had a positive effect on reaction selectivity. This was characterised by the increase in both the $\sum_{semi}/\sum_{iso}$ and $\sum_{semi}/\sum_{full}$ ratios as experimental indicators for a more selective catalyst (Table 5-9). At the same time a steady decrease in rate of semi-hydrogenation (k_1) was observed. For example, on comparing the Pd-B (25) sample with the non-modified Pd-B (0), there was a 23% decrease in the rate k_1 but more than 3 times increase in the $\sum_{semi}/\sum_{iso}$ ratio. The decrease in rate k_1 can be related to:

i) Increasing amounts of B adspecies being deposited on the catalyst surface.

ii) Surface modification effect of Pd catalysts as suggested in a theoretical study on selective hydrogenation of acetylene.[52]

Accordingly, the modification by interstitial B could potentially weaken the average adsorption energies of alkyne and alkene species[53], which can lead to increase in hydrogenation selectivity at the expense of activity as demonstrated in this study.

Interestingly, when comparing the Pd-B (25) and the Pd-B (50) sample, there was 17% decrease in k_1 but no significant difference was observed in the $\sum_{semi}/\sum_{iso}$ ratio (1.02) of was observed. Pd-B(50) sample may have more surface B adspecies on the metal surface, which can explain the decrease in k_1. However, the lack of difference in $\sum_{semi}/\sum_{iso}$ and $\sum_{semi}/\sum_{full}$ ratios between these two catalysts suggests that increased B adspecies site blockage does not appear to reduce the rates of overall

isomerisation processes on the assumption of near saturation of interstitial B populations due to the high molar ratio of BH_3.THF employed for these catalysts. Reduction of isomerisation processes is related to the increasing rates of desorption for alkene species.[39] This implies that the reactivity of surface B may intrinsically be different compared to its subsurface counterparts: Surface B appears only to reduce the overall hydrogenation processes by an ensemble effect of B_xO_y islands, leading to its apparent decrease in activity and increase in selectivity. Earlier study by Krawczyk *et. al*. reported the effect of *surface* B adspecies (borides and borates) on modifying reaction activity/selectivity in the hydrogenation of alkynes.[38] They observed high alkene selectivity by a B adspecies modified catalyst operating through a geometric (ensemble) blockage mechanism. The authors also performed TDS on H_2, ethyne, ethene with the catalyst modified with B adspecies.[29] They found preadsorbed B adspecies had suppressed the surface adsorption of ethyne and ethene but found no shift in their binding energies and so concluded that no electronic effect was observed. On the contrary, *subsurface* B can play a role on intrinsically modifying the electronic properties of surface Pd by increasing desorption rates of alkene, either by an electronic effect from B to Pd or a geometric effect by an expansion of the metal lattice, as evidenced by the change on ratio $\sum_{semi}/\sum_{iso}$ upon increasing dosage of BH_3.THF. Similar results were observed by Tamaki *et. al.* on hydrogenation of 1,3-butadiene using sputtered Pd-B films.[28] The authors observed a change in *trans/cis* ratio population and this change was presumed to be an enhanced electron density exerted from B to Pd. Significant differences in reactivity between surface and subsurface bound species have been known to have a dramatic effect on reaction pathways in the literature. For example, Teschner *et. al.* found formation of subsurface carbon or hydrogen species in Pd is highly dependent upon chemical

composition and pressure. They observed by increasing partial pressure of hydrogen to alkynes can influence the selectivity to the alkene, with an increase in H_2 partial pressure favouring formation of Pd-β-H phase; the reactive hydride is responsible for the propensity of full hydrogenation to the alkane. Bao *et. al.* studied the interaction of silver with oxygen using X-ray photoelectron spectroscopy (XPS), ultraviolet photoelectron spectroscopy (UPS) and ion scattering spectroscopy (ISS). They found oxygen inside the uppermost layer of silver is more strongly bound and interacts differently compared to atomic oxygen adsorbed on the surface.[54] Sachtler *et. al* reviewed the mechanism of ethylene epoxidation, the authors noted the importance of subsurface oxide species relevant to realise partial oxidation, whereas oxygen preadsorbed on the surface lead to complete oxidation to CO_2.[55] In the case of hydrogenation of 3-hexyn-1-ol, it was observed that selectivity to *cis*-hexen-1-ol was enhanced upon addition of B compared to JM 5% Pd/C and the unmodified 3% Pd/C catalyst. The same principles can also be applied in this case.

On the hydrogenation of *o*-CNB, selectivity was much enhanced after addition of BH_3.THF, characterised by the decrease in hydrodechlorination and therefore minimising the desirable formation of AN and other higher boiling products (Table 5-12). At the same time a decrease in activity was observed likely due to the increased particle size but also geometric blockage of B_xO_y adspecies, decreasing the number of Pd active sites. The observation of increased reaction selectivity is consistent to an increased electron density exerted from B on Pd. Liu *et. al.* reported the hydrogenation of *p*-CNB using a partially reduced Pd/γ-Fe_2O_3 catalyst.[40] The partially reduced support donated electron density to Pd, as characterised by the lack of CO being chemisorbed using CO chemisorption and IR. Therefore, similar results

are observed for Pd modified with B, with interstitial B donating electron density to Pd, which leads to enhanced selectivity to *o*-CNB.

5.6.2 ELECTRONIC AND GEOMETRIC MODIFICATION

The theory on bonding of transition metals and to non-transition metals by Gelatt *et. al.* predicted strong hybridisation between B and Pd, which leads to molecular bonding and band broadening. They reported strong hybridisation between metal *d*-band and non-metal *s-p* states.[25] For sufficient mixing they need to be degenerate, as in the case for Pd-B in the formation of tightly bound *d-s* and strong mix in *d-p* bonding states. As boron occupies interstitial sites, a strain effect is exerted on the metal as it is pulled apart. This increases lattice strain resulting in a decrease in *d*-band width. The authors concluded the ligand effect (electronic) is more important than the strain effect (geometric). A similar explanation was evoked on the variations of strain and ligand effects on the (now widely accepted) *d*-band centre theory, which has shown to be a powerful tool to predict catalytic activity/selectivity on varies reactions.[56, 57] As the lattice expands, the metal-metal distance is larger than the relaxed state, causes overlap between the *d* electrons on neighbouring metal atoms is smaller so bandwidth decreases to keep *d* occupancy fixed, the result in d-states moving up in energy. The calculation is consistent for a metal with a more than half filled band and the overall effect is a stronger interaction.[58] However, on the basis of electronic effects, the expansion of metal lattice caused by interstitial B can have a negative influence on alkene selectivity.[59] According to the *d*-band centre theory, expansion of Pd lattice causes Pd *d*-band to be more localised, leading to an up shift of *d*-band centre relative to Fermi level (E_F).[56] An increased *d*-band interaction to E_F results in stronger interaction. This is at variance with the catalytic reactions performed in this study. Pivotal selectivity was observed here by the promotion of

subsurface B leading to enhanced alkene selectivity. This can be interpreted as subsurface B *s-p* states can hybridise with the degenerate Pd *d*-states.[25] The effect of orbital mixing causing an increase in Pd *d*-band width may be more significant compared to expansion in Pd lattice. A greater *d*-band width will lower the *d*-band centre relative to E_F, which can lead to weaker interaction with alkene. Chen *et. al.* performed X-ray absorption spectroscopy studies on transition metal boron compounds monitored the $L_{2,3}$-edge XAS white line, a feature characteristic of the electronic structure of 4 *d* transitional metals.[60] They observed a loss of Pd spectral intensity near the E_F and increased to higher energy with the appearance of anti-bonding states well above the E_F. This agrees with density of states calculation by the aforementioned theoretical study between metals and light element atoms, which predicted a strong mixing of Pd-B hybridisation, leading to formation of bonding and anti-bonding states.[25] In other words, Pd *d*-states are depleted near the E_F, which overall can lead to weaker adsorption/enhanced desorption of substrates such as alkenes and *o*-CNB caused the apparent increase in reaction selectivity.

5.7 CONCLUSION

In conclusion, we report highly concentrated interstitial B in supported Pd particles can be synthesised for the first time by a low temperature technique in the liquid phase using BH_3.THF. Atomic B was found to occupy the interstitial octahedral holes of Pd even at room temperature, in steep contrast to previous high temperature synthesis techniques. Mild heating (200°C) was needed to drive B into Pd. The resulting catalyst was extensively characterised using PXRD, TEM, TPR-MS, TPO-MS, SSNMR, XPS, EXAFS, BET, and CO chemisorption. It was found interstitial B caused the blockage of subsurface H formation, indicative of the presence of B in the Pd. EXAFS demonstrated that no formal Pd-B bond was

observed and that the B indeed occupied in the octahedral holes of Pd thus expanded the lattice. XPS indicated the Pd surface was partially covered with a layer of B_xO_y. The material was tested in a range of alkyne hydrogenations and the hydrogenation of *o*-CNB. It was shown that the B modified Pd/C enhanced selectivities to the desired alkenes and suppressed the undesirable dechlorination pathway, in *o*-CAN formation. Such an increase in reaction selectivity was attributed to the hybridisation of Pd *d*-states and B *sp*-states, the result of which increased the E_F of Pd, facilitating product desorption and therefore maximising reaction selectivity.

5.8 REFERENCES

1. S. Kishore, J. A. Nelson, J. H. Adair and P. C. Eklund, *J. Alloys Compd.*, 2005, **389**, 234-242.
2. M. Yamauchi, R. Ikeda, H. Kitagawa and M. Takata, *J. Phys. Chem. C*, 2008, **112**, 3294-3299.
3. D. Teschner, J. Borsodi, A. Wootsch, Z. Revay, M. Havecker, A. Knop-Gericke, S. D. Jackson and R. Schlogl, *Science*, 2008, **320**, 86-89.
4. S. Nagarajan, K. Thirunavukkarasu and C. S. Gopinath, *J. Phys. Chem. C*, 2009, **113**, 7385-7397.
5. C. S. Gopinath, K. Thirunavukkarasu and S. Nagarajan, *Chem. Asian J.*, 2009, **4**, 74-80.
6. R. A. Alqasmi, H. Brodowsky and H.-J. Schaller, *Zur Konstitution von Palladium-Bor-Legierungen*, 1982, **73**, 331-334.
7. M. Beck, M. Ellner and E. J. Mittemeijer, *Powder Diffr.*, 2001, **16**, 98-101.
8. M. Beck, M. Ellner and E. J. Mittemeijer, *Z. Kristall.*, 2001, **216**, 591-594.
9. R. A. Alqasmi, H. Brodowsky and H. J. Schaller, *Z. Metallk.*, 1986, **77**, 637-642.
10. H. Husemann and Brodowsk.H, *Z. Naturforsch., A: Phys. Sci.*, 1968, **A 23**, 1693-&.
11. H. Brodowsky and H. J. Schaller, *Ber. Bunsen-Ges. Phys. Chem. Chem. Phys.*, 1976, **80**, 656-661.
12. T. G. Berger, A. Leineweber, E. J. Mittemeijer and M. Knapp, *Z. Kristall.*, 2006, 443-448.
13. T. G. Berger, A. Leineweber, E. J. Mittemeijer, C. Sarbu, V. Duppel and P. Fischer, *Z. Kristall.*, 2006, **221**, 450-463.

14. T. G. Berger, A. Leineweber and E. J. Mittemeijer, *Z. Metallk.*, 2006, **97**, 3-9.

15. M. Beck, M. Ellner and E. J. Mittemeijer, *Acta Mater.*, 2001, **49**, 985-993.

16. M. Krawczyk, *Appl. Surf. Sci.*, 1998, **135**, 209-217.

17. J.-Y. Wang, Y.-Y. Kang, H. Yang and W.-B. Cai, *J. Phys. Chem. C*, 2009, **113**, 8366-8372.

18. C. A. Jaska, T. J. Clark, S. B. Clendenning, D. Grozea, A. Turak, Z.-H. Lu and I. Manners, *J. Am. Chem. Soc.*, 2005, **127**, 5116-5124.

19. C. Park and M. A. Keane, *J. Colloid Interface Sci.*, 2003, **266**, 183-194.

20. C. Nützenadel, A. Züttel, D. Chartouni, G. Schmid and L. Schlapbach, *Eur. Phys. J. D*, 2000, **8**, 245-250.

21. R. Van Hardeveld and F. Hartog, *Surf. Sci.*, 1969, **15**, 189-230.

22. R. E. Benfield, *J. Chem. Soc.-Faraday Trans.*, 1992, **88**, 1107-1110.

23. O. M. Wilson, M. R. Knecht, J. C. Garcia-Martinez and R. M. Crooks, *J. Am. Chem. Soc.*, 2006, **128**, 4510-4511.

24. Y. Li, E. Boone and M. A. El-Sayed, *Langmuir*, 2002, **18**, 4921-4925.

25. C. D. Gelatt, A. R. Williams and V. L. Moruzzi, *Phys. Rev. B*, 1983, **27**, 2005.

26. H. W. King, *J. Mater. Sci.*, 1971, **6**, 1157-1167.

27. M. Krawczyk and W. Palczewska, *Surf. Sci.*, 1993, **287-288**, 212-216.

28. J. Tamaki, S. Nakayama, M. Yamamura and T. Imanaka, *J. Mater. Sci.*, 1989, **24**, 1582-1588.

29. M. Krawczyk and W. Palczewska, *Vacuum*, 1995, **46**, 1151-1153.

30. M. Rubinstein and H. A. Resing, *Phys. Rev. B*, 1976, **13**, 959.

31. I. Chorkendorff and J. W. Niemantsverdriet, *Concepts of Modern Catalysis and Kinetics*, John Wiley & Sons, 2003.

32. N. Mahata and V. Vishwanathan, *J. Catal.*, 2000, **196**, 262-270.

33. N. Binsted, R. W. Strange and S. S. Hasnain, *Biochemistry*, 1992, **31**, 12117-12125.

34. B. Lengeler, *Solid State Commun.*, 1985, **55**, 679-682.

35. E. Joannet, C. Horny, L. Kiwi-Minsker and A. Renken, *Chem. Eng. Sci.*, 2002, **57**, 3453-3460.

36. J. C. A. A. Roelofs and P. H. Berben, *Chem. Commun.*, 2004, 970-971.

37. I. T. Caga, E. Shutt and J. M. Winterbottom, *J. Catal.*, 1976, **44**, 271-280.

38. M. Krawczyk, J. Sobczak and W. Palczewska, *Catal. Lett.*, 1993, **17**, 21-28.

39. Á. Molnár, A. Sárkány and M. Varga, *J. Mol. Catal. A: Chem.*, 2001, **173**, 185-221.

40. H. Liu, M. Liang, C. Xiao, N. Zheng, X. Feng, Y. Liu, J. Xie and Y. Wang, *J. Mol. Catal. A: Chem.*, 2009, **308**, 79-86.

41. M. Liang, X. Wang, H. Liu, H. Liu and Y. Wang, *J. Catal.*, 2008, **255**, 335-342.

42. B. Sreedhar, D. K. Devi and D. Yada, *Catal. Commun.*, 2011, **12**, 1009-1014.

43. K. Xu, Y. Zhang, X. Chen, L. Huang, R. Zhang and J. Huang, *Adv. Synth. Catal.*, 2011, **353**, 1260-1264.

44. Z. Yu, S. Liao, Y. Xu, B. Yang and D. Yu, *J. Chem. Soc., Chem. Commun.*, 1995, 1155-1156.

45. X. Yang, H. Liu and H. Zhong, *J. Mol. Catal. A: Chem.*, 1999, **147**, 55-62.

46. W. Tu, S. Cao, L. Yang and W. Wang, *Chem. Eng. J.*, 2008, **143**, 244-248.

47. R. Raja, V. B. Golovko, J. M. Thomas, A. Berenguer-Murcia, W. Zhou, S. Xie and B. F. G. Johnson, *Chem. Commun.*, 2005, 2026-2028.

48. Q. Xu, X.-M. Liu, J.-R. Chen, R.-X. Li and X.-J. Li, *J. Mol. Catal. A: Chem.*, 2006, **260**, 299-305.

49. P. J. Ellis, I. J. S. Fairlamb, S. F. Hackett, K. Wilson and A. F. Lee, *Angew. Chem. Int. Ed.*, 2010, **49**, 1820-1824.

50. A. F. Lee, P. J. Ellis, I. J. S. Fairlamb and K. Wilson, *Dalton Trans.*, 2010, **39**, 10473-10482.

51. N. Maity, P. R. Rajamohanan, S. Ganapathy, C. S. Gopinath, S. Bhaduri and G. K. Lahiri, *J. Phys. Chem. C*, 2008, **112**, 9428-9433.

52. F. Studt, F. Abild-Pedersen, T. Bligaard, R. Z. Sørensen, C. H. Christensen and J. K. Nørskov, *Angew. Chem. Int. Ed.*, 2008, **47**, 9299-9302.

53. I. V. Yudanov, K. M. Neyman and N. Rosch, *Phys. Chem. Chem. Phys.*, 2004, **6**, 116-123.

54. X. Bao, M. Muhler, T. Schedel-Niedrig and R. Schlögl, *Phys. Rev. B*, 1996, **54**, 2249.

55. W. M. H. Sachtler, C. Backx and R. A. Van Santen, *Catal. Rev.-Sci. Eng.*, 1981, **23**, 127 - 149.

56. J. R. Kitchin, J. K. Nørskov, M. A. Barteau and J. G. Chen, *Phys. Rev. Lett.*, 2004, **93**, 156801.

57. J. K. Norskov, T. Bligaard, J. Rossmeisl and C. H. Christensen, *Nat Chem*, 2009, **1**, 37-46.

58. M. Mavrikakis, B. Hammer and J. K. Norskov, *Phys. Rev. Lett.*, 1998, **81**, 2819.

59. W. Tang and G. Henkelman, *J. Chem. Phys.*, 2009, **130**, 194504-194506.

60. J. Chen, M. Croft, Y. Jeon, X. Xu, S. A. Shaheen and F. Lu, *Phys. Rev. B*, 1992, **46**, 15639.

CHAPTER 6 – CHARACTERISATIONS OF COLLOIDAL METAL NANOPARTICLES IN FORMIC ACID DECOMPOSITION

6.1 INTRODUCTION

The drive to find alternatives for energy production in order to meet the ever-increasing energy demands in the world remains a global challenge, with an urgent need to mitigate our dependence and finite supplies of fossil fuels. Thus, current developed and emerging alternative technologies include using renewable resources such as biomass, wind, hydroelectric, geothermal etc. Nuclear energy, in particular, is seen as a major driving force towards that goal, which has been deployed in countries to generate large amounts of 'clean' electricity.

Electricity and liquid fuels make up the two large energy sectors as the most viable means for energy distribution. Fossil fuels have been strongly linked as a major factor in contribution to global warming through generation of CO_2 as greenhouse gas. Therefore new alternatives should consider their safe handling, transportation and green technologies for power generation. Many efforts are being devoted in the advancement of fuel cell technology as power generation for the future. There are numerous applications, most notably from transportations to power portable devices. One type of fuel cell is Polymer Electrolyte Membrane Fuel Cell (PEMFC) that use H_2 and O_2 to generate electricity forming H_2O as a by-product.[1] At present, however, most H_2 is produced industrially through fossil fuel derived methods such as methane steam reforming (MSR) processes or the water gas shift (WGS) reaction, where the combination of H_2O and CO produces H_2 and CO_2. However, fuel cells catalysts are sensitive to traces of CO in a H_2 stream, therefore special purification steps are need to remove any remaining CO. Thus, efforts are concentrated to identify cheap, non-fossil fuel derived mass production of clean H_2.

A separate but nevertheless related problem is the generation of H_2 for storage and transport. High pressure gas or liquid fuels are the conventional ways to store H_2

with high energy density. However, obvious safety concerns have prevented its use to transport H_2 under high pressure through pipelines or tankers. Therefore, identifying new ways to handle H_2 must be considered such that it is easily transported, safe to store and can be reversibly recovered and used on demand.

Considering the above problems, the decomposition of formic acid has been identified as a viable alternative for safe transportation and for the on demand generation of clean H_2. Formic acid is a strong corrosive acid, but dilute solutions of formic acid in water are approved by the FDA as a food additive. They are generally non-toxic, easy to transport, store and handle. Currently the method to produce formic acid is as a by-product of hydrocarbon oxidation or by the hydrolysis of methyl formate obtained from the carbonylation of methanol. Formic acid can decompose to CO_2, which can be hydrogenated back to formic acid to form a CO_2 neutral H_2 storage cycle (Fig. 6-1).[2]

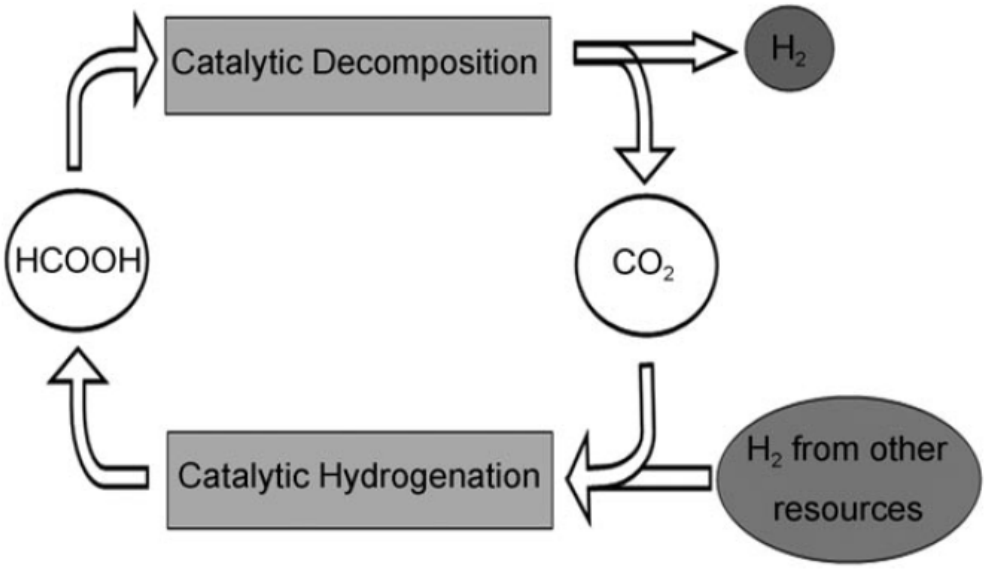

Fig. 6-1 CO_2 neutral cycle for H_2 storage in the formic acid carbon cycle.[2]

Formic acid has a density of 1.22 $g.cm^{-3}$ and a hydrogen content of 4.4 wt.% in the context of its energy density. In volumetric energy density terms, formic acid has

a 53 g of H_2 per litre (theoretical gas composition) compared to methanol steam reforming of 3 part H_2/CO_2 at 148 g of H_2 per litre.[1] However, in the case of formic acid, its decomposition should only form H_2/CO_2 under certain conditions, therefore it is feasible for use directly in fuel cells without CO separation or hydrogen separated if required.

In contrast to the already well established field of homogeneous hydrogenation of CO_2 to formic acid and *vice versa*, decomposition of formic acid back to CO_2 using heterogeneous catalyst is, however, far less developed. Formic acid decomposition using heterogeneous catalytic techniques dates to the 1950s where PdAu alloy wires were used.[3] It has since then received little attention until recent work on Pd/C, bimetallic Pd/C and supported Au catalysts.[4-7] In general, the decomposition of formic acid follows two pathways:

i) Decomposition to H_2 and CO_2.

$$HCOOH \longrightarrow H_2 + CO_2 \qquad \Delta G = -48.4 \text{ kJ.mol}^{-1}$$

ii) Dehydration to yield CO and H_2O.

$$HCOOH \longrightarrow H_2O + CO \qquad \Delta G = -28.5 \text{ kJ.mol}^{-1}$$

Clearly, there is a need to develop a heterogeneous catalyst that is selective towards the H_2 producing formic acid decomposition pathway in order to avoid the formation CO. However, Xing *et. al.* recently reported a bimetallic PdAu/C catalyst promotes the decomposition of formic acid to H_2 and CO_2 with low CO content.[7] They also found the use of conventional Pd/C catalyst suffers from surface poisoning intermediates leading to their rapid deactivation. Whereas, the core-shell nature of the bimetallic catalyst has the beneficial effect of exhibiting high CO counter-poisoning effect. Furthermore, catalytic activities can be further enhanced by co-depositing

CeO_2 particles on the surface of PdAu/C, although the mechanism for its promotion was unclear.[8]

Despite these recent advances, there are no fundamental studies to systemically characterise the adsorption strength of formic acid to different metals under realistic conditions. Traditional surface characterisation techniques used to interrogate metal surface properties typically involve ultra-high vacuum (UHV) conditions. This is of course far from real catalytic conditions. To that end, the use of liquid ^{13}C NMR spectroscopy coupled with small adsorbate molecules to probe surface sites on the metal particles is an interesting alternative. However, previous attempts at in using liquid ^{13}C NMR had been concentrated on studying pre-adsorbed CO species on colloidal metal nanoparticles. Owing to the carbon atom being directly in contact with the metal surface, a typical Knight Shift effect (caused by the hyperfine coupling of the ^{13}C nucleus to the conduction electrons of the metal nanoparticles causing hundreds of ppm shift in peak maxima and peak width), was observed. This loss of vital information on the probing metal with small adsorbates had thwarted the use of this technique for metal surface site determination for over 20 years. This was until initial work from our group that used formic acid as a surface probe, where it was applied to characterise colloidal PVP-Ru nanoparticles by liquid ^{13}C NMR.[9] Metal surface sites such as bridging, multi- and mono-dentate forms of adsorbed formate could be identified from the spectra (Fig. 6-2), of which the integration of these peaks closely relate to changes in population with metal crystallite size as seen by ATR-IR spectroscopy. This level of information was made possible by the fact that the probing ^{13}C nucleus has a two atom distance with an oxygen spacer to the metal surface, hence any residual Knight shift effect due to the mobile electrons was greatly reduced.

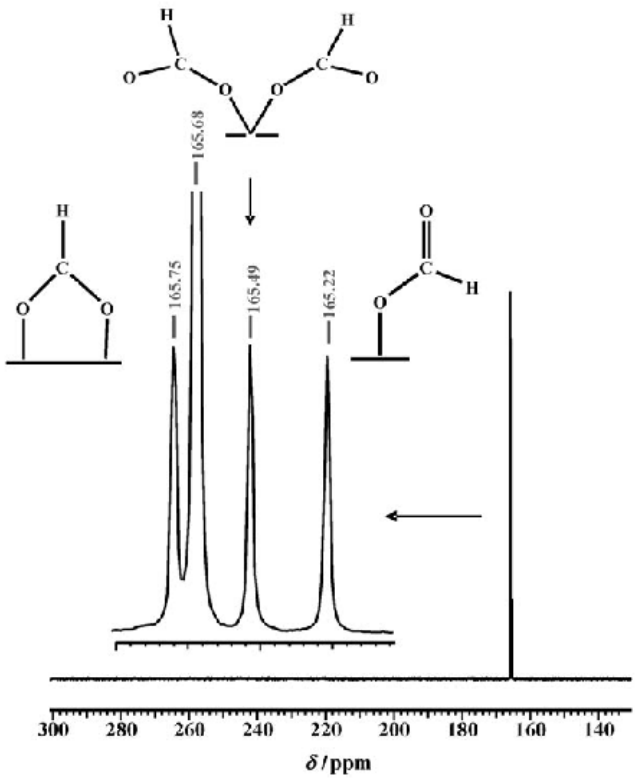

Fig. 6-2 Three adsorbed formate species on PVP-Ru nanoparticles together with chemisorbed formic acid observed by ^{13}C NMR spectroscopy at room temperature.[9]

6.2 OBJECTIVES

This Chapter is effectively an extension to the previous work that details the liquid $H^{13}COOH$ NMR characterisation to probe the surface characteristics of noble metals, such as Au. Colloidal syntheses of metal nanoparticles were prepared in the liquid phase, owing the fact that liquid NMR characterisations have to be in a highly dispersed state. In addition, a new route to prepare colloidal Pd doped with B was investigated. Supported version of this material was characterised extensively in Chapter 5. The material was shown to have an increased electron density of the metal plus an increased lattice parameter of Pd, due to B occupying in the interstitial position. Development of a colloidally stable analogue is of high importance, as an increase in lattice parameter on metal surface has been shown to increase catalytic activity in the electro-oxidation of formic acid.[10] Therefore, colloidally prepared Pd-

^{int}B catalyst characterised using liquid ^{13}C NMR may give further insight into this new material and it may possess interesting electronic and structural properties in this reaction.

6.3 GOLD METAL NANOPARTICLES

6.3.1 SYNTHESIS

The use of nano-dimensional Au has had a major influence in modern nanotechnology. The size dependent properties have potential applications in a range of areas including catalysis, optical materials, sensors and bio-devices. It is therefore vital to further understand the surface of Au nanoparticles. There were two requirements to the synthesis of colloidal Au: i) the metal particle size must be within the 1 - 10 nm size domain. This is important due to the quantum size effect as the metal changes from metallic to non-metallic character; ii) the polymer, polyvinylpyrrolidone (PVP), must be used to have a meaningful comparison with previous work in our group.[9] A change in the polymer stabiliser with different functional groups is known to change electronic properties of metal nanoparticles, which may obscure any size effect coming from the metal itself.[11] This also enables the subsequent particles to be dispersed in aqueous solvent systems such that the analyte can also be solubilised. Thus, Au nanoparticles with well controlled sizes were prepared using a seed mediated growth method (Scheme 6-1).[12] It uses a rapid reduction of the Au (III) salt, and the subsequent particles capped by the PVP stabiliser. A fast addition step, coupled with the strong reducing nature of $NaBH_4$, ensures all the Au were reduced instantaneously. This was done to minimise the particles nucleating with different time histories, which may affect the final particle size distribution. The reduction was performed at 4°C, as reducing the Au salt at room temperature lead to an overall increase in particle size and particle size

distribution hence the size control is predominantly kinetic. The time where the Au seed was allowed to be stirred (30 min used here) was also found to be important. For example, leaving the Au seed for 2 h after reduction lead to changes in colour from brown to red, indicating the growth of Au seed;[13] this is possibly due to leaching in the presence of by-products from the reduction as well as oxidative etching.[14] This assumption was demonstrated since the growth of the Au seed stopped after several desalination steps using ultra-centrifugal dialysis (where no colour change was observed after 1 month).

$$HAuCl_4 + PVP\ (60\ eq) \xrightarrow[H_2O,\ 4^oC,\ 30\ min]{NaBH_4\ (10\ eq)} Au{:}PVP\ Seed$$

Scheme 6-1 Preparation of Au seed by fast reduction method.

Larger sizes of Au were grown by the further reduction of Au in the presence of a Au seed (Table 6-1, Scheme 6-2).[13] The weak reducing power of Na_2SO_3 coupled with the presence of Au seed maximised Au salt being reduced on Au metal surfaces and at the same time minimised self-nucleation. It was found that poor quality samples (larger particle size and distributions) were obtained where dissolved oxygen was present in the solution. Oxidative etching is known to occur where combinations of O_2 and Cl^- ions are present.[14] Therefore, removal of O_2 was achieved by completely degassing standard solutions of Au seed, Au salt and Na_2SO_3 by using the freeze-pump-thaw technique or by bubbling N_2 into the reaction.

$$Au{:}PVP\ Seed + n\ HAuCl_4 + PVP\ (60\ eq) \xrightarrow[H_2O,\ N_2,\ 3\ h]{Na_2SO_3\ (3\ eq)} Au{:}PVP\ G\mathit{n}$$

Scheme 6-2 Preparation of Au seed by the $NaBH_4$ method.

Sample	Au Seed (mL)	$HAuCl_4$ (mL)	Na_2SO_3 (mL)	PVP (mmol)	H_2O (mL)	Ratio of $HAuCl_4$ to Seed
G1[a]	40	0.332	0.334	0.600	9.4	0.25
G2	25	0.830	0.834	1.500	23.4	1.0
G3	12	1.245	1.251	2.250	35	3.0
G4	7	1.423	1.429	2.571	40	6.0

Table 6-1 Growth conditions used to prepare larger Au nanoparticles. [a]Au seed solution was basified with K_2CO_3 (0.03 mmol).

6.3.2 UV-VIS SPECTROSCOPY

The size of the Au seed and subsequently grown nanoparticles were characterised by UV-Vis spectroscopy. This technique is ideal to characterise materials such as Au, as they exhibit a phenomena called a surface plasmon resonance (SPR). The SPR occurs when free electrons in the metal driven in the electric field to oscillate in phase with the irradiated light source.[15] This oscillation leads to their scattering and absorption of light at a specific wavelength and that gives nano-dimensional coinage metals distinctive colours. At their nanosized regime, however, they exhibit the quantum size effect arising from transition from metallic to non-metallic behaviour. Thus, the intensity of the SPR peak around 510 nm of these Au samples gives an indication about their size (Fig. 6-3). The SPR band for Au seed was undetectable, indicating their extremely small size due to the mentioned quantum size effect and that they were brown in colour. For samples prepared using the slow growth method, all the samples appeared red apart from G1 with a slight tint of brown. The SPR band had grown and sharpened upon higher ratio of the Au salt to Au, indicating a controlled increase in particle size under the applied reaction condition. No higher wavelength absorption was detected, which indicates the

particles were spherical rather than anisotropic shapes.[16] On closer inspection of the grown samples, the SPR red shifted steadily from ~505 to 516 nm on moving from sample G1 to G4, also indicating the Au particle size increased. This agreed with the literature in that the maximum absorption for larger Au nanoparticles were observed at ~520 nm and reached a constant value.[17]

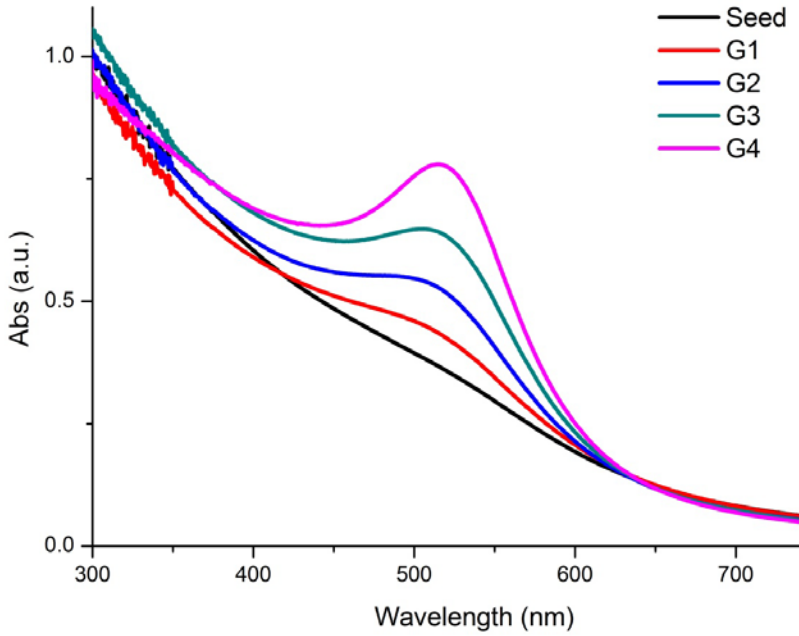

Fig. 6-3 UV-Vis spectra for Au seed and seeded growth samples.

6.3.3 TEM

TEM was used to determine Au crystallite size and particle distributions (Fig. 6-4). More than 300 particles were analyzed for each sample to obtain statistically meaningful comparison of particle sizes. No anisotropic shapes were detected for all the above sample, which agreed with results from UV-Vis. However, it was found that the standard deviation for the samples increased by ~10% when compared to the literature.[13] This is because of the slightly lower ratio of polymer PVP (60 eq.) used in this study. Reducing the polymer ratio to metal was necessary in order to apply the whole the sample for subsequent NMR study to keep moles of metal constant. Thus it

was found that 60 eq. was the highest ratio. Nevertheless, all the measured samples agreed with results obtained by UV-Vis, in that the size increase was observed in the order of seed < G1 < G2 < G3 < G4.

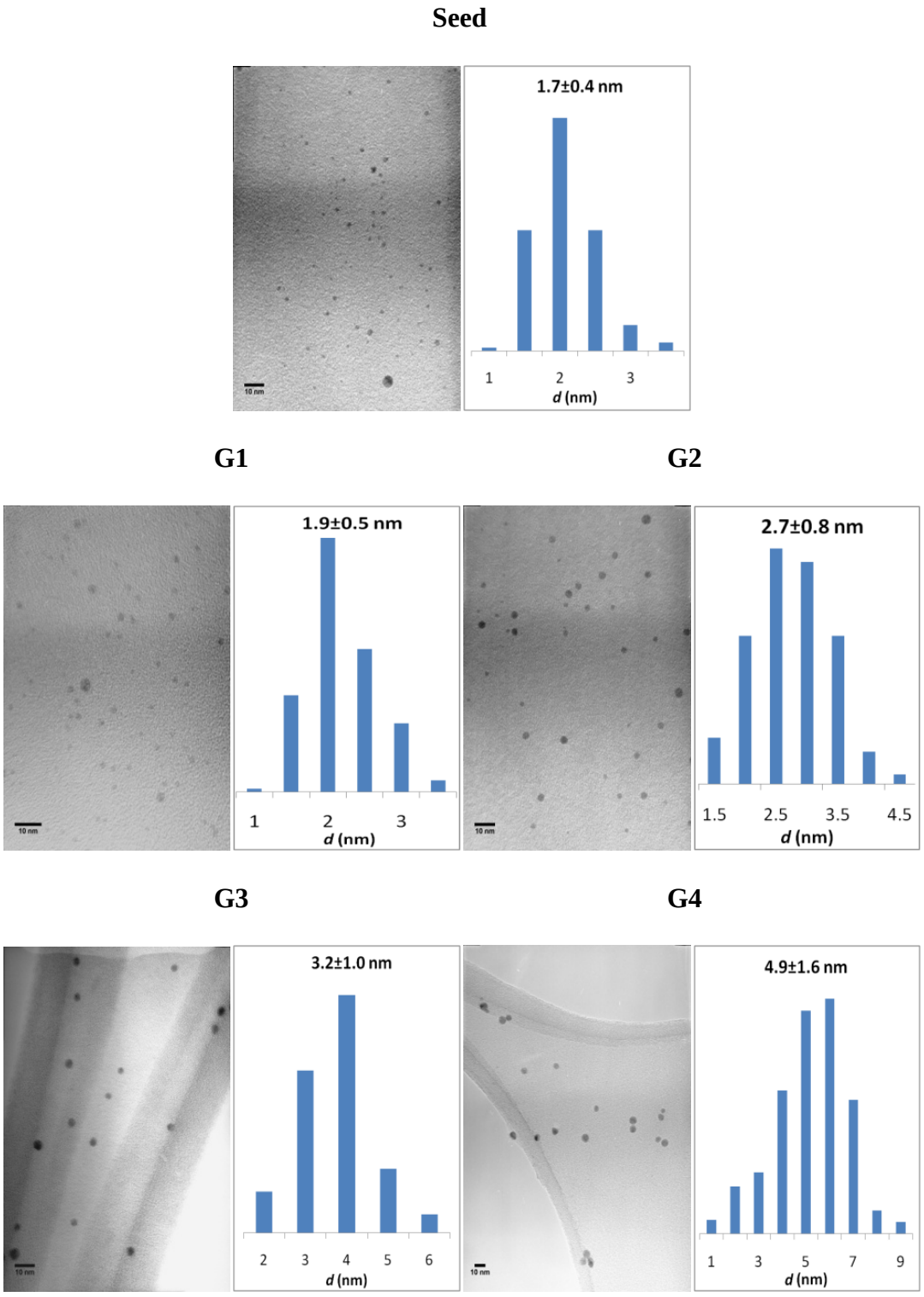

Fig. 6-4 TEM micrograph of seed and seed mediated growth of Au nanoparticles.

6.3.4 PXRD

The average Au crystallite size of seed growth samples were examined using PXRD (Fig. 6-5). The samples were prepared by re-dispersing the Au nanoparticles in water and then depositing them into a glass plate followed by evaporation to dryness. It was observed the larger Au sizes were comparable to those size observed using TEM. However, small crystallite sizes such as the seed and G1 could not be determined by PXRD due to their overly broad and very weak peak and/or overlapping Au (111) with (200) intensities.

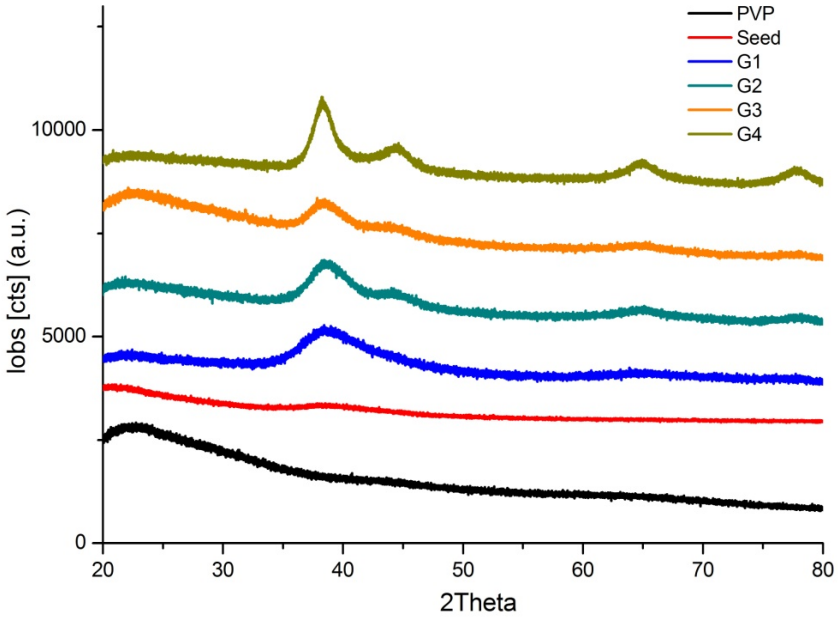

Fig. 6-5 PXRD of PVP-Au nanoparticles.

6.3.5 NMR

The prepared Au nanoparticles were investigated using liquid ^{13}C NMR with $H^{13}COOH$ as a probe molecule. Fig. 6-6 shows a typical spectra obtained from the Au seed sample. The PVP peaks are just about discernible at ~177, 46, 44, 42, 31 and 17 ppm. The first peak was assigned to the amide centre on the PVP with others constituting to the hydrocarbon ring and backbone in different chemical

environments.[18] The peak at 66.39 ppm was 1,4-dioxane as the internal standard. The peak at 124.47 ppm was assigned to dissolved $^{13}CO_2$ in solution from the decomposition of $H^{13}COOH$. No decomposition was observed without the metal colloid, indicating the decomposition occurs on the metal surface. The peak at 166.17 ppm was therefore assigned to adsorbed formic acid in rapid exchange with the non-bounded molecular form in solution. This is reasonable as:

i) It is shifted more downfield compared to the free formic acid without any metal at 165.64 ppm.

ii) Its intensity decreased with the increase of the CO_2 peak.

It was noted that no adsorption modes were observed for the Au sample. This result differs compared to previous studies using Ru nanoparticles as well as other metals such as Pd and Pt, where the formate species were observed to adsorb to the metal to form bridging, multi-monodentate and mono-dentate modes.[9, 19] Here, the lack of adsorption modes may indicate that formic acid weakly adsorbs on the Au surface.[20] Nevertheless, the fact that $^{13}CO_2$ was observed means adsorption does occur although a detailed mechanism is not yet known.

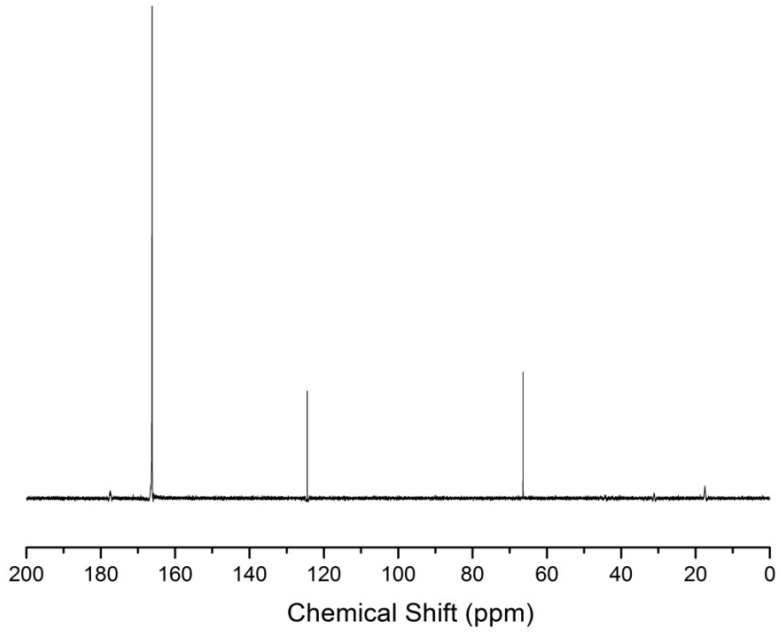

Fig. 6-6 Liquid ^{13}C NMR spectra (125.8 MHz, D_2O, 298K) for the Au seed nanoparticles mixed with 200 μL of 1 M $H^{13}COOH$ in D_2O. 1,4-Dioxane was added as an internal standard.

Larger sizes of Au prepared using the seeded growth method were also examined (Fig. 6-7, left). Again no adsorption peaks were observed in any of the samples. This was also the case when a larger Au sample was prepared using ethylene glycol (EG) reduction. The synthesis was performed at 90°C basified with $NaHCO_3$ to afford a Au metal crystallite size of 8.6 nm, as estimated by PXRD. Thus, the lack of adsorption even at larger sizes is most likely due to the mentioned weak interaction with formic acid. Interestingly, it was found the main resonance peak varies significantly below the 3 nm size regime. Such changes in the chemical shift of adsorbed formic acid varies greatly in contrast to other metals studied such as Ru, Pd and Pt, of which Ru showed no such size effect.[19] The relationship between the initial rate of formic acid decomposition to that of Au particle size and chemical shift values was investigated with the rate of CO_2 formation was also monitored *in situ* (Fig. 6-7, right). It was found that a higher initial rate of formic acid decomposition to $^{13}CO_2$

was indeed observed for smaller Au sizes (higher chemical shift values). Lastly, note that the chemical shift value of adsorbed formic acid for sizes above 3 nm were all shifted downfield from the free formic acid (at 165.64 ppm) is rather intriguing.

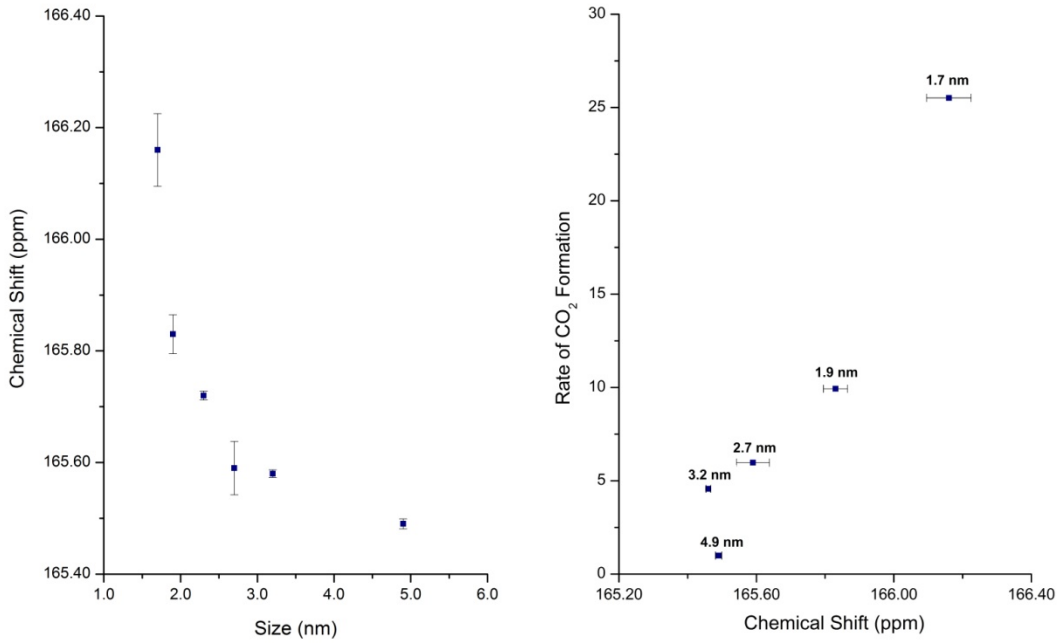

Fig. 6-7 Correlation between Au particle size and ^{13}C chemical shift of adsorbed formic acid in exchange with its free form (left); Correlation between initial rate of CO_2 formation over different sizes of Au nanoparticles against ^{13}C chemical shift of adsorbed formic acid in exchange with its free form (right). Error bars represent average values obtained for three repeated measurements.

6.3.6 DISCUSSION

As mentioned, no separate adsorption peaks corresponding to formate chemisorption modes were observed for all Au sizes studied here ranging from 1.7 - 9.0 nm. According to the theoretical atom statistical model[21], metal nanoparticles have dramatic changes in population of surface coordinate sites. Thus, different adsorption modes should be seen under this size regime. However, the fact that no adsorption modes were seen could be attributed to the inertness of Au. Electronic band theory suggests the strength of bonding between metal and surface adsorbate is

dependent on the filling of adsorbate-metal antibonding states, the magnitude of coupling matrix element V_{sd}^2 and also cohesive energy of the metal.[20] Au, a electron-rich 5*d* metal, has a large cohesive energy plus a large V_{sd}^2 value, both of these lead to its *d*-states more tightly bound leading to a higher effective nuclear charge (Fig. 6-8).[22] In the context of formate interaction with Au, it is mainly dictated by Pauli repulsion that is caused by a totally filled and low lying *d*-band, resulting in more overlap, more repulsion and therefore weaker adsorption. On the other hand, HCOOH adsorption on the metal surface is known to occur *via* O-H dissociation to form formate species on Pd(110).[23] Formate species are intermediates for HCOOH decomposition, and it has been highlighted that their formation is rate limiting on metals like Au.[24] Here, the lack of adsorption modes suggests the high barrier for formate formation, after which any formate species may selectively dehydrogenate to form H_2 and CO_2.[25] Interestingly in this study, the formation of CO_2 even occurs on Au nanoparticles as particles were clearly observed in TEM. This differs to the study that well dispersed Au species that are undetectable by TEM are needed to dehydrogenate HCOOH to CO_2.[24] This could be due to the difference between effects to the PVP polymer used in our study to that of Au species supported on TiO_2 and Al_2O_3.

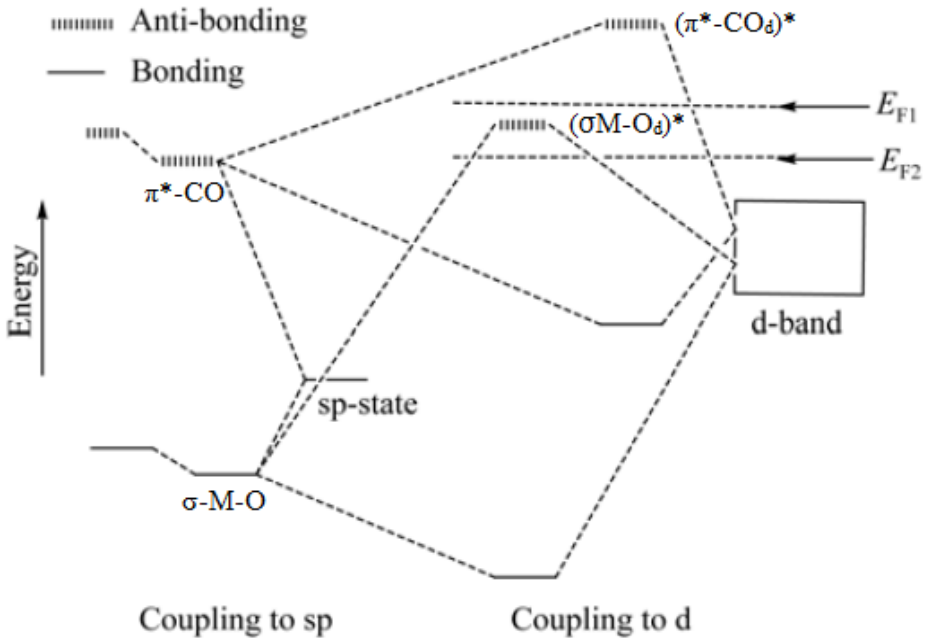

Fig. 6-8 Modified illustration of the interactions between adsorbed formate with electronic states of transition metals. E_{F1} refers to Fermi level of Au which lie above the filled antibonding bands.[22]

If Au is so inert then why, out of all the metals studied between Ru, Pd and Pt[19], that Au exhibits the largest change in ^{13}C chemical shift as particle size decreases? As seen, the E_F of Au lies totally above the antibonding orbitals of the formate, leading to a weakened chemisorption (Fig. 6-8). Accordingly, any change in chemical shift is related to changes in the adsorbate interaction with metal *d*-states. A higher chemical shift (downshift) therefore leads to increased electron density donated into the antibonding orbitals of the adsorbate.[19] Dramatic size effects may be due to the quantum size effect[26], where the metal undergoes metal to non-metal transition as observed by the lack of SPR on the UV-Vis for the seed sample. Such a size effect can be explained by an effective upshift of Au *d*-band centre (or downshift of E_F relative to *d*-band centre due to decreased coordination numbers), facilitating electron delocalisation between the adsorbate antibonding orbitals and Au E_F. However, other studies suggest changes in population of low coordinate sites may potentially

outweigh any electronic effect. FTIR spectroscopic studies in adsorption of CO on Au suggest only one adsorption mode was seen and its peak area is more pronounced for smaller Au clusters.[27] This could be due to smaller sizes possess higher degree of low coordinated sites. Recently, Au supported in mixed metal oxides characterised by HAADF-STEM coupled with volumetric CO adsorption experiments was reported.[28] The authors concluded that only sites that have coordination numbers equal and less than 7 were responsible for CO adsorption. No adsorptions were found on sites that are 8 coordinated (100 sites) and 9 coordinated (111 sites). Janssens *et. al.* suggests increasing amounts of corner sites are the dominant active sites towards CO oxidation and O adsorption.[29] This is because of much higher lying *d*-orbital states for low coordinated sites, which leads to stronger adsorption. A large change in *d*-states relative to E_F is only observed for electron-rich metal such as Au. This is in agreement with that fact that decreasing Au size have much higher activity towards the initial rate of formic acid decomposition (or rate of $^{13}CO_2$ formation, Fig. 6-7 right). The same authors also reported any adsorption behaviour that is dependent on the population of low coordinated sites should follow the term $1 / d^3$, where d is the particle size.[30] Interestingly, our NMR size study in relation to the chemical shift of $H^{13}COOH$ result show a similar trend. According to DFT calculations, they concluded that adsorption of CO or O on surface plane sites of Au (111) and (100) does not occur and essentially non-interacting to CO and O that Pauli repulsion dominates. This may explain why the $H^{13}COOH$ chemical shift is more upfield (lower ppm) than even free formic acid without metal at larger Au sizes (Fig. 6-7, left). This is in agreement with the *d*-band centre theory that high coordinated sites have much lower *d*-band centre relative to E_F hence no adsorption occurs.

6.3.7 CONCLUSION

Au nanoparticles were synthesised using a modified seeded growth method. The particles appeared spherical in shape and no other heterostructures were observed as characterised by UV-Vis, PXRD and TEM. The nature of metal surface was examined using liquid $H^{13}COOH$ NMR spectroscopy. It was found the chemical shift of adsorbed HCOOH was greatly influenced by a change in Au particle size in the nanosize regime, with smaller sizes leading to higher adsorbed $H^{13}COOH$ chemical shifts. Timed ^{13}C NMR decomposition study by examining the $^{13}CO_2$ peak *in situ* revealed higher chemical shifts did indeed correlate to a decrease in nanoparticle size and therefore decomposition activity. Such dramatic changes between the size and catalytic activity can be explained by an increase in lower coordinated sites as the Au particle size decreases. Interestingly, the chemical shift adsorbed $H^{13}COOH$ peak for bigger Au particles lie further upfield than $H^{13}COOH$ solution without metal. This effect was ascribed to Au surface being totally inert, leading to an overall net repulsion of $H^{13}COOH$ on the Au surface, therefore lower chemical shift.

6.4 PALLADIUM BORON METAL NANOPARTICLES

6.4.1 SYNTHESIS

In Chapter 5, it was shown that supported Pd/C doped with ^{int}B atoms has beneficial effects towards the selective semi-hydrogenations of alkynes to alkenes and chemoselective hydrogenation of *o*-CNB to *o*-CAN. The promotional effect was attributed to an increase in electron density of the surface Pd, leading to an increase in the observed selectivity. Therefore, it was interesting to design a colloidal Pd-^{int}B analogue in order to study effects of increased electron donation and lattice expansion of Pd in HCOOH dehydrogenation.

The design of colloidal Pd metal nanoparticles and subsequently doping with BH_3.THF was particularly challenging. A number of experimental design parameters must be satisfied before evaluation using ^{13}C NMR spectroscopy:

i) Maintain the same polymer, PVP, in order for meaningful comparisons with other metals as was the case for Au.

ii) Polymer must be thermally stable up to 200°C at the borylation step. In this case, PVP matches this criteria as it has thermal stability of over 300°C under an inert atmosphere.

iii) Polymer must disperse in THF.

iv) Pd particle size must be sufficiently large to avoid low coordination/quantum size effects.[19]

Therefore, colloidal Pd was prepared using the well established EG reduction with modifications (Scheme 6-3).[31] The first step of the synthesis determines the particle size of the sample. Thus, by using a 1:1 polymer to metal ratio, the size of Pd particles should be sufficiently large. The second step was employed to enhance particle stability during the borylation step.

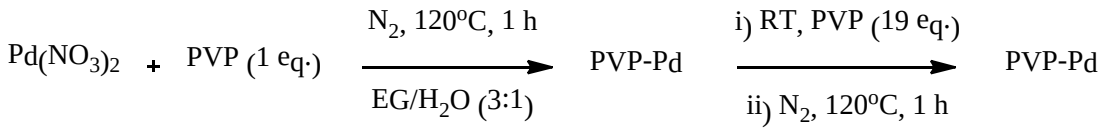

Scheme 6-3 Modified preparation of PVP stabilised Pd nanoparticles using EG reduction.

Borylation of the as-synthesised PVP-Pd was undertaken by addition of excess BH_3.THF, as shown in Scheme 6-4. Experiments found PVP-Pd sample without the addition of 19 eq. of PVP stabiliser during the second step lead to total aggregation after borylation at 90°C. This implies the additional PVP indeed enhanced the Pd particle stability during the borylation step. Other attempts performed by mixing

BH_3.THF with PVP-Pd were unsuccessful owing to limited or no solubility of PVP in THF. Thus, DCM was added to disperse the PVP-Pd followed by addition of the B source. Note that DCM to THF ratio must be above 4:1 as higher fraction of THF lead to the PVP-Pd clumping up, which ultimately lead to poor B content in the sample. It was found that residual water from the first synthesis also had a detrimental effect of particles clumping up upon addition of BH_3.THF. The suspension was allowed to stir under an inert atmosphere until dry, followed by heating up to 90°C. Heating the sample to 90°C maintained particle dispersion during the subsequent re-dispersion step with H_2O. Higher temperatures such as 200°C lead to total particle aggregation, whereas some aggregation was observed even at 100°C. Interestingly, we observed thermal decomposition of BH_3.THF to B_2O_3 at 200°C (characterised by its white colour). This may explain the prevalence of B oxidised species as observed by XPS and SSNMR for our supported analogues that were heat treated in this manner.

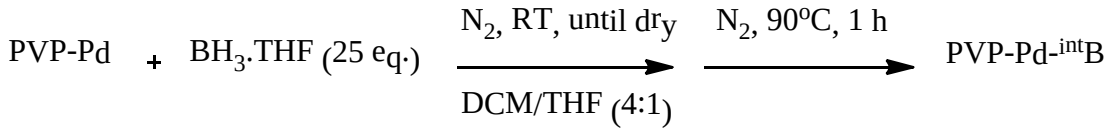

Scheme 6-4 Borylation of PVP-Pd using 25 eq. of BH_3.THF.

6.4.2 PXRD

PXRD was used to determine the B content for the sample employed in the above synthesis (Fig. 6-9). For PVP-Pd, the average metal crystallite size was estimated at 7.8 nm by PXRD (Fig. 6-9, black). A large particle size obtained here was deemed sufficient to investigate any subsurface B effects and intrinsic size effects can be ruled out. Note that no subsurface C impurities were obtained as evidenced from the lattice parameter matches well to that of metallic Pd. This is

because the temperature employed in the synthesis was below the critical temperature of 150°C for atomic C incorporation.[32, 33] Accordingly, this provided a clean Pd without any other interstitial atoms for comparison.

PVP-Pd doped with BH_3.THF was investigated (Fig. 6-9, red). Interestingly, maximum B at.% was obtained even when the sample was heated only to 90°C (Table 6-2), although a slight shouldering to the left of Pd-^{int}B peaks were observed, indicative of partial interstitial occupation in some Pd sites. Other satellite peaks were also observed (at angles 31.0°, 33.6°, 35.9°, 40.5°, 43.3°, 47.8°, 50.3° and 51.2°). These peaks were reminiscent of the peaks also observed for the supported 3% Pd-^{int}B/C (see Fig. 5-4, chapter 5). The fact that no support was used here suggests these peaks were tentatively assigned as (partially) oxidised B from the excess of BH_3.THF. The formation of alloyed Pd_xB_y phases could be ruled out for a number of reasons:

i) XPS for the supported Pd-^{int}B/C showed no observation on the reported Pd_xB_y phase (see Chapter 5).

ii) EXAFS study suggested the major phase of Pd-^{int}B/C remains an *fcc* structure, although some minor phases may remain undetected by this technique.

iii) The peaks did not match any of the known ordered Pd_xB_y phases.[34-40]

Furthermore, according to a PdB phase diagram, it is known that Pd_5B alloy is the most probable phase for B content between ~17-24 at.% and at temperatures below 320°C.[40] However, the peaks observed here did not match the above Pd_5B phase.[37]

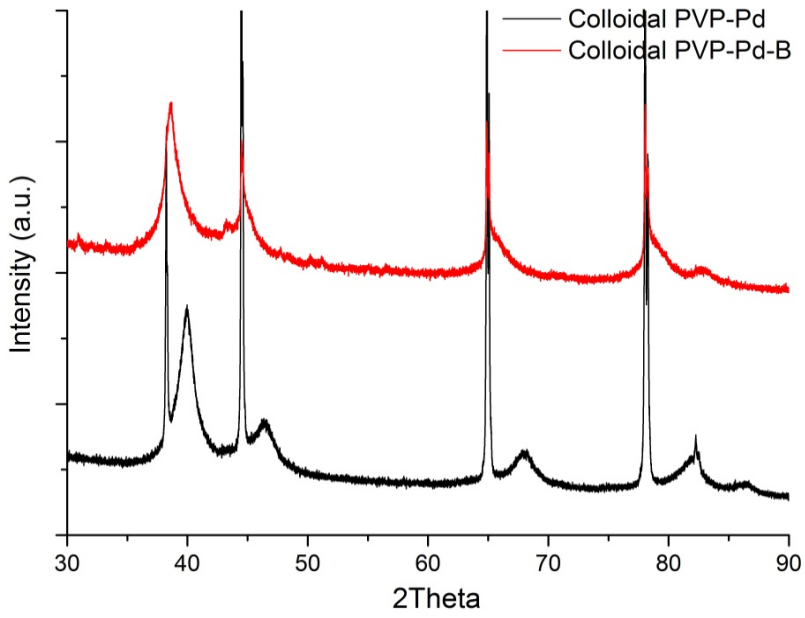

Fig. 6-9 PXRD measurement for i) colloidal PVP-Pd (black); ii) colloidal PVP-Pd doped with 25 eq. of BH_3.THF (red).

Sample	Lattice Parameter a_0	B at.%
Colloidal PVP-Pd	0.3984(4)	-
Colloidal PVP-Pd-^{int}B	0.4032(10)	20.3

Table 6-2 Lattice parameter calculated from PXRD for above samples and the atomic ratio of B for colloidal PVP-Pd-^{int}B.

6.4.3 ATR-FTIR

6.4.3.1 CO ADSORPTION

Vibrational IR spectroscopy coupled with small molecule adsorption (such as CO) is well established in the literature. The nature of CO_{ads} largely depends on its electronic interactions with the metal, surface coverage and size effects.[41-43] The C≡O stretching frequency decreases as its coordination with metal increases, an effect that weakens the bond due to back donation of metal *d*-electrons into the LUMO antibonding CO 2π* orbital. Therefore, sites specific information can be obtained

from changes in populations of metal coordination (surface or defect sites) as the size changes as well as any electronic changes due to shifts in the C≡O stretching frequency can be realised.

ATR-FTIR was used to study colloidal PVP-Pd and PVP-Pd-^{int}B with CO adsorption (Fig. 6-10). The PVP >C=O carbonyl stretching can be observed at 1667 cm^{-1}. The peaks between 1500-1000 cm^{-1} can be characterised by the PVP amide ring and carbon backbone (C-N stretch, C-H, C-C, etc). Peaks at 3000-2800 cm^{-1} were assigned to C-H stretch in alkanes. CO adsorption study for the colloidal PVP-Pd sample showed only one peak at 1937 cm^{-1} was assigned CO adsorbed on the bridging mode. The adsorption *via* the bridging mode configuration is prevalent mainly for big particles with flat surface dominant sites. The observation of a single peak for our 7.8 nm particle agreed with the literature (7.5 nm Pd particles exhibit only one peak at 1944 cm^{-1}).[44]

For the colloidal PVP-Pd-^{int}B sample, additional peaks can be observed compared to PVP-Pd. O-H stretches can be seen in the regions 3500-3000 cm^{-1} due to boric acid peaks containing O-H groups and are also characterised by broad peaks around 1450-1250 cm^{-1} and 1200-950 cm^{-1} assigned as B-O stretching of trigonal BO_3- and tetrahedral BO_4- units, respectively.[45] Note that no B-H stretching was detected in the region 2650-2350 cm^{-1},[46] indicative that all the initial borane material had converted to boric acid when contacted with water. The PVP >C=O carbonyl peak had shifted down in wavenumbers from 1667 to 1641 cm^{-1}. The shift down is likely due to its interaction with boron species in close proximity to the carbonyl. CO adsorption performed on this sample showed a single peak that corresponds to bridging species only. Interestingly, the peak had shifted from 1937 to 1920 cm^{-1}. This peak is slightly less intense compared to PVP-Pd, probably due to surface

adsorbed boron species leading to reduced surface sites. Accordingly, the shift could be coverage dependent or that of an electronic effect from subsurface B with electrons donated to Pd, leading to the observed downshift in wavenumbers.

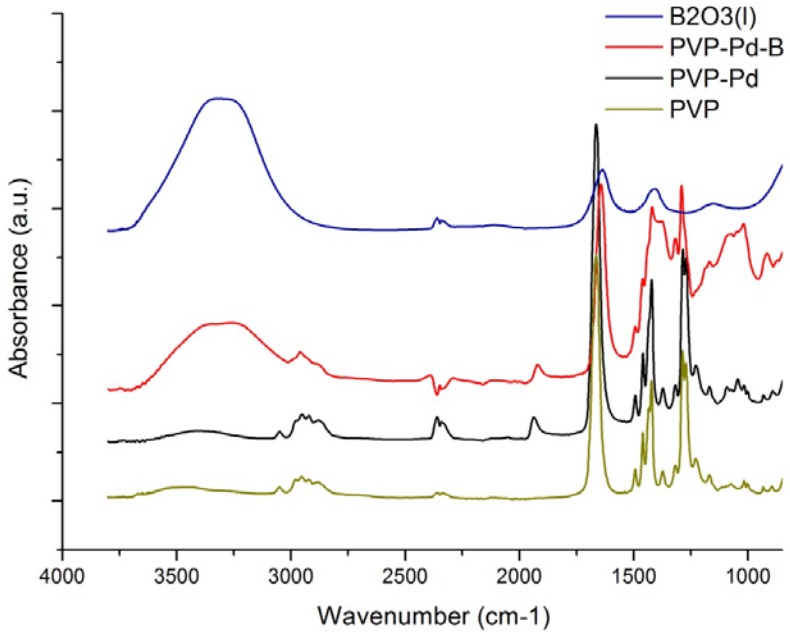

Fig. 6-10 ATR-FTIR spectra for i) Wet B_2O_3 (blue); ii) Colloidal PVP-Pd doped with 25 eq. BH_3.THF (red); iii) Colloidal PVP-Pd (black); iv) PVP as reference (gold).

6.4.3.2 FORMIC ACID ADSORPTION

ATR-FTIR was used to study the interaction of formic acid to the metal surface. As mentioned, formic acid dissociatively adsorbs on the metal surface by O-H scission to form formate species. Therefore, the adsorption of formate species in different binding modes characterised by IR may give an insight in the nature binding on different metallic nanostructures/sizes. The characterisation was done by mixing a 0.5M HCOOH solution to the metal colloid followed by blow drying the samples at 50°C to dryness to remove excess formic acid and water. This was necessary as the >C=O of free formic acid in solution greatly interferes with the characterisation as it is in the same region as formates and >C=O stretching band of PVP. Fig. 6-11 shows

the results obtained for colloidal PVP-Pd and PVP-Pd-^{int}B. For both HCOOH adsorbed on PVP-Pd and PVP-Pd-^{int}B, a broad feature at 1750-1700 cm^{-1} observed was assigned to adsorbed formic acid. Two small peaks (barely discernible) can be seen in the region 2750-2450 cm^{-1} due to O-H stretching of adsorbed formic acid. Other minor features at 3000-2800 cm^{-1} were the C-H stretching and 1170 cm^{-1} due to C-H out of plane deformation. Other than the peak at 1660 cm^{-1} due to ν(CO) of PVP, one additional peak can be clearly seen at 1635 cm^{-1}. This was assigned to asymmetric ν(OCO) stretching of monodentate formate species. It was concluded that multi-monodentate modes (monodentate formates bind to one metal atom) was unlikely as it is likely it was swamped from the main >C=O PVP peak.[9] It must be noted that no bridging formate mode at ~1585 cm^{-1} was observed was probably its facile decomposition *via* C-H scission on the Pd surface.[23] In the case of the PVP-Pd-^{int}B sample, a small shouldering can be seen at 1626 cm^{-1} is indicative of the presence of the monodentate mode. Strikingly, on the other hand, a peak at 1586 cm^{-1} was also observed. This peak was not existent for the free HCOOH solution and that of dried PVP-Pd-^{int}B references. The observation of this peak was therefore assigned as bridging formates occurring on the Pd-^{int}B surface. The account as to why we observe bridging formate configuration and not on the PVP-Pd could be owing to an increased lattice parameter for the Pd-^{int}B as evidenced by PXRD. Increased lattice parameter (both on the surface and the inter-atomic layers) could dramatically alter the adsorption behaviour of HCOOH to metal, leading to changes in kinetic barriers for formate decomposition. Interestingly, the effect of lattice parameter against the electro-oxidation of HCOOH has been reported.[10] The authors noted that a Pd pseudomorphic overlayer with increased lattice parameter lead to an increase in the onset of oxidation current when compared to the activity of compressed overlayers.

Although it is widely accepted that, an increase in inter-atomic layer distance due to the increase in lattice parameter, would lead to shifting up of *d*-band centre (as is the case for more than half filled metals) relative to Fermi level, which could lead to stronger adsorption. The increase in surface lattice parameter within the top surface may subsequently alter the formate adsorption geometry. Therefore, the formation of bridging formate may become more stable, hence decreasing the overall catalytic activity.

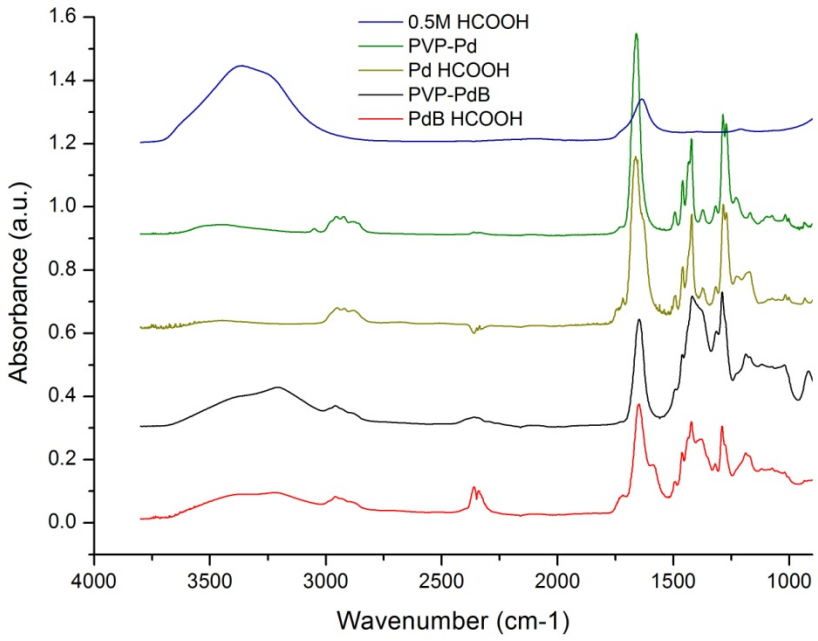

Fig. 6-11 ATR-FTIR spectra of: i) 0.5 M HCOOH solution (blue); ii) PVP-Pd as reference (green); iii) PVP-Pd mixed with 0.5 M HCOOH solution until dried (gold); iv) PVP-Pd-^{int}B as reference (black); v) PVP-Pd-^{int}B mixed with 0.5 M HCOOH solution until dried (red).

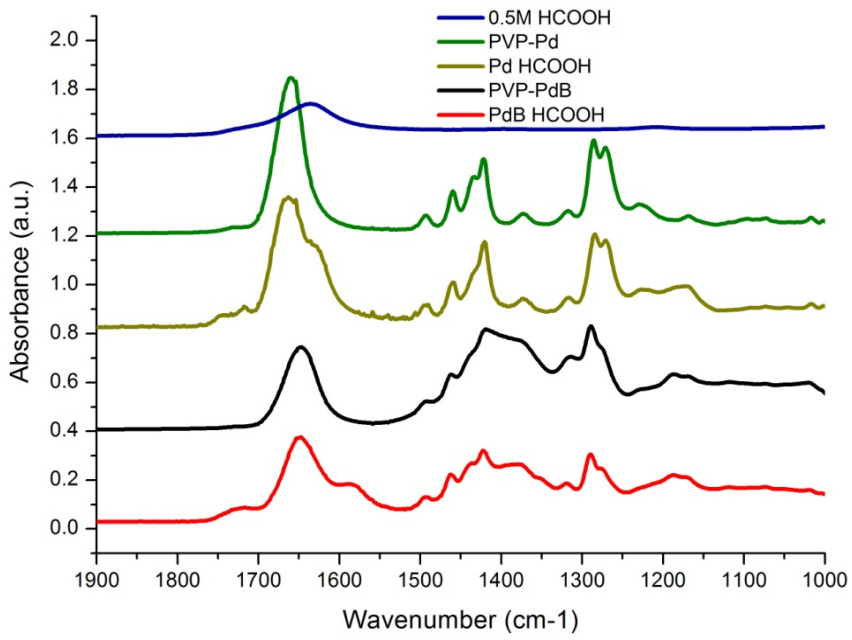

Fig. 6-12 A close-up ATR-FTIR spectra of Fig. 6-11: i) 0.5M HCOOH solution (blue); ii) PVP-Pd as reference (green); iii) PVP-Pd mixed with 0.5M HCOOH solution until dried (gold); iv) PVP-Pd-^{int}B as reference (black); v) PVP-Pd-^{int}B mixed with 0.5M HCOOH solution until dried (red).

6.4.4 NMR

6.4.4.1 ^{11}B NMR

Liquid ^{11}B NMR on PVP-Pd-^{int}B was studied to examine the nature of B species in the sample (Fig. 6-13). Three background peaks at 36.1, -3.3 and -49.2 ppm are observed due to the boron contained in the NMR tube. In addition, one peak at 19.77 ppm was observed, which matched well with boric acid in solution (at 19.36 ppm).[47] Note that no subsurface B species were detected probably due to the severe Knight shift from its close proximity to Pd atoms.

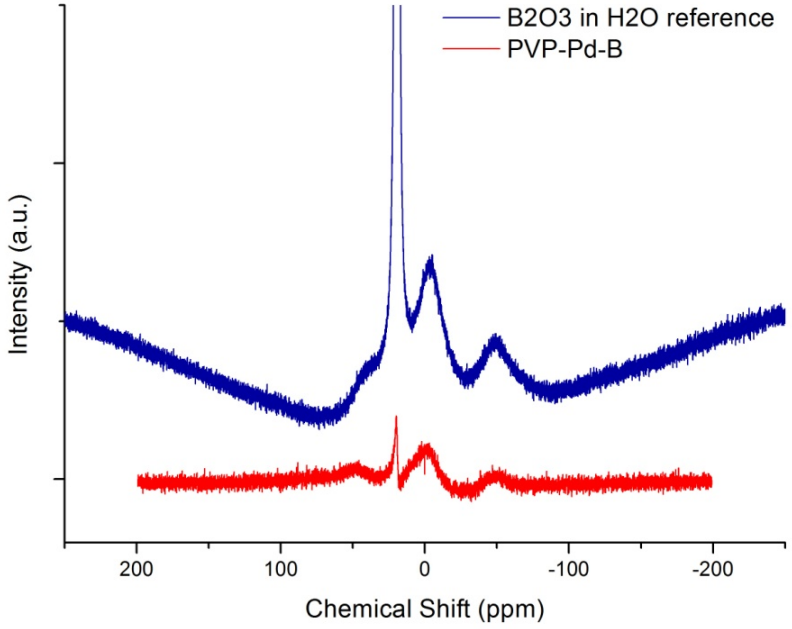

Fig. 6-13 Liquid ^{11}B spectra (96 MHz, 298K) for i) B_2O_3 dissolved in H_2O as reference (blue); ii) Colloidal PVP-Pd-^{int}B in D_2O (red).

6.4.4.2 ^{13}C NMR

Adsorbed formate species on the PVP-Pd was studied by liquid ^{13}C NMR (Fig. 6-14). The ratios of adsorbed formates and chemical shifts can provide information on the size and electronic characteristics of the metal surface. For all the Pd samples studied, HCOOH was rapidly decomposed to $^{13}CO_2$, as seen by a peak at 124.64 ppm even when analysed immediately. The high activity for HCOOH decomposition is attributed to the unique electronic and surface structure of Pd surface compared to other metals.[48] Apart from the peak arising from free H^{13}COOH in rapid exchange with Pd surface at 165.60 ppm, three other peaks observed at 165.68, 165.41 and 165.15 ppm were assigned to bridging, multi-monodentate and monodentate formates, respectively (Table 6-3).[9] The bridging peak appears to have merged to the main adsorbed H^{13}COOH peak more so compared to smaller particles sizes, where the peaks are well separated. This merging effect is consistent for larger size of Pd

(7.8 nm here). Peaks were deconvoluted using peak fitting revealed the absolute peak areas between these three formate species, which matches well to that of the literature.[19]

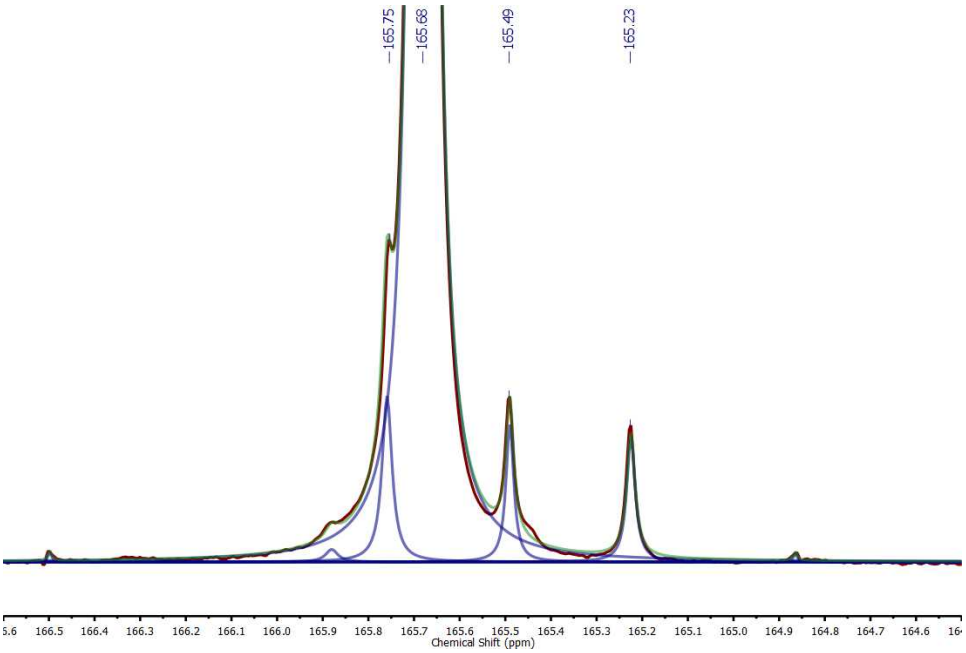

Fig. 6-14 Liquid ^{13}C NMR spectra for the colloidal PVP-Pd (125.8 MHz, D_2O, 298K). Red line is the real experimental data. Blue line is the fitted data. Green line is the sum of fitted data.

Size (nm)	Corrected chemical shift of formate species (ppm)				Ratio of Bridging: Multi: Mono (%)
	Bridging	Adsorbed Formic Acid	Multi-Monodentate	Mono-dentate	
7.8	165.68	165.60	165.41	165.15	44:28:28

Table 6-3 ^{13}C NMR values for the formate species observed for the PVP-Pd sample. Ratios of different formate modes were calculated by fitting the total peak area from the raw data.

Adsorbed formate species were examined for the PVP-Pd-^{int}B (Fig. 6-15, Table 6-4). Two distinct features can be observed:

i) The chemical shift for all formate and adsorbed H^{13}COOH peak shifted to higher ppm values compared to the PVP-Pd sample.

ii) The peaks are significantly broadened here especially evident for the multi-monodentate mode just about discernible by eye but was unable to be computationally fitted.

In comparison to the PVP-Pd sample, a higher chemical shift could be due to several factors:

i) Effects of subsurface B leading to a more electron rich Pd surface.

ii) An increase in lattice parameter (inter-atomic layers) leading to a stronger adsorption, which changes the formate adsorption geometry owing to a change in surface lattice parameter.

iii) An increase in surface acidity due to boric acid.

Unfortunately, further controlled experiments by adding B_2O_3 to a sample of colloidal PVP-Pd particles in water had concluded that we cannot neglect the effects of surface acidity, as higher concentrations of boric acid (confirmed higher concentrations of boric acid by ^{11}B NMR) indeed increased the overall chemical shift of adsorbed formates and surface exchanged $H^{13}COOH$. The second feature of peak broadening (half width of 11.4 Hz compared to dissolved $^{13}CO_2$ at 1.4 Hz) could be due to particle anisotropy and magnetic field inhomogenity.[19] Accordingly, the sample may have encountered some degree of sintering even additional PVP was added to enhance stability during the borylation step.

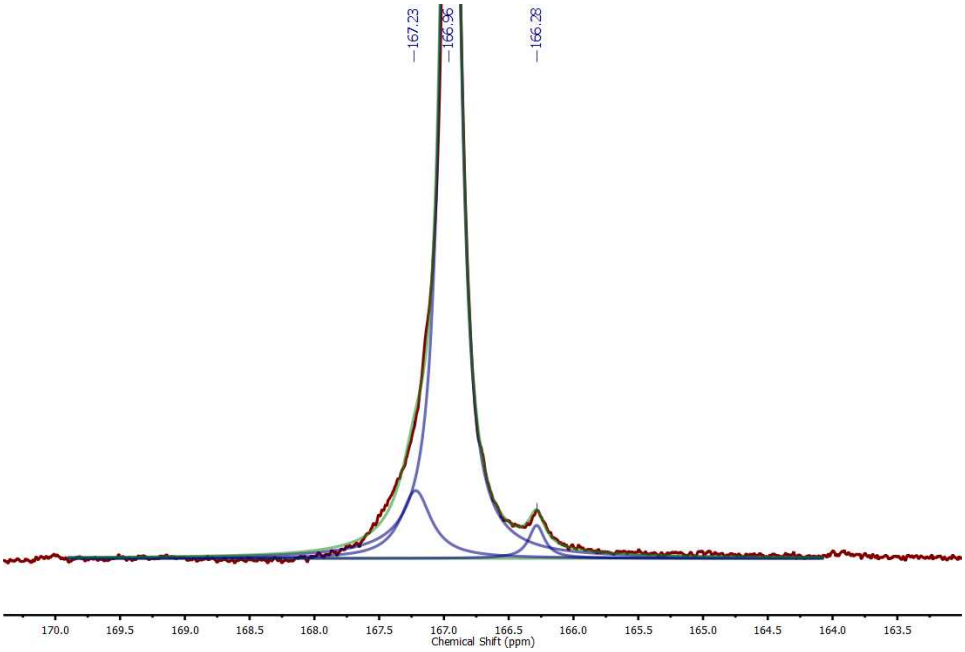

Fig. 6-15 Liquid ^{13}C NMR spectra for the colloidal PVP-Pd-^{int}B (125.8 MHz, D_2O, 298K). Red line is the real experimental data. Blue line is the fitted data. Green line is the sum of fitted data.

Sample	Corrected chemical shift of formate species (ppm)			
	Bridging	**Adsorbed formic acid**	**Multi-monodentate**	**Mono-dentate**
PVP-Pd-^{int}B	167.24	166.97	-	166.29

Table 6-4 ^{13}C NMR values for the formate species observed for the PVP-Pd-^{int}B sample.

6.4.5 DECOMPOSITION OF FORMIC ACID

The decomposition of HCOOH was tested on both the supported Pd/C compared to that of 3% Pd-^{int}B/C (Fig. 6-16). It was found that the borylated catalyst exhibited much lower TOF (defined as molecules of HCOOH assuming full conversion into H_2 and CO_2 per minute per surface Pd) compared to the non doped catalyst (Table 6-5). Such a decrease in activity observed here cannot simply be ascribed to a decrease in metal dispersion (from 3.6% to 2.3% before and after borylation as measured by CO chemisorption) since results here already accounted

for the total metal surface area. Therefore, a decrease in apparent decomposition activity could be linked to two factors:

i) Increased surface acidity due to the presence of boric acid leading to decreased rate.

ii) A change in surface lattice parameter, leading to a change in adsorption geometry hence lower kinetics for HCOOH decomposition, despite an increase in electron density on Pd.[10]

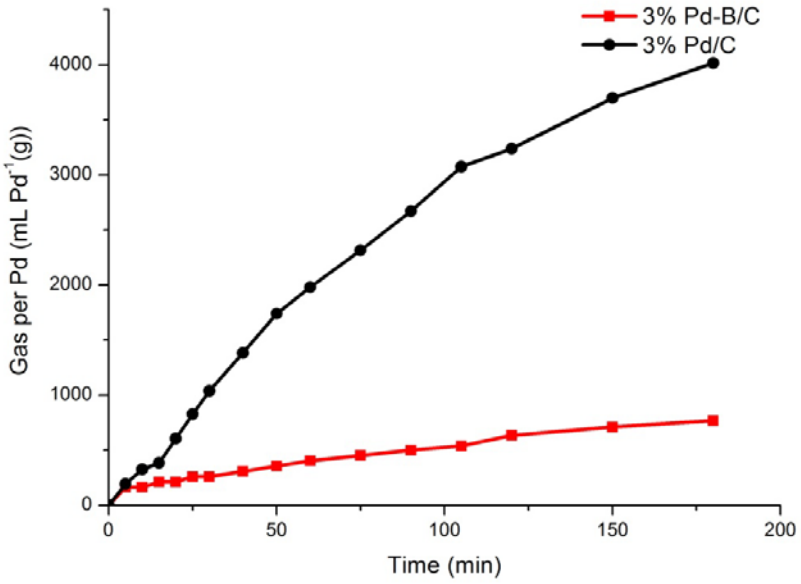

Fig. 6-16 Activity measurements for formic acid decomposition: i) 3% Pd/C (black); ii) 3% Pd-^{int}B/C doped with 25 eq. of BH_3.THF (red).

Catalyst	$Pd_{(s)}$ (Pd atoms $g^{-1}_{(cat)}$)	Decomposition rate (HCOOH molecules min^{-1})	TOF (HCOOH molecules min^{-1} $Pd(s)^{-1}$)
3% Pd/C	6.10×10^{18}	4.43×10^{18}	70
3% Pd-^{int}B/C	3.91×10^{18}	1.11×10^{18}	27

Table 6-5 Turnover frequencies for the HCOOH decomposition for 3% Pd/C and 3% Pd-^{int}B/C catalysts assuming total dehydrogenation of HCOOH to H_2 and CO_2 at room temperature. 10.41 mg of Pd metal was used in the reaction. Decomposition rates were based on gas evolved at 30 min of the reaction. The density of the surface Pd atoms was determined from CO chemisorption measurements.

6.4.6 CONCLUSION

Colloidal PVP stabilised Pd nanoparticles were synthesised using a modified ethylene glycol reduction. The PVP-Pd nanoparticles were doped with B using BH_3.THF solution in a DCM/THF suspension. PXRD revealed the existence of subsurface B in Pd in near saturation. ATR-FTIR confirmed no B-H_x species were in the sample and only that of oxidised boron. CO adsorption revealed a red shift in wavenumbers for bridging CO for the PVP-Pd-^{int}B sample, which could be due to a surface coverage effect or increased back donation to CO anti-bonding orbitals due to increased electron density on Pd. Adsorption of HCOOH on PVP-Pd revealed the presence of monodentate mode and no bridging mode was due to rapid HCOOH decomposition on the Pd surface. This was in contrast to the observation of bridging mode for PVP-Pd-^{int}B, which was assigned to a change in kinetics for HCOOH decomposition accompanied with a change in surface lattice parameter, leading to observation of this mode. Liquid ^{13}C NMR of the PVP-Pd-^{int}B revealed the chemical shift of H^{13}COOH was further downfield compared to the PVP-Pd. This was attributed to an increased surface acidity due to boric acid and increased electron density on the Pd surface. Decomposition of HCOOH solution was studied on the supported catalysts. It was found the borylated Pd/C catalyst exhibited much lower turnovers compared to before addition of boron. Such decrease in activity was assigned to increased surface acidity due to boric acid as well as increased surface lattice parameter leading to a change in kinetics to HCOOH decomposition, leading to the decreased rate observed. This study highlighted that the surface acidity and surface Pd lattice parameter are important for HCOOH decomposition.

6.5 REFERENCES

1. F. Joó, *ChemSusChem*, 2008, **1**, 805-808.
2. H. L. Jiang, S. K. Singh, J. M. Yan, X. B. Zhang and Q. Xu, *ChemSusChem*, 2010, **3**, 541-549.
3. D. D. Eley and P. Luetic, *Trans. Faraday Soc.*, 1957, **53**, 1483-1487.
4. D. M. Ruthven and R. S. Upadhye, *J. Catal.*, 1971, **21**, 39-47.
5. S. P. Hill and J. M. Winterbottom, *Journal of Chemical Technology & Biotechnology*, 1988, **41**, 121-133.
6. X. Zhou, Y. Huang, C. Liu, J. Liao, T. Lu and W. Xing, *ChemSusChem*, 2010, **3**, 1379-1382.
7. Y. Huang, X. Zhou, M. Yin, C. Liu and W. Xing, *Chem. Mater.*, 2010, **22**, 5122-5128.
8. X. Zhou, Y. Huang, W. Xing, C. Liu, J. Liao and T. Lu, *Chem. Commun.*, 2008, 3540-3542.
9. Karaked Tedsree, Adam T S Kong and Shik C. Tsang, *Angew. Chem. Int. Ed.*, 2009, **48**, 1443-1446.
10. L. A. Kibler, A. M. El-Aziz, R. Hoyer and D. M. Kolb, *Angew. Chem. Int. Ed.*, 2005, **44**, 2080-2084.
11. R. B. Grubbs, *Polymer Reviews*, 2007, **47**, 197-215.
12. H. Tsunoyama, H. Sakurai, N. Ichikuni, Y. Negishi and T. Tsukuda, *Langmuir*, 2004, **20**, 11293-11296.
13. H. Tsunoyama, H. Sakurai and T. Tsukuda, *Chem. Phys. Lett.*, 2006, **429**, 528-532.
14. B. Lim, M. Jiang, J. Tao, P. H. C. Camargo, Y. Zhu and Y. Xia, *Adv. Funct. Mater.*, 2009, **19**, 189-200.

15. Y. X. B. L. Sara E. S. Younan Xia, *Angew. Chem. Int. Ed.*, 2009, **48**, 60-103.

16. C. E. Hoppe, M. Lazzari, I. Pardinas-Blanco and M. A. Lopez-Quintela, *Langmuir*, 2006, **22**, 7027-7034.

17. M. Zhou, B. Wang, Z. Rozynek, Z. Xie, J. O. Fossum, X. Yu and S. Raaen, *Nanotechnology*, 2009, **20**, 505606.

18. K. Chari and W. C. Lenhart, *J. Colloid Interface Sci.*, 1990, **137**, 204-216.

19. K. Tedsree, C. W. A. Chan, S. Jones, Q. Cuan, W.-K. Li, X.-Q. Gong and S. C. E. Tsang, *Science*, 2011, **332**, 224-228.

20. B. Hammer and J. K. Norskov, *Nature*, 1995, **376**, 238-240.

21. R. Van Hardeveld and F. Hartog, *Surf. Sci.*, 1969, **15**, 189-230.

22. H. Ma, G. Wang, Y. Morikawa and J. Nakamura, *Sci. China, Ser. B Chem.*, 2009, **52**, 1427-1433.

23. N. Aas, L. Yongxue and M. Bowker, *J. Phys. Condens. Matter*, 1991, **3**, S281.

24. M. Ojeda and E. Iglesia, *Angew. Chem. Int. Ed.*, 2009, **48**, 4800-4803.

25. P. Mars, J. J. F. Scholten, P. Zwietering, H. P. D.D. Eley and B. W. Paul, in *Advances in Catalysis*, Academic Press, 1963, pp. 35-113.

26. M. Valden, X. Lai and D. W. Goodman, *Science*, 1998, **281**, 1647-1650.

27. H. Tsunoyama, N. Ichikuni, H. Sakurai and T. Tsukuda, *J. Am. Chem. Soc.*, 2009, **131**, 7086-7093.

28. M. López-Haro, Juan J. Delgado, José M. Cies, E. del Rio, S. Bernal, R. Burch, Miguel A. Cauqui, S. Trasobares, José A. Pérez-Omil, P. Bayle-Guillemaud and José J. Calvino, *Angew. Chem. Int. Ed.*, 2010, **49**, 1981-1985.

29. T. Janssens, B. Clausen, B. Hvolbæk, H. Falsig, C. Christensen, T. Bligaard and J. Nørskov, *Top. Catal.*, 2007, **44**, 15-26.

30. N. Lopez, T. V. W. Janssens, B. S. Clausen, Y. Xu, M. Mavrikakis, T. Bligaard and J. K. Nørskov, *J. Catal.*, 2004, **223**, 232-235.

31. F. Bonet, V. Delmas, S. Grugeon, R. Herrera Urbina, P. Y. Silvert and K. Tekaia-Elhsissen, *Nanostruct. Mater.*, 1999, **11**, 1277-1284.

32. S. B. Ziemecki, G. A. Jones, D. G. Swartzfager, R. L. Harlow and J. Faber, *J. Am. Chem. Soc.*, 1985, **107**, 4547-4548.

33. S. B. Zlemecki and G. A. Jones, *J. Catal.*, 1985, **95**, 621-622.

34. T. G. Berger, A. Leineweber, E. J. Mittemeijer, C. Sarbu, V. Duppel and P. Fischer, *Z. Kristall.*, 2006, **221**, 450-463.

35. J. Tamaki, S. Nakayama, M. Yamamura and T. Imanaka, *J. Mater. Sci.*, 1989, **24**, 1582-1588.

36. M. Beck, M. Ellner and E. J. Mittemeijer, *Powder Diffr.*, 2001, **16**, 98-101.

37. M. Beck, M. Ellner and E. J. Mittemeijer, *Z. Kristall.*, 2001, **216**, 591-594.

38. M. Beck and E. J. Mittemeijer, *Z. Metallk.*, 2001, **92**, 1271-1276.

39. P. Liao, K. Spear and M. Schlesinger, *J. Phase Equilib. Diffus.*, 1996, **17**, 340-345.

40. P. Rogl, G. Effenberg and Editors, *Phase Diagrams of Ternary Metal-boron-carbon Systems*, ASM International, 1998.

41. E. A. Baranova, C. Bock, D. Ilin, D. Wang and B. MacDougall, *Surf. Sci.*, 2006, **600**, 3502-3511.

42. J. S. Bradley, J. Millar, E. W. Hill and M. Melchior, *J. Chem. Soc., Chem. Commun.*, 1990, 705-706.

43. D. de Caro and J. S. Bradley, *Langmuir*, 1998, **14**, 245-247.

44. J. S. Bradley, J. M. Millar, E. W. Hill, S. Behal, B. Chaudret and A. Duteil, *Faraday Discuss.*, 1991, **92**, 255-268.

45. D. Peak, G. W. Luther Iii and D. L. Sparks, *Geochim. Cosmochim. Acta*, 2003, **67**, 2551-2560.

46. B. H. Stuart, *Infrared Spectroscopy-Fundamentals and Applications. (Analytical Techniques in the Sciences (AnTs))*, John Wiley & Sons, 2004.

47. M. Bishop, N. Shahid, J. Yang and A. R. Barron, *Dalton Trans.*, 2004, 2621-2634.

48. K. Tedsree, T. Li, S. Jones, C. W. A. Chan, K. M. K. Yu, P. A. J. Bagot, E. A. Marquis, G. D. W. Smith and S. C. E. Tsang, *Nat. Nanotechnol.*, 2011, **6**, 302-307.

CHAPTER 7 - CONCLUSION AND FUTURE PERSPECTIVE

7.1 CONCLUSION

Within this thesis a series of novel materials have been developed with subsurface metal modifications to tune the surface reactivity, which can have dramatic changes in reaction activity and selectivity. It was demonstrated for the first time that carbon atoms trapped inside the octahedral holes of Pd increases stereoselective hydrogenation of alkynes to alkenes in the liquid phase, of which the reaction has importance in the fine chemical and pharmaceutical industry.

This methodology was then extended to synthesise for the first time, Pd with a high concentration of interstitial B in the liquid phase at low temperatures whilst maintaining high metal surface are for catalysis. The new material was shown to be highly selective towards a variety of liquid phase hydrogenation reactions.

Other research detailed in this thesis is the use of liquid phase ^{13}C NMR to characterise the surface of Au and Pd-B nanoparticles. The research here demonstrated that the overall adsorption strength of the substrate molecule can be examined using this method, which can aid the search for new catalysts.

7.2 FUTURE PERSPECTIVE

The field of nanotechnology will continue to grow in the foreseeable future. This research area is deeply rooted in our society and one will continue to develop new catalyst for new processes, or improving existing plant in activity, selectivity and stability. Chemical companies such as BASF, BP, DuPont, Exxon Mobil, Johnson Matthey and Shell continue to expand their portfolio of new solid catalysts through increasing numbers of patents and publications based in nano approaches. I see the field of heterogeneous catalysis continuously re-inventing itself to meet the social, economic and environmental challenges of the future.